THE PARAMETRIC GENERALIZED FRACTIONAL NIKIFOROV-UVAROV METHOD AND ITS APPLICATIONS†

M. Abu-Shady[a,*], H.M. Fath-Allah[b]

aDepartment of Mathematics and Computer Sciences, Faculty of Science, Menoufia University, Egypt
bHigher Institute of Engineering and Technology, Menoufia, Egypt
*Corresponding Author e-mail: dr.abushady@gmail.com

By using generalized fractional derivative, the parametric generalized fractional Nikiforov-Uvarov (NU) method is introduced. The second-order parametric generalized differential equation is exactly solved in the fractional form. The obtained results are applied on the extended Cornell potential, the pesudoharmonic potential, the Mie potential, the Kratzer-Fues potential, the harmonic oscillator potential, the Morse potential, the Woods-Saxon potential, the Hulthen potential, the deformed Rosen-Morse potential and the Pöschl-Teller potential which play an important role in the fields of molecular and hadronic physics. The special of classical cases are obtained from the fractional cases at $\alpha = \beta = 1$ which are agreements with recent works.

Keywords: *Nonrelativistic models; Generalized fractional derivative; Molecular physics; Hadronic physics*
PACS: 12.39.Jh, 31.15.-p, 02.70.−c

1. INTRODUCTION

Many researchers have been interested in the fractional calculus (FC) during the past three decades in the previous and current centuries [1-2]. The importance of FC has significantly increased in a variety of scientific and technical fields and explain the advantages of the (FC) over the other numerical methods because we can get exact solution but numerical method can get approximate solution also, there are a lot of problems in solving partial equations. In fact, there are many papers using symmetry methods to solve differential equations including fractional differential equations such as in Ref. [3]. They study modified Gardner-type equation and its time fractional form. They derived these two equations from Fermi-Pasta-Ulam model, and found that these two equations are related with nonlinear Schrodinger equation. They not only derive these two equations, but also use perturbation analysis to find the connection between them and the Schrodinger equation. Non- integer order differentiation and integration form the basis of FC. Numerous definitions of the fractional differential equations have been put out in the literature. The definitions of Jumarie [4], Riemann-Liouville [5], and Caputo [6] have gotten a lot of attention and are the most suitable for physical conditions. Al-Raeei and El-Daher [7], used a numerical technique to rely on the definition of Riemann-Liouville fractional derivative. Khalil et al. [8] represented a new definition of a fractional derivative, referred to as a conformable fractional derivative (CFD) which follows to basic classical principles. Abdeljawad [9] extended the definition and established the fundamental notions of the CFD. A new concept for the fractional derivative known as the generalized fractional derivative (GFD) was recently proposed by Abu-Shady and Kaabar [10]. Because it offers more features than the previous definitions [4-6,10], where the CFD may be produced as a special case from the GFD, the GFD definition is regarded as a comprehensive type for the fractional derivative.

Solving Schrödinger equation (SE) with the intention of examining a physical system is a fundamental challenge in quantum mechanics and particle physics [11-17]. In Ref. [18]. the conformable fractional of the Nikiforov-Uvarov (CF-NU) method is used to analytically solve the radial Schrödinger equation and the dependent temperature potential is used to obtain the energy eigenvalues, corresponding wave functions, and heavy quarkonium masses like charmonium and bottomonium in a hot QCD medium in the 3D and higher dimensions. In Ref. [19], the trigonometric Rosen-Morse potential is employed to examine the effect of the fraction-order parameter. The N-radial fractional Schrödinger equation has analytical solutions established using the extended Nikiforov-Uvarov method. The energy eigenvalues in the fractional forms and the masses of mesons such as charmonium and bottomonium were also obtained.

Using the generalized fractional NU method, the fractional N-dimensional radial Schrödinger equation (SE) with the Deng-Fan potential is evaluated in Ref. [20] in which the analytical formulas are generated for the energy eigenvalues and corresponding eigenfunctions at three-dimensional space and higher dimensions to study the energy spectra of various molecules. The analytical-exact iteration method with a conformable fractional derivative is used in Ref. [21] in which the radial Schrödinger equation can be solved analytically with the trigonometric Rosen-Morse potential. In Ref. [22], the fractional nonrelativistic potential model is used to explore the dissociation of heavy quarkonium in a hot magnetized medium in which the energy eigenvalues and the radial wave functions are obtained. The generalized fractional analytical iteration method is used as in Ref. [23] to solve the hyper-central Schrödinger

equation and studied its applications on the theory baryons with single, double, and triple in the ground state. In addition, the SE can be exactly solved, the system can be fully described as in [24, 25, 26] using the Nikiforov Uvarov method. This method is very good because we get on a good result compared by another methods as in Refs. [22, 23].

The aim of the present work is to generalize the second-order parametric differential equation in the fractional form by using generalized fractional derivative. The special cases are obtained at $\alpha = \beta = 1$. Many applications are introduced such as the extended Cornell potential, the Pesudoharmonic potential, the Mie potential, the Kratzer-Fues potential, the harmonic oscillator potential, the Morse potential, the Woods-Saxon potential, the Hulthen potential, the Deformed Rosen-Morse potential and Pöschl-Teller potential. This work is not considered in the recent works.

This paper is arranged as follows. In Sec. 2, the generalized fractional derivative is briefly introduced. In Sec. 3, the generalized fractional Nikiforov-Uvarov (NU) method is explained. In Sec. 4, Some Applications are obtained. In Sec. 5, the conclusion is written.

2. THE GENERALIZED FRACTIONAL DERIVATIVE

A new formula for a fractional derivative called the generalized fractional derivative (GFD) is proposed. The generalized fractional Derivative has been suggested to provide more advantages than other classical Caputo and Riemann–Liouville fractional derivative definitions such that the derivative of two functions, the derivative of the quotient of two function, Rollés theorem and the mean value theorem which have been satisfied in the GFD and which gives a new direction for simply solving fractional differential equations see Ref. [10]. For a function $Z : (0,\infty) \to R$, the generalized fractional derivative of order $0 < \alpha \le 1$ of $Z(t)$ at > 0 is defined as

$$D^{GFD} Z(t) = \lim_{\varepsilon \to 0} \frac{Z\left(t + \frac{\Gamma(\beta)}{\Gamma(\beta - \alpha + 1)} \varepsilon t^{1-\alpha}\right) - Z(t)}{\varepsilon}; \beta > -1, \beta \epsilon R^+ \tag{1}$$

The properties of the generalized fractional derivative are,

    I. $D^{\alpha}[Z_{nl}(t)] = k_1 \, t^{1-\alpha} \, \dot{Z}_{nl}(t),$ (2)

    II. $D^{\alpha}[D^{\alpha} Z(t)] = k_1{}^2 \, [(1-\alpha) \, t^{1-2\alpha} \, \dot{Z}_{nl}(t) + t^{2-2\alpha} \, Z_{nl}''(t)],$ (3)

where, $k_1 = \frac{\Gamma[\beta]}{\Gamma[\beta - \alpha + 1]}$, with $0 < \alpha \le 1, 0 < \beta \le 1$

    III. $D^{\alpha} D^{\beta} t^m = D^{\alpha + \beta} t^m$ for function derivative of $Z(t) = t^m$, $m \epsilon R^+$

    IV. $D^{GFD}(XY) = X D^{GFD}(Y) + Y D^{GFD}(X)$ where X, Y be $\alpha -$ differentiable function

    V. $D^{GFD}\left(\frac{X}{Y}\right) = \frac{Y D^{GFD}(X) - X D^{GFD}(Y)}{Y^2}$ where X, Y be α- differentiable function

    VI. $D^{\alpha} I_{\alpha} Z(t) = Z(t)$ for ≥ 0 and Z is any continuous function in the domain.

2.1. The Generalized Fractional Nikiforov-Uvarov (NU) Method.

By using generalized fractional derivative, the parametric generalized fractional Nikiforov-Uvarov (NU) method is introduced. The second-order parametric generalized differential equation is exactly solved in the fractional form as in Ref. [27]

$$D^{\alpha}[D^{\alpha}\psi(s)] + \frac{\bar{\tau}(s)}{\sigma(s)} D^{\alpha}\psi(s) + \frac{\overline{\sigma}(s)}{\sigma^2} \psi(s) = 0, \tag{4}$$

where $\overline{\sigma}$, $\sigma(s)$ and $\bar{\tau}(s)$ are polynomials of $2\alpha -$th, $2\alpha -$th and $\alpha -$th degree.
where,

$$\pi(s) = \frac{D^{\alpha}\sigma(s) - \bar{\tau}(s)}{2} \pm \sqrt{\left(\frac{D^{\alpha}\sigma(s) - \bar{\tau}(s)}{2}\right)^2 - \overline{\sigma}(s) + K\sigma(s)}, \tag{5}$$

and

$$\lambda = K + D^{\alpha}\pi(s), \tag{6}$$

λ is constant and $\pi(s)$ is $\alpha -$th degree polynomial. The values of K in the square-root of Eq. (5) is possible to determine whether the expression under the square root is square of expression. Replacing K into Eq. (5), we define

$$\tau(s) = \bar{\tau}(s) + 2\pi(s), \tag{7}$$

the derivative of τ should be negative [28], since $\rho(s) > 0$ and $\sigma(s) > 0$ then this is solution. If λ in Eq. (6) is

$$\lambda = \lambda_n = -n D^{\alpha} \tau - \frac{n(n-1)}{2} D^{\alpha}[D^{\alpha}\sigma(s)]. \tag{8}$$

The hypergeometric type equation has a particular solution with degree α. Eq. (4) has a solution which is the product of two independent parts

$$\psi(s) = \phi(s)\, y(s), \tag{9}$$

where,

$$y_n(s) = \frac{B_n}{\rho(s)}\,(D^\alpha)^n(\,\sigma(s)^n\,\rho_n(s)), \tag{10}$$

$$D^\alpha[\sigma(s)\,\rho(s)] = \tau(s)\,\sigma(s), \tag{11}$$

$$\frac{D^\alpha \phi(s)}{\phi(s)} = \frac{\pi(s)}{\sigma(s)} \tag{12}$$

2.2. Second Order Parametric Generalized Differential Equation

The following equation is a general form of the Schrödinger equation which can be obtained by transforming into a second-order parametric generalized differential equation.

$$D^\alpha[\,D^\alpha \psi(s)] + \frac{\alpha_1 - \alpha_2\, s^\alpha}{s^\alpha(1-\alpha_3\, s^\alpha)}\, D^\alpha \psi(s) + \frac{-\,\xi_1\, s^{2\alpha} + \xi_2\, s^\alpha - \xi_3}{(s^\alpha(1-\alpha_3\, s^\alpha))^2}\,\psi(s) = 0. \tag{13}$$

$$\bar{\tau}(s) = \alpha_1 - \alpha_2\, s^\alpha, \tag{14}$$

$$\sigma(s) = s^\alpha(1 - \alpha_3\, s^\alpha), \tag{15}$$

$$\breve{\sigma}(s) = -\,\xi_1\, s^{2\alpha} + \xi_2\, s^\alpha - \xi_3. \tag{16}$$

Substituting these into Eq. (5), we obtain

$$\pi = \alpha_4 + \alpha_5\, s^\alpha \pm \sqrt{(\alpha_6 - K\,\alpha_3)\, s^{2\alpha} + (\alpha_7 + K)\, s^\alpha + \alpha_8}\,, \tag{17}$$

where,

$$\alpha_4 = \tfrac{1}{2}\,(\,k_1 \alpha - \alpha_1) \tag{18}$$

$$\alpha_5 = \tfrac{1}{2}\,(\alpha_2 - 2\,\alpha_3\, k_1 \alpha) \tag{19}$$

$$\alpha_6 = \alpha_5{}^2 + \xi_1 \tag{20}$$

$$\alpha_7 = 2\,\alpha_4\,\alpha_5 - \xi_2 \tag{21}$$

$$\alpha_8 = \alpha_4{}^2 + \xi_3 \tag{22}$$

In Eq. (17), the function under square root must be the square of a polynomial according to the NU method, so that

$$K = -\,(\alpha_7 + 2\,\alpha_3 \alpha_8) \pm 2\,\sqrt{\alpha_8 \alpha_9}, \tag{23}$$

where,

$$\alpha_9 = \alpha_3\,\alpha_7 + \alpha_3{}^2\,\alpha_8 + \alpha_6. \tag{24}$$

In case K is negative in the form

$$K = -\,(\alpha_7 + 2\,\alpha_3 \alpha_8) - 2\,\sqrt{\alpha_8 \alpha_9} \tag{25}$$

So that π becomes

$$\pi = \alpha_4 + \alpha_5\, s^\alpha - [(\sqrt{\alpha_9} + \alpha_3\,\sqrt{\alpha_8})\, s^\alpha - \sqrt{\alpha_8}] \tag{26}$$

From Eqs. (7), (17) and (26), we get

$$\tau = \alpha_1 + 2\,\alpha_4 - (\alpha_2 - 2\,\alpha_5)\, s^\alpha - [(\sqrt{\alpha_9} + \alpha_3\,\sqrt{\alpha_8})\, s^\alpha - \sqrt{\alpha_8}] \tag{27}$$

From Eqs. (2) and (27), we get,

$$D^\alpha\,\tau = k_1\,[-\,\alpha\,(\alpha_2 - 2\,\alpha_5) - 2\,\alpha\,(\sqrt{\alpha_9} + \alpha_3\,\sqrt{\alpha_8})\,] = k_1\,[-\,2\,\alpha^2\,\alpha_3 - 2\,\alpha\,(\sqrt{\alpha_9} + \alpha_3\,\sqrt{\alpha_8})] < 0 \tag{28}$$

From Eqs. (6, 8), we get the equation of the energy spectrum

$$n\,k_1\,\alpha\,\alpha_2 - (2n+1)\,k_1\,\alpha\,\alpha_5 + (2n+1)\,k_1\,\alpha\,(\sqrt{\alpha_9} + \alpha_3\,\sqrt{\alpha_8}) + n\,(n-1)\,k_1{}^2\,\alpha^2\,\alpha_3 + \alpha_7 + 2\,\alpha_3\,\alpha_8 + 2\,\sqrt{\alpha_8 \alpha_9} = 0 \tag{29}$$

If $\alpha = 1 = \beta$ then $k_1 = 1$, we get the classical equation of the energy eigenvalue as Ref. [25]

$$n\,\alpha_2 - (2n+1)\,\alpha_5 + (2n+1)\,(\sqrt{\alpha_9} + \alpha_3\,\sqrt{\alpha_8}) + n\,(n-1)\,\alpha_3 + \alpha_7 + 2\,\alpha_3\,\alpha_8 + 2\,\sqrt{\alpha_8 \alpha_9} = 0. \tag{30}$$

from Eq. (11), we get

$$\rho(s) = s^{\frac{\alpha_{10}-\alpha}{k_1}} (1 - \alpha_3 s^\alpha)^{\frac{\alpha_{11}}{\alpha k_1 \alpha_3} - \frac{\alpha_{10}}{\alpha k_1} - \frac{1}{k_1}} \tag{31}$$

From Eq. (10), we get

$$y_n = P_n^{(\frac{\alpha_{10}-\alpha}{k_1}, \frac{\alpha_{11}}{\alpha k_1 \alpha_3} - \frac{\alpha_{10}}{\alpha k_1} - \frac{1}{k_1})} (1 - 2 \alpha_3 s^\alpha) \tag{32}$$

where,

$$\alpha_{10} = \alpha_1 + 2 \alpha_4 + 2 \sqrt{\alpha_8} \tag{33}$$

$$\alpha_{11} = \alpha_2 - 2 \alpha_5 + 2 (\sqrt{\alpha_9} + \alpha_3 \sqrt{\alpha_8}) \tag{34}$$

From Eq. (9), the generalized solution of the wave function becomes,

$$\psi(s) = s^{\frac{\alpha_{12}}{k_1}} (1 - \alpha_3 s^\alpha)^{\frac{-\alpha_{13}}{\alpha k_1 \alpha_3} - \frac{\alpha_{12}}{\alpha k_1}} P_n^{(\frac{\alpha_{10}-\alpha}{k_1}, \frac{\alpha_{11}}{\alpha k_1 \alpha_3} - \frac{\alpha_{10}}{\alpha k_1} - \frac{1}{k_1})} (1 - 2 \alpha_3 s^\alpha) \tag{35}$$

where,
$P_n^{(\gamma,\delta)}$ are Jacobi polynomials.

$$\alpha_{12} = \alpha_4 + \sqrt{\alpha_8} \tag{36}$$

$$\alpha_{13} = \alpha_5 - (\sqrt{\alpha_9} + \alpha_3 \sqrt{\alpha_8}) \tag{37}$$

Some problems, in case $\alpha_3 = 0$.

$$\lim_{\alpha_3 \to 0} P_n^{(\frac{\alpha_{10}-\alpha}{k_1}, \frac{\alpha_{11}}{\alpha k_1 \alpha_3} - \frac{\alpha_{10}}{\alpha k_1} - \frac{1}{k_1})} (1 - \alpha_3 s^\alpha) = L_n^{\frac{\alpha_{10}-\alpha}{k_1}} (\frac{\alpha_{11}}{\alpha k_1} s^\alpha) \tag{38}$$

$$\lim_{\alpha_3 \to 0} (1 - \alpha_3 s^\alpha)^{\frac{-\alpha_{13}}{\alpha k_1 \alpha_3} - \frac{\alpha_{12}}{\alpha k_1}} = e^{\frac{\alpha_{13}}{\alpha k_1} s^\alpha} \tag{39}$$

Eq. (35), becomes

$$\psi(s) = s^{\frac{\alpha_{12}}{k_1}} e^{\frac{\alpha_{13}}{\alpha k_1} s^\alpha} L_n^{\frac{\alpha_{10}-\alpha}{k_1}} (\frac{\alpha_{11}}{\alpha k_1} s^\alpha). \tag{40}$$

Where, L_n being the Laguerre polynomials.
The second solution of Eq. (23) in the following case

$$K = - (\alpha_7 + 2 \alpha_3 \alpha_8) + 2 \sqrt{\alpha_8 \alpha_9} \tag{41}$$

then, the wave function is,

$$\psi(s) = s^{\frac{\alpha_{12}^*}{k_1}} (1 - \alpha_3 s^\alpha)^{\frac{-\alpha_{13}^*}{\alpha k_1 \alpha_3} - \frac{\alpha_{12}^*}{\alpha k_1}} P_n^{(\frac{\alpha_{10}^*-\alpha}{k_1}, \frac{\alpha_{11}^*}{\alpha k_1 \alpha_3} - \frac{\alpha_{10}^*}{\alpha k_1} - \frac{1}{k_1})} \times (1 - 2 \alpha_3 s^\alpha) \tag{42}$$

The generalized solution of the energy eigenvalue is,

$$n k_1 \alpha \alpha_2 - 2n k_1 \alpha \alpha_5 + (2n+1) k_1 \alpha (\sqrt{\alpha_9} - \alpha_3 \sqrt{\alpha_8}) + n(n-1) k_1^2 \alpha^2 \alpha_3 + \alpha_7 + 2 \alpha_3 \alpha_8 - 2\sqrt{\alpha_8 \alpha_9} + k_1 \alpha \alpha_5 = 0 \tag{43}$$

where,

$$\begin{rcases} \alpha_{10}^* = \alpha_1 + 2 \alpha_4 - 2 \sqrt{\alpha_8}, \\ \alpha_{11}^* = \alpha_2 - 2 \alpha_5 + 2 (\sqrt{\alpha_9} - \alpha_3 \sqrt{\alpha_8}) \quad \alpha_{12}^* = \alpha_4 - \sqrt{\alpha_8}, \\ \alpha_{13}^* = \alpha_5 - (\sqrt{\alpha_9} - \alpha_3 \sqrt{\alpha_8}). \end{rcases} \tag{44}$$

3. SOME APPLICATIONS
Case (1): Extended Cornell potential
We note that Cornell potential has two features the Coulomb potential and the confinement potential. The Coulomb potential describes the interaction at the short distance and confinement part describes the interaction at the long distances, and the harmonic potential to support the confinement force and it is mainly used to describe bound states of hadrons as in Ref. [29].

$$V(r) = ar^2 + b r - \frac{c}{r}, \tag{45}$$

The radial Schrodinger equation where, the interaction potential is the extended Cornell potential defined as in Ref. [29] and $s = e^{-\lambda r}$ that we get,

$$\frac{d^2R}{dr^2} + \frac{1}{s} \frac{dR}{dr} + \frac{1}{s^2(1-s)^2} \{-\xi_1 s^2 + \xi_2 s - \xi_3\} R(s) = 0 \tag{46}$$

where,

$$\xi_1 = -\frac{2\mu E}{\hbar^2\lambda^2} + t_1, \ \xi_2 = -\frac{4\mu E}{\hbar^2\lambda^2} + t_2, \ \xi_3 = -\frac{2\mu E}{\hbar^2\lambda^2} + t_3, \tag{47}$$

with,

$$
\left.
\begin{aligned}
t_1 &= \frac{12\mu a}{\lambda^4\hbar^2} + \frac{6\mu b}{\lambda^3\hbar^2}, \\
t_2 &= \frac{8\mu a}{\lambda^4\hbar^2} + \frac{6\mu b}{\lambda^3\hbar^2} - \frac{2\mu c}{\lambda\,\hbar^2}, \\
t_3 &= \frac{2\mu a}{\lambda^4\hbar^2} + \frac{2\mu b}{\lambda^3\hbar^2} - \frac{2\mu c}{\lambda\,\hbar^2} + l(l+1),
\end{aligned}
\right\} \tag{48}
$$

and we get the generalized fractional radial part of the Schrödinger equation is

$$D^\alpha[\,D^\alpha R(s)] + \frac{1-s^\alpha}{s^\alpha(1-s^\alpha)} D^\alpha R(s) + \frac{-\xi_1 s^{2\alpha} + \xi_2 s^\alpha - \xi_3}{(s^\alpha(1-s^\alpha))^2} R(\mathrm{s}) = 0, \tag{49}$$

By using the following parameters, we get

$$
\left.
\begin{aligned}
\alpha_1 &= 1, \alpha_2 = 1, \alpha_3 = 1, \ \alpha_4 = \frac{1}{2}(k_1\alpha - 1), \\
\alpha_5 &= \frac{1}{2}(1 - 2k_1\alpha), \alpha_6 = \frac{1}{4}(1 - 2k_1\alpha)^2 - \frac{2\mu E}{\hbar^2\lambda^2} + t_1, \\
\alpha_7 &= \frac{1}{2}(k_1\alpha - 1)(1 - 2k_1\alpha) + \frac{4\mu E}{\hbar^2\lambda^2} - t_2, \\
\alpha_8 &= \frac{1}{4}(k_1\alpha - 1)^2 - \frac{2\mu E}{\hbar^2\lambda^2} + t_3, \alpha_9 = \frac{1}{4}k_1^2\alpha^2 + t_1 - t_2 + t_3, \\
\alpha_{10} &= k_1\alpha + 2\sqrt{\frac{1}{4}(k_1\alpha - 1)^2 - \frac{2\mu E}{\hbar^2\lambda^2} + t_3}, \\
\alpha_{11} &= 2k_1\alpha + 2\left(\sqrt{\frac{1}{4}k_1^2\alpha^2 + t_1 - t_2 + t_3} + \sqrt{\frac{1}{4}(k_1\alpha - 1)^2 - \frac{2\mu E}{\hbar^2\lambda^2} + t_3}\right), \\
\alpha_{12} &= \frac{1}{2}(k_1\alpha - 1) + \sqrt{\frac{1}{4}(k_1\alpha - 1)^2 - \frac{2\mu E}{\hbar^2\lambda^2} + t_3}, \\
\alpha_{13} &= \frac{1}{2}(1 - 2k_1\alpha) - \left(\sqrt{\frac{1}{4}k_1^2\alpha^2 + t_1 - t_2 + t_3} + \sqrt{\frac{1}{4}(k_1\alpha - 1)^2 - \frac{2\mu E}{\hbar^2\lambda^2} + t_3}\right),
\end{aligned}
\right\} \tag{50}
$$

We get, the generalized fractional of the energy eigenvalue is

$$E = \frac{\hbar^2\lambda^2}{2\mu}\left(t_3 + \frac{1}{4}(k_1\alpha - 1)^2\right) - \frac{\hbar^2\lambda^2}{2\mu}\left(\frac{t_1 - t_3 - \left(\left(n+\frac{1}{2}\right)k_1\alpha + \sqrt{\frac{1}{4}k_1^2\alpha^2 + t_1 - t_2 + t_3}\right)^2}{2\left(\left(n+\frac{1}{2}\right)k_1\alpha + \sqrt{\frac{1}{4}k_1^2\alpha^2 + t_1 - t_2 + t_3}\right)}\right)^2 \tag{51}$$

where, $t = t_1 - t_2 + t_3$,

The generalized fractional of the wave function is,

$$\psi(s) = A\, s^{\frac{\frac{1}{2}(k_1\alpha - 1) + \sqrt{\frac{1}{4}(k_1\alpha - 1)^2 - \frac{2\mu E}{\hbar^2\lambda^2} + t_3}}{k_1}} (1s^\alpha)^{\frac{-\left(\frac{1}{2}(1 - 2k_1\alpha) - \left(\sqrt{\frac{1}{4}k_1^2\alpha^2 + t} + \sqrt{\frac{1}{4}(k_1\alpha - 1)^2 - \frac{2\mu E}{\hbar^2\lambda^2} + t_3}\right)\right)}{k_1\alpha} - \frac{\frac{1}{2}(k_1\alpha - 1) + \sqrt{\frac{1}{4}(k_1\alpha - 1)^2 - \frac{2\mu E}{\hbar^2\lambda^2} + t_3}}{k_1\alpha}}$$

$$P_n^{\left(\frac{-\alpha + k_1\alpha + 2\sqrt{\frac{1}{4}(k_1\alpha - 1)^2 - \frac{2\mu E}{\hbar^2\lambda^2} + t_3}}{k_1}, \ \frac{2k_1\alpha + 2\left(\sqrt{\frac{1}{4}k_1^2\alpha^2 + t} + \sqrt{\frac{1}{4}(k_1\alpha - 1)^2 - \frac{2\mu E}{\hbar^2\lambda^2} + t_3}\right)}{k_1\alpha} - \frac{k_1\alpha + 2\sqrt{\frac{1}{4}(k_1\alpha - 1)^2 - \frac{2\mu E}{\hbar^2\lambda^2} + t_3}}{k_1\alpha} - \frac{1}{k_1}\right)} \times (1 - 2s^\alpha) \tag{52}$$

where A is a normalization constant.

If $\alpha = \beta = 1$ then $k_1 = 1$, so that we get the energy eigenvalue and the corresponding wave function as Ref. [29]. as follows

$$E = \frac{\hbar^2\lambda^2}{2\mu}t_3 - \frac{\hbar^2\lambda^2}{2\mu}\left(\frac{t_1 - t_3 - \left(\left(n+\frac{1}{2}\right) + \sqrt{\frac{1}{4} + t_1 - t_2 + t_3}\right)^2}{2\left(\left(n+\frac{1}{2}\right) + \sqrt{\frac{1}{4} + t_1 - t_2 + t_3}\right)}\right)^2 \tag{53}$$

$$\psi(s) = A\, s^{\sqrt{-\frac{2\mu E}{\hbar^2\lambda^2} + t_3}} (1 - s)^{\frac{1}{2} + \sqrt{\frac{1}{4} + t}} P_n^{\left(2\sqrt{-\frac{2\mu E}{\hbar^2\lambda^2} + t_3}, \, 2\sqrt{\frac{1}{4} + t}\right)} (1 - 2s) \tag{54}$$

Case (2): Pesudoharmonic Potential

Pesudoharmonic Potential is mainly used to describe bound states of spectroscopy of die-atomic molecules and may be used for energy spectra of linear and non-linear systems, see Refs. [30,31] for details.

$$V(r) = V_0 \left(\frac{r}{r_0} - \frac{r_0}{r}\right)^2, \tag{55}$$

where, V_0 is dissociation energy between two atoms in a solid, r_0 is the equilibrium intermolecular separation and r is the internuclear separation.

After transformation $s = A^2 r^2$, where $(A = 1\ (eV))$, we get the generalized fractional radial part of the Schrödinger equation is

$$D^\alpha [\, D^\alpha R(s)] + \frac{3/2}{s^\alpha} D^\alpha R(s) + \frac{-\gamma^2 s^{2\alpha} + \varepsilon\, s^\alpha - \beta}{s^{2\alpha}}\, R(s) = 0. \tag{56}$$

where, the following dimensionless parameters

$$\left. \begin{array}{c} \gamma^2 = \dfrac{V_0\,\mu}{2\,r_0{}^2\,A^4\,\hbar^2}, \\[2mm] \varepsilon = \dfrac{\mu}{\hbar^2 A^2}\,(E_{n,l} + 2\,V_0) \\[2mm] \beta = \dfrac{\mu}{\hbar^2}\,\left(V_0 r_0{}^2 + \dfrac{L(L+1)\hbar^2}{2\mu}\right), \end{array} \right\} \tag{57}$$

by using the following parameters,

$$\left. \begin{array}{c} \xi_1 = \gamma^2,\, \xi_2 = \varepsilon,\, \xi_3 = \beta, \\[2mm] \alpha_1 = \dfrac{3}{2},\, \alpha_2 = 0,\, \alpha_3 = 0,\, \alpha_4 = \dfrac{1}{2}\,(k_1\alpha - 3/2), \\[2mm] \alpha_5 = 0,\, \alpha_6 = \gamma^2,\, \alpha_7 = -\varepsilon,\, \alpha_8 = \dfrac{1}{4}\,(k_1\alpha - 3/2)^2 + \beta, \\[2mm] \alpha_9 = \gamma^2,\, \alpha_{10} = k_1\alpha + 2\sqrt{\dfrac{1}{4}\,(k_1\alpha - 3/2)^2 + \beta},\, \alpha_{11} = 2\gamma, \\[2mm] \alpha_{12} = \dfrac{1}{2}\,(k_1\alpha - 3/2) + \sqrt{\dfrac{1}{4}\,(k_1\alpha - 3/2)^2 + \beta},\, \alpha_{13} = -\gamma, \end{array} \right\} \tag{58}$$

We get, the generalized fractional of the energy eigenvalue is,

$$\varepsilon = (2n+1)\,\gamma\,k_1\,\alpha + 2\sqrt{\frac{1}{4}\,(k_1\alpha - 3/2)^2 + \beta}, \tag{59}$$

And, the generalized fractional of the wave function is,

$$\left. \begin{array}{c} \psi(s) = s^{\frac{1}{k_1}\left(\frac{1}{2}\left(k_1\alpha - \frac{3}{2}\right) + \sqrt{\frac{1}{4}\left(k_1\alpha - \frac{3}{2}\right)^2 + \beta}\right)}\, e^{\frac{-\gamma}{k_1\alpha}s^\alpha} \\[4mm] L_n^{\frac{1}{k_1}\left(k_1\alpha + 2\sqrt{\frac{1}{4}\left(k_1\alpha - \frac{3}{2}\right)^2 + \beta}\right) - \alpha}\left(\frac{2\gamma}{k_1\alpha}s^\alpha\right), \end{array} \right\} \tag{60}$$

If $\alpha = \beta = 1$ then $k_1 = 1$, so that we get the energy eigenvalue and the corresponding wave function as Ref. [25].

$$\varepsilon = \left((2n+1) + 2\sqrt{\frac{1}{16} + \beta}\right)\gamma, \tag{61}$$

$$\psi(s) = s^{\left(\frac{-1}{4} + \sqrt{\frac{1}{16} + \beta}\right)}\, e^{-\gamma s}\, L_n^{\left(2\sqrt{\frac{1}{16} + \beta}\right)}(2\gamma s), \tag{62}$$

Case (3): Mie Potential

The Mie potential possess the general features of the true interaction energy and it is special kind of exactly solvable power-law and inverse power-law potentials other than the Coulombic and harmonic oscillator as in Refs. [32-33]

$$V(r) = V_0 \left(\frac{1}{2}\left(\frac{a}{r}\right)^2 - \frac{a}{r}\right) \tag{63}$$

where, V_0 is dissociation energy, a is the positive constant which is strongly repulsive at shorter distances and r is the internuclear separation

After transforming $s = r A$, $(A = 1eV)$, we get the generalized fractional radial part of the Schrödinger equation is

$$D^\alpha[\, D^\alpha R(s)] + \frac{2}{s^\alpha} D^\alpha R(s) + \frac{\varepsilon^2 s^{2\alpha} - \beta\, s^\alpha - \gamma}{s^{2\alpha}}\, R(s) = 0. \tag{64}$$

where, the following dimensionless parameters:

$$\left.\begin{aligned}
\varepsilon^2 &= \frac{2\,\mu}{\hbar^2 A^2}\, E_{n,l},\\
\beta &= -\frac{2\,\mu}{\hbar^2 A}\, V_0 a,\\
\gamma &= \frac{2\,\mu}{\hbar^2}\left(\frac{1}{2}V_0 a^2 + \frac{L(L+1)\hbar^2}{2\mu}\right).
\end{aligned}\right\} \tag{65}$$

By using the following parameters,

$$\left.\begin{aligned}
\xi_1 &= -\varepsilon^2, \xi_2 = -\beta, \xi_3 = \gamma,\\
\alpha_1 &= 2, \alpha_2 = 0, \alpha_3 = 0, \alpha_4 = \frac{1}{2}\,(k_1\,\alpha - 2),\\
\alpha_5 &= 0, \alpha_6 = -\varepsilon^2, \alpha_7 = \beta, \alpha_8 = \frac{1}{4}\,(k_1\,\alpha - 2)^2 + \gamma\\
\alpha_9 &= -\varepsilon^2, \alpha_{10} = k_1\,\alpha + 2\sqrt{\frac{1}{4}\,(k_1\,\alpha - 3/2)^2 + \gamma},\\
\alpha_{11} &= 2\sqrt{-\varepsilon^2}, \alpha_{12} = \frac{1}{2}\,(k_1\,\alpha - 2) + \sqrt{\frac{1}{4}\,(k_1\,\alpha - 2)^2 + \gamma},\\
\alpha_{13} &= -\sqrt{-\varepsilon^2}.
\end{aligned}\right\} \tag{66}$$

The generalized fractional of the energy eigenvalue is given,

$$-\varepsilon^2 = \beta^2\left((2n + 1)k_1\,\alpha + 2\sqrt{\frac{1}{4}\,(k_1\,\alpha - 2)^2 + \gamma}\right)^{-2}, \tag{67}$$

The generalized fractional of the wave function is,

$$\psi(s) = A\, s^{\frac{1}{k_1}\left(\frac{1}{2}(k_1\,\alpha - 2) + \sqrt{\frac{1}{4}(k_1\,\alpha - 2)^2 + \gamma}\right)}\, e^{\frac{-i\varepsilon}{k_1\alpha}s^\alpha}\, L_n^{\frac{1}{k_1}\left(k_1\,\alpha + 2\sqrt{\frac{1}{4}(k_1\,\alpha - 2)^2 + \gamma}\right) - \alpha}\left(\frac{2\,i\,\varepsilon}{k_1\,\alpha}s^\alpha\right), \tag{68}$$

If $\alpha = \beta = 1$ then $k_1 = 1$, so that we get the energy eigenvalue and the corresponding wave function as Ref. [25].

$$\varepsilon^2 = -\beta^2\,(2n + 1 + \sqrt{1 + 4\gamma})^{-2} \tag{69}$$

$$\psi(s) = A\, s^{\frac{-1}{2} + \frac{1}{2}\sqrt{1 + 4\gamma}}\, e^{-i\,\varepsilon\, s} L_n^{\sqrt{1 + 4\gamma}}\,(2\,i\,\varepsilon\, s), \tag{70}$$

Case (4): Kratzer-Fues Potential

The Kratzer-Fues potential has a long-range attraction and a repulsive part and it is approaches infinity as the inter-nuclear distance approaches zero and it is used to describe molecular structure between two atoms as in Ref. [34]

$$V(r) = D_e\left(\frac{r - r_e}{r}\right)^2 \tag{71}$$

After transforming $s = r A, A = 1eV$ the generalized fractional radial part of the Schrödinger equation is

$$D^\alpha[\, D^\alpha R(s)] + \frac{2}{s^\alpha} D^\alpha R(s) + \frac{\varepsilon^2 s^{2\alpha} - \beta\, s^\alpha - \gamma}{s^{2\alpha}}\, R(s) = 0, \tag{72}$$

where, the following dimensionless parameters

$$\left.\begin{aligned}
\varepsilon^2 &= \frac{2\mu(E_{n-} D_e)}{A^2 \hbar^2},\\
\beta &= \frac{-4\,\mu\, D_e\, r_e}{A\,\hbar^2},\\
\gamma &= \frac{2\,\mu(D_e\, r_e^2 + \frac{l(l+1)\hbar^2}{2\mu})}{\hbar^2},
\end{aligned}\right\} \tag{73}$$

By using the following parameters,

$$
\begin{aligned}
\xi_1 &= -\varepsilon^2, \xi_2 = -\beta, \xi_3 = \gamma, \\
\alpha_1 &= 2, \alpha_2 = 0, \alpha_3 = 0, \alpha_4 = \frac{1}{2}(k_1\alpha - 2), \\
\alpha_5 &= 0, \alpha_6 = -\varepsilon^2, \alpha_7 = \beta, \alpha_8 = \frac{1}{4}(k_1\alpha - 2)^2 + \gamma \\
\alpha_9 &= -\varepsilon^2, \alpha_{10} = k_1\alpha + 2\sqrt{\frac{1}{4}(k_1\alpha - 2)^2 + \gamma}, \\
\alpha_{11} &= 2\sqrt{-\varepsilon^2}, \alpha_{12} = \frac{1}{2}(k_1\alpha - 2) + \sqrt{\frac{1}{4}(k_1\alpha - 2)^2 + \gamma}, \\
\alpha_{13} &= -\sqrt{-\varepsilon^2},
\end{aligned}
\tag{74}
$$

the generalized fractional solution of eigenvalue is given,

$$
-\varepsilon^2 = \beta^2 \left((2n + 1)k_1\alpha + 2\sqrt{\frac{1}{4}(k_1\alpha - 2)^2 + \gamma}\right)^{-2},
\tag{75}
$$

The generalized fractional of the wave function is,

$$
\left.
\begin{aligned}
\psi(s) &= A\, s^{\frac{1}{k_1}\left(\frac{1}{2}(k_1\alpha - 2) + \sqrt{\frac{1}{4}(k_1\alpha - 2)^2 + \gamma}\right)} e^{\frac{-i\varepsilon}{k_1\alpha}s^\alpha} \\
&\quad L_n^{\frac{1}{k_1}\left(k_1\alpha + 2\sqrt{\frac{1}{4}(k_1\alpha - 2)^2 + \gamma}\right) - \alpha}\left(\frac{2i\varepsilon}{k_1\alpha}s^\alpha\right),
\end{aligned}
\right\}
\tag{76}
$$

If $\alpha = \beta = 1$ then $k_1 = 1$, so that we get the energy eigenvalue and the corresponding wave function as Ref. [25]

$$
-\varepsilon^2 = \beta^2 (2n + 1 + \sqrt{1 + 4\gamma})^{-2}
\tag{77}
$$

$$
\psi(s) = A\, s^{\frac{-1}{2} + \frac{1}{2}\sqrt{1 + 4\gamma}} e^{-i\varepsilon s} L_n^{\sqrt{1 + 4\gamma}}(2i\varepsilon s),
\tag{78}
$$

Case (5): Harmonic Oscillator Potential

Harmonic Oscillator Potential function is as in Ref. [35]

$$
V(r) = \frac{1}{2}m\omega^2 r^2,
\tag{79}
$$

where, ω is the angular frequency of the oscillator.

The generalized fractional radial part of the Schrödinger equation is

$$
D^\alpha[D^\alpha\psi(s)] + \frac{1}{2s^\alpha}\psi^\alpha R(s) + \frac{-s^{2\alpha} + \beta^2 s^\alpha - l(l+1)}{4s^{2\alpha}}\psi(s) = 0.
\tag{80}
$$

where,

$$
\beta^2 = \frac{2E}{\hbar\omega}
\tag{81}
$$

By using the following parameters,

$$
\begin{aligned}
\xi_1 &= \frac{1}{4}, \xi_2 = \frac{1}{4}\beta^2, \xi_3 = \frac{1}{4}l(l+1), \\
\alpha_1 &= \frac{1}{2}, \alpha_2 = 0, \alpha_3 = 0, \alpha_4 = \frac{1}{2}(k_1\alpha - \frac{1}{2}), \\
\alpha_5 &= 0, \alpha_6 = \frac{1}{4}, \alpha_7 = \frac{-1}{4}\beta^2, \alpha_8 = \frac{1}{4}(k_1\alpha - \frac{1}{2})^2 + \frac{1}{4}l(l+1), \\
\alpha_9 &= \frac{1}{4}, \alpha_{10} = k_1\alpha + \sqrt{(k_1\alpha - 1/2)^2 + l(l+1)}, \alpha_{11} = 1, \\
\alpha_{12} &= \frac{1}{2}(k_1\alpha - \frac{1}{2}) + \frac{1}{2}\sqrt{(k_1\alpha - \frac{1}{2})^2 + l(l+1)}, \alpha_{12} = \frac{-1}{2},
\end{aligned}
\tag{82}
$$

the generalized fractional eigenvalue is given,

$$
E = \hbar\omega\left[(2n + 1)k_1\alpha + \sqrt{(k_1\alpha - 1/2)^2 + l(l+1)}\right]
\tag{83}
$$

The generalized fractional wave function is

$$\psi(s) = s^{\frac{1}{k_1}\left((k_1\alpha)+\sqrt{\left(k_1\alpha-\frac{1}{2}\right)^2+l(l+1)}\right)} e^{\frac{-1}{k_1\alpha}s^\alpha} \times L_n^{\frac{1}{k_1}\left(k_1\alpha+1/2\sqrt{(k_1\alpha-1/2)^2+l(l+1)}\right)-\frac{\alpha}{k_1}} \left(\frac{1}{k_1\alpha}s^\alpha\right)$$

(84)

If $\alpha = \beta = 1$ then $k_1 = 1$, so that we get the energy eigenvalue and the corresponding wave function as Ref. [35]

$$E = \hbar\omega\left[(2n+1)+\sqrt{\frac{1}{4}+l(l+1)}\right]$$

(85)

$$\psi(s) = s^{\left(1+\sqrt{\frac{1}{4}+l(l+1)}\right)} e^{-s} L_n^{\left(1/2\sqrt{\frac{1}{4}+l(l+1)}\right)}(s).$$

(86)

Case (6): Morse Potential

The Morse potential has contributed a significant role in describing the interaction of atoms in diatomic and polyatomic molecules as in Refs. [36, 37]

$$V(r) = D_0(1-e^{-\delta r})^2$$

(87)

where D_0 is dissociation energy and δ is the range of the potential. After transforming the generalized fractional radial part of the Schrödinger equation is

$$D^\alpha[D^\alpha\psi(s)] + \frac{1}{s^\alpha}D^\alpha\psi(s) + \frac{-Ps^{2\alpha}+Qs^\alpha-R}{s^{2\alpha}}\psi(s) = 0.$$

(88)

where,

$$\varepsilon_n^2 = \frac{-2\mu E}{\hbar^2}, \gamma = \frac{2\mu D_0}{\hbar^2}, P = \frac{\gamma}{\delta^2}, Q = \frac{2\gamma}{\delta^2}, R = \frac{\varepsilon_n^2+\gamma}{\delta^2},$$

(89)

By using the following parameters,

$$\left.\begin{aligned}
\xi_1 &= P, \xi_2 = Q, \xi_3 = R, \\
\alpha_1 &= 1, \alpha_2 = 0, \alpha_3 = 0, \alpha_4 = \frac{1}{2}(k_1\alpha-1), \\
\alpha_5 &= 0, \alpha_6 = P, \alpha_7 = -Q, \alpha_8 = \frac{1}{4}(k_1\alpha-1)^2+R \\
\alpha_9 &= P, \alpha_{10} = k_1\alpha+2\sqrt{\frac{1}{4}(k_1\alpha-1)^2+R}, \alpha_{11} = 2\sqrt{P}, \\
\alpha_{12} &= \frac{1}{2}(k_1\alpha-1)+\sqrt{\frac{1}{4}(k_1\alpha-1)^2+R}, \alpha_{13} = -\sqrt{P},
\end{aligned}\right\}$$

(90)

the generalized fractional of the energy eigenvalue is given,

$$E = D_0 - \frac{\hbar^2\delta^2}{8\mu}\left[-(k_1\alpha-1)^2+\left((2n+1)k_1\alpha-2\sqrt{\frac{2\mu D_0}{\hbar^2\delta^2}}\right)^2\right]$$

(91)

The generalized fractional of the wave function is

$$\psi(s) = \mathbb{N}_n\, s^{\frac{\frac{1}{2}(k_1\alpha-1)+\sqrt{\frac{1}{4}(k_1\alpha-1)^2+R}}{k_1}} e^{\left(\frac{-\sqrt{P}}{k_1\alpha}\right)s^\alpha} L_n^{\frac{k_1\alpha+2\sqrt{\frac{1}{4}(k_1\alpha-1)^2+R}-\alpha}{k_1}}\left(\frac{2\sqrt{P}}{k_1\alpha}s^\alpha\right)$$

(92)

where, $\mathbb{N}_n$ is a normalization constant,
If $\alpha = \beta = 1$ then $k_1 = 1$, so that we get the energy eigenvalue and the corresponding wave function as in Ref. [36].

$$E = D_0 - \frac{\hbar^2\delta^2}{8\mu}\left[\left((2n+1)-2\sqrt{\frac{2\mu D_0}{\hbar^2\delta^2}}\right)^2\right]$$

(93)

$$\psi(s) = \mathbb{N}_n s^{\sqrt{R}} e^{(-\sqrt{P})s} L_n^{2\sqrt{R}}(2\sqrt{P}s)$$

(94)

Case (7): Woods-Saxon Potential

It is used to describe heavy-ion reactions which the interaction of a neutron with a heavy nucleus as in Refs. [26, 38-39]

$$V(r) = \frac{-V_0}{1+e^{\frac{r-R_0}{a}}}$$

(95)

where V_0 is the potential depth, R_0 is width of the potential, $r - R_0 \equiv r$ and $\frac{1}{a} = 2\lambda$

After transforming the generalized fractional radial part of the Schrödinger equation is

$$D^\alpha[\, D^\alpha \psi(s)] + \frac{1 - q\, s^\alpha}{s^\alpha(1 - q\, s^\alpha)} D^\alpha \psi(s) + \frac{-\varepsilon\, q^2\, s^{2\alpha} + (2\,\varepsilon\, q - \beta\, q)\, s^\alpha + \beta - \varepsilon}{(s^\alpha(1 - q\, s^\alpha))^2}\, \psi(s) = 0. \tag{96}$$

where,

$$\varepsilon = \frac{-m\, E}{2\, \hbar^2\, \lambda^2} > 0, \qquad \beta = \frac{m\, V_0}{2\, \hbar^2\, \lambda^2}, \tag{97}$$

By using the following parameters,

$$
\left.
\begin{aligned}
\xi_1 &= \varepsilon\, q^2, \xi_2 = 2\,\varepsilon\, q - \beta q, \xi_3 = \varepsilon - \beta, \\
\alpha_1 &= 1, \alpha_2 = q, \alpha_3 = q, \alpha_4 = \frac{1}{2}(k_1\alpha - 1), \\
\alpha_5 &= \frac{1}{2}q\,(1 - 2k_1\alpha), \alpha_6 = \frac{1}{4}q^2\,(1 - 2k_1\alpha)^2 + \varepsilon\, q^2, \\
\alpha_7 &= \frac{1}{2}q\,(1 - 2k_1\alpha)\,(k_1\alpha - 1) - 2\,\varepsilon\, q - \beta q, \\
\alpha_8 &= \frac{1}{4}(k_1\alpha - 1)^2 + \varepsilon - \beta, \alpha_9 = \frac{1}{4}q^2\, k_1{}^2\alpha^2, \\
\alpha_{10} &= k_1\alpha + 2\sqrt{\frac{1}{4}(k_1\alpha - 1)^2 + \varepsilon - \beta}, \\
\alpha_{11} &= 3\, k_1\alpha\, q + 2\, q\sqrt{\frac{1}{4}(k_1\alpha - 1)^2 + \varepsilon - \beta}, \\
\alpha_{12} &= \frac{1}{2}(k_1\alpha - 1) + \sqrt{\frac{1}{4}(k_1\alpha - 1)^2 + \varepsilon - \beta}, \\
\alpha_{13} &= \frac{1}{2}q\,(1 - 2k_1\alpha) - (\frac{1}{2}k_1\alpha\, q + q\sqrt{\frac{1}{4}(k_1\alpha - 1)^2 + \varepsilon - \beta}).
\end{aligned}
\right\} \tag{98}
$$

The generalized fractional of the energy eigenvalue is given,

$$\varepsilon = -\frac{1}{4}(k_1\alpha - 1)^2 + \frac{\beta}{2} + \frac{\beta^2}{(2(n+1)k_1\alpha)^2} + \left(\frac{(n+1)k_1\alpha}{2}\right)^2, \tag{99}$$

The generalized fractional of the wave function is,

$$\psi(s) = \mathbb{N}_n\, s^{\frac{1}{k_1}\left(\frac{1}{2}(k_1\alpha - 1) + \sqrt{\frac{1}{4}(k_1\alpha - 1)^2 + \varepsilon - \beta}\right)}\, (1 -$$

$$q\, s^\alpha)^{\left(\frac{-(\frac{1}{2}q\,(1 - 2k_1\alpha) - (\frac{1}{2}k_1\alpha\, q + q\sqrt{\frac{1}{4}(k_1\alpha - 1)^2 + \varepsilon - \beta}))}{k_1\alpha\, q} - \frac{\frac{1}{2}(k_1\alpha - 1) + \sqrt{\frac{1}{4}(k_1\alpha - 1)^2 + \varepsilon - \beta}}{k_1\alpha}\right)} \times$$

$$P_n^{\left(\frac{-\alpha + k_1\alpha + 2\sqrt{\frac{1}{4}(k_1\alpha - 1)^2 + \varepsilon - \beta}}{k_1}, \frac{3\, k_1\alpha\, q + 2\, q\sqrt{\frac{1}{4}(k_1\alpha - 1)^2 + \varepsilon - \beta}}{k_1\alpha\, q} - \frac{k_1\alpha + 2\sqrt{\frac{1}{4}(k_1\alpha - 1)^2 + \varepsilon - \beta}}{k_1\alpha} - \frac{1}{k_1}\right)} \times (1 - 2\, q\, s^\alpha) \tag{100}$$

If $\alpha = \beta = 1$ then $k_1 = 1$, and $q = 1$, so that we get the energy eigenvalue and the corresponding wave function as in Ref. [26]

$$\varepsilon = \frac{\beta}{2} + \frac{\beta^2}{(2(n+1))^2} + \left(\frac{(n+1)}{2}\right)^2, \tag{101}$$

$$\psi(s) = \mathbb{N}_n\, s^{\sqrt{\varepsilon - \beta}}\,(1 - s)\, P_n^{(2\sqrt{\varepsilon - \beta},1)}\,(1 - 2s) \tag{102}$$

Case (8): Hulthen Potential

The Hulthen Potential is a short-range potential and it is obtained in the form as in Ref. [40]

$$V(r) = -\frac{P}{p}\, \frac{1}{e^{\frac{r}{p}} - 1}, \tag{103}$$

where, P, p are the strength and the range parameter of the potential function.

After transforming the generalized fractional radial part of the Schrödinger equation is

$$D^\alpha[\,D^\alpha\psi(s)\,] + \frac{1-s^\alpha}{s^\alpha(1-s^\alpha)}D^\alpha\psi(s) + \frac{-(A+B)s^{2\alpha}+(2\,A+B-C)\,s^\alpha-A}{(s^\alpha(1-s^\alpha))^2}\,\psi(s) = 0. \tag{104}$$

where,

$$A = \frac{-2\,\mu\,E\,p^2}{\hbar^2},\ B = \frac{2\,\mu\,E\,p\,P}{\hbar^2},\ C = l(l+1). \tag{105}$$

By using the following parameters,

$$
\left.
\begin{aligned}
\xi_1 &= A+B\,,\xi_2 = (2\,A+B-C),\xi_3 = A,\\
\alpha_1 &= 1,\alpha_2 = 1,\alpha_3 = 1,\alpha_4 = \tfrac{1}{2}\,(k_1\alpha-1),\\
\alpha_5 &= \tfrac{1}{2}\,(1-2\,k_1\,\alpha),\alpha_6 = \tfrac{1}{4}\,(1-2\,k_1\,\alpha)^2 + A+B,\\
\alpha_7 &= \tfrac{1}{2}\,(k_1\,\alpha-1)\,(1-2\,k_1\,\alpha) - 2\,A-B+C\ \alpha_8 = \tfrac{1}{4}\,(k_1\,\alpha-1)^2 + A,\\
\alpha_9 &= \tfrac{1}{4}\,k_1^{\,2}\,\alpha^2 + C,\alpha_{10} = k_1\,\alpha + 2\sqrt{\tfrac{1}{4}\,(k_1\,\alpha-1)^2+A},\\
\alpha_{11} &= 2\,k_1\,\alpha + 2\,(\sqrt{\tfrac{1}{4}\,k_1^{\,2}\,\alpha^2+C}+\sqrt{\tfrac{1}{4}\,(k_1\,\alpha-1)^2+A}),\\
\alpha_{12} &= \tfrac{1}{2}\,(k_1\,\alpha-1) + \sqrt{\tfrac{1}{4}\,(k_1\,\alpha-1)^2+A},\\
\alpha_{13} &= \tfrac{1}{2}\,(1-2\,k_1\,\alpha) - (\sqrt{\tfrac{1}{4}\,k_1^{\,2}\,\alpha^2+C}+\sqrt{\tfrac{1}{4}\,(k_1\,\alpha-1)^2+A}).
\end{aligned}
\right\} \tag{106}
$$

The generalized fractional of the energy eigenvalue is given

$$E_n = \frac{-\hbar^2}{8\,\mu p^2}\,\left\{ \frac{\left[\frac{2\,\mu\,p\,P}{\hbar^2}-l(l+1)-\frac{k_1\,\alpha}{2}\left(k_1\,\alpha+\sqrt{k_1^{\,2}\,\alpha^2+4\,l\,(l+1)}\right)-n\,k_1\,\alpha\left(\frac{(n+1)}{2}k_1\,\alpha+\sqrt{k_1^{\,2}\,\alpha^2+4\,l\,(l+1)}\right)\right]^2-(k_1\,\alpha-1)^2\}}{\left[nk_1\,\alpha+\frac{1}{2}(k_1\,\alpha+\sqrt{k_1^{\,2}\,\alpha^2+4\,l\,(l+1)})\right]^2} \tag{107}$$

The generalized fractional of the wave function is

$$\psi\,(s) = \mathbb{N}_n s^{\frac{1}{k_1}\left(\frac{1}{2}(k_1\,\alpha-1)+\sqrt{\frac{1}{4}(k_1\,\alpha-1)^2+A}\right)}\,(1-s^\alpha)^{\frac{-\left(\frac{1}{2}(1-2\,k_1\,\alpha)-(\sqrt{\frac{1}{4}k_1^{\,2}\,\alpha^2+C}+\sqrt{\frac{1}{4}(k_1\,\alpha-1)^2+A})\right)}{k_1\,\alpha}-\frac{\frac{1}{2}(k_1\,\alpha-1)+\sqrt{\frac{1}{4}(k_1\,\alpha-1)^2+A}}{k_1\,\alpha}}$$
$$P_n^{\frac{\left(k_1\,\alpha+2\sqrt{\frac{1}{4}(k_1\,\alpha-1)^2+A}\right)-\alpha}{k_1},\ \frac{2\,k_1\,\alpha+2\,(\sqrt{\frac{1}{4}k_1^{\,2}\,\alpha^2+C}+\sqrt{\frac{1}{4}(k_1\,\alpha-1)^2+A})}{k_1\,\alpha}-\frac{k_1\,\alpha+2\sqrt{\frac{1}{4}(k_1\,\alpha-1)^2+A}}{k_1\,\alpha}-\frac{1}{k_1}}\,(1-2\,s^\alpha) \tag{108}$$

If $\alpha = \beta = 1$ then $k_1 = 1$, so that we get the energy eigenvalue and the corresponding wave function as in Ref. [26]

$$E_n = \frac{-\hbar^2}{8\,\mu p^2}\,\left\{ \frac{\left[\frac{2\,\mu\,p\,P}{\hbar^2}-l(l+1)-\frac{1}{2}(1+\sqrt{1+4\,l\,(l+1)})-n\left(\frac{(n+1)}{2}+\sqrt{1+4\,l\,(l+1)}\right)\right]^2\}}{\left[n+\frac{1}{2}(1+\sqrt{1+4\,l\,(l+1)})\right]^2} \tag{109}$$

$$\psi(s) = \mathbb{N}_n\ s^{\sqrt{A}}\,(1-s)^{-\left(\frac{-1}{2}-(\sqrt{\frac{1}{4}+C}+\sqrt{A})\right)-\sqrt{A}}\,P_n^{2\sqrt{A},2\,(\sqrt{C})}\,(1-2\,s) \tag{110}$$

Case (9): Deformed Rosen-Morse Potential

Deformed Rosen-Morse potential is used to describe bound state of die-atomic molecules and it is given in the following form as in Ref. [41]

$$V(r) = \frac{V_1}{1+q\,e^{-2\alpha^* r}} - V_2 q\,\frac{e^{-2\alpha^* r}}{\left(1+q\,e^{-2\alpha^* r}\right)^2} \tag{111}$$

After transforming $-s = e^{-2\alpha^* r}$ the generalized fractional radial part of the Schrödinger equation is

$$D^\alpha[\,D^\alpha\psi(s)\,] + \frac{1-q\,s^\alpha}{s^\alpha(1-q\,s^\alpha)}D^\alpha\psi(s) + \frac{-\varepsilon\,q^2\,s^{2\alpha}+(2\,\varepsilon\,q+\beta\,q-\gamma)\,s^\alpha-(\beta+\varepsilon)}{(s^\alpha(1-q\,s^\alpha))^2}\,\psi(s) = 0. \tag{112}$$

where,

$$\varepsilon = \frac{-\mu E}{2\alpha^{*2}\hbar^2}, \beta = \frac{\mu V_1 q}{2\alpha^{*2}\hbar^2}, \gamma = \frac{\mu V_2 q}{2\alpha^{*2}\hbar^2}, \tag{113}$$

By using the following parameters,

$$
\left.
\begin{aligned}
\xi_1 &= \varepsilon\, q^2, \xi_2 = (2\,\varepsilon\, q + \beta\, q - \gamma), \xi_3 = (\beta + \varepsilon),\\
\alpha_1 &= 1, \alpha_2 = q, \alpha_3 = q, \alpha_4 = \frac{1}{2}\,(k_1\,\alpha - 1),\\
\alpha_5 &= \frac{q}{2}\,(1 - 2\,k_1\,\alpha), \alpha_6 = \frac{q^2}{4}\,(1 - 2\,k_1\,\alpha)^2 + \varepsilon\, q^2,\\
\alpha_7 &= \frac{q}{2}\,(k_1\,\alpha - 1)\,(1 - 2\,k_1\,\alpha) - 2\,\varepsilon\, q - \beta\, q + \gamma\\
\alpha_8 &= \frac{1}{4}\,(k_1\,\alpha - 1)^2 + \beta + \varepsilon,\\
\alpha_9 &= \frac{q^2}{4}\,k_1{}^2\,\alpha^2 + \gamma\, q, \alpha_{10} = k_1\,\alpha + 2\,\sqrt{\frac{1}{4}\,(k_1\,\alpha - 1)^2 + \beta + \varepsilon},\\
\alpha_{11} &= 2\,k_1\,q\,\alpha + 2\,(\sqrt{\frac{1}{4}\,k_1{}^2 q^2\,\alpha^2 + \gamma\, q} + q\,\sqrt{\frac{1}{4}\,(k_1\,\alpha - 1)^2 + \beta + \varepsilon}\,),\\
\alpha_{12} &= \frac{1}{2}\,(k_1\,\alpha - 1) + \sqrt{\frac{1}{4}\,(k_1\,\alpha - 1)^2 + \beta + \varepsilon},\\
\alpha_{13} &= \frac{q}{2}\,(1 - 2\,k_1\,\alpha) - (\sqrt{\frac{1}{4}\,k_1{}^2 q^2\,\alpha^2 + \gamma\, q} + q\,\sqrt{\frac{1}{4}\,(k_1\,\alpha - 1)^2 + \beta + \varepsilon}),
\end{aligned}
\right\} \tag{144}
$$

we get, the generalized fractional of the energy eigenvalue is,

$$\varepsilon = \frac{-1}{4}\,(k_1\,\alpha - 1)^2 - \frac{\beta}{2} + \frac{\beta^2}{\left((2\,n+1)k_1\,\alpha + \sqrt{k_1{}^2\,\alpha^2 + \frac{4\gamma}{q}}\right)^2} + \frac{1}{16}\left((2\,n+1)k_1\,\alpha + \sqrt{k_1{}^2\,\alpha^2 + \frac{4\gamma}{q}}\right)^2 \tag{115}$$

The generalized fractional of the wave function is,

$$\psi(s) = s^{\frac{\frac{1}{2}(k_1\,\alpha - 1) + \sqrt{\frac{1}{4}(k_1\,\alpha - 1)^2 + \beta + \varepsilon}}{k_1}}(1 - q\, s^\alpha)^{-\left(\frac{q}{2}(1 - 2\,k_1\,\alpha) - (\sqrt{\frac{1}{4}k_1{}^2 q^2\,\alpha^2 + \gamma\, q} + q\sqrt{\frac{1}{4}(k_1\,\alpha - 1)^2 + \beta + \varepsilon})\right)\frac{1}{k_1\,\alpha\, q} - \frac{\frac{1}{2}(k_1\,\alpha - 1) + q\sqrt{\frac{1}{4}(k_1\,\alpha - 1)^2 + \beta + \varepsilon}}{k_1\,\alpha}}$$

$$P_n^{(\frac{k_1\,\alpha + 2\sqrt{\frac{1}{4}(k_1\,\alpha - 1)^2 + \beta + \varepsilon} - \alpha}{k_1}, \frac{2\,k_1\,q\,\alpha + 2\left(\sqrt{\frac{1}{4}k_1{}^2\,\alpha^2 + \gamma\, q} + q\sqrt{\frac{1}{4}(k_1\,\alpha - 1)^2 + \beta + \varepsilon}\right)}{k_1\,\alpha\, q} - \frac{k_1\,\alpha + 2\sqrt{\frac{1}{4}(k_1\,\alpha - 1)^2 + \beta + \varepsilon}}{k_1\,\alpha} - \frac{1}{k_1})}(1 - 2\,q\, s^\alpha) \tag{116}$$

If $\alpha = \beta = 1$ then $k_1 = 1$, so that we get the energy eigenvalue and the corresponding wave function as in Ref. [25]

$$\varepsilon = -\frac{\beta}{2} + \frac{\beta^2}{\left((2\,n+1) + \sqrt{1 + \frac{4\gamma}{q}}\right)^2} + \frac{1}{16}\left((2\,n+1) + \sqrt{1 + \frac{4\gamma}{q}}\right)^2, \tag{117}$$

$$\psi(s) = s^{\sqrt{\beta + \varepsilon}}(1 - q\, s)^{\frac{1}{2}\left(1 + \sqrt{1 + \frac{4\gamma}{q}}\right)}P_n^{(2\sqrt{\beta + \varepsilon}, \sqrt{1 + \frac{4\gamma}{q}})}(1 - 2\,q\, s) \tag{118}$$

Case (10): Pöschl-Teller Potential

Pöschl-Teller Potential used to describe bound state of die-atomic molecules and it is given in the following form as in Refs. [42-43]

$$V(r) = -4V_0\,\frac{e^{-2\alpha^* r}}{\left(1 + q\, e^{-2\alpha^* r}\right)^2} \tag{119}$$

After transforming $-s = e^{-2\alpha^* r}$, the generalized fractional radial part of the Schrödinger equation is

$$D^\alpha[D^\alpha\psi(s)] + \frac{1 - q\, s^\alpha}{s^\alpha(1 - q\, s^\alpha)}D^\alpha\psi(s) + \frac{-\varepsilon^2\, q^2\, s^{2\alpha} + (2\,\varepsilon^2\, q - \beta^2)\, s^\alpha - \varepsilon^2}{(s^\alpha(1 - q\, s^\alpha))^2}\,\psi(s) = 0. \tag{120}$$

where,

$$\varepsilon^2 = \frac{-\mu E}{2\alpha^{*2}\hbar^2}, \ \beta^2 = \frac{2\mu V_0}{\alpha^{*2}\hbar^2} \tag{121}$$

By using the following parameters,

$$
\begin{aligned}
\xi_1 &= \varepsilon^2 q^2, \xi_2 = (2\varepsilon^2 q - \beta^2), \xi_3 = \varepsilon^2, \\
\alpha_1 &= 1, \alpha_2 = q, \alpha_3 = q, \alpha_4 = \frac{1}{2}(k_1\alpha - 1), \\
\alpha_5 &= \frac{q}{2}(1 - 2k_1\alpha), \alpha_6 = \frac{q^2}{4}(1 - 2k_1\alpha)^2 + \varepsilon^2 q^2, \\
\alpha_7 &= \frac{q}{2}(k_1\alpha - 1)(1 - 2k_1\alpha) - 2\varepsilon^2 q + \beta^2 \ \alpha_8 = \frac{1}{4}(k_1\alpha - 1)^2 + \varepsilon^2, \\
\alpha_9 &= \frac{q^2}{4}k_1{}^2\alpha^2 + \beta^2 q, \alpha_{10} = k_1\alpha + 2\sqrt{\frac{1}{4}(k_1\alpha - 1)^2 + \varepsilon^2}, \\
\alpha_{11} &= 2q k_1\alpha + 2(\sqrt{\frac{1}{4}k_1{}^2 q^2\alpha^2 + \beta^2 q} + q\sqrt{\frac{1}{4}(k_1\alpha - 1)^2 + \varepsilon^2}) \\
\alpha_{12} &= \frac{1}{2}(k_1\alpha - 1) + \sqrt{\frac{1}{4}(k_1\alpha - 1)^2 + \varepsilon^2}, \\
\alpha_{13} &= \frac{q}{2}(1 - 2k_1\alpha) - (\sqrt{\frac{1}{4}k_1{}^2 q^2\alpha^2 + \beta^2 q} + q\sqrt{\frac{1}{4}(k_1\alpha - 1)^2 + \varepsilon^2}),
\end{aligned}
\right\} \tag{122}
$$

the generalized fractional of the energy eigenvalue is given,

$$\varepsilon = \frac{-1}{4}(k_1\alpha - 1)^2 - \frac{1}{4}\left((2n + 1)k_1\alpha + \sqrt{k_1{}^2\alpha^2 + \frac{4\beta^2}{q}}\right). \tag{123}$$

The generalized fractional of the wave function is given,

$$\psi(s) = s^{\frac{\frac{1}{2}(k_1\alpha - 1) + \sqrt{\frac{1}{4}(k_1\alpha - 1)^2 + \varepsilon^2}}{k_1}} (1 - q s^\alpha)^{-\left(\frac{\frac{q}{2}(1 - 2k_1\alpha) - (\sqrt{\frac{1}{4}k_1{}^2 q^2\alpha^2 + \beta^2 q} + q\sqrt{\frac{1}{4}(k_1\alpha - 1)^2 + \varepsilon^2})}{k_1\alpha q}\right) - \frac{\frac{1}{2}(k_1\alpha - 1) + \sqrt{\frac{1}{4}(k_1\alpha - 1)^2 + \varepsilon^2}}{k_1\alpha}}$$

$$P_n^{(\frac{k_1\alpha + 2\sqrt{\frac{1}{4}(k_1\alpha - 1)^2 + \varepsilon^2} - \alpha}{k_1}, \ \frac{2k_1 q\alpha + 2\left(\sqrt{\frac{1}{4}k_1{}^2\alpha^2 + \beta^2 q} + q\sqrt{\frac{1}{4}(k_1\alpha - 1)^2 + \varepsilon^2}\right)}{k_1\alpha q} - \frac{k_1\alpha + 2\sqrt{\frac{1}{4}(k_1\alpha - 1)^2 + \varepsilon^2}}{k_1\alpha} - \frac{1}{k_1})} (1 - 2q s^\alpha) \tag{124}$$

If $\alpha = \beta = 1$ then $k_1 = 1$, so that we get the energy eigenvalue and the corresponding wave function as in Ref. [25].

$$\varepsilon = -\frac{1}{4}\left((2n + 1) + \sqrt{1 + \frac{4\beta^2}{q}}\right), \tag{125}$$

$$\psi(s) = s^\varepsilon (1 - q s)^{\frac{1}{2}(1 + \sqrt{1 + \frac{4\beta^2}{q}})} P_n^{(2\varepsilon, \sqrt{1 + 4\frac{\beta^2}{q}})} (1 - 2q s) \tag{126}$$

4. CONCLUSION

By using generalized fractional derivative, we obtained the solution the parametric second-order differential equation by using the NU method which is more effective than the power series method, numerical methods, or approximation methods because we get on good results by using this method as in Refs. [22,23]. The parametric second-order differential equation is the general case and we get the special case when $\alpha = \beta = 1$ as in Ref. [25]. We get a solution of the Schrödinger equation by using the parametric generalized fractional Nikiforov-Uvarov (NU) method and we get the energy eigenvalues and the corresponding wave function for some known potentials such that the Cornell potential, the pesudoharmonic potential, the Mie Potential, the Kratzer-Fues potential, the harmonic oscillator potential, the Morse potential, the Woods-Saxon potential, the Hulthen Potential, the deformed Rosen-Morse Potential and the Pöschl-Teller Potential. At $\alpha = \beta = 1$, we get the special classical solutions of Refs. [25,26,29,35,36]. These applications play an important role in the fields of molecular and hadronic physics.

ORCID

M. Abu-Shady, https://orcid.org/0000-0001-7077-7884

REFERENCES
[1] R. Hilfer, editor, *Applications of Fractional Calculus in Physics*, (World Scientific, Singapore, 2000). http://dx.doi.org/10.1142/9789812817747_0002

[2]   M. Dalir, and M. Bashour, Appl. Math. Sci. **4**(21), 1021–540 (2010). https://www.m-hikari.com/ams/ams-2010/ams-21-24-2010/bashourAMS21-24-2010.pdf

[3]   G. Wang, and A.-M. Wazwaz, "On the modified Gardner type equation and its time fractional form," Chaos, Solitons & Fractals **155**, 111694 (2022). https://doi.org/10.1016/j.chaos.2021.111694

[4]   G. Jumarie, "Modified Riemann-Liouville derivative and fractional Taylor series of nondifferentiable functions further results," Computers & Mathematics with Applications, **51**(9-10), 1367-1376 (2006). https://doi.org/10.1016/j.camwa.2006.02.001

[5]   A. Atangana and A. Secer, "A note on fractional order derivatives and table of fractional derivatives of some special functions," Abstract and Applied Analysis, **2013**, 279681 (2013). https://doi.org/10.1155/2013/279681

[6]   K.S. Miller, and B. Ross, *An Introduction to the Fractional Calculus and Fractional Differential Equations*, (Wiley, New York, 1993).

[7]   M. Caputo, "Linear models of dissipation whose Q is almost frequency independent – II," Geophysical Journal International, **13**(5), 529-539 (1967). https://doi.org/10.1111/j.1365-246X.1967.tb02303.x

[8]   M. Al Horani, A. Yousef, and M. Sababheh, "A new definition of fractional derivative," Journal of computational and applied mathematics, **264**, 65-70 (2014). https://doi.org/10.1016/j.cam.2014.01.002

[9]   T. Abdeljawad, "On conformable fractional calculus," Journal of computational and Applied Mathematics, **279**, 57-66 (2015). https://doi.org/10.1016/j.cam.2014.10.016

[10] M. Abu-Shady, and M.K.A. Kaabar, "A generalized definition of the fractional derivative with applications," Mathematical Problems in Engineering, **2021**, 9444803 (2021). https://doi.org/10.1155/2021/9444803

[11] M. Abu-Shady, T.A. Abdel-Karim, and E.M. Khokha, "Exact Solution of the N-dimensional Radial Schrödinger Equation via Laplace Transformation Method with the Generalized Cornell Potential," Journal of Quantum Physics, **45**, 587 (2018). https://doi.org/10.48550/arXiv.1802.02092

[12] M. Abu-Shady, and E. M. Khokha. "Heavy-light mesons in the nonrelativistic quark model using laplace transformation method," Advances in high energy Physics, **2018**, 7032041 (2018). https://doi.org/10.1155/2018/7032041

[13] M. Abu-Shady, H.M. Mansour, and A.I. Ahmadov, "Dissociation of quarkonium in hot and dense media in an anisotropic plasma in the nonrelativistic quark model," Advances in High Energy Physics, **2019**, 4785615 (2019). https://doi.org/10.1155/2019/4785615

[14] M. Abu-Shady, and H.M. Fath-Allah. "Melting of quarkonium in an anisotropic hot QCD medium in the presence of a generalized Debye screening mass and Nikiforov–Uvarov's method," International Journal of Modern Physics A, **35**(21), 2050110 (2020). https://doi.org/10.1142/S0217751X20501109

[15] M. Abu-Shady, and A.N. Ikot, "Dissociation of nucleon and heavy baryon in an anisotropic hot and dense QCD medium using Nikiforov–Uvarov method," The Eurpean Physical Journal Plus, **135**(5), 1-17 (2020). https://doi.org/10.1140/epjp/s13360-020-00436-2

[16] M. Abu-Shady, "Multidimensional Schrödinger Equation and Spectral Properties of Heavy-Quarkonium Mesons at Finite Temperature," Advances in Mathematical Physics, **2016**, 4935940 (2016). https://doi.org/10.1155/2016/4935940

[17] M. Abu-Shady, "Heavy quarkonia and Bc-mesons in the cornell potential with harmonic oscillator potential in the N-dimensional Schrodinger equation," International Journal of Applied Mathematics and Theoretical Physics, **2**, 16-20 (2015). https://article.sciencepublishinggroup.com/pdf/10.11648.j.ijamtp.20160202.11.pdf

[18] M. Abu-Shady, "Quarkonium masses in a hot QCD medium using conformable fractional of the Nikiforov–Uvarov method," International Journal of Modern Physics A, **34**(31), 1950201 (2019). https://doi.org/10.1142/S0217751X19502014

[19] M. Abu-Shady, and E.P. Inyang, "Heavy-Light Meson Masses in the Framework of Trigonometric Rosen-Morse Potential Using the Generalized Fractional Derivative," East European Journal of Physics, **4**, 80-86 (2022). https://doi.org/10.26565/2312-4334-2022-4-06

[20] M. Abu-Shady, T.A. Abdel-Karim, and E.M. Khokha, "The Generalized Fractional NU Method for the Diatomic Molecules in the Deng-Fan Model," The European Physical Journal D, **67**, 159 (2022). https://doi.org/10.1140/epjd/s10053-022-00480-w

[21] M. Abu-Shady, and Sh.Y. Ezz-Alarab, "Conformable Fractional of the Analytical Exact Iteration Method for Heavy Quarkonium Masses Spectra," Few-Body Systems, **62**(2), 13 (2021). https://doi.org/10.1007/s00601-021-01591-7

[22] M. Abu-shady, A.I. Ahmadov, H.M. Fath-Allah, and V.H. Badalov, "Spectra of heavy quarkonia in a magnetized-hot medium in the framework of fractional non-relativistic quark model," Journal of Theoretical and Applied Physics, **16**(3), 1-8 (2022). https://doi.org/10.30495/jtap.162225

[23] M. Abu-shady, and H.M. Fath-Allah, "Masses of Single, Double, and Triple Heavy Baryons in the Hyper-Central Quark Model by Using GF-AEIM," Advances in High Energy Physics, **2022**, 4539308 (2022). https://doi.org/10.1155/2022/4539308

[24] H. Karayer, D. Demirhan, and F. Büyükkılıç, "Conformable fractional Nikiforov-Uvarov method," Communications in Theoretical Physics, **66**(1), 12 (2016). https://doi.org/10.1088/0253-6102/66/1/012

[25] C. Tezcan, and R. Sever, "A general approach for the exact solution of the Schrödinger equation," International Journal of Theoretical Physics, **48**(2), 337-350 (2009). https://doi.org/10.1007/s10773-008-9806-y

[26] A. Berkdemir, C. Berkdemir, and R. Sever, "Eigenvalues and eigenfunctions of Woods–Saxon potential in PT-symmetric quantum mechanics," Modern Physics Letters A, **21**(27), 2087-2097 (2006). https://doi.org/10.1142/S0217732306019906

[27] M.M. Hammad, et al. "Analytical study of conformable fractional Bohr Hamiltonian with Kratzer potential," Nuclear Physics A, **1015**, 122307 (2021). https://doi.org/10.1016/j.nuclphysa.2021.122307

[28] A.F. Nikiforov, and V.B. Uvarov, *Special Functions of Mathematical Physics*, (Birkhäuser, Basel, 1988).

[29] V. Kumar, R.M. Singh, S.B. Bhardwaj, and F. Chand, "Spectrum Analysis of Mesons using Nikiforov-Uvarov Functional Analysis Method," Materials Research Proceedings, **22**, 7-12 (2022). https://doi.org/10.21741/9781644901878-2

[30] S. Ikhdair, and R. Sever, "Exact polynomial eigensolutions of the Schrödinger equation for the pseudoharmonic potential," Journal of Molecular Structure: THEOCHEM, **806**(1-3), 155-158 (2007). https://doi.org/10.1016/j.theochem.2006.11.019

[31] R. Sever, C. Tezcan, M. Aktaş, and Ö. Yeşiltaş, "Exact solution of Schrodinger equation for Pseudoharmonic potential," Journal of Mathematical Chemistry, **43**, 845–851 (2008). https://doi.org/10.1007/s10910-007-9233-y

[32] R. Sever, M. Bucurgat, C. Tezcan, and Ö. Yeşiltaş, "Bound state solution of the Schrodinger equation for Mie potential," Journal of Mathematical Chemistry, **34**, 749-755 (2007). https://doi.org/10.1007/s10910-007-9228-8

[33] Sß. Erkoç, and R. Sever, "1/N expansion for a Mie-type potential," Physical Review D, **33**(2), 588 (1986). https://doi.org/10.1103/PhysRevD.33.588

[34] G.C. Maitland, M. Rigby, E.B. Smith, and W.A. Wakeham, *Intermolecular Forces*, (Oxford Univ. Press, Oxford, 1987).

[35] M.R. Pahlavani, editor, *Theoretical Concepts of Quantum Mechanics*, (InTech, 2012). https://doi.org/10.5772/2075

[36] P.M. Morse, "Diatomic molecules according to the wave mechanics. II. Vibrational levels," Physical review, **34**(1), 57 (1929). https://doi.org/10.1103/PhysRev.34.57

[37] U.S. Okorie, A.N. Ikot, G.J. Rampho, P.O. Amadi, and H.Y. Abdullah, "Analytical solutions of fractional Schrödinger equation and thermal properties of Morse potential for some diatomic molecules," Modern Physics Letters A, **36**(07), 2150041 (2021). https://doi.org/10.1142/S0217732321500413

[38] C. Berkdemir, A. Berkdemir, and R. Sever, "Shape-invariance approach and Hamiltonian hierarchy method on the Woods-Saxon potential for $\ell \neq 0$ states," Journal of mathematical chemistry, **43**(3), 944-954 (2008). https://doi.org/10.1007/s10910-007-9335-6

[39] B. Gönül, and K. Köksal, "Solutions for a generalized Woods–Saxon potential," Physica Scripta, **76**(5), 565 (2007). https://doi.org/10.1088/0031-8949/76/5/026

[40] C.O. Edet, and P.O. Okoi, "Any l-state solutions of the Schrödinger equation for q-deformed Hulthen plus generalized inverse quadratic Yukawa potential in arbitrary dimensions," Revista mexicana de Física, **65**(4), 333-344 (2019). https://doi.org/10.31349/RevMexFis.65.333

[41] H. Eğrifes, D. Demirhan, and F. Büyükkiliç, "Exact solutions of the Schrödinger equation for two "deformed" hyperbolic molecular potentials," Physica Scripta, **60**(3), 195 (1999). https://doi.org/10.1238/Physica.Regular.060a00195

[42] S.-H. Dong, W.-C. Qiang, and J. Garcia-Ravelo, "Analytical approximations to the Schrödinger equation for a second Pöschl–Teller-like potential with centrifugal term," International Journal of Modern Physics A, **23**(10), 1537-1544 (2008). https://doi.org/10.1142/S0217751X0803944X

[43] M. Şimęk, and Z. Yalçin, "Generalized Pöschl-Teller potential," Journal of Mathematical Chemistry, **16**(1), 211-215 (1994). https://doi.org/10.1007/BF01169207

ПАРАМЕТРИЧНИЙ УЗАГАЛЬНЕНИЙ ДРОБОВИЙ МЕТОД НІКІФОРОВА-УВАРОВА ТА ЙОГО ЗАСТОСУВАННЯ

М. Абу-Шаді[a], Х.М. Фатх-Аллах[b]
[a]Кафедра математики та комп'ютерних наук, факультет природничих наук, Університет Менуфія, Єгипет
[b]Вищий інженерно-технологічний інститут, Менуфія, Єгипет

За допомогою узагальненої дробової похідної введено параметричний узагальнений дробовий метод Нікіфорова-Уварова (НУ). Параметричне узагальнене диференціальне рівняння другого порядку точно розв'язується у дробовій формі. Отримані результати застосовано до розширеного потенціалу Корнелла, псудогармонійного потенціалу, потенціалу Мі, потенціалу Кратцера-Фюса, потенціалу гармонічного осцилятора, потенціалу Морзе, потенціалу Вудса-Саксона, потенціалу Хюльтена, деформованого потенціалу Розена-Морса. і потенціалу Пошля-Теллера, які відіграють важливу роль у галузях молекулярної та атомної фізики. Особливі класичні випадки отримані з дробових випадків $\alpha = \beta = 1$, які узгоджуються з останніми роботами.

Ключові слова: *нерелятивістські моделі; узагальнена дробова похідна; молекулярна фізика; адронна фізика*

FIRST-PRINCIPLES CALCULATION OF STRUCTURAL, ELECTRONIC, AND OPTICAL PROPERTIES OF CUBIC PEROVSKITE CsPbF3[†]

Zozan Y. Mohammed[§], Sarkawt A. Sami[‡], Jalal M. Salih*

Department of Physics, College of Science, University of Duhok, Kurdistan Region-Iraq
[§]*e-mail: zozan.abde@uod.ac; [‡]e-mail: sarkawt@uod.ac*
Corresponding Author e-mail: jalal@uod.ac
Received February 16, 2023; revised March 7, 2023; accepted March 9, 2023

Lead halide perovskites have attracted considerable attention as one of the most promising materials for optoelectronic applications. The structural, electronic, and optical properties of the cubic perovskite $CsPbF_3$ were studied using density functional theory in conjunction with plane waves, norm-conserving pseudopotentials, and Perdew-Berg-Erzenhof flavor of generalized gradient approximation. The obtained structural parameters are a good agreement with the experimentally measured and other's theoretically predicted values. The obtained electronic band structure revealed that cubic $CsPbF_3$ has a direct fundamental band gap of 2.99 eV at point R. The calculated energy band gaps at the high symmetry points agree with the other available theoretical results. The GW method is adapted to correct the underestimated fundamental energy gap value to 4.05 eV. The contribution of the different bands was analyzed from the total and partial density of states. The electron densities show that Cs and F have strong ionic bonds, whereas Pb and F have strong covalent bonds. The optical properties of $CsPbF_3$ were calculated using the density functional perturbation theory and Kramers-Kronig relations. The wide and direct bandgap nature and the calculated optical properties imply that cubic $CsPbF_3$ can be used in optical and optoelectronic devices for high frequencies visible and low frequencies ultraviolet electromagnetic radiation.
Keywords: *CsPbF3; Perovskite; Structural properties; Bandgap; Optoelectronic properties; First-principles method*
PACS: 71.15._m; 71.15.Mb; 71.20.−b; 71.20.Nr

1. INTRODUCTION

Based on first principles approaches, several computational techniques have been developed to investigate the properties of materials. Using these first principles techniques, it is possible to predict many of the physical and chemical characteristics of the condensed matter with acceptable accuracy.

Perovskites have become extremely important from both a technological and science due to their commonly observed characteristics, such as high thermoelectric power, spin-dependent transport, superconductivity, ferroelectricity, charge ordering, colossal magneto-resistance, and the interplay of magnetic, structural and optical properties [1], [2]. These materials are often employed as substrates, sensors, and catalytic electrodes in fuel cells, and they also represent interesting optoelectronics material choices [3]–[6]. Inorganic halide-based cubic perovskite structures have also been researched and shown to have excellent absorption and low reflection coefficients as used in solar cells and optoelectronic devices [7]. Besides that, the progression of the perovskite solar cells' efficiency rose by more than 6% in the range of 10 years, as a result of their lowering costs and friendly environment [8], [9].

Perovskite fluorides are widely used as antireflective and protective coatings due to their distinctive optoelectronic characteristics. They are recognized for having fast ion conduction. In $CsPbF_3$, rapid fluoride ion conduction has been recognized [10], [11]. The single crystal of $CsPbF_3$ is a useful perovskite for studies of ionic diffusion due to its chemical bonding, relatively simple crystal structure, and excellent fluorine diffusivity throughout a wide temperature range [10]. $CsPbF_3$ has a cubic perovskite (*Pm3m*), according to a preliminary analysis of the diffraction pattern at room temperature [12]. $CsPbF_3$, which has a direct bandgap and is good in optical characteristics, may be employed successfully in photonic and optoelectronic devices despite being a possible compound for high-frequency optical systems.

There have been some theoretical studies written on $CsPbF_3$, which, reported by many researchers, who has been computed the Cubic Perovskite structural, and optoelectronic properties, which used the DFT method to analyze the Kohn-Sham equations, together with the full-potential linearized augmented plane-wave (FPLAP-W) approximation within the Wu-Cohen generalized gradient approximation (GGA)[3]. [13] another researcher applied projector augmented wave (PAW) Potentials under the PBEsol functional to study the structural properties of $CsPbF_3$.

Other studies have been published, by utilizing the DFT and the PAW method with (PBE-GGA) Perdew-Burke-Ernzerhof generalized gradient approximation, which calculated bandgap in cubic phase with *Pm3m* space group and rhombohedral phase with *R3c* space group of $CsPbF_3$ and polarizability, Rashba parameters for optoelectronic applications [14].

Also, first principle calculations have been used to calculate the structural and optoelectronic properties of $CsPbF_3$-yIy (y = 0, 1, 2), and the exchange and correlation were handled by both the GGA and HSE06 functionals [15].

Also, the structural and optoelectronic properties of Cs-based fluoroperovskites $CsMF_3$ (M = Ge, Sn or Pb) were studied and used (DFT) method with (GGA-PBE)[16].

The aim of this study is the investigation of the structural, electronic, and optical properties of cubic perovskite $CsPbF_3$ theoretically in the context of (DFT) by using ab initio calculations, by ABINIT code. Accordingly, all calculations were conducted using the plane waves with the norm-conserving pseudopotentials (PW-PP) schemes. Specifically, we compute a Kohn Sham gap in the frame of a known (PBE-GGA). Furthermore, Green's function and screened Coulomb-interaction (GW) approximations have been used to update band gap values (E_g). The current study will present a better aid in understanding the possible applications of the chosen candidate, $CsPbF_3$.

2. COMPUTATION DETAIL

In the present work, the structural, electronic, and optical characteristics of the cubic perovskite $CsPbF_3$ have been computed using the DFT framework. The wave functions were expanded in plane waves (PWs) as basis sets. The interaction between the valence electrons and ions was accounted for by the optimized norm-conserving Vanderbilt pseudopotentials [17]. The exchange-correlation term in the Kohn-Sham equations was treated by the Perdew-Berg-Erzenhof flavor of generalized gradient approximation (PBE-GGA). All calculations were performed by the ABINIT code [18]–[20]. A cubic perovskite structure, its general formula is ABX_3, has five atoms per unit cell, and belongs to the space group Pm–3m (#221). The locations of the five atoms are considered as follows: A, B, and the three X atoms occupy 0.0 0.0 0.0, 0.5 0.0 0.5, 0.5 0.5 0.0, 0.5 0.0 0.5 and 0.0 0.5 0.5, respectively (Figure 1).
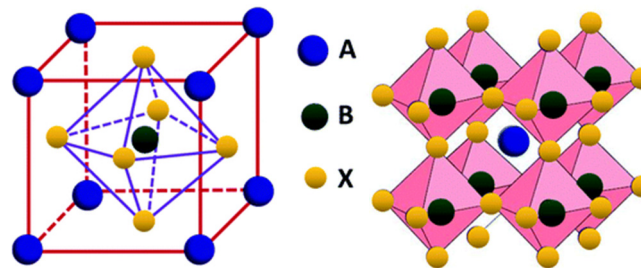
Figure 1. The cubic perovskite structure ABX_3 [21]

Convergence calculations have resulted in the cut-off energy of 1632.68 eV and (336) k points, which correspond to the 14×14×14 k-point grid of Monkhorst–Pack. The structural geometry was optimized depending on the achievement of atomic coordinates relaxation. The resulting optimized values of *a* and relaxed atomic coordinates were exploited to calculate band structure. They have also been used in the calculations of the total density of states (TDOS), the partial density of states (PTDOS), and optical properties. To correct the well-known DFT underestimation of the energy gap value [22], the GW approximation on energies and wavefunctions was carried out.

Optical properties have been calculated using density functional perturbation theory (DFPT) [23] and Kramers-Kronig relations[24]. The later were used to obtain the real and imaginary parts of the dielectric function. In addition, the refractive index, extinction coefficient, reflectivity, and absorption coefficient of the cubic $CsPbF_3$ for incident photons of energies from 0.08 eV to 40 eV have been computed. In calculating the optical properties, the interaction between the valence electrons and ions was accounted for by the norm-conserving, separable, dual-space Gaussian-type pseudopotentials by Goedecker, Teter, and Hutter (GTH) [25], [26].

3. RESULTS AND DISCUSSION
Structural properties

The optimization calculation produced the values of total energy, E_{tot}, and pressure, P, for various values of *a* (hence, unit cell volume). Figure (2) shows the total energy E_{tot} plot versus lattice constant *a*, from which the optimized value of *a* for the cubic $CsPbF_3$ was taken, see Table 1. The pressure P against the volume of the unit cell is plotted in Figure (3), from which the unit cell volume at P = 0, V_o, was calculated, see Table (1).
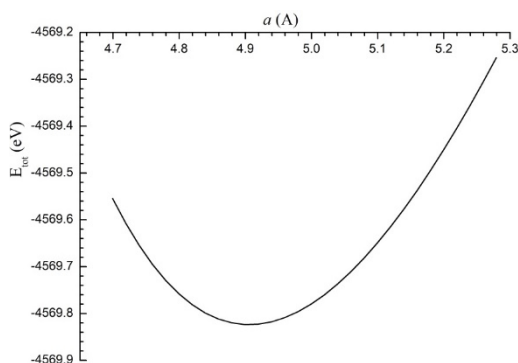

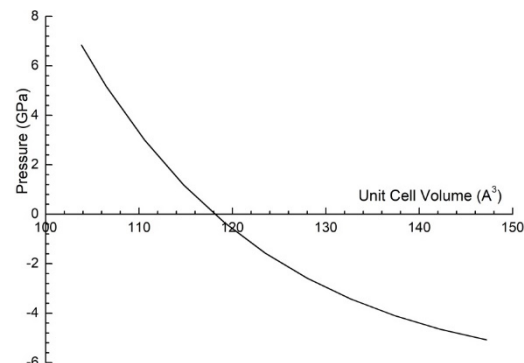**Figure 2.** Total energy, E_{tot}, versus lattice parameter, *a*, of cubic $CsPbF_3$

Figure 3. Pressure versus the corresponding unit cell volume of cubic $CsPbF_3$

Table 1. Optimized structural properties of cubic CsPbF$_3$ calculated using PBE-GGA flavor

Parameter	Present work	Theoretical	Experimental
a (A)	4.9051866	4.80652[c],4.800[a], 4.777[b],4.773[f],4.653[b],4.90[h]	4.795[a,e] 4.774[b], 4.7748[f,g]
E_{tot} (eV)	−4569.8241	−60201.5279 [b]	n.a*
B_o (GPa)	39.013	52 [b], 27.19 [d],39.035[f]	n.a
B_o`	4.811	5.11[b], 5.765[f]	n.a
V_o (A^3)	118.022986	109.041[b],116.02[f]	108.864 [b, g]
Bond length (A)			
Cs-F	3.469	3.98[b]	n.a
Pb-F	2.453	2.33[b]	n.a

* Here and below the notation, "n.a." stands for "not available".
[a] Ref. [29], [b] Ref [3], [c] Ref. [14], [d] Ref. [30], [e] Ref. [10], [f] Ref. [15], [g] Ref. [12].[h] Ref.[16]

The change of pressure P with the unit cell volume V of the cubic CsPbF$_3$ was fitted to the second-order Birch-Murnaghan equation of state [27]:

$$P(V) = \frac{3B_0}{2}\left[\left(\frac{V_0}{V}\right)^{7/3} - \left(\frac{V_0}{V}\right)^{5/3}\right]\left[1 + \frac{3}{4}(B_o' - 4)\left\{\left(\frac{V_0}{V}\right)^{2/3} - 1\right\}\right], \tag{1}$$

where B$_o$ and B$_o$′ are the zero-pressure value of bulk modulus and its pressure derivative, respectively.

From the fitting, the values of B$_o$ and B$_o$′ were obtained and they are given in Table (1). The length of the bonds Cs-F and Pb-F were also calculated and are given also in Table (1). The results of the bond length calculation show that the bond Cs-F is longer than the bond Pb-F. Referring to the electronegativity of atoms [28], this agrees with the fact that the electronegativity difference between atoms Cs and F is larger than that between Pb and F. Thus, all optimized structural properties, calculated with GGA-PBE flavor, were obtained and are listed in Table (1).

The calculated structural properties agree well with those from experiments as well as other theoretical investigations that have been done utilizing various DFT implementations, see Table (1).

Electronic properties

The electronic properties of the cubic CsPbF$_3$ were investigated through the computation of the band structure, TDOS, and PDOS. The energy of the bands was computed at the high symmetry k-points from point R to Γ along the symmetry lines R−Γ−X−M− Γ. The computed band structure is plotted in Figure (4). The figure reveals that both the minimum of the bottom conduction band (BCB), band 23, and the maximum of the top valence band (TVB), band 22, are located at the symmetry point R. That is, the cubic CsPbF$_3$ has a direct fundamental energy band gap at the symmetry point R, E_g^{R-R}. The energy gaps at k points R, Γ, X and M were calculated and are given in Table (2) along with other available theoretical results.
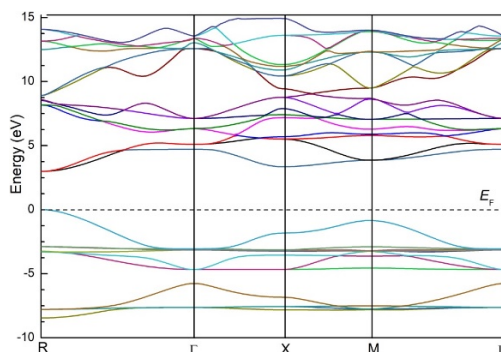

Figure 4. Band structure of cubic CsPbF$_3$

Table 2. Computed energy gaps in (eV) at some high symmetry points in the PBE-GGA approach. Results of other theoretical works are also given.

CsPbF$_3$	Eg^{R-R}	$Eg^{\Gamma-\Gamma}$	Eg^{X-X}	Eg^{M-M}
Present work	2.99336	7.77865	5.18326	4.71271
Theoretical works	2.55 [a, d], 2.62[c],2.642 [d], 2.98[e]	n.a.	5.9 [b]	5.7 [b]

[a] Ref. [29], [b] Ref. [3], [c] Ref. [14], [d] Ref. [15], [e] Ref.[16].

The present work reveals that the PBE-GGA value of the fundamental energy gap, E_g^{R-R}, is 2.99336 eV, see Table (2). It is also clear from Table (2) that the present calculated energy band gaps of the cubic CsPbF$_3$ using the PBE-GGA method are consistent with other available theoretical studies. The calculated E_g^{R-R} value using PBE-GGA suffers from the well-known problem of the DFT's underestimation of the energy gap. To correct this underestimated value of

E_g^{R-R}, the GW method on energies and wavefunctions was used. The obtained corrected value of E_g^{R-R} was 4.052 eV, which agrees well with other available theoretical results, see Table (3). Unfortunately, no experimental value is available on the fundamental band gap of the cubic $CsPbF_3$.

Table 3. Fundamental band gap E_g^{R-R} computed using PBE-GGA and GW along with results of other works

CsPbF₃	E_g^{R-R} (eV)		
	PBE-GGA value	Actual value	
		GW	Other methods
Present work	2.99336	4.052	---
Theoretical	2.98[f], 2.55[e, d], 2.62[c], 2.642[d]	n.a	3.8[a], 3.92[b], 2.42[c], 2.642[d], 3.707[d],
Experimental	n.a	n.a	

[a] Ref. [3], [b] Ref. [30], [c] Ref. [14], [d] Ref. [15], [e] Ref. [29], [f] Ref. [16].

The electronic properties can be further elaborated in terms of the density of states. That is, understanding the electronic band structure becomes more comprehensive when enlightened by DOS. For this purpose, the TDOS and PDOS for the cubic $CsPbF_3$ were calculated and are presented in Figure (5) and Figure (6), respectively. The PDOS is essential to know the contributions of different atomic states to the bands.
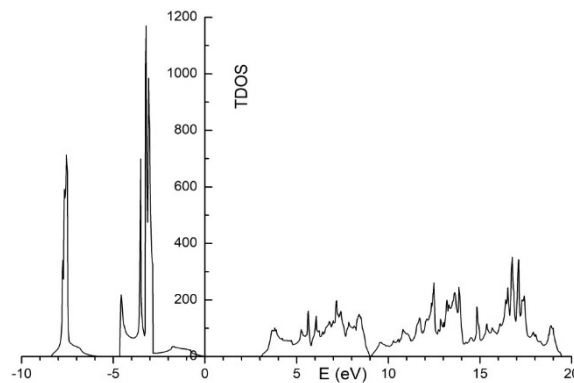
Figure 5. Total density of state (TDOS) of cubic CsPbF₃
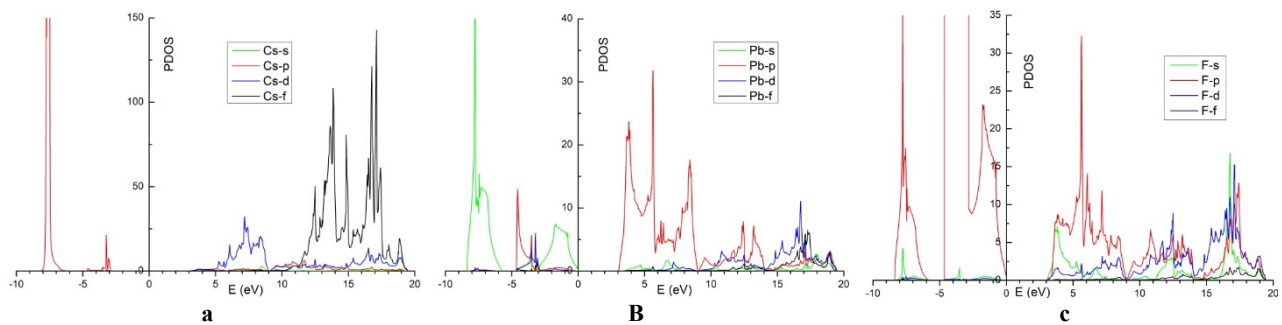
Figure 6. Partial density of states (PDOS) for the atoms (a) Cs, (b) Pb, and (c) F

The band structure of the cubic $CsPbF_3$ from –10 eV to 20 eV (looking at TDOS, Fig. (5) is divided into three dense VB regions and three dense CB regions. The three VB regions are in the energy ranges –8.5 eV to –6.0 eV, –4.7 eV to -2.8 eV, and –2.8 eV to 0 eV. The three CB regions boundaries are 3 eV, 9 eV, 14 eV, and 20 eV. It is interesting to investigate the amount of contribution of the atomic orbitals of the three atoms to each of these six regions. However, because of their role in the optical response, only the upper region of VB and the lower region of CB will be investigated. To realize the amount of the contribution of each of the atoms Cs, Pb, and F to the upper region, ~ (–2.8 to 0) eV, of VB, the full PDOS of the three atoms corresponding to the VB have been plotted alongside, see Fig. (7).

It is clear from Fig. (7) that the bands in this range, ~ (–2.8 to 0) eV, arise mainly from the F-p orbital. The Pb-s orbital contribution is small, namely, one-third of F-p, the contribution of Pb-p is very small, and Pb-d and F-s contributions are almost insignificant. It is clear from Fig. (6) that the lower region of the CB, (14 to 200) eV, arises mainly from Cs-d, Pb-p, and F-p orbitals, which nearly contribute equally, while the contribution of F-s is less, namely, about one fifth. The contribution of F-d is small, that of Cs-s, Pb-d, and Pd-f are very small and Cs-p, Cs-f, and F-s contribute almost insignificantly.

Figures (5) – (7) reveal that the top most four states in VB, above –4.7 eV, arise mainly from F-p orbital and much less from Pb-s. The bottom most nine states of CB, below 9 eV, arise mainly from the orbitals Cs-d, Pb-p, and F-p, which equally contribute. It is also clear that the lower edge of the fundamental band gap is determined by the F-p orbital,

Fig. (7), while the upper edge of the fundamental band gap arises from the Pb-p orbital, Fig. (6b). This implies that the fundamental band gap arises from the higher occupied orbital of the F atom and the higher occupied orbital of Pb, which are F-$2p^5$ and Pb-$6p^2$, respectively. Accordingly, one realizes that the fundamental band gap can be tuned by changing the atoms F and/or Pb, provided the new structure be stable.

In summary, see Fig. 6, the formation of VB is mostly due to the contribution of the s state of Pb and p states of Cs and F, while CB is mostly due to the contributions of the f state of Cs and p states of Pb and F. The calculated DOS is in good agreement with the previous theoretical results [3], [15].
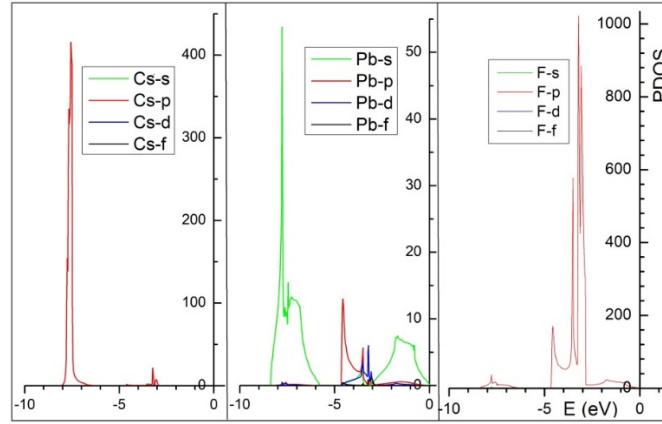
Figure 7. Partial density of states (PDOS) of VB for the atoms (a) Cs, (b) Pb, and (c) F.

Optical properties

To predict a material's possibilities for use in photovoltaic devices, the investigation of its optical properties is crucial. The most important frequency-dependent optical properties are the refractive index $n(\omega)$, extinction coefficient $k(\omega)$, reflectivity $R(\omega)$, and absorption coefficient $\alpha(\omega)$. These characteristics can be calculated using [31]:

$$n(\omega) = \left[\frac{\varepsilon_1(\omega)}{2} + \frac{\sqrt{\varepsilon_1(\omega)^2 + \varepsilon_2(\omega)^2}}{2}\right]^{1/2} \tag{2}$$

$$k(\omega) = \left[\frac{\varepsilon_1(\omega)}{2} - \frac{\sqrt{\varepsilon_1(\omega)^2 + \varepsilon_2(\omega)^2}}{2}\right]^{1/2} \tag{3}$$

$$R(\omega) = \left|\frac{\sqrt{\varepsilon(\omega)} - 1}{\sqrt{\varepsilon(\omega)} + 1}\right|^2 \tag{4}$$

and

$$\alpha(\omega) = \frac{4\pi k(\omega)}{\lambda} \tag{5}$$

respectively, where $\varepsilon_1(\omega)$ and $\varepsilon_2(\omega)$ are the real and imaginary components of the dielectric function ε:

$$\varepsilon(\omega) = \varepsilon_1(\omega) + i\varepsilon_2(\omega) \tag{6}$$

The real component ε_1 of the dielectric function indicates the retaining ability of the material while the imaginary component ε_2 determines its absorptive ability. As much as solar cells are concerned, ε_1 determines the ability of the cell to store energy, and ε_2 determines its absorption limitations and, thus, capability to gain energy [32].
It is clear from Eqs. (2)–(5) that if the real and imaginary components of the dielectric function are known, it is possible to compute those optical properties. Using DFPT [18] and Kramers-Kronig relations [33], the real and imaginary components of the dielectric function were computed for incident photon energies from 0.08 eV to 40 eV. Then, the frequency-dependent optical properties were calculated using Eqs. (2)–(5). The computed real and imaginary components of the dielectric function, n, k, R, and α spectra are shown in Figure (8).

Figure (8a) reveals that the value of the zero-frequency limit $\varepsilon_1(0)$, known also as the static dielectric constant, for cubic CsPbF$_3$ is 3.14. The knowledge of the value of the static dielectric constant is important in optoelectronic and photovoltaic technology. The higher the $\varepsilon_1(0)$ value, the greater the potentiality of the material for designing optoelectronic devices [34]. The figure shows that starting from the zero-frequency limit $\varepsilon_1(0)$, $\varepsilon_1(\omega)$ begins to rise and, after a few peaks, reaches its maximum value of 5.42 at 4.65 eV beyond which gradually declines passing through many peaks and becoming negative in the energy range (15.10-17.71) eV. Thus, the cubic CsPbF$_3$ has a dielectric behavior $(\varepsilon_1(\omega) > 0)$ in response to the most investigated photon spectra except for the energy range 15.10 – 17.71 eV for which it has a metallic characteristic $(\varepsilon_1(\omega) < 0)$. The negative $\varepsilon_1(\omega)$ in an energy range indicates the attenuation of the incident photon in that range, thus, a metallic behavior of the material [35].
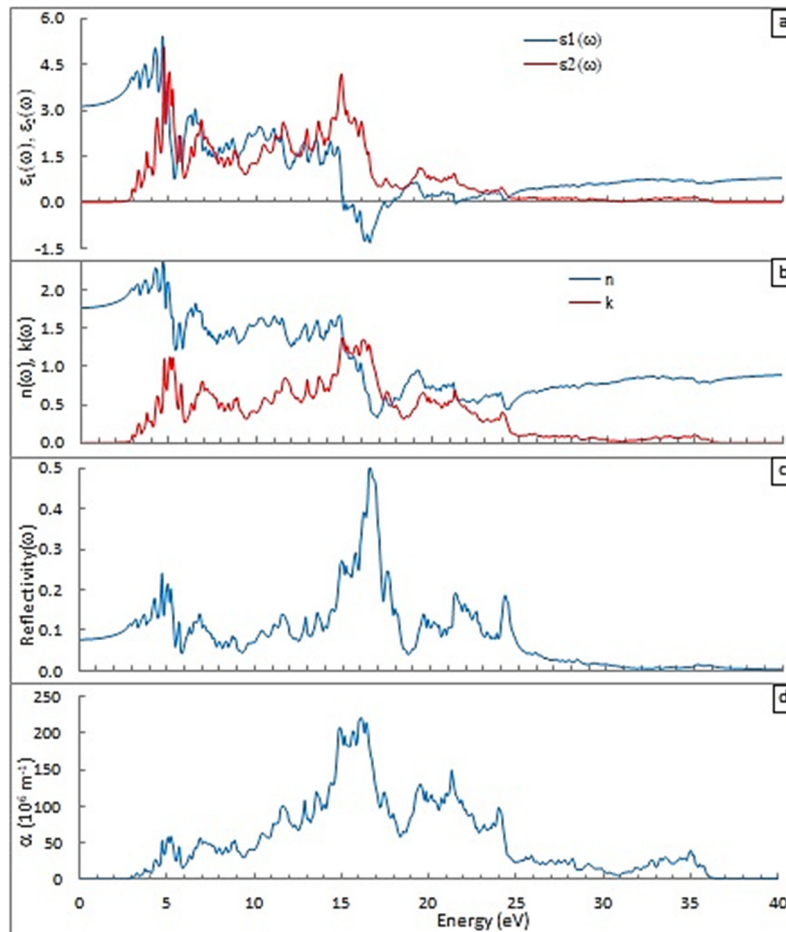
Figure 8. Optical properties versus the energy of cubic $CsPbF_3$: (a) Real ε_1 and imaginary ε_2 parts of the dielectric function, (b) Refractive index n and extinction coefficient k, (c) Reflectivity R, and (d) Absorption coefficient α.

The $\varepsilon_2(\omega)$ illustrates the absorption of incoming radiation impinging at the surface, and the excellent optical materials absorb the incoming photons, almost entirely, within the top surface. Its values are compatible with those estimated from the electronic band structures and are closely connected to the optical band gap.

It is noticed from Figure (8a) that the threshold point in the spectrum of $\varepsilon_2(\omega)$ is nearly at 2.9 eV. This threshold corresponds to the transition from the VB state that arises from the orbitals F-2p and Pb-6s to the CB state that arises from the Pb-6p orbital, see Fig. (6). The value of the threshold is solely determined by the fundamental band gap. The figure shows that starting from the threshold, $\varepsilon_2(\omega)$ starts increasing and, after a few peaks, reaches its maximum value of 5.07 at 4.74 eV, then, passing through many peaks, reaches another high-value peak of 4.20 at 14.86 eV beyond which it decreases and almost vanishes beyond 24.00 eV.

Figure (8b) shows that the variation of the refractive index $n(\omega)$ and extinction coefficient $k(\omega)$ follow the same pattern as ε_1 and ε_2, respectively. The $n(\omega)$ increases from its zero-frequency limit n(0), 1.77, and reaches its maximum value of 2.38 at 4.65 eV. The $k(\omega)$ spectrum indicates that the maximum extinction coefficient is 1.37 and occurs at 14.94 eV. Beyond 24.41 eV, $k(\omega)$ almost vanishes. For incident photons having energies greater than 15.67 eV, the refractive index $n(\omega)$ becomes less than one which implies that the group velocity, $\upsilon_g = c/n$, is greater than the speed of light c. The conversion from n > 1 to n < 1 occurs at the same energy at which $\varepsilon_1(\omega)$ has the largest negative value, see Fig. (8a and 8b).

Figure (8c) represents the computed frequency-dependent reflectivity $R(\omega)$. The figure reveals that the zero-frequency limit of reflectivity, R(0), is about 0.08. The figure shows that starting from the zero-frequency limit R(0), $R(\omega)$ begins to rise and, after a few peaks, reaches its maximum value of 0.50 at 16.57 eV then decreases passing through many peaks and approaches zero beyond 30 eV, that is, cubic $CsPbF_3$ becomes almost transparent to photons of energies higher than 30 eV.

One can notice, in Fig. (8a – 8c), that the maximum negative value of $\varepsilon_1(\omega)$ and transition of $n(\omega)$ value to less than one, both, occur at the same photon energy, ~16.5 eV, and coincide with the maximum value of $R(\omega)$. This implies that, at that energy, cubic $CsPbF_3$ becomes superluminal, a common behavior in perovskites [36], [37].

The computed absorption coefficient $\alpha(\omega)$ is presented in Fig. (8d). $\alpha(\omega)$ spectrum predicts how many photons of various energies are absorbed, thus, is directly connected to the fundamental energy gap. The photons with energies lower than the fundamental energy gap are transmitted, while photons with equal and higher energies are absorbed. Figure (8d)

shows that the absorption starts around 2.99 eV and then increases to its maximum value of 220.23×10^6 m^{-1} at 16.16 eV. Figures (8a) and (8d) reveal that absorption is higher for energies at which $\varepsilon_1(\omega)$ is negative and maximum absorption occurs where $\varepsilon_1(\omega)$ has a maximum negative value. The significant values of $\alpha(\omega)$, see Fig. (8d), cover a wide range of energy, namely, about (2.9 – 36.5) eV and, thus, for high energies visible light and low ultraviolet, the cubic CsPbF$_3$ perovskite is a promising material for a variety of optical and optoelectronic devices.

CONCLUSIONS

The structural, electronic, and optical properties of cubic CsPbF$_3$ have been investigated by using first-principles computations, namely, the DFT with the PBE-GGA flavor as the exchange-correlation energy. The structural properties, band structure, and total and partial density of states were calculated. The GW approximation was implemented to correct the underestimated energy band gap. The optical properties were also computed using Kramer–Kronig relations.

The calculated structural characteristics, such as lattice constant, bond length, bulk modulus, and its pressure derivative, agree well with other theoretical and experimental findings. The calculated length of the bonds Cs-F and Pb-F are consistent with the electronegativity of the three atoms. The computed band structure reveals that cubic CsPbF$_3$ has a direct fundamental energy band gap that is located between band 22 and band 23 at the symmetry point R. The calculated energy band gaps at the high symmetry points R, Γ, X and M are in good agreement with those of other theoretical studies. The calculated value of the fundamental energy band gap, 4.025 eV, suggests that cubic CsPbF$_3$ is a wide band gap semiconductor.

The real and imaginary parts of the dielectric function, refractive index, extinction coefficient, reflectivity, and absorption coefficient were calculated for incident photon energies from 0.08 eV to 40 eV. In the spectrum of the imaginary part of the dielectric function, different characteristics are seen, mostly as a result of the transitions from the VB states that arise from Cs-p and F-p orbitals to unoccupied states in the CB. The spectrum of the real part of the dielectric function revealed that cubic CsPbF$_3$ has a metallic behavior in response to the incident photon energies from 15.10 eV to 17.71 eV.

The calculated absorption coefficient is appreciable in the high-frequency visible and low-frequency ultraviolet regions, thus, indicating the feasibility of cubic CsPbF$_3$ to be used in optoelectronic devices for such regions of electromagnetic radiation.

ORCID

Jalal M. Salih, https://orcid.org/0000-0002-9587-3351

REFERENCES
[1] C. Weeks, and M. Franz, "Topological insulators on the Lieb and perovskite lattices," Phys. Rev. B - Condens. Matter Mater. Phys. **82**(8), 1-5 (2010), https://doi.org/10.1103/PhysRevB.82.085310
[2] A.S. Moskvin, A.A. Makhnev, L.V. Nomerovannaya, N.N. Loshkareva, and A.M. Balbashov, "Interplay of p-d and d-d charge transfer transitions in rare-earth perovskite manganites," **82**(3), 035106 (2018), https://doi.org/10.1103/PhysRevB.82.035106
[3] G. Murtaza, I. Ahmad, M. Maqbool, H.A.R. Aliabad, and A. Afaq, "Structural and optoelectronic properties of cubic CsPbF3 for novel applications," Chinese Phys. Lett. 28(11), 117803 (2011), https://doi.org/10.1088/0256-307X/28/11/117803.
[4] J. Burschka, N. Pellet, S.-J. Moon, R. Humphry-Baker, P. Gao, M.K. Nazeeruddin, and M. Grätzel, "Sequential deposition as a route to high-performance perovskite-sensitized solar cells," Nature, **499**(7458), 316-319 (2013), https://doi.org/10.1038/nature12340
[5] S.D. Stranks, G.E. Eperon, G. Grancini, C. Menelaou, M.J.P. Alcocer, T. Leijtens, L.M. Herz, et al., "Electron-hole diffusion lengths exceeding 1 micrometer in an organometal trihalide perovskite absorber," Science (80)., **342**(6156), 341-344 (2013), https://doi.org/10.1126/science.1243982
[6] J. Duan, Y. Zhao, X. Yang, Y. Wang, B. He, and Q. Tang, "Lanthanide Ions Doped CsPbBr3 Halides for HTM-Free 10.14%-Efficiency Inorganic Perovskite Solar Cell with an Ultrahigh Open-Circuit Voltage of 1.594 V," Adv. Energy Mater. **8**(31), 1802346 (2018), https://doi.org/10.1002/aenm.201802346
[7] M. Roknuzzaman, K.K. Ostrikov, H. Wang, A. Du, and T. Tesfamichael, "Towards lead-free perovskite photovoltaics and optoelectronics by ab-initio simulations," Sci. Rep. **7**(1), 14025 (2017), https://doi.org/10.1038/s41598-017-13172-y
[8] A. Kojima, K. Teshima, Y. Shirai, and T. Miyasaka, "Organometal halide perovskites as visible-light sensitizers for photovoltaic cells," J. Am. Chem. Soc. **131**(17), 6050 (2009), https://doi.org/10.1021/ja809598r
[9] F. Sahli, J. Werner, B.A. Kamino, M. Bräuninger, R. Monnard, B. Paviet-Salomon, L. Barraud, et al., "Fully textured monolithic perovskite/silicon tandem solar cells with 25.2% power conversion efficiency," Nat. Mater. **17**(9), 820-826 (2018), https://doi.org/10.1038/s41563-018-0115-4
[10] V.M. Bouznik, Yu.N. Moskvich, and V.N. Voronov, "Nuclear Magnetic Resonance Study Of "F Motion In CssPbF," Chem. Phys. Lett. **37**(3), 464-467 (1976), https://doi.org/10.1016/0009-2614(76)85014-2
[11] A.V Chadwick, J.H. Strange, G.A. Ranieri, and M. Terenzi, "Studies of ionic motion in perovsmite fluorides," Solid State Ionics, **9**, 555-558 (1983), https://doi.org/10.1016/0167-2738(83)90294-1
[12] P. Berastegui, S. Hull, and S.-G. Eriksson, "A low-temperature structural phase transition in CsPbF 3," J. Phys. Condens. Matter, **13**(22), 5077 (2001), https://doi.org/10.1088/0953-8984/13/22/305
[13] E.H. Smith, N.A. Benedek, and C.J. Fennie, "Interplay of Octahedral Rotations and Lone Pair Ferroelectricity in CsPbF3," Inorg. Chem. **54**(17), 8536-8543 (2015), https://doi.org/10.1021/acs.inorgchem.5b01213
[14] P. Bhumla, D. Gill, S. Sheoran, and S. Bhattacharya, "Origin of Rashba spin-splitting and strain tunability in ferroelectric bulk CsPbF3," J. Phys. Chem. Lett. **12**(39), 9539-9546 (2021), https://doi.org/10.1021/acs.jpclett.1c02596
[15] A. Amudhavalli, R. Rajeswarapalanichamy, R. Padmavathy, and K. Iyakutti, "Electronic structure and optical properties of CsPbF3-yIy (y = 0, 1, 2) cubic perovskites," Acta Phys Pol A, **139**(6), 692-697 (2021), https://doi.org/10.12693/APHYSPOLA.139.692

[16] Y. Selmani, H. Labrim, M. Mouatassime, and L. Bahmad, "Structural, optoelectronic and thermoelectric properties of Cs-based fluoroperovskites CsMF3 (M = Ge, Sn or Pb)," Mater. Sci. Semicond. Process. **152**, 107053 (2022), https://doi.org/10.1016/j.mssp.2022.107053

[17] D.R. Hamann, "Optimized norm-conserving Vanderbilt pseudopotentials," Phys. Rev. B, **88**(8), 085117 (2013), https://doi.org/10.1103/PhysRevB.88.085117

[18] X. Gonze, B. Amadon, P.-M. Anglade, J.-M. Beuken, F. Bottin, P. Boulanger, F. Bruneval, and D. Caliste, *et al.*, "ABINIT: First-principles approach to material and nanosystem properties," Comput. Phys. Commun. **180**(12), 2582-2615 (2009), https://doi.org/10.1016/j.cpc.2009.07.007

[19] X. Gonze, F. Jollet, F. A. Araujo, D. Adams, and B. Amadon, "Recent developments in the ABINIT software package," Comput. Phys. Commun. **205**, 106-131 (2016), https://doi.org/10.1016/j.cpc.2016.04.003

[20] The ABINIT Group, maintained by Jean-Michel Beuken, https://www.abinit.org/

[21] Z. Yi, N. H. Ladi, X. Shai, H. Li, Y. Shen, and M. Wang, "Will organic-inorganic hybrid halide lead perovskites be eliminated from optoelectronic applications?," Nanoscale Adv. **1**(4), 1276-1289 (2019), https://doi.org/10.1039/c8na00416a

[22] B.M. Ilyas, and B.H. Elias, "Theoretical Study of the Structural, Elastic, Electronic, Optical and Thermodynamic Properties of CsXCl3 (X = Pb, Cd) under Pressure," Phys. B Condens. Matter, **S0921-4526**(16), 30587 (2016), https://doi.org/10.1016/j.physb.2016.12.019

[23] S. Sharma, and C. Ambrosch-Draxl, "Second-harmonic optical response from first principles," Phys. Scr. T, **T109**, 128 (2004), https://doi.org/10.1238/Physica.Topical.109a00128

[24] L.A. Collins *et al.*, "Dynamical and optical properties of warm dense hydrogen," Phys. Rev. B, **63**(18), 184110 (2001), https://doi.org/10.1103/PhysRevB.63.184110

[25] S. Goedecker, and M. Teter, "Separable dual-space Gaussian pseudopotentials," Phys. Rev. B, **54**(3), 1703 (1996), https://doi.org/10.1103/PhysRevB.54.1703

[26] C. Hartwigsen, S. Goedecker, and J. Hutter, "Relativistic separable dual-space Gaussian pseudopotentials from H to Rn," Phys. Rev. B, **58**(7), 3641 (1998), https://doi.org/10.1103/PhysRevB.58.3641

[27] F. Birch, "Finite elastic strain of cubic crystals," Phys. Rev. **71**(11), 809-824 (1947), https://doi.org/10.1103/PhysRev.71.809

[28] R.1. K. H. James E. Huheey, Ellen A. Keiter, and Collins, "lnorganic Chemistry: Principles of Structure and Reactivity," Annu. Rev. Psychol. **8**(4), 257-271 (1993), http://www.ncbi.nlm.nih.gov/pubmed/8434894

[29] L.Q. Jiang, J.K. Guo, H.B. Liu, M. Zhu, X. Zhou, P. Wu, and C.H. Li, "Prediction of lattice constant in cubic perovskites," J. Phys. Chem. Solids, **67**(7), 1531-1536 (2006), https://doi.org/10.1016/j.jpcs.2006.02.004

[30] Q. Mahmood, M. Hassan, M. Rashid, B. U. Haq, and A. Laref, "The systematic study of mechanical, thermoelectric and optical properties of lead based halides by first principle approach," Phys. B Condens. Matter, **571**, 87-92 (2019), https://doi.org/10.1016/j.physb.2019.06.061

[31] K.E. Babu, A. Veeraiah, D.T. Swamy, and V. Veeraiah, "First-principles study of electronic and optical properties of cubic perovskite CsSrF," Mater. Sci. Pol. **30**(4), 359-367 (2012), https://doi.org/10.2478/s13536-012-0047-7

[32] N.A. Abdulkareem, "First principle study of structural, electronic and optical behaviour of CsPbX₃ (X= Br, Cl, I) under hydrostatic pressure," University of Zakho Zakho, Kurdistan region-Iraq, 2011.

[33] L.A. Collins *et al.*, "Dynamical and optical properties of warm dense hydrogen," Phys. Rev. B - Condens. Matter Mater. Phys. **63**(18), 184110 (2001), https://doi.org/10.1103/PhysRevB.63.184110

[34] S.K. Mitro, M. Saiduzzaman, T.I. Asif, and K.M. Hossain, "Band gap engineering to stimulate the optoelectronic performance of lead-free halide perovskites RbGeX 3 (X = Cl, Br) under pressure," J. Mater. Sci. Mater. Electron. **33**(17), 13860-13875 (2022), https://doi.org/10.1007/s10854-022-08318-2

[35] B. Xu, X. Li, J. Sun, and L. Yi, "Electronic structure, ferroelectricity and optical properties of CaBi2Ta2O9," Eur. Phys. J. B, **66**, 483-487 (2008), https://doi.org/10.1140/epjb/e2008-00461-9

[36] L.J. Wang, A. Kuzmich, and A. Dogariu, "Gain-assisted superluminal light propagation," Nature, **406**(6793), 277-279 (2000), https://doi.org/10.1038/35018520

[37] N.P. Bigelow, and C.R. Hagen, "Comment on 'observation of superluminal behaviors in wave propagation,'" Phys. Rev. Lett. **87**(5), 59401-1 (2001), https://doi.org/10.1103/PhysRevLett.87.059401

ПЕРШОПРИНЦИПИ РОЗРАХУНКУ СТРУКТУРНИХ, ЕЛЕКТРОННИХ І ОПТИЧНИХ ВЛАСТИВОСТЕЙ КУБІЧНОГО ПЕРОВСКІТУ CsPbF₃

Зозан Ю. Мохаммед, Саркаут А. Самі, Джалал М. Саліх
Департамент фізики, Науковий коледж, Університет Духок, Курдистан, Ірак

Перовскіти галогенідів свинцю привернули значну увагу як один із найбільш перспективних матеріалів для оптоелектронних застосувань. Структурні, електронні та оптичні властивості кубічного перовскіту CsPbF₃ були вивчені з використанням теорії функціоналу густини в поєднанні з плоскими хвилями, псевдопотенціалами, що зберігають норму, і узагальненим градієнтним наближенням Пердью-Берг-Ерценгофа. Отримані структурні параметри добре узгоджуються з експериментально виміряними та іншими теоретично прогнозованими значеннями. Отримана електронна структура зон показала, що кубічний CsPbF₃ має пряму фундаментальну заборонену зону в точці R 2,99 еВ. Розраховані енергетичні заборонені зони в точках високої симетрії узгоджуються з іншими доступними теоретичними результатами. Метод GW адаптовано для корекції заниженого значення фундаментальної енергетичної щілини до 4,05 еВ. Внесок різних смуг аналізувався з повної та часткової щільності станів. Електронна густина показує, що Cs і F мають міцні іонні зв'язки, тоді як Pb і F мають міцні ковалентні зв'язки. Оптичні властивості CsPbF₃ розраховано з використанням теорії збурень функціоналу густини та співвідношень Крамерса-Кроніга. Широка та пряма заборонена зона та розраховані оптичні властивості означають, що кубічний CsPbF₃ можна використовувати в оптичних та оптоелектронних пристроях для високочастотного видимого та низькочастотного ультрафіолетового електромагнітного випромінювання.

Ключові слова: *CsPbF₃; перовскіт; структурні властивості; заборонена зона; оптоелектронні властивості; метод першопринципів*

ECO-FRIENDLY GREEN SYNTHESIS AND PHOTOCATALYST ACTIVITY
OF Ag- ZnO NANOCOMPOSITE†

Noorullah Mohammed Nemma, Zainab Sabeeh Sadeq*

Department of Physics, College of Science, University of Baghdad, Baghdad, Iraq
Corresponding Author e-mail: zainab.sadeq@sc.uobaghdad.edu.iq
Received June 21, 2023; revised July 8, 2023; accepted July 11, 2023

The study successfully synthesized Ag NPs, ZnO NPs, and Ag/ZnO nanocomposites using an easy, cost effect and sustainable green synthetic approach. The purpose of synthesizing Ag/ZnO nanocomposites using two different plant extracts was to study their photo-degradation activity on Methylene Blue (MB) dye. (XRD) diffraction analysis confirmed the presence of Ag crystalline size and the wurtzite hexagonal structure of ZnO. (FE-SEM) results indicated spherical, nanorods and there is Clustering of NPs with an irregular shape. The resulting metal/semiconductor oxide nanocomposites possessed unique photo degradation characteristics that were absent in the individual Ag NPs and ZnO NPs.

Keywords: *Nanoparticles; Nanocomposite; Wastewater treatment; Catalyst*
PACS: 61.82.Fk, 81.07.Bc, 81.07.De, 81.16.Be, 81.16.Hc

1. INTRODUCTION

In recent decades, the disposal of harmful and toxic contaminants, such as organic dyes and heavy metal ions, has led to water pollution, which has become a significant environmental issue. Industrial effluent streams are the primary sources through which heavy metals and dyes enter the ecological system, posing substantial risks to human health [1]. Dyes have diverse applications across various fields in industries such as textiles, cosmetics, printing, and pharmaceuticals. Furthermore, these dyes are known to be environmentally stable and resistant to biodegradation unless a catalyst is present [2]. Effluents containing dyes are typically treated using chemical, physicochemical, or biological methods [3]. However, the utilization of these methods may prove to be both expensive and time-intensive. As a result, it is crucial to explore highly efficient and environmentally friendly approaches to degrade these pollutants in the environment.

Among the different methods proposed for wastewater treatment [4-6], the photocatalytic process utilizing nano-sized materials has emerged as a reliable and environmentally safe technique. This process offers complete mineralization of dyes on the surface of these materials and is known for its high sensitivity, reasonable costs, and effectiveness [7-16].

Photo catalysis process is a technique that uses ultraviolet or visible light to break down organic dirt on surfaces [17-20]. A typical photo-catalysis process has a high photocatalytic activity under ultraviolet or visible light for the degradation of Methylene blue. A semiconductor photo catalyst absorbs photons to generate charge separation and activate the oxidation process. Light capturing, electron-hole pair formation and separation, and catalytic reaction have all been recognized as key processes in photo catalysis in latest years [21]. While numerous nanomaterials are used for wastewater treatment, many of them exhibit limitations such as low catalytic activity, limited adsorption capacity, constraints on photocatalytic efficiency, light absorption, and expensive production costs. [22, 23]

Researchers have dedicated significant attention to studying metal nanoparticles (MNPs) during the past few decades [24-27]. Noble metal NPs have garnered greater interest compared to other metal nanoparticles because of their small size and high surface-to-volume ratio [28], the utilization of MNPs as heterogeneous catalysts offers notable advantages. [26, 29–33]. However, one challenge that arises is the tendency of MNPs to aggregate. To address this issue and minimize the aggregation of nanoparticles (NPs), we require a support ideal material. Various inorganic compounds, including TiO_2, ZnO, Fe_2O_3, Ta_2O_3, CuO, NiO, Cr_2O_3, RuO_2, etc.), transition metal oxides with wide band gaps and stability can play an important role on the photocatalytic to remove organic [34]. Between of the different heterogeneous photo catalysts, zinc oxide, silver and gold NPs appeared as a more attractive alternative for controlling the pollution-related environmental issues [35-38].

The combination of metal nanoparticles (NPs) with metal oxide semiconductor nanocomposites has garnered significant attention from researchers worldwide. This is primarily due to their remarkable optical, electrical, and chemical properties, as well as their promising potential in various applications [39-41].

Nanoparticles (NPs) are commonly produced through various methods, including solvothermal processes, chemical reduction methods, and sol-gel techniques [42–47]. However, these methods are often highly cost and require the utilization of harmful chemicals. These chemicals are pose potential risks to the environment and biological systems [42-47].

Recently, there has been a development of biosynthetic approaches for the synthesis of MNPs. These methods make use of solvents that are comparatively less toxic, such as water, biological extracts, biological systems, and microwave technology [48–51].

Utilizing plant extracts for various applications offers several advantages, including their widespread availability, ease of handling, and possessing a diverse range of metabolites, although plant extracts contain a variety of secondary

metabolites with notable reducing potential, they can be effectively utilized as both reducing and stabilizing agents in the production of environmentally friendly nanoparticles (NPs) [52]. These characteristics make plant extracts a favorable option when compared to other biosynthetic approaches [53].

The aim of the present work is synthesis Ag- ZnO Nanocomposite by eco-green approach in ambient conditions using the extract of plant which work as both reducing and stabilizing agents and study their Photo catalysis activity.

2. EXPERIMENTAL
2.1 Materials

Silver nitrate (AgNO₃), zinc nitrate hexahydrate (Zn(NO₃)₂·6H₂O), sodium hydroxide (NaOH), and methylene blue were obtained from Carlo Erba and Himedia chemical companies in highly pure form and used without further purification. The aloe vera plant and Hibiscus sabdariffa leaves were acquired from nearby markets. All glassware used in the experiment underwent thorough cleaning, including washing twice with distilled water (DW) and ethanol, followed by drying in the oven prior to use.

2.2 Preparation of Ag NPs, ZnO NPs and Ag-ZnO nanocomposite via Aloe vera plant extract

Initially, we produced the aloe vera extract by washing and cutting the leaves, extracting the gel, and blending it with a mixer. We took 100 grams of the gel and mixed it with 300 milliliters of distilled water, before placing it on a magnetic stirrer for 30 minutes. Subsequently, once it had cooled down we centrifuged the solution at 4000 rotations per minute for approximately 10 minutes. Then to get the Ag NPs, we prepared 0.1M of AgNO₃ solution, the solution was stirred for 30 min at 60 C° on the magnetic stirrer and then we added 50 ml of the aloe vera extract to 100 ml of AgNO₃. On the other hand, we prepared other solution from mixing 20 ml of aloe vera gel which was diluted with 150 ml of deionized water. After filtered and purified, 2 g of zinc nitrate hexahydrate (Zn(NO₃)₂ · 6H₂O) was dissolved in 150 ml of the plant extract with stirring using the magnetic stirrer for 1 h at an 80 °C. Leave the zinc solution overnight. Separately, 4 g of Sodium hydroxide (NaOH) is dissolved in 35 ml of deionized water. Then 12 ml of NaOH solution was added to the precursor solution with the extract. Following the formation of a white precipitate, the Ag/ZnO nanocomposite is produced by gradually adding 100 milliliters of Ag nanoparticles to 100 milliliters of ZnO nanoparticles at 60 degrees Celsius, while continuously stirring to ensure thorough mixing. Final indicate was Ag/ZnO nanocomposite. Then all solutions were deposit on slides for further work.

2.3 Preparation of Ag NPs, ZnO NPs and Ag-ZnO nanocomposite via Hibiscus sabdariffa plant extract

Similar method was adapted to prepare Ag/ZnO nano-campsite via Hibiscus sabdariffa. First, we take the Hibiscus flowers then washed thoroughly with DW. Then they were sun dried and grinded into small pieces we mixed 2 gr with 100 ml of DW then placed on a magnetic stirrer at 60 C° for 30 min. The red extract was filtered twice with cotton wool balls. After the completion of the extraction process, we take 50 ml of aqueous extract and repeat the same operation to prepare the Ag NPs. Then to prepare ZnO NPs, 4g of zinc nitrate hexahydrate (Zn(NO₃)₂ 6H₂O) was dissolved in 150 ml of the plant extract with stirring using the magnetic stirrer for 1 h at an 80 °C. Leave the solution overnight. Separately, 4 g of Sodium hydroxide (NaOH) is dissolved in 35 ml of deionized water. Then 20 ml of NaOH solution was added to the precursor solution with the extract. After the formation of a white precipitate, the Ag/ZnO nanocomposite is also produced by gradually adding 100 milliliters of Ag nanoparticles to 100 milliliters of ZnO nanoparticles at 60 degrees Celsius, while continuously stirring to ensure thorough mixing. Then we deposit all the solutions on slides for further experiments.

2.4 Photocatalytic activity

The procedure was conducted in according to previous work [54, 55]. The efficiency of the synthesized photocatalyst samples were assessed by monitoring the degradation of MB dye as a model pollutant. To control the photo-catalytic degradation process, the optical absorption peak of MB dye at 664.5 nm was determined. We prepared solution of MB dye by dissolving 10 mg in 1000 ml of distilled water and stirring it on a magnetic stirrer for two hours. The solution was left overnight to ensure complete dissolution of the MB dye before using it. Approximately 30 mg of nanomaterial (Samples) was adding, 50 ml of MB (10 mg/ml), the solution was stirred in a dark room for one hour to ensure adsorption equilibrium between Methylene Blue (MB) and the catalyst surfaces. Subsequently, the solution was exposed to UV light from a 6W lamp with a wavelength of 254 nm serving as the irradiation source. At equal intervals of time (15 minutes), samples were collected, filtered, and monitored for MB degradation using UV-visible spectroscopy (Shimadzu 1900i-Japan). Using the following eqution [56] to calculate the degradation efficiency.

$$\text{Efficiency} = \frac{(C_0 - C)}{C_0} \times 100\% = \frac{(A_0 - A)}{A_0} \times 100\% \qquad (1)$$

C_0, C, A_0, and A refer to the concentration and absorbance of methylene blue (MB) before and after exposure to UV light, respectively.

3. RESULTS AND DISCUSSION
3.1 X-ray diffraction (XRD) analysis

First, analysis of Ag NPs via A. vera leaves and H. sabdariffa flower extracts. (Figure 1.a) shows XRD pattern and the crystalline size of the synthesized Ag NPs with diffraction peaks at 2θ = 35.2°, 43°, 67°, and 74.8° for the Aloe vera, and

diffraction peaks with $2\theta = 35°$, $46.4°$, $65°$, and $72.2°$ for Hibiscus sabdariffa respectively. Which both can be corresponded to the (1 1 1), (2 0 0), (2 2 0) and (3 1 1) Braggs planes. Also, the X-ray diffraction powder pattern in the two extract also had small peaks. This could be formed because of the organic ingredients of the leaves and flower extracts and because of the small residual amounts of AgNO₃ that it is did not diminished. It is notable that the peak was associated with the (111) plane is the highest and most intense of the peaks. The Ag NPs produced in the present process are naturally crystalline with an FCC structure and the determined patterns of XRD matched closely with the standard (JCPDS: 01-1164) [57].

On the other hand, the diffraction pattern of the ZnO NPs samples that prepared via Aloe vera and Hibiscus sabdariffa plants extract fig (Figure 1.b) shows diffraction peaks at $2\theta = 31.96°$, $34.6°$, and $36.52°$, corresponding to Braggs planes of (100), (002), and (101), respectively, while the other peaks at $2\theta = 47.68°$, $56.8°$, $63.16°$, $66.36°$, $68.16°$, and $69.4°$, corresponding to lattice planes of (102), (110), (103), (200), (112), and (201), respectively. It has been that all the major peaks characteristic of hexagonal wurtzite structure of ZnO and determined patterns of XRD matched closely with the standard (JCPDS: 36-1451) [58].
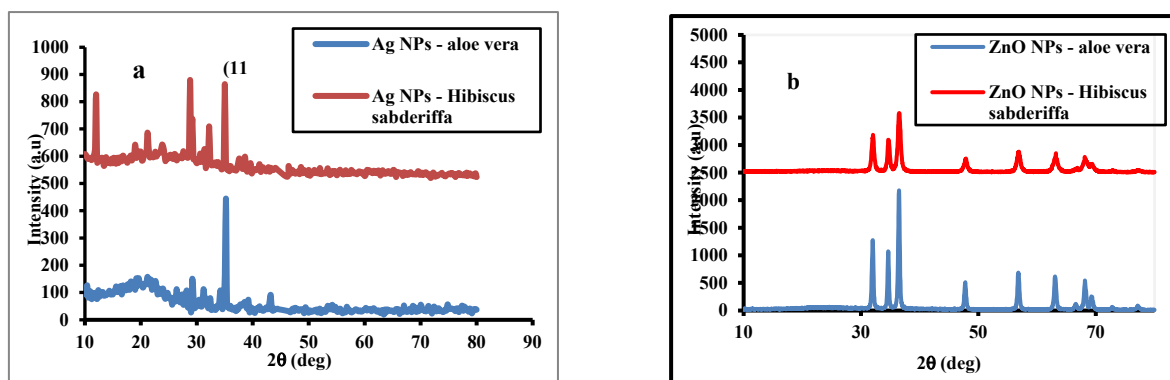
Figure 1. XRD of (a) Ag NPs, (b) of ZnO NPs via Aloe vera and Hibiscus sabdariffa.

3.2 Field emission scanning electron microscopy (FE-SEM)

The FE-SEM images in Figure (2) illustrate the morphology of Ag NPs, ZnO NPs and Ag/ZnO NCPs synthesized via a green method using plant extracts like Aloe vera and Hibiscus sabdariffa respectively.
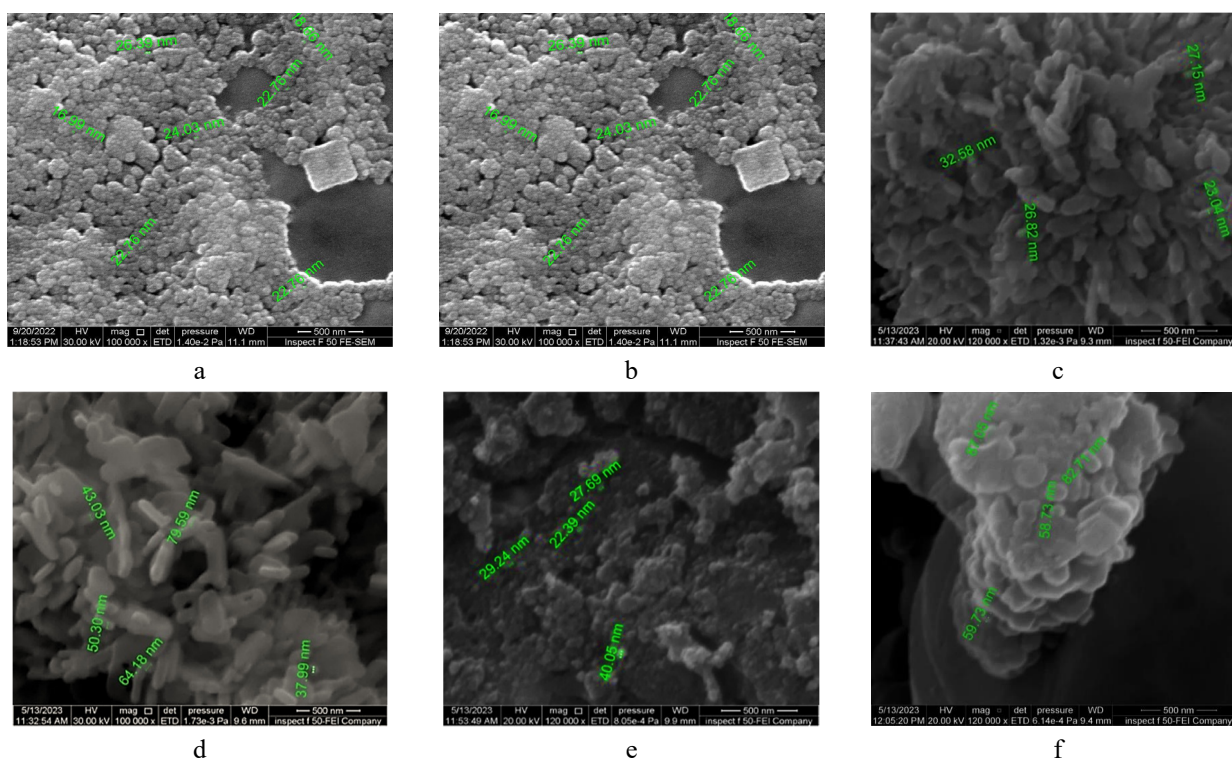
Figure 2. FE- SEM of Ag NPs formed via (a) aloe vera, (b) hibiscus sabdariffa, FE- SEM of ZnO NPs formed via (c) aloe vera, (d) hibiscus sabdariffa, FE- SEM of Ag/ZnO nanocomposite formed via (e) aloe vera, (f) hibiscus sabdariffa.

These images exhibit a spherical shape of Ag NPs, with particle sizes ranging from (16.99 -26.39) nm and (13.11 - 29.50) nm using Aloe vera and Hibiscus sabdariffa respectively as shown in Fig. 2 (a & b), while Fig. 2 (c & d)

demonstrate the formation of agglomerate ZnO NPs with hexagonal nanorod shape, with particle sizes ranging from (23.04 – 32.58) nm and (37.99 - 79.59) nm, the metallic silver nanospheres are evenly dispersed on the surface of ZnO NPs, loose agglomerations of NPs have grown larger and formed clusters, resulting in the formation of nanorod-like Ag/ZnO NCPs with particle sizes ranging from (22.39 - 40.05) nm and (59.73 -87.05) nm as in Fig. 2 (e & f). It is evident that the agglomerations of Ag/ZnO NCPs were significantly larger in size compared to pure Ag NPs and ZnO NPs.

In this process, silver nanoparticles form an outer layer coating on the surface of ZnO particles. In one possible method, that the silver nanoparticles introduced to a solution containing ZnO particles and allowed to bond with the ZnO surface due to attractive electrostatic forces or chemical interactions. The silver nanoparticles can then continue to accumulate on the surface of the ZnO particles, forming a layer. This can be facilitated by agitation or heating of the solution. Our results agree with the results of other work [59-61].

3.3 Dye degradation activity

The photocatalytic effectiveness of Ag nanoparticles, ZnO nanoparticles, and Ag/ZnO nanocomposite powder, the degradation rate of Methylene Blue dye in a solution was measured under UV light. Samples of the degraded dye solutions were collected at different time intervals, and their absorbance was determined using a UV-Visible Spectrophotometer to quantify the dye degradation rate using the equation (1) above. Figure 3 showed UV-visible absorption spectra of the 6 samples, where Fig. 3 (a & b) represent the Ag NPs efficiency from Aloe vera, Hibiscus sabdariffa respectively. Fig. 3 (c & d) represented the ZnO NPs efficiency from Aloe vera, Hibiscus sabdariffa respectively. And Fig. 3 (e & f) represented the Ag/ZnO nanocomposite efficiency from Aloe vera, Hibiscus sabdariffa respectively.
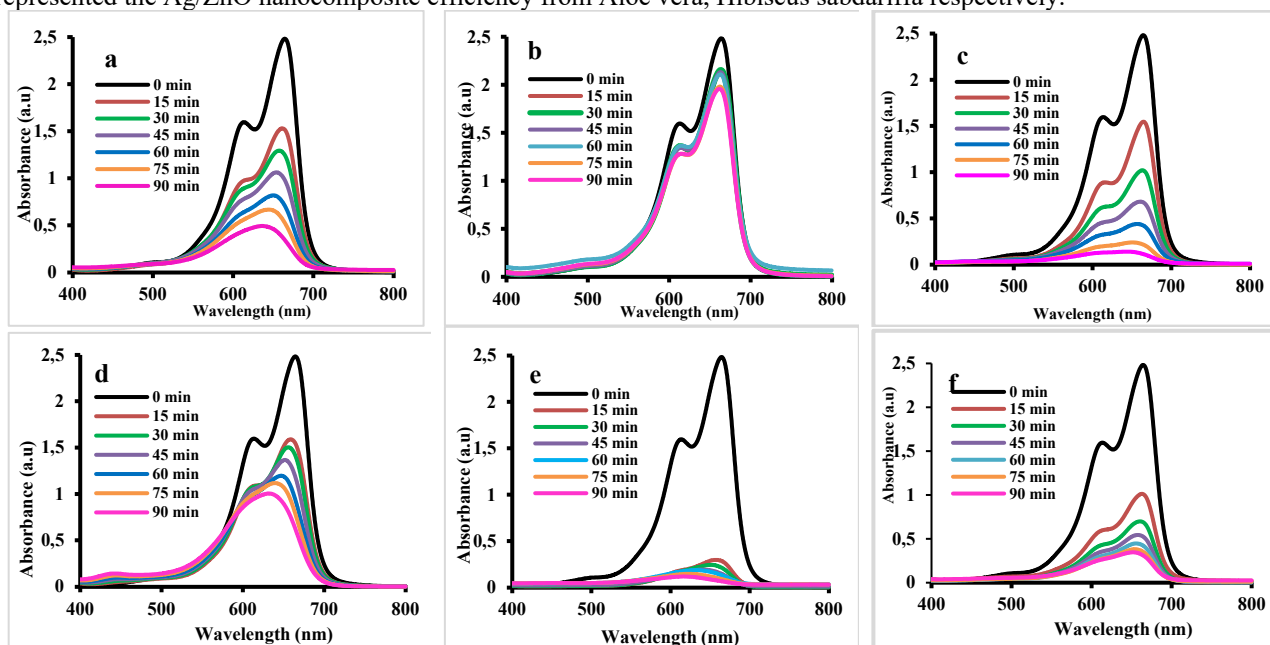
Figure 3. UV-Vis absorption spectra of Ag NPs via (a) aloe vera, (b) hibiscus sabdariffa, UV-Vis absorption spectra of ZnO NPs via (c) aloe vera, (d) hibiscus sabdariffa, UV-Vis absorption spectra of Ag/ZnO NCs via (e) aloe vera, (f) hibiscus sabdariffa of photo degradation samples against MB.

The above results indicate that the Ag/ZnO nano composite had the highest photo degradation activity as shown in Figure 4, with a degradation rate of 97% for Aloe vera and 87% for Hibiscus sabdariffa.
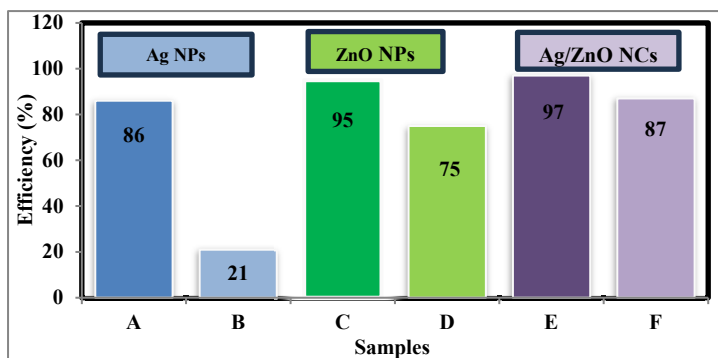
Figure 4. The efficiency of Ag NPs, ZnO NPs and Ag/ZnO NCs against MB dye.

The ZnO NPs also showed a high level of photo degradation activity, with degradation rates of 95% and 75% for Aloe vera and Hibiscus sabdariffa, respectively, while the Ag NPs had lower levels of activity, with degradation rates of

86% and 21% for Aloe vera and Hibiscus sabdariffa, respectively. These results suggest that the Ag/ZnO nano composite could be a promising material for photocatalytic applications.

To determine the rate of photocatalytic reactions, the pseudo-first order rate constant (k min^{-1}) can be calculated by estimating the slope of the lines in Figure (5).

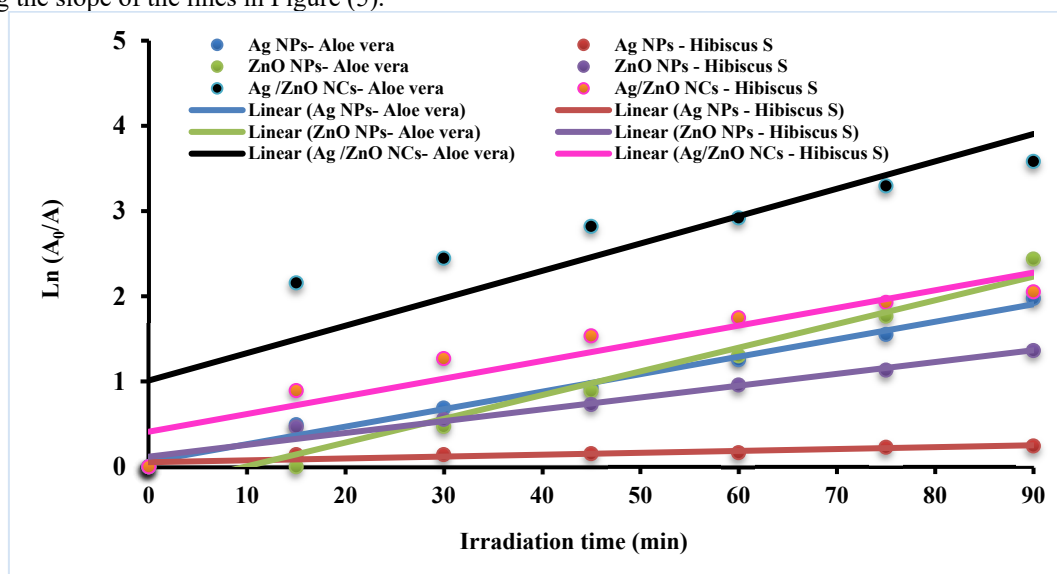**Figure 5.** First-order kinetics of MB dye degradation against Ag NPs, ZnO NPs, Ag/ZnO NCs using different plant extracts with irradiation time.

These lines are plotted between ln (A0/A) and irradiation time, and the results indicate an increase in the value of k for samples prepared from Aloe vera extract. Table (1) presents the efficiency values and k for each sample. Figure (6) demonstrates a possible mechanism of the Ag/ZnO NCs photocatalyst.
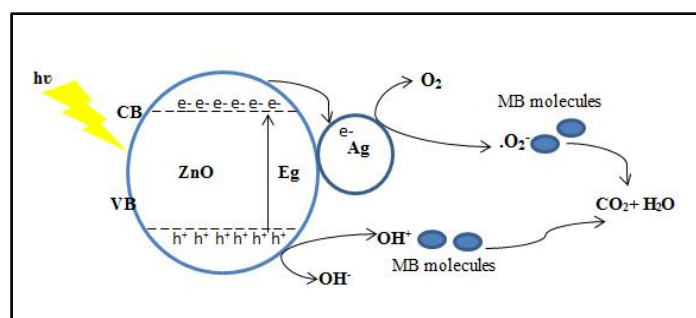
Figure 6. A possible mechanism of Ag/ZnO NCs photocatalyst.

When exposed to UV light, electrons in the Ag/ZnO NCs can absorb photon energy and move to the conduction band (CB), generating an equal number of holes in the valence band (VB). Since the conduction band CB energy level of ZnO is higher than the Fermi level of Ag-ZnO, the electrons can transfer from ZnO to Ag. Consequently, the photogenerated electrons can be trapped by Ag, preventing their recombination with holes. This leads to an accumulation of more electrons and holes at the Ag/ZnO interface, ultimately enhancing the photocatalytic activity of the Ag/ZnO NCs.

The conduction band (CB) electrons may subsequently generate superoxide anion radicals (O2−), while the valence band (VB) holes may react with H2O to create hydroxyl radicals (•OH). These hydroxyl radicals can facilitate the degradation of MB. The reactions can be summarized as follows [62 - 64].

$$Zn0 + Photon\ energy \rightarrow e^-(CB) + h^+(VB) \tag{2}$$

$$Ag^+ + e^-(CB) \rightarrow Ag \tag{3}$$

$$e^-_{(CB)} + O_{2(adsorbed)} \rightarrow O_2^- \tag{4}$$

$$h^+_{(VB)} + H_2O_{(adsorbed)} \rightarrow OH \cdot + H^+ \tag{5}$$

$$h^+_{(VB)} + OH^- \rightarrow OH \tag{6}$$

$$O_2^- + MB\ dye \rightarrow degradation\ products \tag{7}$$

$$OH \cdot + MB\ dye \rightarrow degradation\ products \tag{8}$$
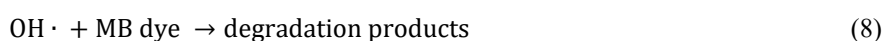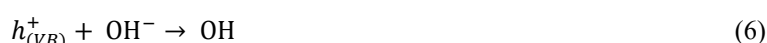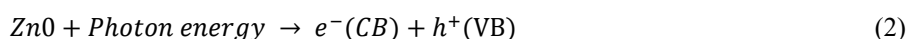
Table 1. The efficiency values and pseudo-first-order rate constant (k) for each sample.

Prepared samples	Degradation efficiency	K (min⁻¹)
Ag NPs via A. vera	86	0.020507143
Ag NPs via H. sabdariffa	21	0.00220619
ZnO NPs via A. vera	95	0.033383333
ZnO NPs via H. sabdariffa	75	0.01387381
Ag/ZnO NCPs via A. vera	97	0.032133333
Ag/ZnO NCPs via H. sabdariffa	87	0.020735714

4. CONCLUSION

In summary, Ag/ZnO NPs, Ag NPs, ZnO NPs were successfully prepared via nontoxic, fast, low cost, eco-friendly and simple green method using two kind of plant extracts that is having comparable functional groups that could potentially aid in the production of NCPs and ultimately be transformed into valuable nanomaterial. XRD and FE-SEM analyses were utilized to check structural properties. Ag/ZnO NCs showed powerful photocatalytic activity compared with Pure Ag NPs and Pure ZnO NPs, against MB which totally decolorized as a wastewater pollutant. The novelty of the investigated results of Ag/ZnO NCs which utilizes leave and fruit extract as a cost effect and eco-friendly additive that have a significant effect in the enhancement of wastewater treatment.

ORCID
Noorullah Mohammed Nemma, https://orcid.org/0000-0002-7697-2143
Zainab Sabeeh Sadeq, https://orcid.org/0000-0003-1450-785X

REFERENCES
[1] C. Forstner, T.G. Orton, P. Wang, M.P. Kopittke, and P.G. Dennis, "Wastewater treatment processing of silver nanoparticles strongly influences their effects on soil microbial diversity", Environmental Science and Technology, **54** (21), 13538-13547 (2020). https://doi.org/10.1021/acs.est.0c01312

[2] R. Dai, J. Chen, J. Lin, S. Xiao, S. Chen, and Y. Deng, "Reduction of nitro phenols using nitroreductase from E. coli in the presence of NADH", J. Hazard. Mater., **170**(1), 141-143 (2009). https://doi.org/10.1016/j.jhazmat.2009.04.122

[3] C.A. Martínez-Huitle, and E. Brillas, "Decontamination of wastewaters containing synthetic organic dyes by electrochemical methods: a general review," Appl. Catal. B: Environ. **87**(3-4), 105-145 (2009). https://doi.org/10.1016/j.apcatb.2008.09.017

[4] W. Sami, and Z.S. Sadeq, "MgFe₂O₄@ZnFe₂O₄ nanocomposite as a magnetic catalyst: Synthesis and oil spill removal from water," Journal of Physics: Conference Series, **2437**, 020054 (2022). https://doi.org/10.1063/5.0094019

[5] C.K. Mbamba, D.J. Batstone, X.F. Alsina, and S.A. Tait, "Generalised chemical precipitation modelling approach in wastewater treatment applied to calcite," Water Res. **68**, 342-353 (2015). https://doi.org/10.1016/j.watres.2014.10.011

[6] M.L. Christensen, K. Keiding, P.H. Nielsen, M.K. Jorgensen, "Dewatering in biological wastewater treatment: a review," Water Res. **82**, 14-24 (2015). https://doi.org/10.1016/j.watres.2015.04.019

[7] K.Y. Kumar, H.B. Muralidhara, Y.A. Nayaka, J. Balasubramanyam. and H. Hanumanthappa, "Low-cost synthesis of metal oxide nanoparticles and their application in adsorption of commercial dye and heavy metal ion in aqueous solution," Powder Tech. **246**, 125-136 (2013). https://doi.org/10.1016/j.powtec.2013.05.017

[8] H. Zangeneh, A.A.L. Zinatizadeh, M. Habibi, M. Akia, and M.H. Isa, "Photocatalytic oxidation of organic dyes and pollutants in wastewater using diferent modifed titanium dioxides: a comparative review," J. Ind. Eng. Chem. **26**, 1-36 (2015). https://doi.org/10.1016/j.jiec.2014.10.043

[9] L. Mingxin, et al. "Photocatalytic performance and mechanism research of Ag/HSTiO₂ on degradation of methyl orange," ACS Omega, **5**, 21451-21457 (2020). https://doi.org/10.1021/acsomega.0c01832

[10] M. Li, R. Guan, J. Li, Z. Zhao, J. Zhang, Y. Qi, H. Zhai, and L. Wang, "Efects of Ag doping content and dispersion on the photocatalytic and antibacterial properties in ZnO nanoparticles," Chem. Res. Chin. Univ. **35**, 271-276 (2019). https://doi.org/10.1021/acsomega.0c01832

[11] L. Jiaxi, G. Renquan, Z. Junkai, Z. Zhao, Z. Hongju, S. Dewu, and Q. Yunfeng, "Preparation and photocatalytic performance of dumbbell Ag₂CO₃–ZnO heterojunctions", ACS Omega, **5**, 570–577, 2020.

[12] J. Liu, Y. Yue, L. Ge, P. Chen, F. Tan, W. Wang, X. Wang, "Facile fabrication of magnesium peroxide with diferent morphologies via the isomorphic transformation of magnesium oxide for Fenton-like degradation of methylene blue," Colloids Surf. A Physicochem. Eng. Aspects, **607**, 125499 (2020). https://doi.org/10.1016/j.colsurfa.2020.125499

[13] J. Liu, Y. Yue, W. Wang, F. Tan, H. Xia, X. Wang, X. Qiao, "Facile one-step synthesis of 3D hierarchical fower-like magnesium peroxide for efficient and fast removal of tetracycline from aqueous solution", J. Hazard. Mater. **397**, 122877 (2020). https://doi.org/10.1016/j.jhazmat.2020.122877

[14] P. Chen, F. Sun, W. Wang, F. Tan, X. Wang, and X. Qiao, "Facile one-pot fabrication of ZnO particles for the efcient Fenton-like degradation of tetracycline," J. Alloys Compd. **834**, 155220 (2020). https://doi.org/10.1016/j.jallcom.2020.155220

[15] Y. Yue, P. Zhang, W. Wang, Y. Cai, F. Tan, X. Wang, and X. Qiao, *et al*., "Enhanced dark adsorption and visible-light-driven photocatalytic properties of narrower-band-gap Cu2S decorated Cu2O nanocomposites for efcient removal of organic pollutants," J. Hazard. Mater. **384**, 121302 (2020). https://doi.org/10.1016/j.jhazmat.2019.121302

[16] D. Wu, Y. Bai, W. Wang, H. Xia, F. Tan, S. Zhang, B. Su, et al., "Highly pure MgO₂ nanoparticles as robust solid oxidant for enhanced Fenton-like degradation of organic contaminants," J. Hazard. Mater. **374**, 319-328 (2019). https://doi.org/10.1016/j.jhazmat.2019.04.058

[17] H.A. Alrubaie, and B.M. Alshabander, "The effect of ZnO nanoparticles on the self-cleaning of ZnO/epoxy composites", AIP Conference Proceedings, **2437**, 020184 (2022). https://doi.org/10.1063/5.0094219

[18] X. Zhang, A. Fujishima, M. Jin, A.V. Emeline, and T. Murakami, "Double-layered TiO2− SiO2 nanostructured flms with self-cleaning and antirefective properties", J. Phys. Chem. B. **110**(50), 25142-25148 (2006). https://doi.org/10.1021/jp064442u

[19] S. Tek, D. Yucel, and G. Celiker, "High Optical Efciency of ZnO Nanoparticles", in: *Conference on Lasers and Electro-Optics/Pacific Rim 2007*, (Optica Publishing Group, 2007), paper WF3_7. https://opg.optica.org/abstract.cfm?URI=CLEOPR-2007-WF3_7

[20] S.N. Zailan, A. Bouaissi, N. Mahmed, M. Mustafa, A. AlBakri, "Influence of ZnO nanoparticles on mechanical properties and photocatalytic activity of self-cleaning ZnO-based geopolymer Paste", J. Inorg. Organomet. Polym. Mater. **30**, 2007-2016 (2020). https://doi.org/10.1007/s10904-019-01399-3

[21] Y. Li, C. Gao, R. Long, and Y. Xiong, "Photocatalyst design based on two-dimensional materials," Mater. Today Chem. **11**, 197 (2019). https://doi.org/10.1016/j.mtchem.2018.11.002

[22] V.K. Gupta, R. Kumar, A. Nayak, T.A. Saleh, and M.A. Barakat, "Adsorptive removal of dyes from aqueous solution onto carbon nanotubes: a review," Adv. Colloid Interface Sci. **193**, 24-34 (2013). https://doi.org/10.1016/j.cis.2013.03.003

[23] W. Konicki, M. Aleksandrzak, D. Moszynski, and E. Mijowska, "Adsorption of anionic azo dyes from aqueous solutions onto graphene oxide: equilibrium, kinetic and thermodynamic studies", J. Colloid Interface Sci. **496**, 188-200 (2017). https://doi.org/10.1016/j.jcis.2017.02.031

[24] W. Sami, and Z.S. Sadeq, "Role of Glycine-to-Nitrate Ratio in Physical and Magnetic Properties of Zn- Ferrite Powder," Iraqi Journal of Science, **63**, 170-181 (2022). https://doi.org/10.24996/ijs.2022.63.1.18

[25] X. Lu, X. Bian, G. Nie, C. Zhang, C. Wang, and Y, Wei, "Encapsulating conducting polypyrrole into electrospun TiO2 nanofibers: a new kind of nanoreactor for in situ loading Pd nanocatalysts towards p-nitrophenol hydrogenation,", J. Mater. Chem, **22**, 12723-12730 (2012). https://doi.org/10.1039/C2JM16559G

[26] M. Nasrollahzadeh, M. Atarod, and S.M. Sajadi, "Green synthesis of the Cu/Fe3O4 nanoparticles using Morinda morindoides leaf aqueous extract: a highly efficient magnetically separable catalyst for the reduction of organic dyes in aqueous medium at room temperature," Appl. Surf. Sci. **364**, 636-644 (2016). https://doi.org/10.1016/J.APSUSC.2015.12.209

[27] S. Wei, Z. Dong, Z. Ma, J. Sun, and J. Ma, "Palladium supported on magnetic nanoparticles as recoverable catalyst for one-pot reductive amination of aldehydes with nitroarenes under ambient conditions," Catal. Commun. **30**, 40-44 (2013). https://doi.org/10.1016/j.catcom.2012.10.024

[28] P. Dauthal, and M. Mukhopadhyay, "Noble metal nanoparticles: plant-mediated synthesis, mechanistic aspects of synthesis, and applications," Ind. Eng. Chem. Res. **55**(36), 9557-9577 (2016). https://doi.org/10.1021/acs.iecr.6b00861

[29] M. Bordbar, and N. Mortazavimanesh, "Green synthesis of Pd/walnut shell nanocomposite using Equisetum arvense L. leaf extract and its application for the reduction of 4-nitrophenol and organic dyes in a very short time," Environ. Sci. Pollut. Res. **24**, 4093-4104 (2017). https://doi.org/10.1007/s11356-016-8183-y

[30] J. Lee, J. Chung, S.M. Byun, B.M. Kim, and C. Lee, "Direct catalytic C-H arylation of imidazo[1,2-a] pyridine with aryl bromides using magnetically recyclable PdFe3O4 nanoparticles," Tetrahedron. **69**, 5660-5664 (2013). https://doi.org/10.1016/j.tet.2013.04.031

[31] G.K. Naik, P.M. Mishra, and K. Parida, "Green synthesis of Au/TiO2 for effective dye degradation in aqueoussystem," Chem. Eng. J. **229**, 492-497 (2013). https://doi.org/10.1016/j.cej.2013.06.053

[32] A. Hatamifard, M. Nasrollahzadeh, and S.M. Sajadi, "Biosynthesis, characterization and catalytic activity of an Ag/zeolite nanocomposite for base- and ligand-free oxidative hydroxylation of phenylboronic acid and reduction of a variety of dyes at room temperature," New J. Chem. **40**, 2501-2513 (2016). https://doi.org/10.1039/C5NJ02909K

[33] M. Bordbar, Z. Sharifi-Zarchi, and B. Khodadadi, "Green synthesis of copper oxide nanoparticles/clinoptilolite using Rheum palmatum L. root extract: high catalytic activity for reduction of 4-nitro phenol, rhodamine B, and methylene blue," J. Sol-Gel Sci. Technol. **81**, 724-733 (2017). https://doi.org/10.1007/s10971-016-4239-1

[34] M.S.S. Danish, L.L. Estrella, I.M.A. Alemaida, A. Lisin, N. Moiseev, M. Ahmadi, M. Nazari, *et al*., Metals, "Photocatalytic applications of metal oxides for sustainable environmental remediation", J. Metals, **11**, 80 (2021). https://doi.org/10.3390/met11010080

[35] V. Prasad, S.G. Gnanamani, E.M. Ansha, N. Jayaprakash, "Microwave Assisted Synthesis, Characterization and Photo-catalytic Study of Cu/ZnO Nanocomposite," Rasayan J. Chem, **12**, 860 (2019). http://dx.doi.org/10.31788/RJC.2019.1225226

[36] K.M. Lee, C.W. Lai, K.S. Ngai, and J.C. Juan, "Recent Developments of Zinc Oxide Based Photocatalyst in Water Treatment Technology", Water Res. **88**, 428 (2016). https://doi.org/10.1016/j.watres.2015.09.045

[37] E. Murugan, and P. Shanmugam, "Surface Grafted Hyper-Branched Polyglycerol Stabilized Ag and AuNPs Heterogeneous Catalysts for Efficient Reduction of Congo Red," J. Nanosci. Nanotechnol. **16**, 426 (2016). https://doi.org/10.1166/jnn.2016.10655

[38] E. Murugan, and J.N. Jebaranjitham, "Environmentally benign heterogeneous nano-particle catalysts: synthesis, characterization and catalytic activity of 4-nitrophenol," J. Biomed. Nanotechnol. **7**, 158 (2011). https://doi.org/10.1166/jbn.2011.1248

[39] F.H. Dowlatababdi, G. Amiri, and S.M. Mohammadi, "Investigation of the antimicrobial effect of silver doped Zinc Oxide nanoparticles," Nanomedicine Journal, **4**, 50-54 (2017). https://doi.org/10.22038/nmj.2017.8053

[40] B. Baruwati, and R.S. Varma, "High Value Products from Waste: Grape Pomace Extract - A Three -in -One Package for the Synthesis of Meta Nanoparticles", Chem. Sus. Chem. **2**, 1041-1044 (2009). https://doi.org/10.1002/cssc.200900220

[41] R. Sahay, V.J. Reddy, and S. Ramakrishna, "Synthesis and applications of multifunctional composite nanomaterials," **9**, 25 (2014). https://doi.org/10.1186/s40712-014-0025-4

[42] Z.S. Sadeq, Z.F. Mahdi, and A.M. Hamza, "Low cost, Fast and Powerful Performance Interfacial Charge Transfer Nanostructured Al2O3 Capturing of Light Photocatalyst Eco-Friendly System using Hydrothermal Method," Materials Letters, 120-124 (2019). https://doi.org/10.1016/j.matlet.2019.07.050

[43] E.C.H. Sykes, F.J. Williams, and M.S. Tikhov, "Nucleation, growth, sintering, mobility, and adsorption properties of small gold particles on polycrystalline titania," J. Phys. Chem. B, **106**(21), 5390-5394 (2002). https://doi.org/10.1021/jp014562w

[44] X.Z. Li, and F.B. Li, "Study of Au/Au3+-TiO2 photocatalysts towards visible photooxidation for water and wastewater treatment," Environ. Sci. Technol. **35**(11), 2381-2387 (2001). https://doi.org/10.1021/es001752w

[45] X. Wang, D.R.G. Mitchell, and K. Prince, "Gold nanoparticle incorporation into porous titania networks using an agarose gel templating technique for photocatalytic applications,", Chem. Mater. **20**(12), 3917-3926 (2008). https://doi.org/10.1021/cm703509f

[46] M. Bordbar, T. Alimohammadi, and B. Khoshnevisan, "Preparation of MWCNT/TiO$_2$–Co nanocomposite electrode by electrophoretic deposition and electrochemical study of hydrogen storage," Int. J. Hydrog. Energy, **40**, (31), 9613-9620 (2015). https://doi.org/10.1016/j.ijhydene.2015.05.138

[47] B. Khodadadi, M. Bordbar, and A. Yeganeh-Faal, "Optical, structural, and photocatalytic properties of Cd-doped ZnO powders prepared via sol–gel method," J. Sol-Gel Sci. Technol. **77**(3), 521-527 (2016). https://doi.org/10.1007/s10971-015-3877-z

[48] E.S. Abdel-Halim, M.H. El-Rafie, and S.S. Al-Deyab, "Polyacrylamide/guar gum graft copolymer for preparation of silver nanoparticles," Carbohydr. Polym. **85**(3), 692-697 (2011). https://doi.org/10.1016/j.carbpol.2011.03.039

[49] S.P. Dubey, M. Lahtinen, and M. Sillanpää, "Tansy fruit mediated greener synthesis of silver and gold nanoparticle," Process Biochem. **45**(7), 1065-1071 (2010). https://doi.org/10.1016/j.procbio.2010.03.024

[50] G. Zhan, J. Huang, and M. Du, "Green synthesis of Au–Pd bimetallic nanoparticles: single-step bioreduction method with plant extract," Mater. Lett. **65**(19-20), 2989-2991 (2011). https://doi.org/10.1016/j.matlet.2011.06.079

[51] X. Huang, H. Wu, and S. Pu, "One-step room-temperature synthesis of Au@Pd core–shell nanoparticles with tunable structure using plant tannin as reductant and stabilizer," Green Chem. **13**, 950-957 (2011). https://doi.org/10.1039/C0GC00724B

[52] S. Jain, and M.S. Mehata, "Medicinal plant leaf extract and pure flavonoid mediated green synthesis of silver nanoparticles and their enhanced antibacterial property", Scientific Reports, 7(1), 15867 (2017). https://doi.org/10.1038/s41598-017-15724-8

[53] S. Matussin, M.H. Harunsani, A. Tan, and L.M. Khan, "Plant-extract-mediated SnO$_2$ nanoparticles: synthesis and applications," ACS Sustainable Chemistry and Engineering, **8**(8), 3040-3054 (2020). https://doi.org/10.1021/acssuschemeng.9b06398

[54] R.S. Sabry, W.J. Aziz, and M.I. Rahmah, "Enhanced photocatalytic activity of Ag and Fe$_2$O$_3$ co-doped ZnO nanostructure under visible light irradiation," Materials Technology, **35**(6), 326-334 (2020). https://doi.org/10.1080/10667857.2019.1681717

[55] M.I. Rahmah, H.S. Majdi, W.K. Al-Azzawi, M.J. Rasn, H.H. Jasim, M.S. Jabir, R.A.S.A. Al Kareem, and T.M. Rashid, "Synthesis of ZnO/Ag-doped C/N heterostructure for photocatalytic application", International Journal of Modern Physics B, 235-239 (2023). https://doi.org/10.1142/S0217979223502399

[56] N.C. Joshi, A. Gaur, and A. Singh, "Synthesis, Characterisations, Adsorptive Performances and Photo-catalytic Activity of Fe$_3$O$_4$-SiO$_2$ Based Nanosorbent (Fe3O4-SiO2 BN)," Journal of Inorganic and Organometallic Polymers and Materials, **30**, 4416-4425 (2020). https://doi.org/10.1007/s10904-020-01622-6

[57] Y. Jhuang, and W. Cheng, "Fabrication and characterization of silver/titanium dioxide composite nanoparticles in ethylene glycol with alkaline solutio n through sonochemical process,"Ultrasonics Sonochemistry, **28**, 327-333 (2016). https://doi.org/10.1016/j.ultsonch.2015.08.011

[58] G. Madhumitha, J. Fowsiya, N. Gupta, A. Kumar, and M. Singh, "Graphical abstract SC," J. Phys. Chem. Solids, **127**, 43-51 (2019). https://doi.org/10.1016/j.jpcs.2018.12.005

[59] N.M. Nemma, and Z.S. Sadeq, "Green Route of Synthesis Ag NPs Using Reductant and Stabilizer Agent from Plants Extract as an Efficient Antibacterial and Antifungal Activity," Chemical methodologies, **7**(4), 325-334 (2023). https://doi.org/10.22034/chemm.2023.381408.1646

[60] R. Viswanatha, Y.A. Nayaka, C.C. Vidyasagar, and T.G. Venkatesh, "Structural and optical properties of Mg doped ZnO nanoparticles," J. Chem. Pharm. Res. **4**, 1983-1989 (2012).

[61] J. Iqbal, N. Safdar, T. Jan, M. Ismail, S.S. Hussain, A. Mahmood, S. Shahzad, and Q. Mansoor, "Facile Synthesis as well as Structural, Raman, Dielectric and Antibacterial Characteristics of Cu Doped ZnO Nanoparticles," J. Mater. Sci. Technol. **31**, 300-304 (2015). https://doi.org/10.1016/j.jmst.2014.06.013

[62] M. Samadi, M. Zirak, A. Naseri, E. Khorashadizade, and A.Z. Moshfegh, "Recent progress on doped ZnO nanostructures for visible-light photocatalysis," Thin Solid Films, **605**, 2-19 (2016). http://dx.doi.org/10.1016%2Fj.tsf.2015.12.064

[63] C.B. Ong, L.Y. Ng, and A.W. Mohammad, "A review of ZnO nanoparticles as solar photocatalysts: synthesis, mechanisms and applications," Renew. Sustain. Energy Rev. **81**, 536-551 (2018). https://doi.org/10.1016/j.rser.2017.08.020

[64] F. Kayaci, S. Vempati, I. Donmez, N. Biyikliab, and T, Uyar, "Role of zinc interstitials and oxygen vacancies of ZnO in photocatalysis: a bottom-up approach to control defect density," Nanoscale, **6**(17), 10224-10234 (2014). https://doi.org/10.1039/C4NR01887G

ЕКОЛОГІЧНО ЧИСТИЙ ЗЕЛЕНИЙ СИНТЕЗ, ТА ФОТОКАТАЛІЗАТОРНА АКТИВНІСТЬ НАНОКОМПОЗИТУ Ag-ZnO

Нуруллах Мохаммед Немма, Зейнаб Сабіх Садек
Факультет фізики, Науковий коледж, Багдадський університет, Багдад, Ірак

Дослідження успішно синтезувало наночастинки Ag, наночастинки ZnO та нанокомпозити Ag/ZnO, використовуючи простий, економічний та стійкий екологічний синтетичний підхід. Мета синтезу нанокомпозитів Ag/ZnO з використанням двох різних рослинних екстрактів полягала у дослідженні їх фотодеградаційної активності на барвнику метиленового синього (MB). (XRD) дифракційний аналіз підтвердив наявність розміру кристалів Ag і гексагональної структури вюрциту ZnO. Результати (FE-SEM) показали сферичність, наностржні та наявність кластеризації НЧ неправильної форми. Отримані нанокомпозити метал/напівпровідник оксид володіли унікальними характеристиками фотодеградації, які були відсутні в окремих наночастинках Ag і наночастинках ZnO.

Ключові слова: *наночастинки; нанокомпозит; очищення стічних вод; каталізатор*

A COMPARATIVE STUDY OF MICROSTRUCTURE AND PROPERTIES OF MULTICOMPONENT COATINGS BASED ON (TIZRSIY)N SYSTEM PREPARED BY THE VACUUM ARC DEPOSITION[†]

Vyacheslav M. Beresnev[a], Serhii V. Lytovchenko[a*], Mykola O. Azarenkov[a,b],

Olga V. Maksakova[a], Denis V. Horokh[a], Bohdan O. Mazilin[a]

[a] V.N. Karazin Kharkiv National University
4, Svoboby Sq., 61022 Kharkiv, Ukraine
[b] National Science Center "Kharkov Institute of Physics and Technology"
1, Akademicheskaya St., 61108 Kharkiv, Ukraine
*Corresponding Author e-mail: s.lytovchenko@karazin.ua
Received July 10, 2023; revised August 7, 2023; accepted August 10, 2023

The effect of reaction gas (nitrogen) pressure on the structural-phase state and properties of vacuum-arc nitride coatings of (TiZrSiY)N system has been studied. On the surface of the coatings, a significant amount of the droplet fraction and solidified macroparticles of the sputtered cathode is observed, which is typical for vacuum-arc condensates obtained from unseparated plasma flows. In all samples, titanium nitride with a cubic fcc lattice is identified. In the coating obtained at nitrogen pressures 0.08 Pa and 0.2 Pa, the α-Ti phase was determined, and the measured lattice parameter of this phase suggests that it is a solid solution of nitrogen in titanium. The texture coefficient of the multicomponent coating obtained at the highest nitrogen pressure of 0.55 Pa has the highest value of 5.95 compared to others. The Vickers hardness of multicomponent coatings increases depending on the partial pressure of nitrogen from 25.0 GPa to 36.0 GPa. According to the complex of tribo-mechanical parameters (hardness, elastic modulus, elastic strain to failure, friction coefficient etc.), suggested multicomponent (TiZrSiY)N coatings can be very attractive for tribological applications.

Keywords: *Vacuum-arc coatings; Multicomponent nitride coatings; Nitrogen partial pressure; Texture; Vickers hardness; Adhesive strength*
PACS: 61.46.-w; 62.20.Qp; 62-25.-g; 81.15.Cd

INTRODUCTION

The formation of functional coatings on the surface of various materials is an effective method for improving their performance under various thermobaric impacts. The high mechanical properties of the coating, combined with the thermal stability of the protective layer, can provide the necessary long-term performance of various machine parts, cutting tools, friction pairs, and other elements of different devices. However, practical experiments have shown that with an increase in specific loads, worsening in some cases of lubrication conditions for parts, tightening of requirements for the reliability and durability of various parts and products, coatings based on simple refractory compounds cease to meet the put forward requirements.

An effective approach that allows, on the one hand, to significantly change the physical and mechanical properties of the coatings, and, on the other hand, to improve the performance characteristics of structural materials on which such coatings are deposited, is the use of coatings based on multicomponent systems. Such coatings can be obtained by alloying well-known coatings based on nitrides and carbides of the refractory metals with the specific elements that provide increased surface hardness, low coefficient of friction, good adhesion to the substrate, oxidation resistance, and wear resistance [1–5]. The deposition method of such systems is based on the fact that a multicomponent system can be obtained in the state of a solid single-phase substitution solution, which by its nature is both stronger and more thermodynamically stable compared to a multi-phase solution.

The physical and mechanical characteristics of nitride coatings based on multicomponent systems mainly depend on the amount of nitride-forming elements in the system, as well as on the method and technological parameters of deposition.

A positive increase in properties can be achieved by selecting such a number of components and such a ratio of their concentrations in the material, at which an increased value of the mixing entropy is realized in the calculated composition (therefore, according to the Gibbs equation, a reduced free energy of the system). At the same time, such a value of entropy exists not only in the molten state, but also after solidification. The decrease in free energy causes an increased resistance of the solid solution during subsequent heat treatment [6]. The improved mechanical characteristics at high temperatures are realized due to a strong distortion of the crystal lattice (usually bcc) due to differences in the values of the atomic radii of the substitution elements. In this case, the higher the mixing entropy, the more pronounced the indicated characteristics of the multicomponent material. The use of multicomponent materials as evaporated systems for coating deposition slows down diffusion processes, decomposes the solid solution with the formation of chemical compounds, and, consequently, reduces the entropy of mixing.

Among the proven physical technologies for obtaining such coatings, the ion-plasma technologies (magnetron sputtering as well as vacuum-arc deposition) are the most widely used. The specific characteristics of these technologies significantly affect the structural-phase state of the formed coatings, which, in turn, determines the achieved physical and mechanical characteristics [7–11].

The crucial physical and technological parameters of deposition that affect the microstructure and physical and mechanical properties of coatings are the magnitude of the negative bias potential applied to the substrate, the partial pressure of the reaction gas in the chamber, as well as the amount, concentration, and type of alloying elements. It is known that the addition of silicon to two- or three-element coatings based on titanium nitride, aluminum nitride, and zirconium nitride increases the thermal stability of the nanostructural state by thermodynamically controlled segregation of secondary phases that are insoluble in the volume of crystalline grains [12]. The high hardness of such coatings is due to the fact that at grain sizes between 5 to 8 μm, the generation and propagation of dislocations are not possible, the crack propagation and grain boundary sliding are suppressed, and the yield stress has a value close to the theoretical shear resistance.

It is known, the addition of yttrium to the coating promotes an increase in the resistance to oxidation due to the formation of the YO_x phase at the grain boundaries [13, 14]. In addition, this element leads to grain crushing and destruction of the columnar microstructure of condensates, which is important for improving friction wear resistance when operating in an oxidizing environment. In this regard, the use of yttrium as an alloying element to improve the thermal and mechanical properties of nitride multicomponent systems is of scientific and practical interest.

In order to develop modern ideas about the physical processes of the formation of multicomponent nitride coatings of (TiZrSiY)N-type under highly nonequilibrium conditions of the vacuum-arc deposition, in this paper, we consider the effect of the nitrogen partial pressure on the structural-phase state (surface morphology, elemental and phase composition), as well as the tribo-mechanical characteristics of the formed coatings.

EXPERIMENT DESCRIPTION

The all-metal target material was obtained by vacuum-arc melting in a cooled copper mold. The ingot was produced by pre-mixing the required amount of alloy components, followed by fusion in a high-purity inert gas atmosphere. To achieve the most uniform distribution of the metal components, the vacuum-arc melting of the target material was carried out five times, and after each melting, the ingot was turned over in the mold. Then, the target cathode was made from the obtained ingot. Before coatings deposition for several minutes in an argon atmosphere, a surface layer was preliminarily sputtered from the cathode to remove oxide films formed during the manufacture of the cathode.

Experimental coatings were formed by vacuum arc deposition [15] by evaporation the all-metal target with the following composition of elements (in at %): 72.5 Ti + 20.0 Zr + 5.0 Si + 2.5 Y. The substrates of 18 mm in width, 18 mm in length, and 2.5 mm in thickness were made of steel 12X18H9T (world analogues: USA 321, Japan SUS321, SUS321TK, United Kingdom 321S51).   Technological parameters of coating deposition are submitted in Table 1.

Table 1. Physical and technological parameters adjusted during deposition of multicomponent (TiZrSiY)N coatings

Series No	I_d, A	I_f, A	U_b, V	P_N, Pa	h
1				0.08	
2	100	0.5	-200	0.2	1
3				0.55	

Note: I_d – arc current, I_f – focus coil current, U_b – negative bias potential, P_N – nitrogen pressure, h – deposition time.

Microscopic examination of the surface and cross-section of the coatings was carried out using a scanning electron microscope Nova NanoSEM 450. The thickness of the coatings was measured based on the cross-section images.

The elemental composition of the coatings was determined from the spectra of characteristic X-ray radiation generated by an electron beam in a scanning microscope. The spectra were obtained using an EDAX PEGASUS energy-dispersive X-ray spectrometer installed in a Nova NanoSEM 450 microscope.

The surface topography of the coatings was analyzed using an atomic force microscope produced by NT-MDT company.

The phase composition and sub-structural studies were carried out on an X-ray diffractometer DRON-3M in filtered Cu-Kα radiation (λ = 1.54060 A˚, 45 kV and 40 mA) using a graphite monochromator in the secondary beam. Diffraction spectra were taken in the scheme of θ-2θ scanning with Bregg-Brentano focusing.

The Vickers hardness and the elastic modulus of the coatings were measured on a Shimadzu HMV-G21S instrument. The load was 245.2 mN, the holding time was 10 seconds, the distance between the measurement points was 40 microns. The number of measurements was 10 for each sample, and the average values were calculated in the final.

The adhesive/cohesive strength of the coatings was determined by nanoscale scratching using a Revetest scratch tester (CSM Instruments) in progressive load testing mode. During the tests, changes in the friction coefficient and acoustic emission were recorded, as well as the main critical loads were identified. The following classification of the critical load was chosen: Lc1 is the formation of the first chevron crack at the bottom and diagonal cracks at the edges

of the scratch; Lc2 is the formation of a group of chevron cracks at the bottom of the scratch; Lc3 is the local failure of the coating after the formation of a group of chevron cracks at the bottom of the scratch; Lc4 is the cohesive-adhesive destruction of the coating; Lc5 is the plastic wear of the coating to the base [16]. The critical load Lc5 corresponding to the load when the destruction of the coating occurred, was taken as the criterion for the adhesive strength index.

RESULTS AND DISCUSSIONS

The surface morphology and cross-section of one of the experimental coatings are shown in Figures 1a and 1b. A significant amount of the craters, droplet fraction and solidified macroparticles of the sputtered cathode was fixed on the surface, which is typical for the vacuum-arc deposited materials obtained from unseparated plasma flows [15]. The increase in the size of particles of the droplet fraction, as well as their tendency to agglomerate, is apparently associated with the erosion of zirconium. The data of different authors on the erosion coefficient of Zr are somewhat different while indicating that the erosion index for Zr is significantly exceed the erosion coefficients of Ti, Mo, and W [17]. The droplets exist in two main forms: a flat shape when their surface is parallel to the coating and a spherical shape, which is bulging with respect to the coating. The different shapes of droplets are probably formed from materials of different phases. Spherical droplets show the correct geometric shape. Around them, there are regular circles on the surface of the coating. The flat shape droplets have a microstructure of the surface, similar to the microstructure of the coating. According to the visual analysis of the boundary between the flat droplet and the coating, it seems that there is a strong mechanical connection between them. Similar shapes of the droplets on Zr-Si-N coatings deposited by the arc evaporation at different substrate bias voltages were observed in [18]. During tribological investigations using microtribometers, these droplets directly influence the results as they are deformed, pulled out from the coating surface, and participate in the friction process as so-called a third body.

The cross-sectional image shown in Figure 1b was used to measure the coating thickness. The thickness was found to be 7.37 microns. It is also obvious, that the interface between the steel substrate and the coatings is rather clear, the coating repeats the shape of the substrate very fine. There are no voids or cracks, thus, the adhesion of the coating to the based material (substrate) is supposed to be high. The small inclusions of metal drops are visible within the cross-section image, but they did not cause any structural destruction. In this case, we can summaries that the deposition of the experimental coatings went well and the structural integrity is verified.
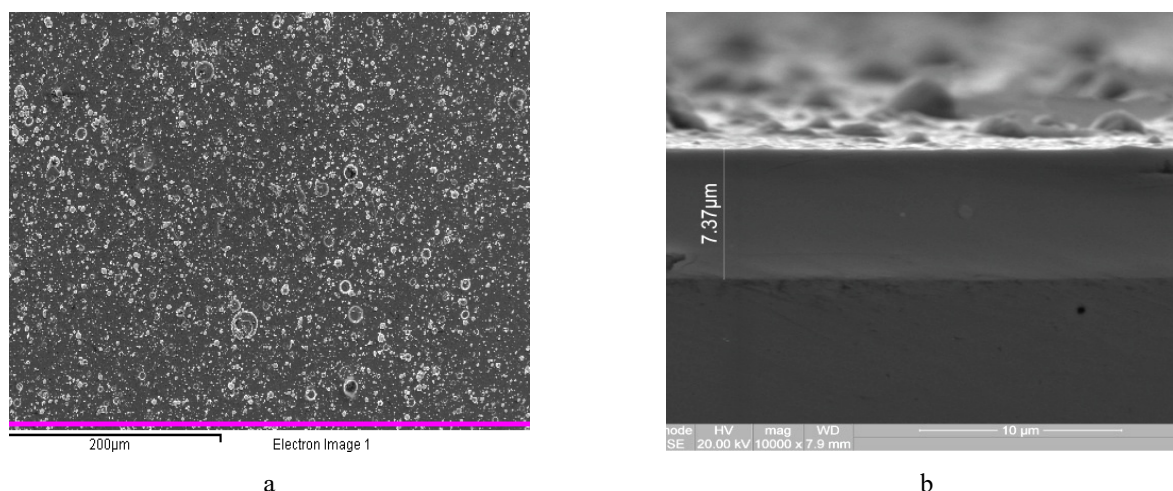

a   b

Figure 1. SEM images of the multicomponent (TiZrSiY)N coating obtained at nitrogen pressure 0.55 Pa (series no. 3):
surface (a) and cross-section (b)

The chemical composition of the experimental coatings obtained via EDX is summarized in Table 2. From the obtained results, one can see the tendency in the concentration change of the structural elements: Zr, Si, and Y concentrations are lowering with the N pressure increasing. This goes due to the re-sputtering during the deposition process.

Figure 2 shows AFM surface images of the multicomponent (TiZrSiY)N coatings obtained at different nitrogen pressures. These figures confirm the rather complex surface topography of both experimental coatings. A comparison of the surface topography shows that the coating obtained at a lower nitrogen pressure, 0.08 Pa, is characterized by a large amount of a droplet component with a higher peak height and a large height spread.

Table 2. Elemental composition of the multicomponent (TiZrSiY)N coatings by EDX

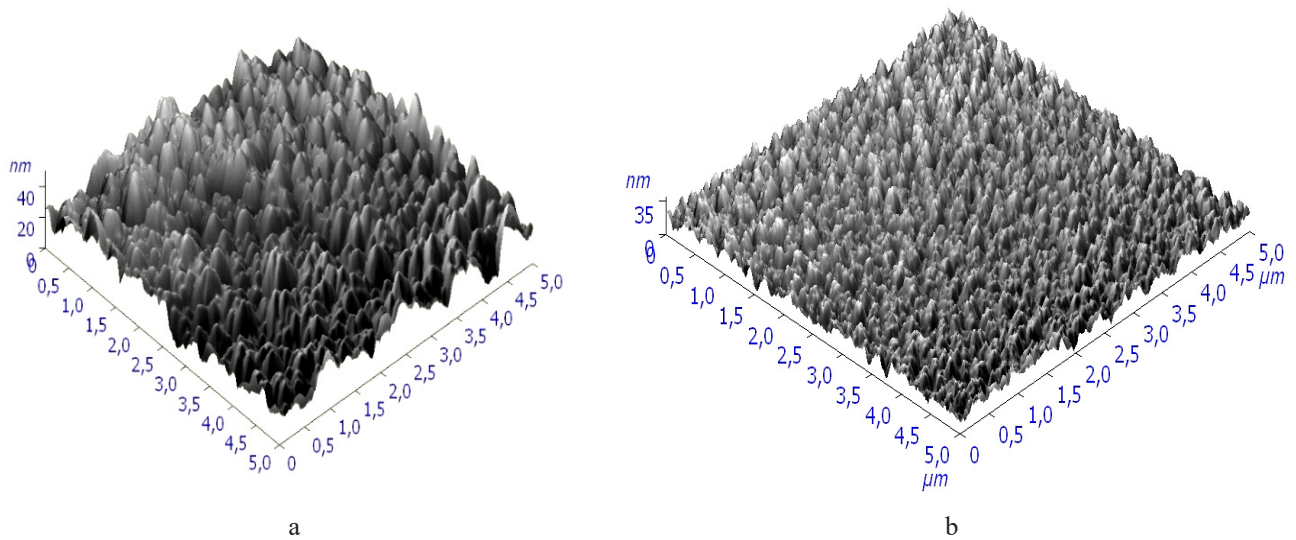| Series No	Element				
	N	Ti	Zr	Si	Y
	Composition, at. %				
1	37.2	46.3	13.4	2.2	0.9
2	43.2	41.9	12.5	1.7	0.7
3	44.2	44.8	9.5	0.9	0.6

Figure 2. 3D AFM surface images of multicomponent (TiZrSiY)N coatings obtained at nitrogen pressure:
0.08 Pa (series no. 1) (a) and 0,55 Pa (series no. 3) (b)

In the coating obtained at the higher nitrogen pressure of 0.55 Pa, better topography uniformity is observed; the height of the peaks is smaller and the scatter of their heights is also smaller. The change in the surface topography is associated with the processes of the energy impact of particles on the surface. The sufficiently high energy of particles incident on the surface, due to a significant bias potential (-200 V), increases the temperature of the substrate. Due to such heating, diffusion, and recrystallization processes are intensified, which, in turn, leads to the evolution of the phase composition of the near-to-surface layers of the coating and the formation of areas with a reduced stress level [19]. The alternation of dark and light protrusions, cones, and pores of nanosized regions is clearly visible, which indicates a change in the height of individual sections of the surface relief.

At the same time, the high energy of metal particles bombarding the coating at low nitrogen pressure and applying a sufficiently high negative bias potential (-200 V) to the substrate, as well as the large difference in the size of the atoms of the multicomponent system (Table 3), leads to the coating deformation as micro- and at macrolevels and stimulates the formation of rough surface topography for the coating series no. 1.

Table 3. Atomic radius of elements of a multicomponent TiZrSiY coating [19]

Element	Ti	Zr	Si	Y
Radius, nm	0.140	0.155	0.110	0.180

Increasing the nitrogen pressure in the deposition chamber leads to a decrease in the average energy of the evaporated particles (losses during collisions in the interelectrode gap affect) and deformation of the coating, as well as to increase the saturation of the coating with nitrogen atoms. The latter form chemical bonds with the metal base and occupy octahedral interstices characteristic of a NaCl-type crystal lattice, thus preventing shear displacement of the planes with the formation of stacking faults. The mentioned structural changes can led to an increase in the mechanical properties of the coating, especially hardness, which is expected to see for the samples obtained at the maximum nitrogen pressure of 0.55 Pa.

Figure 3 shows the diffraction patterns of multicomponent (TiZrSiY)N coatings deposited at different partial pressures. A cubic TiN phase (ICCD: 04-001-2272) with a crystal lattice of NaCl-B1 type is formed in all experimental coatings. For all diffraction spectra, the (111) diffraction line has the highest intensity. There are also a number of low-intensity diffraction reflections corresponding to a mixture of (200) + (220) + (311) + (222) oriented grains.

In the coating deposited at nitrogen pressures of 0.08 Pa (see Figure 3a), the presence of cubic TiN and the α-Ti phase was identified. The lattice parameter of TiN nitride is a = 0.4262 nm. Calculation of substructural characteristics showed that the crystallite size of titanium nitride is 19.5 nm at the level of microdeformations $\varepsilon = 4.66 \cdot 10^{-3}$. The α-Ti lattice in the coating has the following lattice parameters: a = 0.2968 nm, and c = 0.4757 nm, which exceeds the values known from the scientific sources (a = 0.29505 nm, and c = 0.4697 nm) [20]. Therefore, the α-Ti phase is probably a solid solution of nitrogen in titanium.

The coating obtained at nitrogen pressure of 0.2 Pa (see Figure 3b) contain the same phases: cubic titanium nitride TiN and α-Ti. The lattice parameter of TiN nitride is a = 0.4268 nm, while the crystallite size is larger and equal to 26.5 nm at the lower level of microstrains $\varepsilon = 4.27 \cdot 10^{-3}$. The lattice parameters of the α-Ti phase is the same as for the coatings obtained at nitrogen pressure of 0.08 Pa.

In the coatings obtained at nitrogen pressure of 0.55 Pa (see Figure 3c), one phase was identified as cubic titanium nitride, TiN, with a lattice parameter a = 0.4291 nm and the largest crystallite size of 34.9 nm at the lowest microdeformation level $\varepsilon = 3.79 \cdot 10^{-3}$.

It is known that the value of the texture coefficient $T_{C(hkl)}$ is proportional to the number of crystallites (grains) that are oriented in a certain crystallographic direction. In cases of $T_{C(hkl)} > 1$, a large number of crystallites are oriented to a certain crystal plane. When $T_{C(hkl)} \leq 1$, the opposite variant is observed – a significant disorientation of crystallites. The calculated texture coefficient of the coating obtained at nitrogen pressure of 0.55 Pa is 5.95. This coating is characterized by the highest level of texturing compared to the coatings obtained at a lower nitrogen pressure ($T_{C(hkl)} = 3.50$ for the coating obtained at nitrogen pressure of 0.08 Pa, and $T_{C(hkl)} = 4.99$ for the coating obtained at nitrogen pressure of 0.2 Pa).
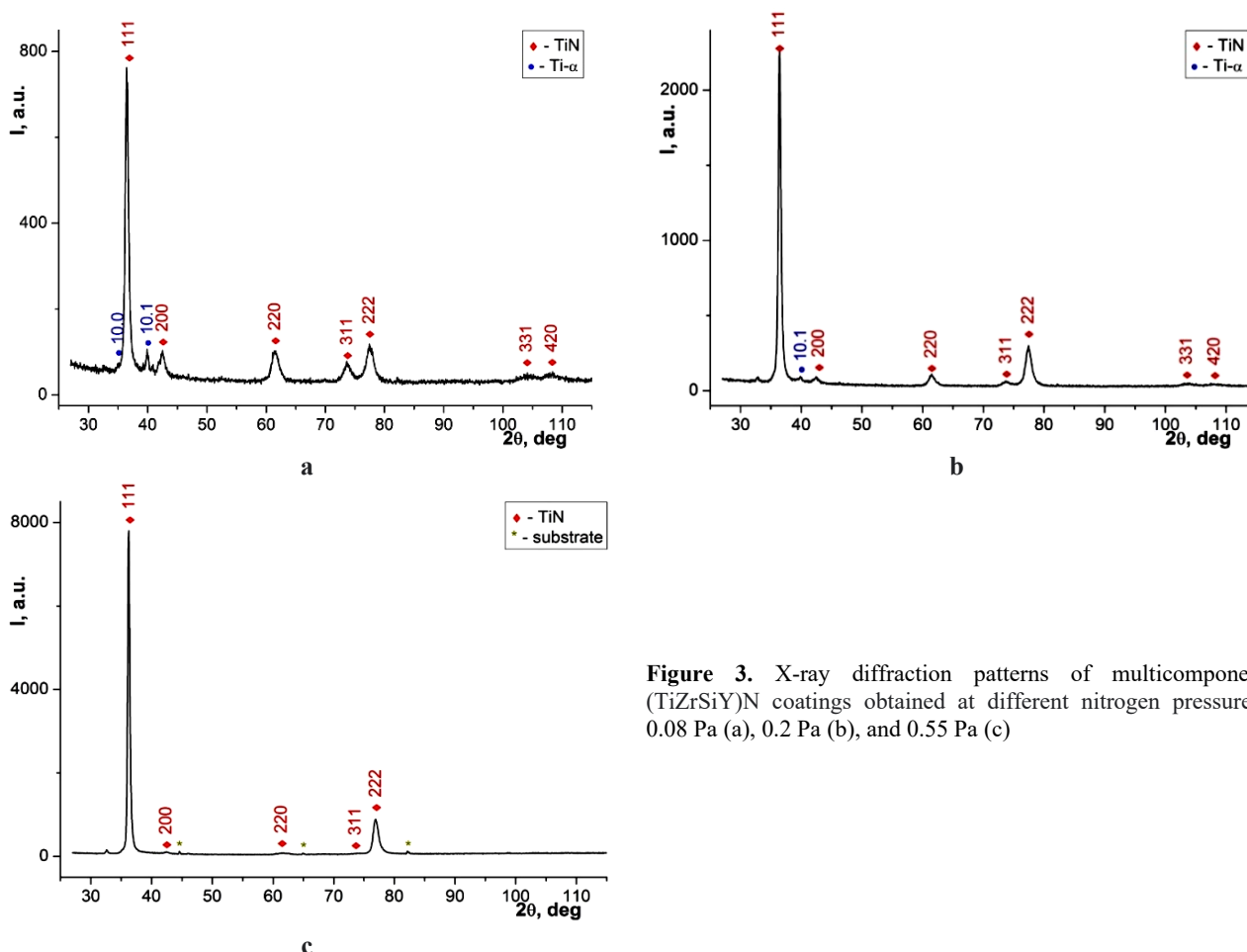
Figure 3. X-ray diffraction patterns of multicomponent (TiZrSiY)N coatings obtained at different nitrogen pressures: 0.08 Pa (a), 0.2 Pa (b), and 0.55 Pa (c)

One of the most important mechanical characteristics of multicomponent coatings are hardness (H) and elastic modulus (E). The results of measuring the abovementioned parameters as well as calculated values of the elastic strain to failure (H/E) and the resistance to plastic deformation (H^3/E^2) are shown in Table 4.

Table 4. Mechanical characteristics of multicomponent (TiZrSiY)N coatings

Series No.	Vickers hardness H, GPa	Elastic modulus E, GPa	H/E	H^3/E^2
1	25	284	0.088	0.19
2	31	327	0.09	0.27
3	36	347	0.1	0.38

The improvement in all mechanical properties with an increase in nitrogen pressure is obvious. Moreover, the coating series no. 3 has the smoothest surface. This means that the coating structure is denser, and, therefore, the hardness is higher.

Generally, such high mechanical properties of the experimental coatings are probably due to the complex influence of several effects, in particular, (1) the nanosize of grains, (2) the formation of a close-packed crystallite texture with the [111] axis, (3) the surface roughness, and (4) a certain level of internal stresses.

For the operational characteristics of coatings, an important criterion is their adhesive strength. In this work, the scratch testing method was used to determine the adhesive strength parameters of the coatings (see Figures 4 and 5). Based on the tests results, the coefficient of friction at different stages of wear, the amplitude of acoustic emission, as well as the critical loads were determined.
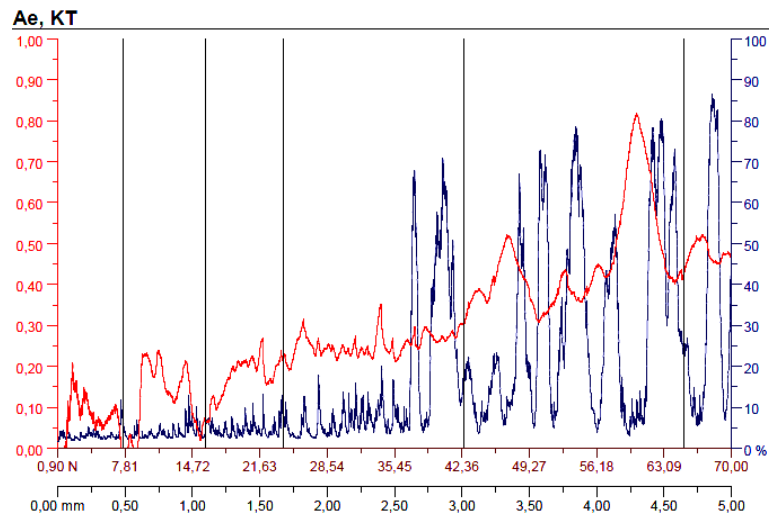
Figure 4. The graph of wear parameters obtained for the multicomponent (TiZrSiY)N coating obtained at nitrogen pressure 0.55 Pa (series no. 3): the coefficient of friction KT (red line, left scale), the amplitude of acoustic emission AE (blue line, right scale), the normal load to the indentor (brown bottom scale), the length of the scratch (black bottom scale)

A significant scatter in the values of the friction coefficient is due to the presence of a droplet fraction on the surface of the particles, which have micron sizes and create a large roughness. The composition of these particles differs greatly from the composition of the main coating layer; therefore, the interaction with the moving indenter also changes, which confirms the change of the course of the friction coefficient curve.

An analysis of the change in the level of the acoustic emission signal shows that the process of accumulation of cracks when approaching the load Lc4 leads to a sharp increase in acoustic emission (approximately 5-7 times), the level of which continues to slightly increase with further loading.

Microscopic images of the scratch at different critical loads for multicomponent (TiZrSiY)N coating obtained at nitrogen pressure of 0.55 Pa is presented in Figure 5.

Lc1   Lc2   Lc3

Lc1=7.61 N

Lc2=16.08 N

Lc3=24.02 N

Lc4=42.61 N

Lc5=65.12 N

Lc4   Lc5
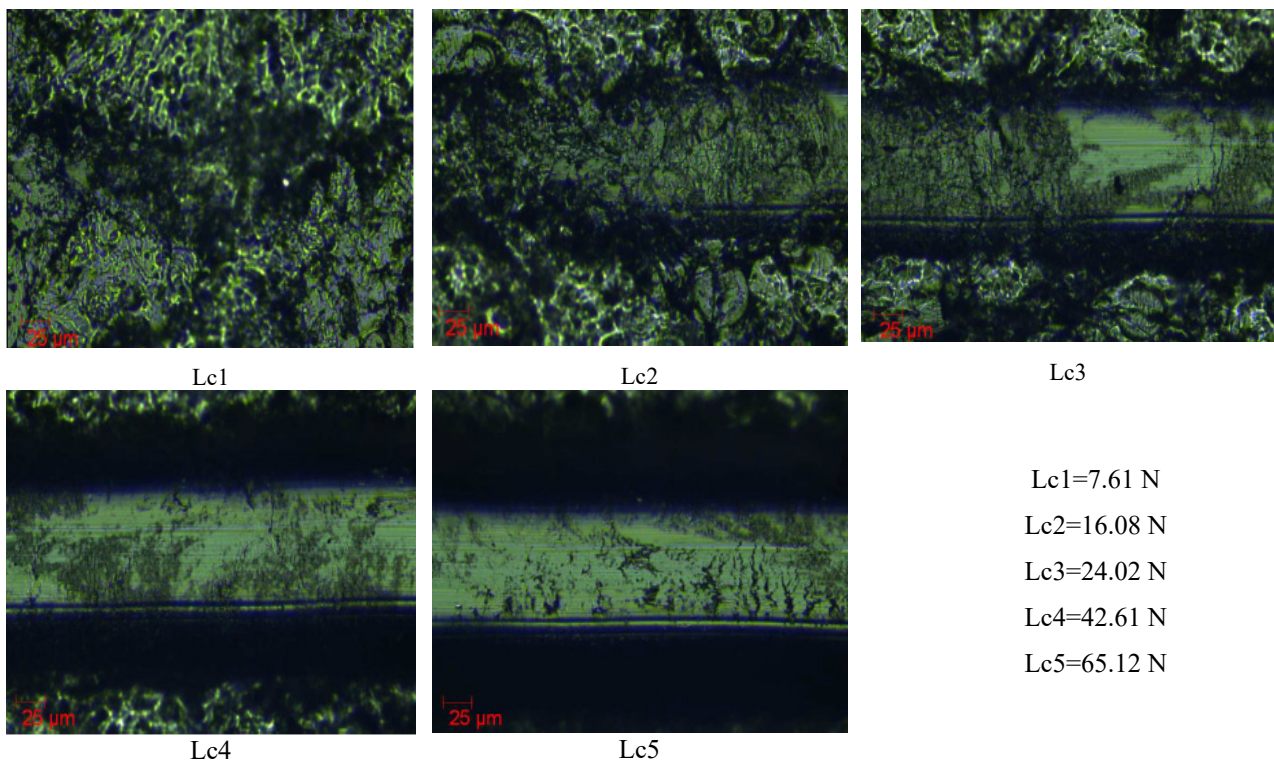
Figure 5. Microscopic images of the scratch at different critical loads for multicomponent (TiZrSiY)N coating obtained at nitrogen pressure of 0.55 Pa (series no. 3)

Table 5 shows the results of adhesion tests of all multicomponent coatings. It is obvious that the coating obtained at the highest nitrogen pressure of 0.55 Pa is characterized by higher critical loads (Lc1-Lc5) compared to other coatings.

Table 5. Critical load values (N) for multicomponent (TiZrSiY)N coatings

Series No.	Lc1	Lc2	Lc3	Lc4	Lc5
1	4.1	12.8	19.9	29.8	42.3
2	6.9	14.8	21.1	38.4	56.2
3	7.6	16.1	24.2	42.6	65.1

When scratching, the coatings are abraded, but do not exfoliate, i.e., they are destroyed by the cohesive mechanism associated with plastic deformation and the formation of fatigue cracks in the coating material. The difference in the level of adhesive strength of the coatings is due, on the one hand, to mechanical interaction due to the roughness of the contacting surfaces, and on the other hand, to chemical-interatomic interaction at the interface of the contacting bodies. In this case, the process of accumulation of cracks and local flaking (at Lc4) occurs in the coating in a rather narrow area of loads, and a large area corresponds to the abrasion of the coating to the substrate (at Lc4 - Lc5).

CONCLUSIONS

Multicomponent (TiZrSiY)N coatings formed using vacuum-arc technique at different nitrogen pressures were investigated. The analysis of the results of the phase composition and surface morphology suggests as follows:

1. During the formation of coatings under conditions of low nitrogen pressure, cubic titanium nitride TiN with the {111} texture and titanium (in the form of a solid solution) were identified.

2. Increasing the nitrogen pressure leads to an increase in the lattice parameter of TiN. In this case, an increase in the crystallite size of titanium nitride and a decrease in the level of microdeformations are observed. The {111} texture in titanium nitride also becomes stronger with increasing nitrogen pressure.

3. With the increase in the partial pressure of nitrogen in the coating, the texture coefficient increases to 5.795, which is associated with the formation of a more perfect substructure and the formation of a larger amount of crystallites with minimal defects.

4. The microhardness of multicomponent (TiZrSiY)N coatings increases with increasing nitrogen pressure during deposition from 25.0 GPa (at the nitrogen pressure of 0.08 Pa) to 36.0 GPa (at the nitrogen pressure of 0.55 Pa).

5. Studies of the process of destruction of coatings indicate that, depending on the structural-phase state of the coatings, their adhesive strength changes. Adhesive destruction of a multicomponent coating obtained at the highest nitrogen pressure of 0.55 Pa occurs at a load of 65.12 N.

6. According to the complex of parameters, H, E, H/E, H^3/E^2, friction coefficient and critical loads, the presented multicomponent (TiZrSiY)N coatings can be very attractive for tribological application.

ORCID
Vyacheslav M. Beresnev, https://orcid.org/0000-0002-4623-3243; Serhiy V. Lytovchenko, https://orcid.org/0000-0002-3292-5468
Mykola O. Azarenkov, https://orcid/org/0000-0002-4019-4933; Olga V. Maksakova, https://orcid.org/0000-0002-0646-6704
Denis V. Horokh, https://orcid.org/0000-0002-6222-4574; Bohdan O. Mazilin, https://orcid.org/0000-0003-1576-0590

REFERENCES
[1] A.D. Pogrebnjak, A.A. Bagdasaryan, I.V. Yakushchenko, and V.M. Beresnev. Russ. Chem. Rev. **83**, 1027 (2014), https://dx.doi.org/10.1070/RCR4407.
[2] W. Li, P. Liu, and P.K. Liaw. Mater. Res. Lett. **6**(4), 199 (2018). https://doi.org/10.1080/21663831.2018.1434248.
[3] J. Li, Y. Huang, X. Meng, and Y. Xie. Adv. Eng. Mater. **21**, 1900343 (2019). https://doi.org/10.1002/adem.201900343.
[4] E. Lewin. J. Appl. Phys. **127**(16) 160901 (2020) https://doi.org/10.1063/1.5144154.
[5] U.S. Nyemchenko, V.M. Beresnev, O.V. Sobol, S.V. Lytovchenko, V.A. Stolbovoy, V.J. Novikov, A.A. Meylekhov, A.A. Postelnyk, and M.G. Kovaleva. PAST, **101**, 112 (2016). https://vant.kipt.kharkov.ua/ARTICLE/VANT_2016_1/article_2016_1_112.pdf
[6] T. Ikeda, and H. Satoh, Thin Solid Films, **195**(1-2), 99 (1999). https://doi.org/10.1016/0040-6090(91)90262-V
[7] A.D. Pogrebnjak, A.P. Shpak, N.A. Azarenkov, and V.M. Beresnev, Physics-Uspekhi, **52**(1), 29 (2009). https://doi.org/10.3367/UFNe.0179.200901b.0035
[8] A.D. Pogrebnjak, and V.M. Beresnev, in: *Nanocomposites – New Trends and Developments,* edited by Farzad Ebrahimi (InTech, 2012), pp. 123-160, https://doi.org/10.5772/3389
[9] O.V. Maksakova, V.M. Beresnev, S.V. Lytovchenko, and D.V. Horokh, in: *2022 12th International Conference Nanomaterials: Applications & Properties* (IEEE, Krakow, Poland, 2022), pp. 01-06, https://doi.org/10.1109/NAP55339.2022.9934659
[10] S. Veprek, M. Veprek-Heijman, P. Karvankova, and J. Prochazka. Thin Solid Films, **476,** 1-29 (2005). https://doi.org/10.1016/j.tsf.2004.10.053
[11] J. Musil, P. Banoch, and P. Zeman, in: *Plasma Surface Engineering and Its Practical Applications,* edited by R. Wei (Research Signpost Publisher, USA, 2007), pp. 1-35.
[12] P.J. Martin, A. Bendavid, J.M. Cairney, and M. Hoffman. Surf. and Coat. Technol. **200**(7), 2228 (2005). https://doi.org/10.1016/j.surfcoat.2004.06.012

[13] V.M. Beresnev, O.V. Sobol', A.D. Pogrebnyak, S.V. Lytovchenko, O.N. Ivanov, U.S. Nyemchenko, P.A. Srebniuk, A.A. Meylekhov, A.Ye. Barmin, V.A. Stolbovoy, V.Yu. Novikov, B.A. Mazilin, E.V. Kritsyna, T.A. Serenko, and L.V. Malikov, PAST, **110**, 88 (2017). https://vant.kipt.kharkov.ua/ARTICLE/VANT_2017_4/article_2017_4_88.pdf
[14] V. Belous, V. Vasyliev, A. Luchaninov, V. Marinin, E. Reshetnyak, V. Strel'nitskij, and S. Goltvyanytsya, Surf. and Coat. Techn. **223,** 68 (2013). https://doi.org/10.1016/j.surfcoat.2013.02.031
[15] I.I. Aksenov, and D.S. Aksyonov, East Eur. J. Phys. **1**(3), 22 (2014). https://doi.org/10.26565/2312-4334-2014-3-02
[16] J. Valli, Journ. of Vac. Sci. and Technol. **A4**, 3007 (1986). https://doi.org/10.1116/1.573616.
[17] J. E. Daalder. Journ. of Phys. D: Appl. Phys. **8**, 1647 (1975). https://dx.doi.org/10.1088/0022-3727/8/14/009/
[18] B. Warcholinski, T.A. Kuznetsova, A. Gilewicz, T.I. Zubar, V.A. Lapitskaya, S.A. Chizhik, A.I. Komarov, et al., J. of Materi. Eng. and Perform. **27**, 3940-3950 (2018). https://doi.org/10.1007/s11665-018-3483-7
[19] J.C. Slater, Journ. of Chem. Phys. **41**(10), 3199 (1964). https://doi.org/10.1063/1.1725697
[20] D.R. Lide, editor, *CRC Handbook of Chemistry and Physics,* 90th edition (CRC Press/Taylor & Francis, 2009).

БАГАТОКОМПОНЕНТНІ ПОКРИТТЯ НА ОСНОВІ СИСТЕМИ (TiZrSiY)N, ОТРИМАНІ МЕТОДОМ ВАКУУМНО-ДУГОВОГО ОСАДЖЕННЯ

В'ячеслав М. Береснєв[а], Сергій В. Литовченко[а], Микола О. Азарєнков [а,б], Ольга В. Максакова[а], Денис В. Горох[а], Богдан О. Мазілін[а]

[а]*Харківський національний університет імені В.Н. Каразіна, майдан Свободи 4, 61022, м. Харків, Україна*
[б]*Національний науковий центр «Харківський фізико-технічний інститут», вул. Академічна, 1, 61108, м. Харків, Україна*

Вивчено вплив тиску реакційного газу (азоту) на структурно-фазовий стан та властивості вакуумно-дугових нітридних покриттів системи (TiZrSiY)N. На поверхні покриттів спостерігається значна кількість краплинної фракції та затверділих макрочастинок розпорошеного катода, що є характерним для вакуумно-дугових конденсатів, які осаджують з несепарованих плазмових потоків. В усіх зразках у покритті зафіксовано нітрид титану з кубічними ГЦК-гратами. У зразках покриттів, осаджених при тисках азоту P_N 0,08 Па і 0,2 Па, також ідентифікована фаза α-Ti, при цьому вимірюваний параметр гратів цієї фази дозволяє припустити, що ця фаза є твердим розчином азоту в титані. Коефіцієнт текстури багатокомпонентного покриття, сформованого при потенціалі зміщення -200 В і P_N = 0,55 Па має високе значення $T_{C(hkl)}$ = 5,95 в порівнянні з іншими зразками. Мікротвердість багатокомпонентних покриттів зростає залежно від парціального тиску азоту від 25,0 до 36 ГПа. Найвищу адгезійну міцність також має покриття, сформоване при найбільшому використаному тиску азоту P_N = 0,55 Па.
Ключові слова: *вакуумно-дугові покриття; багатокомпонентні нітридні покриття; парціальний тиск азоту; текстура; мікротвердість; адгезійна міцність*

THE EFFECT OF THERMAL ANNEALING ON THE ELECTROPHYSICAL PROPERTIES OF SAMPLES n-Si<Ni,Cu>[†]

ⓘNozimjon A. Turgunov, ⓘElmurod Kh. Berkinov*, Raymash M. Turmanova
Institute of Semiconductor Physics and Microelectronics at the National University of Uzbekistan, Tashkent, Uzbekistan
Corresponding Author e-mail: elmurod_8883@umail.uz

This paper presents the results of studies of the effect of isothermal annealing at temperatures T = 673÷1473 K in the time interval 5÷60 minutes on the electrical properties of silicon, simultaneously alloyed with nickel and copper. Samples of n-Si<Ni,Cu> were obtained on the basis of the starting material - single-crystal silicon, grown by the Czochralski method with the initial resistivity ρ = 0.3 Ohm·cm. Diffusion was carried out at a temperature of 1523 K for 2 hours. After that, the samples were cooled at a rate of 0.1 K/s. The morphological parameters of impurity nickel and copper atom clusters formed in the bulk of silicon were measured by electron probe microanalysis on a modern Superprobe JXA-8800R setup. As it turned out, in the volume of n-Si<Ni,Cu> samples, clusters of impurity atoms with different geometric shapes are formed, the sizes of which reach up to 500 nm. The electrical properties of the samples were studied by the Hall effect method using an Ecopia HMS-7000 instrument. It was revealed that under the influence of thermal annealing (TA) at T≥1273 K, impurity clusters decompose, which leads to an increase in the resistivity of n-Si<Ni,Cu> samples. After exposure to TA at T=1273 K for 15 minutes, the density of impurity nanoaccumulations of acicular and lenticular shapes sharply decreases in the sample volume. Under the influence of TA at T = 1473 K for 10 minutes in the volume of the sample, the decay of impurity nanoclusters with a spherical shape is observed. Also presented are the results of changes in the density of impurity clusters, as well as structural analyzes of the samples before and after exposure to thermal annealing.
Keywords: *Silicon; Nickel; Copper; Impurity; Thermal annealing; Nanoclusters, Decay*
PACS: 85.30.-z, 61.72.-y

INTRODUCTION

Currently, in the production of electronic devices, the base material is silicon, on the basis of which more than 90% of all semiconductor devices are produced. Therefore, the quality of this material significantly affects the development of modern semiconductor micro- and nanoelectronics. The manufacture of multifunctional integrated circuits is mainly carried out on single-crystal semiconductor wafers. Electrical, photoelectric, optical and other properties of semiconductor materials and structures based on them are determined by the presence of impurities and structural defects in crystals [1-4]. It should be noted that impurity defects can appear not only at the stage of obtaining materials, but also in the technological processes of manufacturing semiconductor devices [5-7].

Impurity defects formed during high-temperature diffusion doping of silicon single crystals with transition metal elements significantly affect their electrical, photoelectric, and optical properties [8-11]. Usually, when a silicon single crystal is doped with transition metal atoms, its thermal and radiation stability increases. In this direction, special attention is drawn to the behavior of impurity micro- and nanoinclusions under the influence of external influences. The state and behavior of impurity atoms of transition metals during heat treatment (HT) is of great interest from the point of view of controlling the electrophysical properties of silicon single crystals [12-15]. In this regard, this work is devoted to the study of the effect of HT on the resistivity of silicon doped with nickel and copper, as well as the kinetics of the decay of impurity nanoclusters under the influence of HT.

RESULTS AND DISCUSSION

Samples of n-Si<Ni,Cu> obtained on the basis of the starting material - single-crystal silicon, with resistivity ρ = 0.3 Ohm·cm, grown by the Czochralski method with crystallographic orientation (111), which are indicated in manufacturer's passport. The samples had the shape of a parallelepiped with the corresponding dimensions of 2×5×10 mm. Layers of impurity atoms were deposited on these samples, with nickel atoms 400 nm thick on one side of the sample and copper atoms 450 nm thick on the opposite side by vacuum deposition from a molybdenum boat heated to temperatures T_{Ni} ~ 1750 K and T_{Cu} ~ 1400 K. Simultaneous diffusion of nickel and copper into silicon was carried out in vacuum (10^{-5} Pa) at a temperature of 1523 K for 2 hours, after which the samples were cooled at a rate of 0.1 K/s. The results of our previous studies have shown that, at given diffusion parameters, nickel and copper impurity atoms diffuse into the entire volume of the sample. The resulting samples were subjected to isothermal annealing in vacuum (10^{-4} Pa) at temperatures T=673÷1473 K in the time interval 5÷60 minutes, followed by rapid cooling. After each stage of annealing, the electrical properties of the samples were studied. Structural studies were carried out by electron probe microanalysis on a modern Superprobe JXA-8800R setup. The electrical parameters of the samples were measured by the Hall effect method on an Ecopia HMS-7000 instrument. When measuring electrophysical parameters by the Hall

effect method, the surface of the samples had dimensions of 1.8×5×5 mm. From each of the four corners on the sample surface, ohmic contacts were made using Au and In(50%)Sn(50%).

The resistance values of n-Si<Ni,Cu> samples after diffusion annealing are $\rho = 10^4$ Ohm·cm. Such growth values of ρ compared to the original samples are due to the fact that the ejection atoms of impurities, both nickel and copper in silicon, have an acceptor character. The results of studying the dependence of ρ/ρ_0 on the annealing time in the sample show that at an annealing temperature of 673 K observations do not include significant changes in the value of ρ (curve 1, Fig. 1). In the subsequent value of thermal annealing (TA) at and 873 K for 30 minutes, there is a gradual increase in the value of ρ by approximately 50% (curve 2, Fig.1). With a further increase in time, the curve of this dependence slightly decreases and the value of ρ of the samples is $1.3 \cdot 10^4$ Ohm·cm. Under the influence of TA at T = 1073 K for 15÷20 minutes, a significant increase in the resistivity of the samples is observed, which increases almost 3 times (curve 3, Fig. 1). A further increase in the annealing time to 60 minutes does not lead to significant changes in the curve of this dependence.

The dependence of ρ/ρ_0 on the annealing time in n-Si<Ni,Cu> samples under the influence of TA at T = 1273 K is even more noticeable increase (curve 4, Fig.1). At this annealing temperature, in the initial 15 minutes, a sharp increase in the value of ρ/ρ_0 of the samples is observed, which reaches almost 7 times. With a further increase in time, it passes through a maximum, after which, over the next 25 minutes, there is a significant decrease in the value of ρ/ρ_0 and it is approximately 50%. Further, in the time interval of 40÷60 minutes, a moderate decrease in the curve of this dependence is observed and the final value of time, the value of ρ/ρ_0 decreases by approximately 40%.

The most significant increase in the dependence curve of ρ/ρ_0 on annealing time in n-Si<Ni,Cu> samples is observed under the action of TA at T = 1473 K (curve 5, Fig.1). During the initial 10 minutes, the value of ρ/ρ_0 of the samples increases by almost 2 orders of magnitude. And over the next 10 minutes, it decreases to approximately its original value. With a further increase in the annealing time to 60 minutes, it continues to moderately decrease and in the final time value it decreases, relative to the initial value, by almost 50%.

Therefore, under the influence of TA in the temperature range T=673÷1073 K, the dependences of ρ/ρ_0 values on time in n-Si<Ni,Cu> samples show the following trend: in the initial stages, with an increase in the TA temperature, the maximum of the curves of these dependences occurs earlier and the growth rate of the curves increases significantly. With a subsequent increase in the annealing time, the values of ρ/ρ_0 of the samples decrease, and the higher the value of the TA temperature, the more significantly it decreases.

The reason for such an increase in the curves of the dependences of the value of ρ/ρ_0 on the annealing time with an increase in the annealing temperature from 673 K to 1473 K annealing is associated with an increase in the concentration of electroactive impurity atoms of nickel and copper, which in turn depends on the decay of impurity clusters in the bulk of the samples. We have not measured the concentrations of nickel and copper impurity atoms in the volume of impurity clusters, and we will pay attention to this in our further studies.

In order to elucidate the cause of the origin of this phenomenon, we carried out complex structural analyzes of samples before and after exposure to TA. The results of analyzes in the n-Si<Ni,Cu> samples before TA exposure showed that nanoaccumulations of impurity Ni and Cu atoms with different geometric shapes are formed in their bulk (Fig. 2). Such impurity nanoaccumulations have needle-like, lenticular, spherical, and various polyhedral shapes. It should be noted that when measuring the morphological parameters of n-Si<Ni,Cu> samples using the Superprobe JXA-8800R electron probe analyzer, the probe excitation depth was 15–20 μm. The obtained results showed that impurity accumulations are unevenly distributed over the surface of the samples, their sizes reach from several nanometers to 500 nanometers, and their average density reaches ~10^3 cm^{-2}. We have not considered the problem of determining the ratio of quantitative indicators of nickel and copper impurity atoms in the volume of impurity clusters due to the limited capabilities of the measuring devices used by us, and in our further studies we intend to determine changes in these indicators before and after exposure to thermal annealing by comparison.
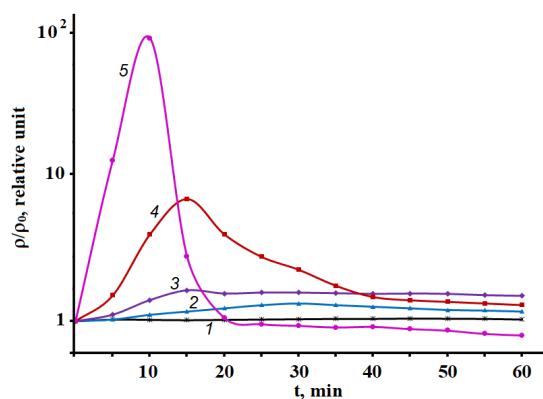

Figure 1. Dependence of the value of ρ/ρ_0 on the annealing time in n-Si<Ni,Cu> samples at TA:
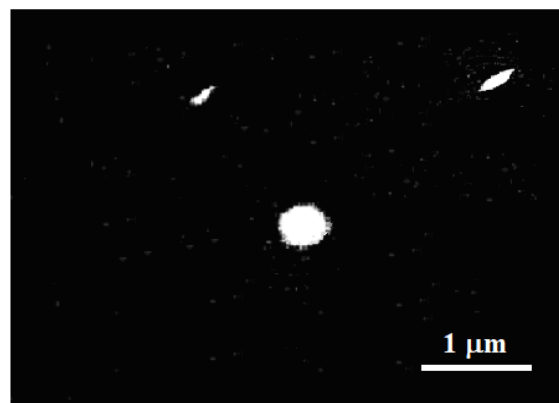1 – 673 K; 2 – 873 K; 3 – 1073 K; 4 – 1273 K; 5 – 1473 K

Figure 2. Micrographs of impurity nanoaccumulations in n-Si<Ni,Cu> samples before heat TA

The results of the structural analysis of the Si<Ni,Cu> samples subjected to thermal annealing in the temperature range T=673÷1073 K showed that the impurity nanoaccumulations formed in their volume after exposure to TA remain in this temperature range. This shows that impurity nanoaccumulations of Ni and Cu atoms formed in the bulk of single-crystal silicon are resistant to TA at temperatures T≤1073 K.

The obtained results of similar studies with n-Si<Ni,Cu> samples after exposure to TA at T=1273 K for 15 minutes showed that the density of impurity nanoaccumulations with needle-shaped and lenticular shapes in the sample volume decreases sharply (Fig.3). The micrographs obtained with a microprobe analyzer clearly show that, under the influence of TA, nanoaccumulations with similar shapes decay. With an increase in the value of TA up to T = 1473 K for 10 minutes, the decay of impurity nanoaccumulations with spherical shapes is observed in the sample volume (Fig.4). Impurity atoms split off from nanoclusters pass into nodes and interstices of the silicon crystal lattice. Such a course of the decay process of impurity nanoaccumulations shows that the sequence of decay of nanoaccumulations mainly depends on their geometric shape. Consequently, it turns out that impurity nanoaccumulations with a spherical shape are more resistant to external influences.
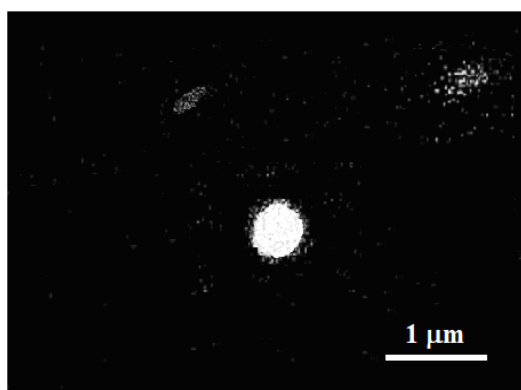
Figure 3. Micrographs of impurity nanoaccumulations in n-Si<Ni,Cu> samples after TA at T=1273 K
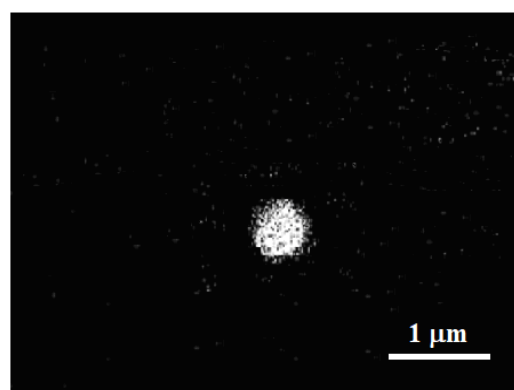
Figure 4. Micrographs of impurity nanoaccumulations in n-Si<Ni,Cu> samples after TA at T=1473 K

CONCLUSION

Thus, on the basis of the experimental results obtained, two stages can be distinguished in the kinetics of changes in the electrical properties of silicon with impurity nanoaccumulations under the influence of TA in the temperature range T=673÷1073 K. At the first stage of TA, the concentration of vacancies in the crystal structure of silicon increases and due to this impurity atoms located in the interstices, in an electrically neutral state, begin to move to the nodes of the crystal lattice. As a result, the value of the resistivity of the samples in the initial period of TA increases and reaches its maximum value. At the second stage, so if with a further increase in the TA time, due to a decrease in the excess concentration of vacancies in the crystal lattice, the transition of impurity atoms to lattice sites slows down. And this leads to a decrease in the resistivity of the samples.

Under the influence of TA at 1273 K for 15 minutes, as well as at 1473 K for 10 minutes, impurity nanoaccumulations decay, as a result of which the released impurity atoms pass into free lattice sites, so if in an electroactive state, which leads to a sharp increase in the specific sample resistance. With a further increase in the annealing time to 60 minutes due to a decrease in the concentration of excess vacancies, this transition is weakened, and the formation of various silicide complexes such as Ni_xSi_y, Cu_xSi_y, or $Ni_xCu_ySi_z$ in the electrically neutral state gradually becomes predominant, which leads to a significant decrease in the resistivity of the samples.

ORCID
Nozimjon A. Turgunov, https://orcid.org/0000-0003-3481-5622; **Elmurod Kh. Berkinov,** https://orcid.org/0009-0000-6745-315X

REFERENCES
[1] C. Sun, H.T. Nguyena, and F.E. Rougieux, Daniel Macdonald. Energy Procedia. **92**, 880 (2016). https://doi.org/10.1016/j.egypro.2016.07.097
[2] S.A. Muzafarova, Sh.B. Utamuradova, A.M. Abdugafurov, K.M. Fayzullaev, E.M. Naurzalieva, and D.A. Rakhmanov, Applied Physics, **4**, 81 (2021). https://applphys.orion-ir.ru/appl-21/21-4/PF-21-4-81.pdf (in Russian)
[3] N.A. Turgunov, Inorganic Materials, **12**(54), 1183 (2018). https://link.springer.com/article/10.1134/S0020168518120178
[4] N.A. Turgunov, E.Kh. Berkinov, and D.X. Mamajonova, Journal of Nano- and Electronic Physics, **13**(5), 05006 (2021). https://doi.org/10.21272/jnep.13(5).05006
[5] G. Gulyamov, M.G. Dadamirzaev, M.K. Uktamova, and B.Z. Mislidinov. AIP Conference Proceedings, **2700**, 050007 (2023). https://doi.org/10.1063/5.0126516
[6] C. Sun, H.T. Nguyen, F.E. Rougieux, and D. Macdonald. Journal of Crystal Growth. **460**, 9 (2017). https://doi.org/10.1016/J.JCRYSGRO.2016.12.084
[7] S. Dehili, D. Barakel, L. Ottaviani, and O.Palais, The European Physical Journal Applied Physics, **93**(4), 40101 (2021). https://doi.org/10.1051/epjap/2021210015

[8] S.Z. Zainabidinov, and N.A. Turgunov, Russian Physics Journal **47**, 1307 (2004). https://doi.org/10.1007/s11182-005-0071-8

[9] Sh.B. Utamuradova, Sh.Kh. Daliev, K.M. Fayzullaev, D.A. Rakhmanov, and J.Sh. Zarifbayev, New materials, compounds and applications, **7**(1), 37 (2023). http://jomardpublishing.com/UploadFiles/Files/journals/NMCA/V7N1/Utamuradova_et_al.pdf

[10] S.Z. Zainabidinov, K.N. Musaev, N.A. Turgunov, and A.R. Turaev, Inorganic Materials, **48**(11), 2012. https://doi.org/10.1134/S0020168512110192

[11] Sh.B. Utamuradova, A.V. Stanchik, K.M. Fayzullaev, B.A. and Bakirov, Applied Physics, **2**, 33 (2022). https://applphys.orion-ir.ru/appl-22/22-2/PF-22-2-33_EN.pdf (in Russian)

[12] N.A. Turgunov, E.H. Berkinov, and D.X. Mamazhonova, Applied Physics, **3,** 40 (2020). https://applphys.orion-ir.ru/appl-20/20-3/PF-20-3-40.pdf (in Russian)

[13] Sh.B. Utamuradova, D.A. Rakhmanov, A.S. Doroshkevich, I.G. Genov, Z. Slavkova, and M.N. Ilyina, Advanced Physical research, 5(1), 5 (2023). http://jomardpublishing.com/UploadFiles/Files/journals/APR/V5N1/Utamuradova_et_al.pdf

[14] Sh.B. Utamuradova, and D.A. Rakhmanov, Annals of University of Craiova, Physics, 32, 132 (2022). https://cis01.central.ucv.ro/pauc/vol/2022_32/15_PAUC_2022_132_136.pdf

[15] Sh.B. Utamuradova, A.V. Stanchik, and D.A. Rakhmanov, East Eur. J. Phys. 2, 201 (2023). https://doi.org/10.26565/2312-4334-2023-2-21

ВПЛИВ ТЕРМІЧНОГО ВІДПАЛУ НА ЕЛЕКТРОФІЗИЧНІ ВЛАСТИВОСТІ ЗРАЗКІВ n-Si<Ni, Cu>

Нозімжон А. Тургунов, Ельмурод Х. Беркінов, Раймаш М. Турманова

Інститут фізики напівпровідників та мікроелектроніки Національного університету Узбекистану, Ташкент, Узбекистан

У даній роботі представлені результати досліджень впливу ізотермічного відпалу при температурах T = 673÷1473 K до в інтервалі часу 5÷60 хвилин на електричні властивості кремнію, одночасно легованого нікелем і міддю. Зразки n-Si<Ni,Cu> були отримані на основі вихідного матеріалу - монокристалічного кремнію, вирощеного за методом Чохральского з початковим питомим опором ρ = 0,3 Ом·см дифузію проводили при температурі 1523 K до протягом 2 годин. Після цього зразки охолоджували зі швидкістю 0,1 K/s. Морфологічні параметри кластерів атомів домішок нікелю і міді, що утворилися в об'ємі кремнію, були виміряні методом електронно-зондового мікроаналізу на сучасній установці Superprobe JXA-8800R. як виявилося, в об'ємі зразків n-Si<Ni,Cu> утворюються кластери атомів домішки різної геометричної форми, розміри яких досягають до 500 нм. Електричні властивості зразків вивчали методом ефекту Холла за допомогою приладу Ecopia HMS-7000. Виявлено, що під впливом термічного відпалу (ТА) при T ≥ 1273 до відбувається розкладання кластерів домішок, що призводить до збільшення питомого опору зразків n-Si<Ni, Cu>. Після впливу TA при T = 1273 до протягом 15 хвилин щільність наноакумуляцій домішок голчастої і лінзоподібної форм в обсязі зразка різко зменшується. Під впливом TA при T = 1473 до протягом 10 хвилин в обсязі зразка спостерігається розпад домішкових нанокластерів сферичної форми. Також представлені результати зміни щільності кластерів домішок, а також структурні аналізи зразків до і після впливу термічного відпалу.

Ключові слова: *кремній; нікель; мідь; домішка; термічний відпал; нанокластери; розпад*

PROPERTIES OF "HIGHER MANGANESE SILICIDE-SILICON" HETEROSTRUCTURE†

Kobiljon K.-ugli Kurbonaliev^a*, **Nurulla F. Zikrillaev^b**, **Akhmadjon Z. Khusanov^c**

^aKokand State Pedagogical Institute named after Mukimiy, Kokand, Uzbekistan
^bTashkent State Technical University, Tashkent, Uzbekistan
^cKokand State Pedagogical Institute named after Mukimiy, Kokand, Uzbekistan
*Corresponding Author e-mail: qurbonaliyevq@gmail.com
Received April 27, 2023; revised June 6, 2023; accepted June 12, 2023

Based on the diffusion technology, many scientists and specialists have conducted research on obtaining materials that are fundamentally different in electrical and photo-thermal parameters from the original material by introducing various input atoms into semiconductor materials and creating deep energy levels in their band gap. The electrical, photoelectric, optical, and magnetic properties of these semiconductor materials have been extensively studied with metal group elements, isovalent elements and rare earth elements added to silicon through the process of growth, ion implantation, or diffusion from the gaseous state. The technology of introducing impurity atoms into silicon by the diffusion method is distinguished from other methods in its simplicity, energy efficiency, and low cost. Up-to-date the technology of changing the resistivity and conductivity of the initial sample by diffusion of manganese atoms into single-crystal silicon is studied insufficiently.In the article, it was determined that when manganese atoms diffuse into silicon, a high-manganese silicide is formed on its surface and in the near-surface layer. Based on the analysis of the experimental results, the thermal EMF (electromotive force) in $Mn_4Si_7 - Si < Mn > - Mn_4Si_7$ structures in a certain temperature range and under illumination (with monochromatic or integrated light) is explained by the fact that it based on the Pelte effect, observed in semiconductors.The volt-ampere characteristics (VAC) of the obtained structures were measured at various temperatures, in the dark and in the light. Formation of a boundary layer with high resistivity at the boundary of the higher manganese-silicon transition, the transition from higher manganese silicide to the base of the structure due to the effect of ionization of pores during illumination of structures and external influence. The applied field was clarified based on VAC results. The manganese high silicide layer formed on the silicon surface has the properties of a semiconductor, and the formation of a heterojunction upon transition to silicon is shown on the basis of the sphere diagram.
Keywords: *Higher; Manganese; Silicide; Forbidden gap; Properties; Structure*
PACS: 85.30.−z, 79.20.Rf, 71.18.+y, 68.43.Jk, 68.47.Fg

INTRODUCTION

Nowadays, the requirements for thermal batteries created on the basis of higher manganese silicides (HMS) are almost the same as the requirements for bulk thermoelements, which implies that their operational performances must be tuned to be perfect [1]-[5]. While heat transfer in bulk thermoelectric materials is carried out on the basis of metal electrodes embedded into the semiconductor, in thin-layer thermoelectric materials and thermal batteries, heat transfer is carried out on the basis of a substrate on which the layer is grown [6],[7]. Since thermal batteries created on the basis of higher manganese silicides (HMS) are ususally grown on the surface of silicon in the form of a thin layer, thus heat exchange occurs fast. Revealing practical application areas of thermal batteries, photodetectors and photodiodes assembled on the basis of the "HMS – silicon" structure is one of the most urgent problems of current scientific research [8]-[10].

Differences in two phases adjacent to "higher manganese silicide – silicon" transition boundary are not only due to the fact that their electrophysical parameters do differ, but also by varying value of the forbidden gap of materials in these phases [11], [12].

Study and analysis of experimental data on "higher manganese silicide – silicon" structures have shown that higher manganese silicide on the basis of Mn_4Si_7 compound, manifests semiconductor properties and its forbidden gap was determined by experimental study of temperature dependence of electric conductivity and Hall factor on HMS-3000 Van-der-Pau equipment.

It was reveald that the value E_g of the forbidden gap of higher manganese silicide was $E_g \approx 0.67 \div 0.8\ eV$ judging by the fact that charge carriers in the sample were holes. Thus, it was shown that in the "higher manganese silicide-silicon" boundary layer, a heterostructure was being formed.

TECHNIQUE AND EXPERIMENTAL

Boron-doped monocrystalline silicon wafer with resistivity of $10\ \Omega \cdot cm$, was used as a reference sample for forming HMS layer on silicon substrate. The authors have utilized the diffusion technique to form HMS layer on sample's two-dimensional large surface. The thickness d of the HMS layer formed on the silicon surface was approximately $\approx 5 \div 7\ \mu m$. The conductivity of the resulting HMS layer was *p*-type (charge carriers holes), and their concentration $p \approx 10^{19} \div 10^{20}\ cm^{-3}$. Such a layer formed on the surface could be viewed as a heavily doped degenerate semiconductor. The

---

value of relative resistance of the base region in the resulting structure was equal to $\rho \approx 10^5 \Omega \cdot cm$, and the concentration of charge carriers in it was approximately close to that in intrinsic silicon.

The resulting $Mn_4Si_7 - Si < Mn > - Mn_4Si_7$ structure in written form was shortly abbreviated as $p^+ - Si < Mn > -p^+$. The electrophysical and photoelectric properties of such structures were studied in a wide temperature range of $80 \div 300\,K$. For experiments, a task-specific cryostat was engineered that was designed to operate in the temperature range from $80K$ to room temperature and with specific glass window for exposure of a sample to integral and monochromatic light.

As a light source, the arsenide galium (GaAs) light emitting diode was used, as well as the IKS-21-type infrared spectrometer. While measuring the volt-ampere characteristics (VAC) of the structures at room temperature, the athors have observed two sections on current-voltage curve. At low temperatures ($T = 80K$), the value of the current would sharply (almost $6 \div 8$ times) decrease whereas relative resistance of the base region of the structure would starkly increase. At forward bias mode, the value of the current in the dark would decrease down to $J_d \approx 10^{-12}A$ whereas after the structures have been exposed to light, the value of photocurrent would increase to $\approx 10^{-3} \div 10^{-2}A$ (Fig.1).
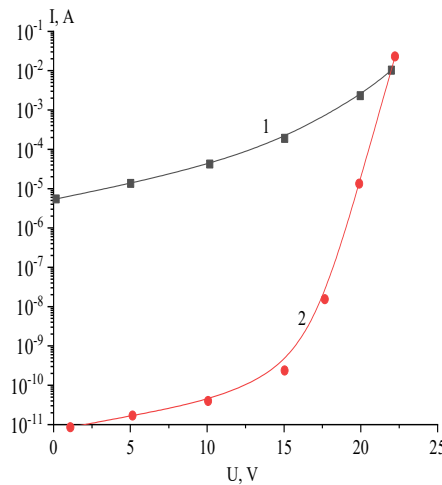
Figure 1. Volt-ampere curve of $p^+ - Si < Mn > -p^+$ structure at T = 300K (1) and T = 80K (2) illuminated by photons with energy hν ≥ E_g

At a low temperatures (T=80K), the value of ΔU_K (voltage falling on boundary transition cross section of the pre-contact surface layer of the structure) have tended to increase due to decrease in relative resistance of the base region of the structure in times of its exposure to light. It is well known that, resistance at boundary area could be deteremined as follows $R_K = S \frac{\Delta U_K}{J}$. Here S – area of the opposite contact side of the structure. Theoretical calculations have revealed that the relative resistance of the base region of resulting structures at room temperature was equal to $\rho_\delta \approx 6 \cdot 10^4 \Omega \cdot cm$. The results of experiments aimed at determining the resistance of the base region of structures by two probe technique ($\rho = S \frac{U}{Jl}$, where l is the distance between probes) have revealed that the relative resistance of manganese high silicides grown on silicon substrate was equal to $\rho_\delta \approx 6,2 \cdot 10^4 \Omega \cdot sm$, which was close to the data of theoretical calculations.

To determine the concentration and mobility of charge carriers at the base region of the structure, the authors have applied the Hall factor technique at various temperatures. Also the authors have studied the photovolt-ampere characteristic at various values of monochromatic illumination at ($hν \geq E_g$).

Having known the value of R_x (Hall factor), the concentration of holes, as well as the the mobility of charge carriers (using the formula $\frac{R_x}{\rho} = \mu_p$) were subsequently calculated. At $J_p = 1mA$ (photocurrent), the concentration of charge carriers (holes) was equal to $p = 2,4 \cdot 10^{14}\,cm^{-3}$ while at $J_p = 2,5mA$, it was respectively $p = 2,5 \cdot 10^{15}\,cm^{-3}$. In both cases, Hall mobility μ_p was in the range $200 \div 300\,sm^2/V \cdot s$. At the same parameters of illumination of $M - Si < Mn > -M$ structure and at external source voltage U=10 V, the current J_p, was $8 \cdot 10^{-5}A$ and the concentration of holes was $p \leq 2.4 \cdot 10^{13}\,cm^{-3}$.

We have observed two section in VAC curve when the distance between the electrodes was negligent (9÷10mm), and when the structures were illuminated by monochromatic light. In this case, there was virtually no difference in parameters of the curves both in dark and exposed modes under voltage of $U \leq 1\,V$. After the voltage U have passed ≥ 2 V, the difference between VAC in dark and exposed modes rather increased, and the difference was stark almost 10^4 times (Fig. 2, 1 and 2 lines).

When the photocurrent value was $J_p \geq 4 \cdot 10^{-3}mA$, at HMS – silicon junction point excess heat was detected. When the photocurrent value reaches $J_p \geq 10^{-2}A$ excess heating at the transition bondary of $Mn_4Si_7 - Si < Mn >$ was significantly greater. When the pole of the constant current source connected to the structure was versed, heating field has moved to the opposite right side of the $Si < Mn > - Mn_4Si_7$ structure.
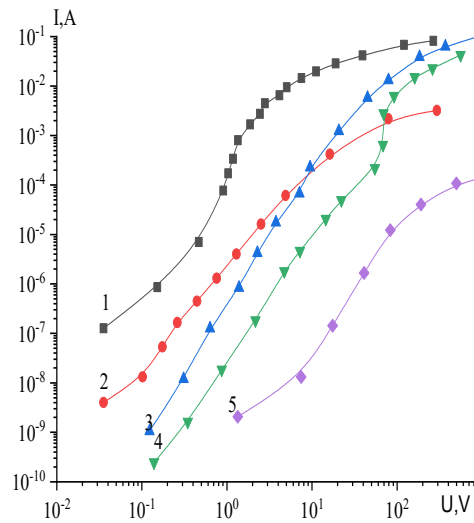
Figure 2. Volt-ampere characteristics of silicide structures at T=80K:
1 – while exposed to illumination when the width of the base section of $p^+ - Si < Mn > -p^+$ structure is 70÷75 µm
2 – $p^+ - Si < Mn > -p^+$ in dark conditions,
3 – $p^+ - Si < Mn > -M$ the width of the base section of the structure is 1.5 mm while forward bias voltage is applied,
4 – $p^+ - Si < Mn > -M$ width of the base section of the structure is 5 mm and while forward bias voltage is applied
5 – $p^+ - Si < Mn > -M$ is 5mm, and when the reverse voltage is connected, the base width of the structure

When the distribution of $U(L)$ (voltage drop on contacts from external voltage source connected to the structure in the base section of the structure) was studied, it was found that the majority of voltage appears to drop at the "*silicide-silicon*" transition boundary. In this case, it was found that primarily voltage drops on boundary section of the photoconductive border, where the resistance of the HMS structure is negligent (Fig. 3).
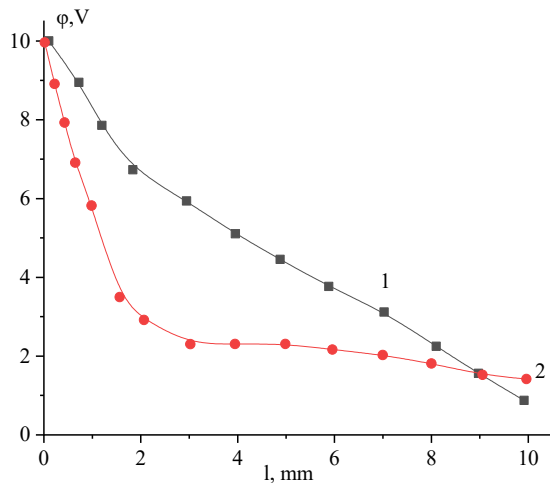
Figure 3. $p^+ - Si < Mn > - p^+$ external voltage drop distribution
1 - T=300K, 2-80K, when illuminated with monochromatic radiation ($h\nu \geq E_g$).
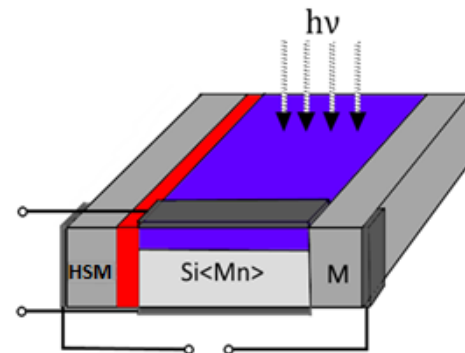
Figure 4. Connection of the structure to an external source at low temperatures and while illuminated by monochromatic light ($h\nu \geq E_g$).
HMS - higher manganese silicides

On Fig. 4 it is shown the structure of the $Mn_4Si_7 - Si < Mn > - Mn_4Si_7$ structure, its connection to an external power supply, the incidence of monochromatic radiation, and the measurement circuit of the generated thermal EMF (electromotive force).

DISCUSSION OF EXPERIMENTAL RESULTS

Tradionally, in times of exposure of the base region of the structure to light the phenomena of photoconductivity occurs due to which, non-equilibrium charge carriers such as electrons and holes are generated. Subsequently, the Fermi level moves towards the valence and the conduction bands, each leading to the formation of quasi Fermi levels. When the structure was illuminated with infrared light with a wavelength $\lambda = 0.9 \div 1$ µm (the depth of absorption of falling photons was up to ~100 µm), the thickness of the holes conductive layer with a small resistivity $\rho \approx 5 \div 10 \, \Omega \cdot cm$

was equal to the depth of absorption of falling photons. In silicon doped with manganese atoms, such physical phenomena due to holes leading to massive photoconductivity were previously reported by several authors [13].

The resistivity value formed when the resulting structures are illuminated by low intensity infrared light happen to be small $\rho \approx 5 \div 10\ \Omega \cdot cm$, and the formation of a conductive layer with with hole conductivity was similar to the formation of non-equilibrium charge carriers (holes) at the base of the structure. At specific resistance of p-type sample (resistivity $\rho \approx 5 \div 10\ \Omega \cdot cm$) the concentration of holes was estimated at $\sim 10^{15} cm^{-3}$.

A similar situation was observed when the silicon samples doped with manganese atoms appeared to have completely compensated boron atoms after the samples were illuminated with photonic energy corresponding to a wavelength of $\lambda \approx 1\ \mu m$ [14],[15]. Such a precedent was not observed in the $p^+ - Si < Mn > -p^+$ structures because the physical phenomena at the contact layers of such structures allegedly happen by injection of charge carriers in the heterojunction layer. Based on the analysis of the obtained experimental results, it was possible to explain the physical mechanism of contact phenomena observed in heterojunction structures.

A layer with a high resistance was formed at the transition boundary of the silicon (*HMS-Si<Mn>*) system doped with HMS and manganese impurity atoms, while the external voltage source was applied, a potential barrier was created due to electric displacement. Thus, the probability that charge carriers (holes) would heat up and migrate to the base region of the structure will increase. This in turn led to the occurrence of a mechanism of shock ionization due to photogeneration by boosting injection of holes heated from the HMS layer into the structure's base region (Si<Mn>).

It was determined that the following preconditions must be met in the heterojunction of the resulting structures in order to generate additional charge carriers:

1. Creation of conditions for the injection of holes into silicon from a layer of higher manganese silicides.

2. The thickness of higher manganese silicides-silicon transition layer shall be enough to induce injection phenomenon of charge carriers through the base region.

In other words, it is necessary that the length of free running path of the holes be greater than the thickness of the transition layer. In this case, the heated holes pass like they go through a tunnel crossing to the base of the structure. In this case, holes carry a certain energy and form an additional electron – hole pair based on the heating of the base region. This increases the value of the photocurrent several times and has led to a decrease in the resistance of the base region. The increase in the concentration of charge carriers at the base region of the the concerned structure in the irradiated position can be reduced by the following mechanism. That the value of photocurrent in $M - Si < Mn > -M$ structures appears to be several degrees higher than that in silicon samples, which are doped solely by manganese atoms in the normal state, was explained by the shock ionization of the charge carriers.
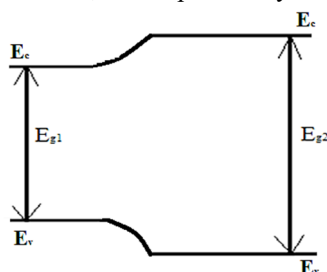

Figure 5. Band diagram of a heterojunction formed at the boundary of higher manganese silicide-silicon $E_{g1} \approx 0{,}67 \div 0{,}8$ eV, $E_{g2} = 1{,}12$ eV

When there are two types of charge carriers in semiconductors, and if a thermal gradient is created in them, the transfer of heat due to the concentration gradient of current carriers is observed (Pelte effect). It was found that the thermal EMF formed in the structure of manganese high silicide - silicon is almost not observed in the structures of the metal-silicon Si<Mn> system.

It was observed that in the resulting HMS – Si<Mn> – HMS structures we have witnessed symmetrical disposition in volt-ampere characteristics in the initial state (at low voltage and low current values) while samples were exposed to light. When replacing one of HMS layers in the structure with a metal contact, that is, in *HMS - Si<Mn> - M* structures, the value of the photocurrent- J_p in cases when the voltage is forward biased and inversed, proved to differ greatly from each other, and the difference is at least $\sim 10^4$. If the voltage supplied from an external source is U≥15 V, this difference is relatively lower ($10^1 - 10^2$ times), but an increase in temperature was observed at the HMS -silicon contact, that is, the structure started to heat up. This, in turn, caused the current to step down under the influence of temperature [15]-[17].

Structures in the first and second regime ($p^+ - Si < Mn > -p^+$ and $M - Si < Mn > -M$, respectively) in the illuminated state, based on the analysis of the results obtained in VAC and the distribution of applied external voltage, manganese high silicide - silicon heterojunction diagram of the structure was proposed (Fig. 5).

CONCLUSION

Based on the scientific analysis of VAC of the resulting higher manganese silicide-silicon and metal-manganese doped silicon structures and the proposed heterojunction diagram, we assume the following:

1.   The manganese high silicide formed on the silicon surface when the manganese atoms diffuse into the silicon (from the gas state or from the manganese metal layer on the silicon surface) has a monopolar injection contact feature that leads to injection of holes into the silicon bulk.

2.   In $Mn_4Si_7 - Si < Mn > -Mn_4Si_7$ or $Mn_4Si_7 - Si < Mn > -M$ structures with high resistance at relatively low temperatures (T = $80 \div 200$K) and when illuminated with photons energy $h\nu \geq E_g$, the value of their resistance is believed to decrease sharply and it switched to a photoconductive state.

3.   It was determined that the photosensitivity of the base region of the resulting structures increased at low temperatures, and the resistance decreased under the influence of light, due to avalanche ionization of charge carriers formed in higher manganese silicide, as well as the injection of certain additional energy into the transition layer.

4.   It was shown that the formation of a heterojunction at the transition boundary of the higher manganese silicide-silicon structure and its VAC change under the influence of infrared radiation.

ORCID IDs

Kobiljon K.-ugli Kurbonaliev, https://orcid.org/0000-0002-9620-3595; **Nurulla F. Zikrillaev**, https://orcid.org/0000-0002-6696-5265; **Akhmadjon Z. Khusanov**, https://orcid.org/0000-0002-0407-2330

REFERENCES

[1]   A.E. Gershinsky, A.V. Rzhanov, and E.I. Cherenkov, "Thin-film silicides in microelectronics," Microelectronics, **11**(2), 83-94 (1982). (in Russian)

[2]   V.K. Zaitsev, V.I. Tarasov, and A.A. Adilbekov, "Metal–nonmetal transition in compensated higher manganese silicide," PTT, **16**(3), 581-584 (1976). (in Russian)

[3]   V.V. Ilchenko, and V.I. Strikha, "Rearangement of the electronic structure of the metal-silicon silicide interface during low-temperature annealing," Ukrainian Physical journal, **28**(2), 248-252 (1983). (in Russian)

[4]   J.Pout, K.Tu, and J.Meyer, *Thin films: Mutual Diffusion and Reaction*, (Mir, Moscow, 1982). (in Russian)

[5]   N.Egwunyenga, B.Josephinea, S.Okunzuwa, and L.Imosobome, "Synthesis of SnS/SnO nanostructure material for photovoltaic application," East Eur. J. Phys. (1), 154 (2023). https://doi.org/10.26565/2312-4334-2023-1-19

[6]   M.K.Bahadyrkhanov, T.S.Kamilov, A.Zh.Khusanov, G.I.Ivakin, and I.S. Zanaveskina, "Investigation of the effect of the transition layer on photovoltaic properties in the structures of higher manganese silicide (HSM) -Si<Mn>-M," Surface. X-ray, synchrotron and neutron studies, (6), 100 (2002).

[7]   A.A. Rysbaev, Zh.B. Khuzhaniyazov, B.E. Khayriddinov, and I.R. Bikbulatov, *Structure and properties of nanoscale films of metal silicides*, (Adad plyus, Tashkent, 2017).

[8]   T.S.Kamilov, V.V.Klechkovskaya, A.A.Rysbaev, A.S. Orekhov, Sh.Kh. Dzhuraev, and A.S. Kasymov, "Influence of structural defects in silicon on formation of photosensitive heterostructures Mn_4Si_7 - Si < Mn > - Mn_4Si_7 and Mn_4Si_7 - Si < Mn > - M," EuroAsian journal of physics and functional materials, **2**(4), 360-366 (2019). https://doi.org/10.29317/ejpfm.2018020408

[9]   M.K. Bakhadyrkhanov, S.B. Islamov, N.F. Zikrillaev, and K. Khaydarov, "Nanoscale varizon structure in silicon with multicharged nanoclusters," Microelectronics, **42**(6), 444-446 (2013). (in Russian)

[10] G.V. Samsonov, L.A. Dvorina, and B.M. Rud, *Silicides*, (Metallurgy, Moscow, 1979). (in Russian)

[11] M.K. Bakhadirkhanov, S.N. Ibodullaev, N.F. Zikrillaev et al., "An Infrared Radiation Photoresistor Based on Silicon with Nanoclusters of Manganese Atoms," Tech. Phys. Lett. **47**, 641-644 (2021). https://doi.org/10.1134/S1063785021070038

[12] V.V. Klechkovskaya, T.S. Kamilov, S.I. Avdasheva, S.S. Khudaiberdiev, and V.I. Muratova, "Features of the crystal structure of films of higher manganese silicide painted on silicon," Crystallography, **39**(5), 894-899 (1994). (in Russian)

[13] M.K. Bakhadyrkhanov, N.F. Zikrillaev, S.B. Isamov, and M.O. Tursunov, "Anamalous Photoelectrics Phenomenia in Silicon with Nanoclusters of Managanese atoms," Semiconductors, **55**(6), 542-545 (2021). https://doi.org/10.21883/FTP.2021.06.50912.9259

[14] M.K. Bakhadyrkhanov, S.B. Isamov, and N.F. Zikrillaev, "Photodetectors of IR radiation in the region λ=1.5÷8 µm based on silicon with multi-charge nanoclusters of manganese atoms," Microelectronics, **42**(6), 444-446 (2012). https://doi.org/10.1134/S1063739712030043

[15] A.A. Rysbaev, Zh.B. Khuzhaniyazov, L.H. Rakhimova, and A.M. Rakhimov, "On the formation of new surface superstructures in the formation of thin nanoscale films of silicides," Uzbek Physical Journal, **15**(2), 26-32 (2013). (in Russian)

[16] V.I. Strikha, *Contact phenomena in semiconductors*, (Vyshcha Shkola, Kyiv, 1982). (in Russian)

[17] M.K. Bakhadyrkhanov, and S.B. Islamov, "Physical foundations of the formation of the silicon-based heterovarizonic structure," Technical Physics, **14**, 2211 (2022). http://dx.doi.org/10.21883/TP.2022.14.55220.60-21

ВЛАСТИВОСТІ ГЕТЕРОСТРУКТУРИ "СИЛІЦИД ВИЩОГО МАРГАНЦЮ-КРЕМНІЮ"
Кобілжон К. углі Курбоналієв[a], Нурулла Ф. Зікріллаєв[b], Ахмаджон З. Хусанов[c]
[a]Кокандський державний педагогічний інститут імені Мукімія, Коканд, Узбекистан
[b]Ташкентський державний технічний університет, Ташкент, Узбекистан
[c]Кокандський державний педагогічний інститут імені Мукімія, Коканд, Узбекистан

На основі дифузійної технології багато вчених і фахівців проводили дослідження з отримання матеріалів, принципово відмінних за електричними і фототермічними параметрами від вихідного матеріалу, шляхом введення в напівпровідникові матеріали різних вхідних атомів і створення глибоких енергетичних рівнів в їх забороненій зоні. Електричні, фотоелектричні, оптичні та магнітні властивості цих напівпровідникових матеріалів були ретельно вивчені з елементами групи металів, ізовалентними елементами та рідкоземельними елементами, доданими до кремнію в процесі росту, іонної імплантації або дифузії з газоподібного стану. Технологія введення домішкових атомів у кремній дифузійним методом відрізняється від інших простотою, енергоефективністю та дешевизною. Сучасна технологія зміни питомого опору та електропровідності вихідного зразка шляхом дифузії атомів марганцю в монокристалічний кремній вивчена недостатньо. У статті встановлено, що при дифузії атомів марганцю в кремній утворюється високомарганцевий на його поверхні і в приповерхневому шарі утворюється силіцид. На основі аналізу експериментальних результатів встановлено термоЕРС (електрорушійна сила) в структурах Mn_4Si_7-Si < Mn > - Mn_4Si_7 в певному інтервалі температур і при освітленні (з монохроматичне або інтероване світло) пояснюється тим, що він заснований на ефекті Пельтьє, який спостерігається в напівпровідниках. Вольт-амперні характеристики (VAC) отриманих структур були виміряні при різних температурах, у темряві та на світлі. Утворення прикордонного шару з високим питомим опором на межі вищого переходу марганець-кремній, переходу від вищого силіциду марганцю до основи структури за рахунок ефекту іонізації пор при освітленні структур і зовнішньому впливі. Область застосування була уточнена на основі результатів VAC. Шар вищого силіциду марганцю, утворений на поверхні кремнію, має властивості напівпровідника, а утворення гетеропереходу при переході на кремній показано на основі сферічної діаграми.
Ключові слова: *вищий; марганець; силіцид; заборонена зона; властивості; структура*

EFFECT OF ZnS AND CdS ON SOME PHYSICAL PROPERTIES OF MgO FILMS†

N.A. Hassan[a], W.H. Albanda[b], M.H. Al-Timimi[a]*

aDepartment of Physics, College of Science, University of Diyala, Iraq
bScience Department - College of Basic Education, Mustansiriyah University, Iraq
Corresponding Author e-mail: muhammadtimimi@yahoo.com

This article reports on the fabrication and characterization of MgO nanostructured films and the effect of ZnS and CdS on their structural, optical, and electrical properties. The MgO, MgO: ZnS, and MgO: CdS thin films were deposited using a Chemical spray pyrolysis technique onto glass substrates at 673 K. The XRD patterns revealed that the MgO thin films had a preferred (111) orientation with a pure cubic crystalline structure, while the ZnS and CdS layers had a hexagonal structure. The FE-SEM images showed that the MgO films had a nanostructured morphology with an average particle size of ~50 nm. The UV-Vis spectroscopy results showed that the addition of ZnS and CdS layers to the MgO films resulted in a shift in the absorption edge towards the visible region of the electromagnetic spectrum, indicating an improvement in their optical properties. These findings suggest that the MgOZnS and MgOCdS films could have potential applications in optoelectronic devices.
Keywords: *MgO films; Doping Effect; ZnS; CdS; Chemical spray pyrolysis; Physical properties*
PACS: 73.20.At, 78.20.-e, 77.55.-f

INTRODUCTION

Magnesium oxide (MgO) thin films have been studied for their potential use in a variety of applications, including as a dielectric material for microelectronic devices [1,2], To improve the performance of these devices, it is often necessary to introduce dopants into the MgO film. Doping involves introducing impurity atoms into the lattice structure of the MgO film to modify its electrical properties [3,4], Commonly used dopants for MgO include boron, phosphorus, and aluminum. These dopants can be introduced into the film during growth by adding them to the source material or by using ion implantation techniques, The effects of doping on the electrical properties of MgO thin films depend on both the type and concentration of dopant used. Generally, boron doping results in an increase in conductivity while phosphorus and aluminum doping results in a decrease in conductivity [5,6]. Magnesium oxide (MgO) thin films can be used to dope ZnS and CdS semiconductor materials. This doping process involves depositing a thin layer of MgO onto the surface of the ZnS or CdS material. The MgO acts as an acceptor dopant, meaning that it can donate electrons to the semiconductor material, thus increasing its conductivity [7,8], This process is often used in optoelectronic devices like solar cells. By doping ZnS and CdS with MgO, it is possible to improve their electrical properties, making them more suitable for use in these types of devices [9,10]. Chemical spray pyrolysis is a technique used to deposit thin films of semiconductor materials such as ZnS and CdS onto substrates. This technique involves spraying a solution of the desired material onto the substrate, followed by heating the substrate in an oven to evaporate the solvent and decompose the material into its constituent elements [11,12], The resulting thin film is then annealed at high temperatures to improve its crystallinity and electrical properties. Doping CdS and ZnS with magnesium oxide (MgO) can be achieved using chemical spray pyrolysis by adding MgO to the solution before spraying it onto the substrate, The MgO will then be incorporated into the thin film during pyrolysis, resulting in a doped semiconductor material [13], The doping concentration can be controlled by adjusting the concentration of MgO in the solution, as well as by varying other parameters such as temperature and time[14,15]. The goal of this research is to study the effect of ZnS and CdS on MgO films on the structural, optical, and electrical properties, The research will focus on understanding the influence of doping on the XRD, Energy gap, absorption coefficient, refractive index, and electrical conductivity of the thin films.

EXPERIMENTAL PART

Spray pyrolysis was used to deposit MgO,(MgO: ZnS), and (MgO: CdS) films. Magnesium chloride ($MgCl_2.6H_2O$), zinc nitrate ($Zn(NO_3).6H_2O$), cadmium chloride ($CdCl2.6H_2O$), and thiourea (CH_4N_2S) dissolved in distilled water with molarity (0.1M). (MgO) doped with 8% (ZnS) and (CdS). The chemical solution was sprayed onto glass substrates at 673K using a 1.5 bar compressor. The structural characteristics were determined using X-ray diffraction, field emission scanning electron microscopy, and An ultraviolet-visible (UV-Vis) spectrophotometer was used to measure the optical characteristics. and Hall effect measurement was used to determine the electrical properties.

RESULTS AND DISCUSSION

Figure (1) shows the X-ray diffraction patterns of (MgO) films doped with (CdS) and (ZnS). Table (1) shows the values of the diffraction angles, the width of the mid-peak, the crystal size, and the interlayer distances separating the

crystalline levels. And Miller coefficients for (MgO) film, (Mg: 6%CdS) and (Mg: 6%ZnS) films respectively. The results showed that the films have a polycrystalline structure and obtain magnesium oxide (MgO) with a pure cubic crystalline structure and that the spectrum of magnesium oxide matches the standard spectrum (JCPDS 074-1225) with a crystalline level (Fm- 3m no.225) and crystal dimensions (a = b = c = 4.22 ˚A), while the angle values were ($\alpha = \beta = \gamma = 90$ °) [16], and after the doping process (6%) of cadmium sulfide (CdS), another hexagonal crystalline phase appeared. (JCPDS 077-2306)) with crystal dimensions (a = b = 4.136 ˚A and c = 6.713 ˚A) and angles ($\alpha = \beta = 90$ ° and $\gamma = 120$ °) [17], and this phase is more clear and crystallized with the doping. The figure (Fig. 1) shows that doping with zinc sulfide (ZnS) resulted in a fall in intensity and an increase in the width of the diagnostic peaks. This is due to (Mg) ion substitution with sulfur and zinc ions (S^{-2} ions Zn^{+2} and), ion diffusion within the crystal lattice of magnesium oxide (MgO), and the appearance of new peaks after doping, indicating the formation of (ZnS) a hexagonal Crystal Structure with (a=b = 3.82 Å, c = 6.25 Å) and ($\alpha=\beta=90°$, $\gamma=120°$), consistent with the standard spectrum (JCPDS 003-7393) [17,18].
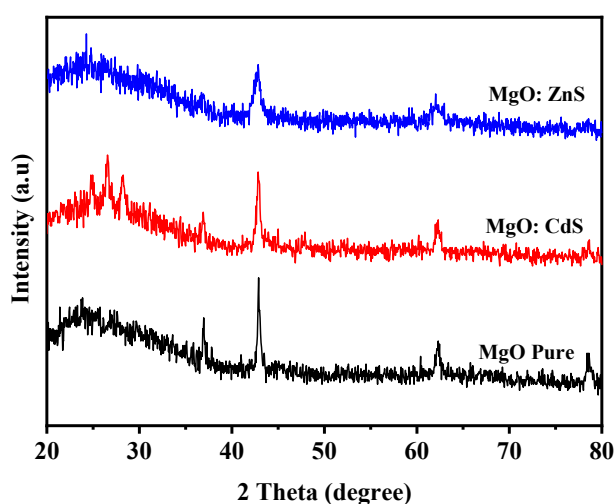
Figure 1. XRD MgO films doped with (CdS) and (ZnS).

Table (1): Some crystal parameters of MgO before and after doping with (6 %) from ZnS and CdS.

Samples	2Θ (deg) Experimental	2Θ (deg) Standard	FWHM (deg)	Crystallite Size (nm)	dhkl (Å) Experimental	dhkl (Å) Standard
MgO	36.85	36.86	0.94	9.30	2.43	2.43
	42.77	42.82	0.55	16.19	2.11	2.11
	62.19	62.16	1.15	8.42	1.49	1.49
	78.63	78.44	0.40	26.80	1.21	1.21
MgO: ZnS	36.74	36.86	0.55	15.86	2.44	2.43
	42.74	42.82	0.39	22.62	2.11	2.11
	61.94	62.16	0.31	30.71	1.49	1.49
	78.72	78.44	0.19	55.87	1.21	1.21
MgO: CdS	36.94	36.86	0.29	29.62	2.43	2.43
	42.90	42.82	0.24	36.22	2.10	2.11
	62.16	62.16	0.48	20.17	1.49	1.49
	24.94	24.80	0.59	14.38	3.56	3.58
	26.59	26.50	0.29	28.87	3.34	3.35
	28.17	28.18	0.39	21.72	3.16	3.16

The Energy Dispersion X-ray Analysis (EDX) in Fig. 2 and Table 2 shows the presence of MgO, MgO:ZnS, and MgO:CdS. Figure 2 describes the investigation of the morphology and surface structure of different films made of magnesium oxide (MgO) doped with different materials, such as zinc sulfide (ZnS) or cadmium (CdS). The investigation was carried out using a field emission scanning electron microscope (FE-SEM), The addition of zinc sulfide (ZnS) or cadmium (CdS) to a magnesium oxide (MgO) film can significantly impact the particle size of the resulting film. This is because the dopant material can affect the growth and formation of the film during the deposition process, leading to changes in the size and distribution of the particles. For example, the addition of ZnS to a MgO film can result in the formation of smaller particles with a more uniform size distribution, as the ZnS can act as a nucleation site for MgO growth [19, 20]. On the other hand, adding CdS can lead to the formation of larger particles due to the interaction between CdS and MgO during the deposition process, These changes in particle size can have significant implications for the properties and performance of the film, as demonstrated in previous studies [21, 22, 23].

Table (2): The Elements of MgO, MgO:ZnS and MgO:CdS from EDX

Element	Weight %	Atomic %
Mg	50.62	40.28
O	49.38	59.72
Total	100	100
Mg	47.07	38.59
Zn	4.51	1.38
S	0.46	0.28
O	47.96	59.75
Total	100	100
Mg	40.94	31.96
Cd	1.74	0.29
S	0.42	0.25
O	56.90	67.50
Total	100	100
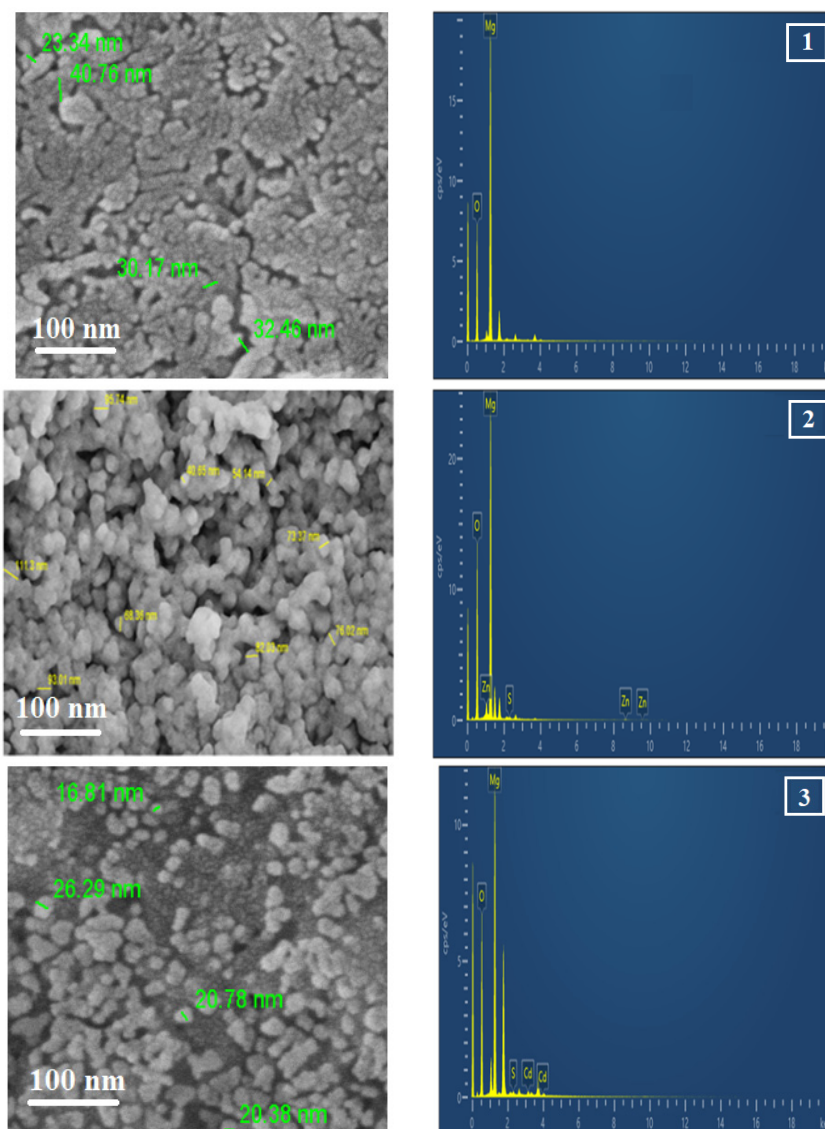
Figure 2. 1- FE-SEM and EDX of MgO films, **2-** MgO:ZnS films , **3-** MgCdS films.

The transmittance and reflectance of MgO films doped with CdS and ZnS can vary depending on the type and concentration of the dopant. Generally, the addition of dopants to MgO films can affect their optical properties, such as their transmittance and reflectance, Studies have shown that the addition of ZnS to MgO films can decrease their transmittance in the visible region, due to the larger particle size and distribution between the particles [24,25]. On the

other hand, the addition of CdS can decrease the transmittance of MgO films, especially at shorter wavelengths, due to the formation of larger particles [26,27]. Reflectance measurements also depend on similar factors, and studies have shown that the addition of ZnS to MgO films can increase their reflectance in the ultraviolet region, while the addition of CdS can decrease their reflectance [28,29].
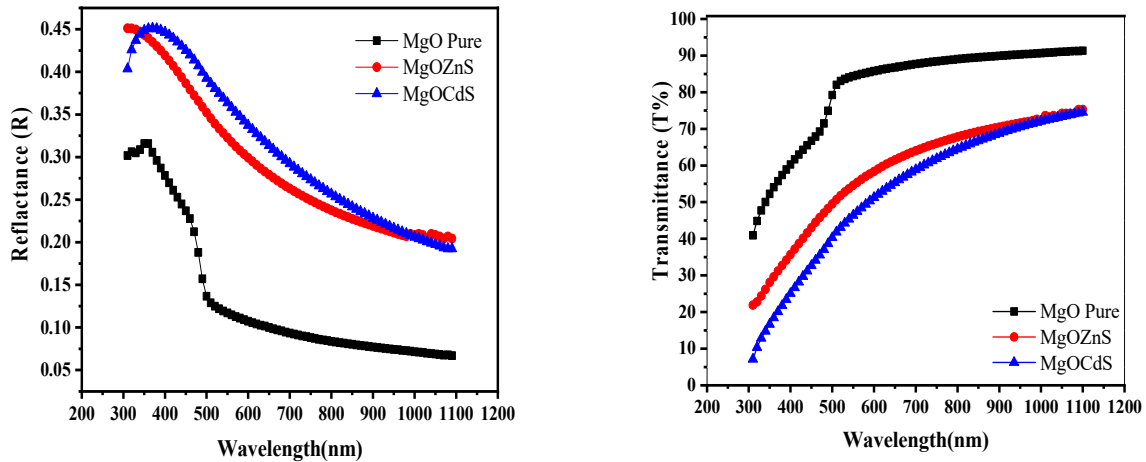
Fig. 3. Transmittance and Reflectance of MgO films doped with (CdS) and (ZnS).

The absorption coefficient and energy gap of MgO films doped with CdS and ZnS are important optical properties that can be affected by the type and concentration of the dopants, as well as the thickness of the film. Studies have shown that the addition of CdS and ZnS to MgO films can result in a decrease in the energy gap, due to the smaller particle size and the increase in the number of defects in the film [30,31]. This decrease in the energy gap can also lead to an increase in the absorption coefficient of the film. The relationship between the energy gap and absorption coefficient can be described by the Tauc plot, which is a method used to determine the optical properties of materials based on their absorption spectra [32]. The Tauc plot shows a linear relationship between the square of the absorption coefficient and the photon energy for direct bandgap materials, while indirect bandgap materials show a nonlinear relationship [33].
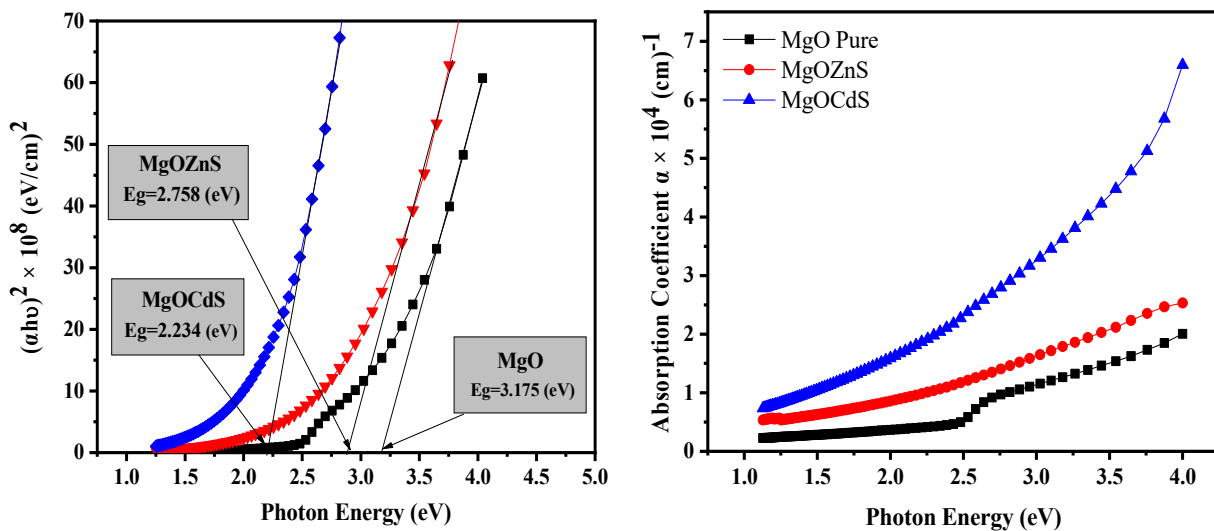
Figure 4. The Absorption coefficient and Energy gap of MgO films doped with (CdS) and (ZnS).

The refractive index and extinction coefficient are important optical parameters that can be used to characterize the optical properties of thin films. MgO films doped with CdS and ZnS have been shown to exhibit interesting changes in their refractive index and extinction coefficient due to the incorporation of dopant atoms into the MgO lattice. Studies have demonstrated that the addition of ZnS and CdS to MgO films can increase the refractive index of the film due to the formation of smaller nanoparticles with a higher degree of order, which leads to a greater degree of light confinement within the film [30-33]. The relationship between the refractive index and the amount of light reflected from a surface is such that higher refractive indices correspond to more reflection. This connection is expressed in equation (1) [34] :

$$n_o = \left[\frac{(1+R)^2}{(1-R)^2} - (k_o^2 - 1)\right]^{\frac{1}{2}} + \frac{(1+R)}{(1-R)} \tag{1}$$

The extinction coefficient of MgO films doped with CdS and ZnS can also be affected by the type and concentration of the dopants. The addition of ZnS and CdS to MgO films can increase the extinction coefficient due to the presence of larger particles with a higher degree of light scattering [3,4]. To determine the extinction coefficient (k_o), equation (2) can be used [35] .

$$k_o = \frac{\alpha\lambda}{4\pi} \tag{2}$$

The refractive index and extinction coefficient of MgO films are shown in Figure (5).
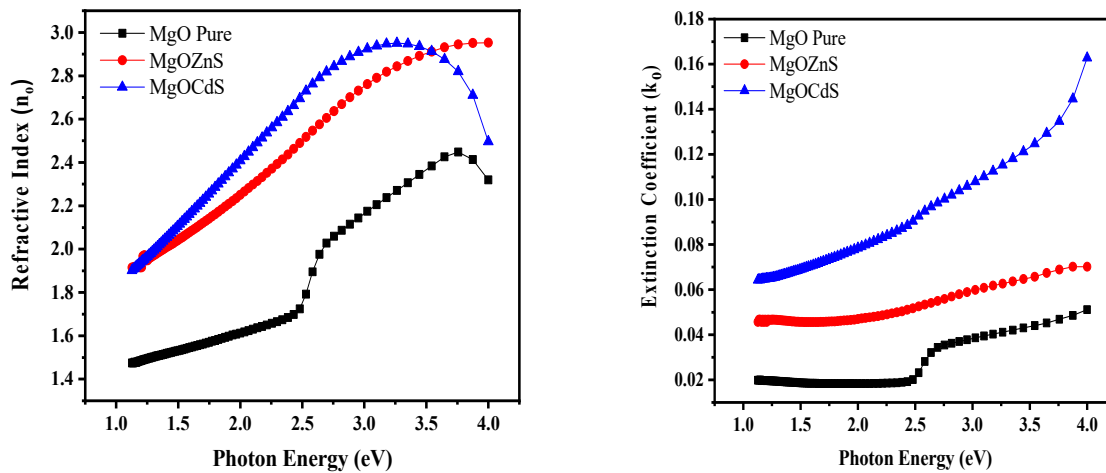
Figure 5. Refractive index and Extinction Coefficient of of MgO films doped with (CdS) and (ZnS)

The dielectric constant of a material is typically given by a complex quantity, with a real part (ε_r) and an imaginary part (ε_i) that relate to the material's ability to store and dissipate energy in an electric field, respectively. Equations (3) and (4) establish a relationship between the behavior of the real dielectric constant and the refractive index, as well as the imaginary dielectric constant and the extinction coefficient[36].

$$\varepsilon_r = n_o^2 - k_o^2 \tag{3}$$

$$\varepsilon_i = 2n_o k_o \tag{4}$$
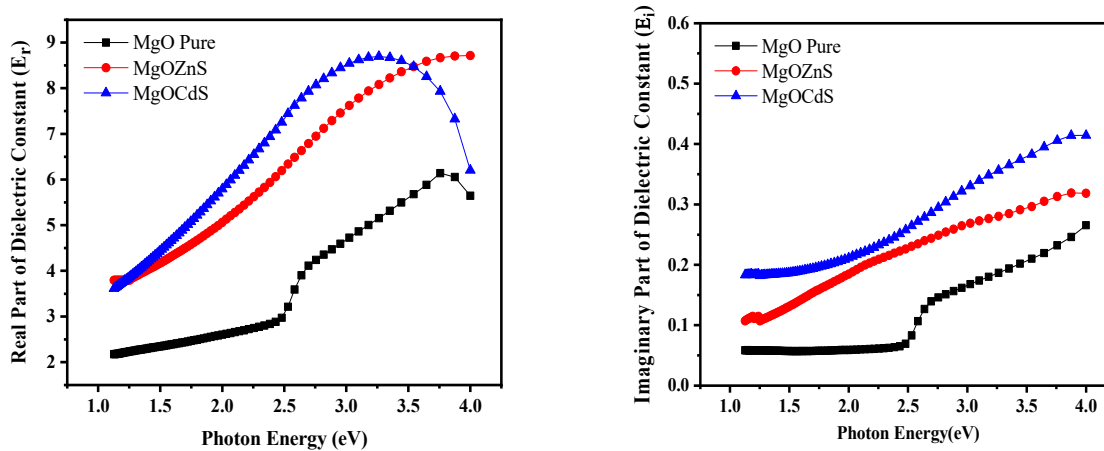
Figure 6. The real and imaginary part of the dielectric constant of MgO films doped with (CdS) and (ZnS).

MgO films doped with CdS and ZnS have been shown to have changes in their electrical properties . After studying Hall effect measurements of (MgO) thin films doped with ZnS and CdS at a 6% ratio, it was discovered that both types of films had negative charge carriers, as evidenced by the negative Hall coefficient (RH). This finding is consistent with previous research [36], The resistivity values of all films were observed to be high, with the films doped with ZnS and

CdS exhibiting the highest values. These high resistivity values are attributed to defects in the crystal structure of the film, which hinder the movement of charge carriers [37].

Table 2. Electrical Properties of MgO, MgO:ZnS , MgO:CdS Films.

Samples	Concentration (cm)$^{-3}$	Hall Coefficient Rh (m^2/C)	Conductivity (Ω.cm)$^{-1}$	Resistivity (Ω.cm)	Mobility (cm^2/v.s)
MgO	2.584×10^6	2.416×10^7	1.035×10^{-5}	9.662×10^4	2.500×10^2
MgO:ZnS	4.325×10^7	-2.886×10^6	5.337×10^{-7}	1.874×10^7	1.540×10^1
MgO:CdS	4.953×10^6	-3.781×10^7	1.309×10^{-5}	7.638×10^4	4.950×10^2

CONCLUSION

The structural and optical properties of magnesium oxide (MgO) films can be significantly influenced by the incorporation of zinc sulfide and cadmium sulfide, These compounds, when added to MgO films, can cause noteworthy changes, including an increase in the refractive index, a reduction in the band gap, and an elevation in the optical absorption coefficient, Various techniques such as X-ray diffraction (XRD), scanning electron microscopy (SEM), UV-visible spectroscopy, and Electrical Properties have been employed in several studies to investigate these effects, The findings conclusively demonstrate the substantial impact of zinc sulfide and cadmium sulfide additions on both the structural and optical characteristics of MgO films, These findings hold promising potential for applications like antireflective coatings and other optoelectronic devices.

N.A. Hassan, https://orcid.org/0009-0008-5813-6265; **Widad H. Albanda,** https://orcid.org/0000-0002-3214-395X
M.H. Al-Timimi, https://orcid.org/0000-0002-9828-6945

REFERENCES

[1] R. Kant, A.K. Singh, and A. Arora, "Tuning of MgO nanoparticles on Ag dopant additions for charge storage applications," Vacuum, **189**, 110247 (2021). https://doi.org/10.1016/j.vacuum.2021.110247

[2] F.A. Miranda, G. Subramanyam, F.W. Van Keuls, R.R. Romanofsky, J.D. Warner, and C.H. Mueller, "Design and development of ferroelectric tunable microwave components for Kuand K-band satellite communication systems," IEEE Transactions on Microwave Theory and Techniques, **48**(7), 1181-1189 (2000). https://doi.org/10.1109/22.853458

[3] K. Gao, Q. Bi, X. Wang, W. Liu, C. Xing, K. Li, D. Xu, *et al.,* "Progress and Future Prospects of Wide-Bandgap Metal-Compound-Based Passivating Contacts for Silicon Solar Cells," Advanced Materials, **34**(26), 2200344 (2022). https://doi.org/10.1002/adma.202200344

[4] S.S. Chiad, N.F. Habubi, W.H. Abass, and M.H. Abdul-Allah, "Effect of thickness on the optical and dispersion parameters of Cd0. 4Se0. 6 thin films," Journal of Optoelectronics and Advanced Materials, **18**(9-10), 822-826 (2016).

[5] Y. Liu, Y. Li, Y. Wu, G. Yang, L. Mazzarella, P. Procel-Moya, A.C. Tamboli, *et al.,* "High-efficiency silicon heterojunction solar cells: materials, devices and applications," Materials Science and Engineering: R: Reports, **142**, 100579 (2020). https://doi.org/10.1016/j.mser.2020.100579

[6] Q. Liu, G. M. Dalpian, and A. Zunger, "Antidoping in insulators and semiconductors having intermediate bands with trapped carriers," Physical Review Letters, **122**(10), 106403 (2019). https://doi.org/10.1103/PhysRevLett.122.106403

[7] Z. Zhang, X.E. Verykios, and M. Baerns, "Effect of electronic properties of catalysts for the oxidative coupling of methane on their selectivity and activity," Catalysis Reviews, **36**(3), 507-556 (1994). https://doi.org/10.1080/01614949408009470

[8] A. Mahroug, B. Mari, M. Mollar, I. Boudjadar, L. Guerbous, A. Henni, and N. Selmi, "Studies on structural, surface morphological, optical, luminescence and Uv photodetection properties of sol–gel Mg-doped ZnO thin films," Surface Review and Letters, **26**(03), 1850167 (2019). https://doi.org/10.1142/S0218625X18501676

[9] A.T. Abood, O.A.A. Hussein, M.H. Al-Timimi, M.Z. Abdullah, H.M.S. Al Aani, and W.H. Albanda, "Structural and optical properties of nanocrystalline SnO2 thin films growth by electron beam evaporation," AIP Conference Proceedings, **2213**(1), 020036 (2020). https://doi.org/10.1063/5.0000454

[10] A.V. Rane, K. Kanny, V.K. Abitha, and S. Thomas, "Methods for synthesis of nanoparticles and fabrication of nanocomposites," in: *Synthesis of inorganic nanomaterials*, (Woodhead publishing, 2018), pp. 121-139.

[11] M.H. Abdullal, R.A. Jaseen, and A.H. Resan, "Annealing effect on the optical energy gap of (CdTe) thin films," J. Pure Sciences, **7**(3), 205-213 (2011). https://www.iasj.net/iasj/pdf/ccf116d82c221e01

[12] A.B. Workie, H.S. Ningsih, and S.J. Shih, "An comprehensive review on the spray pyrolysis technique: historical context, operational factors, classifications, and product applications," Journal of Analytical and Applied Pyrolysis, **170**, 105915. (2023). https://doi.org/10.1016/j.jaap.2023.105915

[13] Z.X. Tang, and B.F. Lv, "MgO nanoparticles as antibacterial agent: preparation and activity," Brazilian Journal of Chemical Engineering, **31**, 591-601 (2014). http://dx.doi.org/10.1590/0104-6632.20140313s00002813

[14] A.J. Mawat, M.H. Al-Timimi, W.H. Albanda, and M.Z. Abdullah, "Morphological and optical properties of Mg1-xCdSx nanostructured thin films," AIP Conference Proceedings, **2475**(1), 090019 (2023). https://doi.org/10.1063/5.0103955

[15] H.S. Al-Rikabi, M.H. Al-Timimi, A.H. Abed, and W. Albanda, "Surface Topography and Optical Properties for (MgOx-1ZnSx) Thin Films Prepared by Chemical Spray Pyrolysis," Diyala Journal for Pure Science, **18**(4), (2022). https://djfps.uodiyala.edu.iq/index.php/Home/article/view/36

[16] W. Cui, P. Li, Z. Wang, S. Zheng, and Y. Zhang, "Adsorption study of selenium ions from aqueous solutions using MgO nanosheets synthesized by ultrasonic method," Journal of Hazardous materials, **341**, 268-276 (2018). https://doi.org/10.1016/j.jhazmat.2017.07.073

[17] G.C. Ozcan, H.M. Gubur, S. Alpdogan, and B.K. Zeyrek, "The investigation of the annealing temperature for CdS cauliflower-like thin films grown by using CBD," Journal of Materials Science: Materials in Electronics, **27**, 12148-12154 (2016). https://doi.org/10.1007/s10854-016-5368-6

[18] A.J. Mawat, and M.H. AL-Timimi, "Structural Properties of (MgO$_{1-x}$CdS$_x$) Thin Films Prepared by Chemical Spray Pyrolysis technique," Journal of the college of basic education, **27**(113) (2021). https://www.iasj.net/iasj/pdf/8e0e961ca70b4e80

[19] S. Barth, F. Hernandez-Ramirez, J.D. Holmes, and A. Romano-Rodriguez, "Synthesis and applications of one-dimensional semiconductors," Progress in Materials Science, **55**(6), 563-627 (2010). https://doi.org/10.1016/j.pmatsci.2010.02.001

[20] N. Izyumskaya, Y.I. Alivov, S.J. Cho, H. Morkoç, H. Lee, and Y.S. Kang, "Processing, structure, properties, and applications of PZT thin films," Critical reviews in solid state and materials sciences, **32**(3-4), 111-202 (2007). https://doi.org/10.1080/10408430701707347

[21] M. Afrooz, H. Dehghani, S.S. Khalili, and N. Firoozi, "Effects of cobalt ion doped in the ZnS passivation layer on the TiO$_2$ photoanode in dye sensitized solar cells based on different counter electrodes," Synthetic Metals, **226**, 164-170 (2017). https://doi.org/10.1016/j.synthmet.2017.02.012

[22] Y. Liu, J. Hua, K. Zhang, J. Zhao, and H. Li, "Effect of MgO shell on electron transfer from Cu doped ZnInS quantum dots to FePt nanoparticles.," Materials Research Bulletin, **103**, 242-246 (2018). https://doi.org/10.1016/j.synthmet.2017.02.012

[23] H.S. Al-Rikabi, M.H. Al-Timimi, and W.H. Albanda, "Morphological and optical properties of MgO$_{1-x}$ZnS$_x$ thin films," Digest Journal of Nanomaterials and Biostructures, **17**(3), (2022). https://doi.org/10.15251/DJNB.2022.173.889

[24] V.S.G.Krishna, S.R. Maidur, P.S. Patil, and M.G. Mahesha, "Role of copper dopant in two-photon absorption and nonlinear optical properties of sprayed ZnS thin films for optical limiting applications," Physics Letters A, **398**, 127276 (2021). https://doi.org/10.1016/j.physleta.2021.127276

[25] M. Ostadebrahim, and H. Dehghani, "ZnS/CdSe$_{0.2}$S$_{0.8}$/ZnSSe heterostructure as a novel and efficient photosensitizer for highly efficient quantum dot sensitized solar cells," Applied Surface Science, **545**, 148958 (2021). https://doi.org/10.1016/j.apsusc.2021.148958

[26] L. Ma, X. Ai, and X. Wu, "Effect of substrate and Zn doping on the structural, optical and electrical properties of CdS thin films prepared by CBD method," Journal of Alloys and Compounds, **691**, 399-406 (2017). https://doi.org/10.1016/j.jallcom.2016.08.298

[27] Z.M. Kakhaki, A.A. Youzbashi, P. Sangpour, N. Naderi, and Y. Orooji, "Influence of Cd salt concentration on the photoconductivity of CdS thin films prepared by chemical bath technique," Materials Science in Semiconductor Processing, **148**, 106773 (2022). https://doi.org/10.1016/j.mssp.2022.106773

[28] T.A. Wassner, B. Laumer, S. Maier, A. Laufer, B.K. Meyer, M. Stutzmann, and M. Eickhoff, "Optical properties and structural characteristics of ZnMgO grown by plasma assisted molecular beam epitaxy," Journal of Applied Physics, **105**(2), 023505 (2009). https://doi.org/10.1063/1.3065535

[29] I. Marozau, A. Shkabko, M. Döbeli, T. Lippert, D. Logvinovich, M. Mallepell, *et al.,* "Optical properties of nitrogen-substituted strontium titanate thin films prepared by pulsed laser deposition," Materials, **2**(3), 1388-1401 (2009). https://doi.org/10.3390/ma2031388

[30] R Bairy, and K.N. Narasimhamurthy, "Effect of annealing temperature on optimizing the structural, linear–nonlinear optical properties of Cd$_{1-x}$Zn$_x$S nanocrystalline thin films," Optical and Quantum Electronics, **53**(10), 579 (2021). https://doi.org/10.1007/s11082-021-03215-0

[31] R. Suganya, A. Revathi, D. Sudha, V. Sivaprakash, and E.R. Kumar, "Evaluation of structural, optical properties and photocatalytic activity of Ag$_2$O coated ZnO nanoparticles," Journal of Materials Science: Materials in Electronics, **33**(29), 23224-23235 (2022). https://doi.org/10.1007/s10854-022-09086-9

[32] S. Yasmeen, F. Iqbal, T. Munawar, M.A. Nawaz, M. Asghar, and A. Hussain, "Synthesis, structural and optical analysis of surfactant assisted ZnO–NiO nanocomposites prepared by homogeneous precipitation method," Ceramics International, **45**(14), 17859-17873 (2019). https://doi.org/10.1016/j.ceramint.2019.06.001

[33] M.H. Saeed, M.H. Al-Timimi, and O.A.A. Hussein, "Structural, morphological and optical characterization of nanocrystalline WO$_3$ thin films," Digest Journal of Nanomaterials and Biostructures, **16**(2), 563-569 (2021). https://chalcogen.ro/563_SaeedMH.pdf

[34] H. Ghasemi, M.H. Mozaffari, and R. Moradian, "Effects of deposition time on structural and optical properties of ZnS and ZnS/Au thin films grown by thermal evaporation," Physica B: Condensed Matter, **627**, 413616 (2022). https://doi.org/10.1016/j.physb.2021.413616

[35] H. Ali, A. Falak, M.A. Rafiq, U. Khan, S. Karim, A., Nairan, *et al.,* "Temperature dependent dielectric and electric modulus properties of ZnS nano particles," Semiconductor Science and Technology, **32**(3), 035008 (2017). https://doi.org/10.1088/1361-6641/aa539c

[36] W.D. Park, "Optical constants and dispersion parameters of CdS thin film prepared by chemical bath deposition," Transactions on Electrical and Electronic Materials, **13**(4), 196-199 (2012). https://doi.org/10.4313/TEEM.2012.13.4.196

[37] J. Tauc, R. Grigorovici, and A. Vancu, "Optical properties and electronic structure of amorphous germanium," Physica Status Solidi (b), **15**(2), 627-637 (1966). https://doi.org/10.1002/pssb.19660150224

ВПЛИВ ZnS ТА CdS НА ДЕЯКІ ФІЗИЧНІ ВЛАСТИВОСТІ ПЛІВОК MgO

Н.А. Хассан[a], В.Х. Альбанда[b], М.Х. Аль-Тімімі[a]
[a]Факультет фізики, Науковий коледж, Університет Діяла, Ірак
[b]Науковий відділ – Коледж базової освіти, Університет Мустансірія, Ірак

У цій статті повідомляється про виготовлення та характеристику наноструктурованих плівок MgO та вплив ZnS і CdS на їхні структурні, оптичні та електричні властивості. Тонкі плівки MgO, MgO: ZnS і MgO: CdS були нанесені за допомогою техніки піролізу хімічним розпиленням. на скляні підкладки при 673 К. Рентгенограми показали, що тонкі плівки MgO мають переважну (111) орієнтацію з чистою кубічною кристалічною структурою, тоді як шари ZnS і CdS мають гексагональну структуру. Зображення FE-SEM показали, що плівки MgO мають наноструктуровану морфологію із середнім розміром частинок ~50 нм. Результати УФ-видимої спектроскопії показали, що додавання шарів ZnS і CdS до плівок MgO призвело до зміщення краю поглинання у бік видимої області електромагнітного спектру, що вказує на покращення їх оптичних властивостей. Ці знахідки свідчать про те, що плівки MgOZnS і MgOCdS можуть мати потенційне застосування в оптоелектронних пристроях.
Ключові слова: *плівки MgO; допінг ефект; ZnS; CdS; хімічний розпилювальний піроліз; фізичні властивості*

A SURFACE STUDY OF Si DOPED SIMULTANEOUSLY WITH Ga AND Sb[†]

X.M. Iliyev, Sobir B. Isamov, Bobir O. Isakov*, U.X. Qurbonova, S.A. Abduraxmonov

Tashkent state technical university, Uzbekistan, 100095, Tashkent, University St., 2.
Corresponding Author e-mail: bobir6422isakov@gmail.com
Received April 29, 2023; revised June 13, 2023; accepted June 14, 2023

The paper is concerned with the study of silicon samples doped with gallium (Ga) and antimony (Sb) atoms. In particular, the elemental analysis, SEM imaging, and Raman spectrometry analysis of the samples are presented. The elemental analysis revealed that the relative concentrations of Ga (0.4) were almost equal to those of Sb (0.39) and both were formed on the surface of Si. The SEM imaging showed that GaSb microsized islands (diameter of 1 to 15 microns) and a density of ~10^6 cm^{-2} were being formed on the surface of Si in the course of the process of diffusion doping. Raman spectral analysis showed that a semiconductor with GaSb molecules self-assemble on Si surface.

Keywords: *Silicon; Gallium; Antimony; Doped; Diffusion; Microsized islands*
PACS: 61.72.uf, 68.43.Jk

INTRODUCTION

Presently, because of such fundamental parameters as high mobility, direct band-band transitions, relatively narrow band gap, the future of *III-Sb* type binary composite semiconductors seems to be promising in the years ahead [1-3]. In electronics and optoelectronics, of greater interest is the possibility to process new materials that are relatively inexpensive in terms of manufacture, and key physical parameters of which are in stark contrast to those of existing semiconductor materials [4–5]. As [6–7] evidenced, thin layers of *GaSb* on various substrates were obtained by using the modern method of molecular beam epitaxy (MBE), and their properties were studied using Raman spectroscopy [8]. The possibility of manufacturing high-frequency electronic devices [9-10] and the possibility of obtaining infrared sensors were shown in [11-13].

Meanwhile, the implementation of such complex technological processes requires the availability of modern and very expensive MBE devices [14]. The diffusion technology we are proposing herewith is comparatively cheap, optimally developed and mastered by our specialists in laboratory conditions. In the present experiment, the silicon (Si) samples diffusional doped with gallium (Ga) and antimony (Sb) atoms, were studied on SEM imaging (SEM EVO MA) and by Raman spectral analysis (Senterra II brand), all studies having been performed at room temperature (T =300 °K).

The lattice constants of silicon (Si) and gallium antimonide (GaSb) are 5.34 Å and 6.1 Å, respectively, and their lattice constant's mismatche accounts ~12%.

MATERIALS AND METHODS

Single-crystal *n*-type silicon samples *($\rho = 1\Omega \cdot cm$, n~$5 \cdot 10^{15}$ cm^{-3})* grown by the Czochralski method were chosen as objects for the study. Before launching the diffusion process, surfaces of the samples were kept in hydrofluoric acid (HF) for 1–2 min and degreased in the standard way. The diffusion process was carried out in a vacuum tube furnace for Laboratory Material Burning type *AOT-GLS-1750X*. The diffusion process was launched starting from room temperature T=30°C to temperature T=1200°C and continued for t=5 hours at this temperature in the gas-phase medium of impurity atoms. After diffusion, the samples were divided into two groups: the First Group (I): GaSb:Si; The Second Group (II): reference Si samples.

Group I - Ga and Sb atoms were doped into silicon samples simultaneously (Si sample, Ga and Sb impurities were all placed into one quartz ampoule).

Group II – reference Si samples without impurities were heated for comparative analysis under the same thermodynamic conditions.

RESULTS AND DISCUSSION
SEM- and EDS analysis

As can be seen from Fig. 1a, white spots of somewhat irregular shape must have formed on the surface of the sample (group I), while there are no such spots on the surface of the sample (group II) (see Fig. 1b). On Fig. 1 the analyzes of elemental compositions of 3 spectra (spectra 11, 12 and 13) are shown. Regarding the 11th spectrum – the elemental analysis was obtained for the area outlined by white circumference transparent on Figure 1-a (Figure 1-c). The elements Si, Ga, Sb, O, and C were determined in the 11th spectrum and their conditional concentrations were calculated as 0.9, 0.08, 0.04, 0.03, and 0.02, respectively. The elemental composition of the spot where white islands are

not being formed are represented on 12th-spectrum of Figure 1-a (Figure 2-a). In 12th spectrum, only the element Si was found, its conditional concentration was calculated as 1.16. The elemental composition of one of the white islands in the 13th spectrum (in Fig. 1-a) was determined (Fig. 2-b). The elements Si, Ga, Sb and O were identified on spectrum 13 and their conditional concentrations were calculated as 0.02, 0.4, 0.39 and 0.06 respectively.
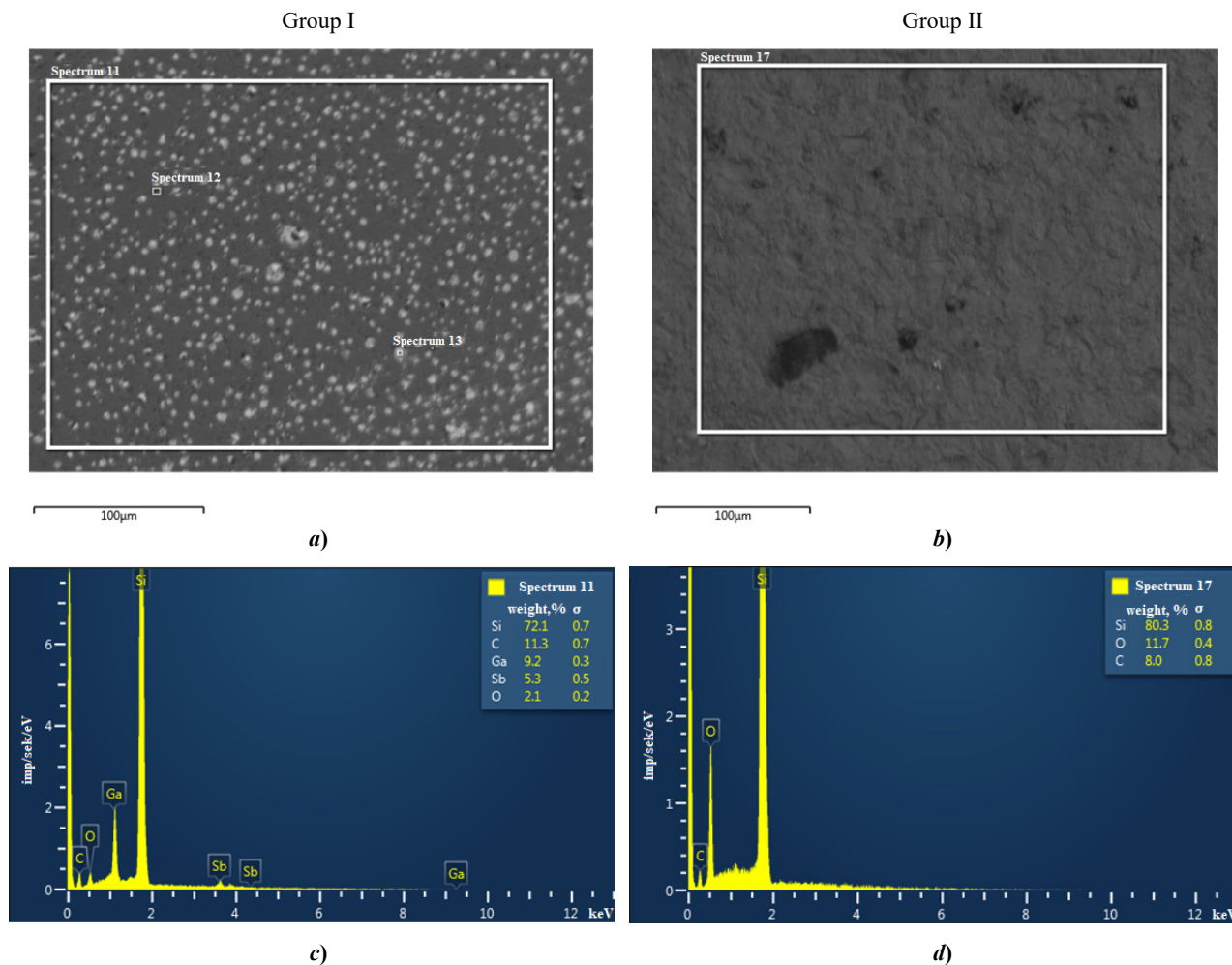
The elemental composition of the area circled by the white line on the surface of the sample of group II was determined (see Fig. 1b) (spectrum 17 in Fig. 1d). The elements Si, O and C were identified in spectrum 17 and their conditional concentrations were calculated as 0.97, 0.16 and 0.01 respectively.

Figure 1. SEM analysis of investigated samples after diffusion; a) SEM imaging of the surface of the I-group sample; b) SEM imaging of the surface of a sample of group II; c) elemental analysis of the surface of a sample of group I; d) elemental analysis of the surface of a sample of group II
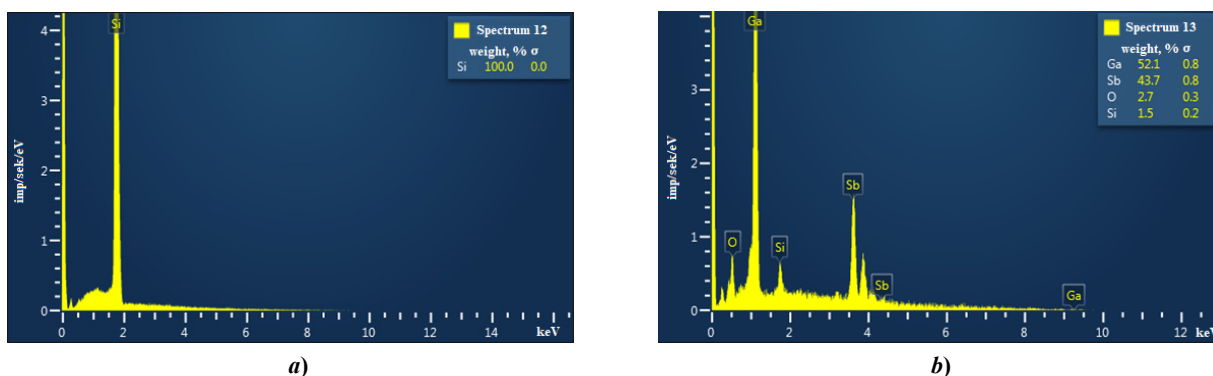
Figure 2. Elemental analysis obtained at local spots on the surface of a group I sample; a) elemental analysis of spectrum 12 in Fig. 1-a); b) Elemental analysis of spectrum 13 in Fig. 1a)

The islands formed on the surface of a I-group sample contain the elements Ga, Sb, O, and Si, which is due to the fact that the conditional concentrations of the elements of Ga and Sb in the islands (0.4 and 0.39, respectively) are

almost the same and significantly exceed the conditional concentrations of elements O and Si. These islands could be regarded as composite *GaSb* semiconductor islands. It can be assumed that O and Si elements found in the formed GaSb islands must have diffused from adjacent genuine Si material into the alien GaSb island (Fig. 2b, Table 1). In addition, it was revealed that the resulting GaSb semiconductor islands serve as attractors for O atoms on the Si surface (Table 1: spectra 11, 12, 13).

Table 1. Results of elemental analysis of samples of groups I and II

Element	Line type	Conditional concentration	Weight.%	Sigma Weight. %
11-spectr				
C	K series	0.02	11.34	0.69
O	K series	0.03	2.12	0.24
Si	K series	0.90	72.12	0.74
Ga	L series	0.08	9.16	0.29
Sb	L series	0.04	5.26	0.50
Sum:			100.00	
12-spectr				
Si	K series	1.16	100.00	0.00
Sum:			100.00	
13-spectr				
O	K series	0.06	2.67	0.26
Si	K series	0.02	1.48	0.19
Ga	L series	0.40	52.14	0.82
Sb	L series	0.39	43.72	0.85
Sum:			100.00	
17-spectr				
C	K series	0.01	7.97	0.79
O	K series	0.16	11.71	0.39
Si	K series	0.97	80.32	0.78
Sum:			**100.00**	

Figure 3 shows the SEM image of the surface of a sample from group I. The Figure shows that islands of GaSb semiconductor compound with a diameter of 1 μm to 15 μm are formed on the Si surface. The density of these microscopic islands, calculated judging from Fig. 3 is approximately 10^6 см$^{-2}$.
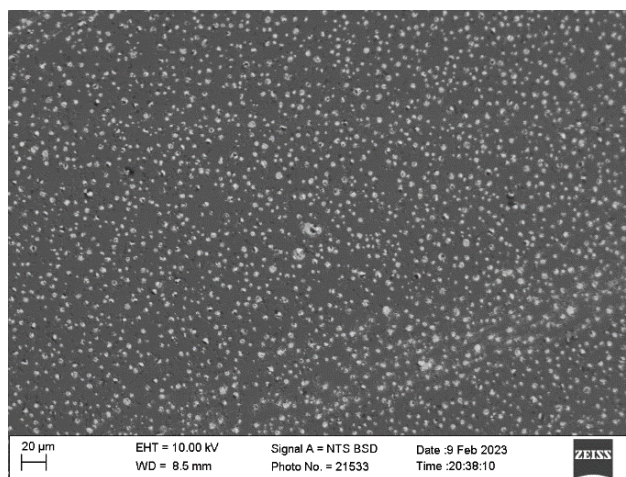
Figure 3. SEM imaging results of the surface of a sample of group I

Raman spectrometry

Raman spectroscopy is the standard method for studying lattice vibrations and their interaction with other induced oscillations. In Raman spectroscopy, only samples of group I were studied, i.e., Si samples doped with Ga and Sb atoms by the diffusion method (Fig. 4). It is known from the literature that the 520 cm^{-1} mode in the vibrational spectrum corresponds to the Si-Si bond [15], whereas 226 cm^{-1} and 220 cm^{-1} modes correspond to the Ga-Sb compounds, respectively, in the LO and TO modes [16].

On Fig. 4-a) one can see that the fundamental mode was observed at 519 cm^{-1}, which is confirmed by the literature [15] and corresponds to the vibration frequency of a Si-Si-type bond. As can be seen from Fig. 4b), the main

peak was observed at vibration frequency of 224.5 cm⁻¹, which is confirmed by the literature data [16], that this peak belongs to the vibration frequency of LO mode of the Ga-Sb compound.
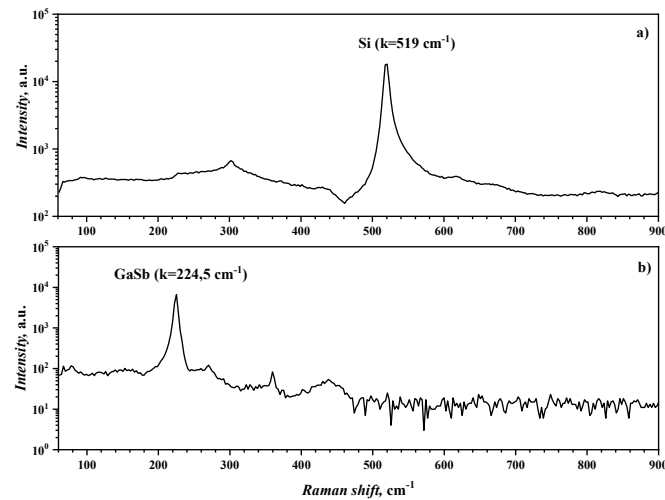
Figure 4. Spectral analysis of Raman spectra of the surface of samples of group I;
a) spectral analysis of the Raman spectrum 12 in Figs. 1-a); b) Spectral analysis of
Raman spectrum 13 in Figure 1a).

CONCLUSION

That the GaSb-type composite semiconductor probably forms on the surface of a Si sample doped with Ga and Sb atoms by diffusion doping, was confirmed by elemental analysis, SEM imaging, and Raman spectral analysis. The results of the experiment showed the possibility of engineering a novel crystal containing GaSb on the Si surface using a comparatively cheap and conventional diffusion technology. The obtained experimental results show that Si containing GaSb islands can be used as the main material in the development of infrared detectors, infrared lasers, infrared LEDs, high-speed electronic devices (for example: transistors) and high-efficiency solar panels.

ORCID
Sobir B. Isamov, https://orcid.org/0000-0001-5669-9306; **Bobir O. Isakov,** https://orcid.org/0000-0002-6072-3695

REFERENCES
[1] M. Niehle, J.-B. Rodriguez, L. Cerutti, E. Tournie, and A. Trampert, "On the origin of threading dislocations during epitaxial growth of III-Sb on Si(001): A comprehensive transmission electron tomography and microscopy study," Acta Materialia, **143**, 121-129 (2018). https://doi.org/10.1016/j.actamat.2017.09.055
[2] M.A. Boshart, A.A. Bailes III, and L.E. Seiberling, "Site Exchange of Ge and Sb on Si(100) during Surfactant-Mediated Epitaxial Growth," Physical review letters, **77**(6), 1087-1090 (1996). https://doi.org/10.1103/PhysRevLett.77.1087
[3] J. Liu, M. Tang, H. Deng, S. Shutts, L. Wang, P.M. Smowton, C. Jin, et al., "Theoretical analysis and modelling of degradation for III–V lasers on Si," Journal of Physics D: Applied Physics, **55**, 404006 (2022). https://doi.org/10.1088/1361-6463/ac83d3
[4] M.K. Bakhadyrkhanov, Z.T. Kenzhaev, S.V. Koveshnikov, A.A. Usmonov, and G.Kh. Mavlonov, "Formation of Complexes of Phosphorus and Boron Impurity Atoms in Silicon," Inorganic Materials, **58**(1). 3-9 (2022). https://doi.org/10.1134/S0020168522010034
[5] H. Wagner, T. Ohrdes,, A. Dastgheib-Shirazi,, B. Puthen-Veettil,, D. Konig,, and P.P. Altermatt, "A numerical simulation study of gallium phosphide/silicon heterojunction passivated emitter and rear solar cells," J. Appl. Phys. Jpn. **115**(4), 044508 (2014). https://doi.org/10.1063/1.4863464
[6] S.V. Ivanov, P.D. Altukhov, T.S. Argunova, A.A. Bakun, A.A. Budza, V.V. Chaldyshev, Yu.A. Kovalenko, et al., "Molecular beam epitaxy growth and characterization of thin (< 2 pm) GaSb layers on GaAs(l00) substrates," Semlcond. Sci. Technol. **8**, 347-356 (1993). https://doi.org/10.1088/0268-1242/8/3/008
[7] H. Ito, and T. Ishibashi, "Gas source MBE growth of GaSb," Japanese Journal of Applied Physics, **27**(8), 1554-1555 (1988). https://doi.org/10.1143/JJAP.27.1554
[8] Y.K. Su, K.J. Gan, J.S. Hwang, and S.L. Tyan, "Raman spectra of Si-implanted GaSb," Journal of Applied Physics, **68**, 5584 (1990). https://doi.org/10.1063/1.346994
[9] P.K. Asthana, "High performance 20 nm GaSb/InAs junctionless tunnel field effect transistor for low power supply," Journal of Semiconductors, **36**(2), 024003 (2015). https://doi.org/10.1088/1674-4926/36/2/024003
[10] Y. Goswami, P. Asthana, and B. Ghosh, "Nanoscale III–V on Si-based junctionless tunnel transistor for EHF band applications," Journal of Semiconductors, **38**(5) 054002 (2017). https://doi.org/10.1088/1674-4926/38/5/054002
[11] X.-Y. Xu, J.-K. Jiang, W.-Q. Chen, S.-N. Cui, W.-G. Zhou, N. Li, F.-R. Chang, et al., "Wet etching and passivation of GaSb-based very long wavelength infrared detectors," Chinese Physics B, **31**(6) 068503 (2022). https://doi.org/10.1088/1674-1056/ac4cc1

[12] H.J. Lee, S.Y. Ko, Y.H. Kim, and J. Nah, "Strain-induced the dark current characteristics in InAs/GaSb type-II superlattice for mid-wave detector," Journal of Semiconductors, **41**, 062302 (2020). https://doi.org/10.1088/1674-4926/41/6/062302

[13] J. Liu, H. Zhu, H. Zhu, M. Li, Y. Huai, Z. Liu, and Y. Huang, "Long-wavelength InAs/GaSb superlattice double heterojunction infrared detectors using InPSb/InAs superlattice hole barrier," Semiconductor Science and Technology, **37**, 055016 (2022). https://doi.org/10.1088/1361-6641/ac62f9

[14] M.K. Bakhadyrkhanov, Kh.M. Iliev, K.S. Ayupov, B.A. Abdurakhmonov, P.Yu. Krivenko, and R.L. Kholmukhamedov, "Self-Organization of Nickel Atoms in Silicon," Inorganic Materials, **47**(9), 962-964 (2011). https://doi.org/10.1134/S0020168511090020

[15] K. Ajito, J.P.H. Sukamto, L.A. Nagahara, K. Hashimoto, and A. Fujishima, "Strain imaging analysis of Si using Raman microscopy," Journal of Vacuum Science & Technology A, **13**, 1234-1238 (1995). https://doi.org/10.1116/1.579867

[16] Y.K. Su, K.J. Gan, J.S. Hwang, and S.L. Tyan, "Raman spectra of Si-implanted GaSb," Journal of Applied Physics, **68,** 5584-5587 (1990). https://doi.org/10.1063/1.346994

ДОСЛІДЖЕННЯ ПОВЕРХНІ Si, ЛЕГОВАНОГО ОДНОЧАСНО Ga ТА Sb
Х.М. Ілієв, Собір Б. Ісамов, Бобір О. Ісаков, У.Х. Курбонова, С.А. Абдурахмонов
Ташкентський державний технічний університет, вул. Університетська, 2, 100095, м. Ташкент, Узбекистан
Стаття присвячена дослідженню зразків кремнію, легованих атомами галію (Ga) і сурми (Sb). Зокрема, представлено елементний аналіз, SEM зображення та спектрометричний аналіз зразків за допомогою комбінаційного розсіювання. Елементний аналіз показав, що відносні концентрації Ga (0,4) майже дорівнюють концентраціям Sb (0,39), і обидва утворилися на поверхні Si. SEM-зображення показало, що в процесі дифузійного легування на поверхні кремнію утворюються острівці мікророзміру GaSb (діаметром від 1 до 15 мікрон) і щільністю ~106 см$^{-2}$. Раманівський спектральний аналіз показав, що напівпровідник із молекулами GaSb самозбирається на поверхні Si.
Ключові слова: *кремній; галій; сурма; легування; дифузія; острови мікророзміру*

OPTICAL AND MAGNETIC RESPONSE OF PURE AND Cu-IONS SUBSTITUTED DYSPROSIUM OXIDE THIN FILMS FOR VARIOUS APPLICATIONS[†]

🟢**Muhammad Tauseef Qureshi***

Basic Science Department, College of Preparatory Year, University of Ha'il, 1560 Ha'il, Kingdom of Saudi Arabia
Corresponding author e-mail: tauseefqureshi1981@gmail.com

Dysprosium oxide (Dy_2O_3) and Cu/Dy_2O_3 thin films of thickness 117.14 nm and 258.30 nm, respectively were successfully deposited via a well-known DC-magnetron sputtering technique. Field emission scanning electron microscopy clarifies the growth of uniform and fine granular particles on silicon substrate. The hexagonal closed pack structure for both the thin films has been observed by the x-ray diffraction analysis and it was observed that by inclusion of copper the HCP structure of thin film was retain with a slight shift in the main peak. The reduction from 3.9 eV to 3.8 eV in the energy band gap value was observed by incorporation of copper ions Dy_2O_3 thin films. The M-H loops obtained through Vibrating Sample Magnetometer (VSM) shows that Dy_2O_3 thin film behave ferromagnetically at low temperature with a saturation magnetization value of 2860 emu/cc and evolves through its phase transition temperatures and behave paramagnetically at room temperature. In Cu/Dy_2O_3 case, the diamagnetic response of Cu dominates and produces reverse hysteresis loop at both temperatures make it a suitable candidate for energy and memory storage devices applications.

Keywords: *Magnetron sputtering; Dy_2O_3; Cu/Dy_2O_3; Thin films; Tauc plot; Magnetic properties; Hysteresis loop*
PACS: 07.55.Jg, 61.10.Nz, 68.37.Hk, 74.25.Gz, 75.20.−g, 75.70.Ak, 81.20.−n

INTRODUCTION

During the last few years, several attempts have been made to improve the properties of rare-earth thin films by employing different methods. Successful approaches were to reduce their anisotropy different rare-earths were alloyed [1]; to include the tensile film stress [2], the preparation conditions were adjusted; to change the amorphous state of the films, small amount of Boron was added [3-4]. Among the rare-earth metals, Dy is considered as a possible solenoid pole piece material which is a suitable candidate for ultra-high moment applications at low temperatures [5-7]. The bulk Dy was considered as a pole material for field concentrators [8] and undulators [9], its tips for magnetic resonant force microscopy which can be used in pulsed-laser deposition, molecules beam epitaxy or plasma sputtering for its high yield and scalability [10]. Brilliant magneto-optical properties are resulted in the case of Copper (Cu) mixed with Manganese (Mn) for example, being Cu as optical and Mn as magnetic material [11]. The value of magnetic anisotropy of Dy is very large which when coupled with transition metals (Fe, Co, Ni, Cu) [12-14] and other ferromagnetic rare earths (Er, Ho, Gd) [15-20], much attention has been paid to DyFeCo [21], FeNdDyB [22] and FeDyTb alloys [23]. The slight structural changes incorporated because of guest molecules exchange, produce different dipole−dipole interactions which then effect the relaxation rate of incoherent quantum tunneling to acquire different effective relaxation barriers [24]. In this case, the structure of the near surface region of this phase becomes distorted; this leads to the nucleation of reverse magnetization domains to an experimentally observed decrease in H_{ci} [25].

Different properties of thin films are achieved by varying the production procedures as well as on the parameters of deposition, like deposition rate, temperature control, variation of substrate etc. In recent times, various physical and chemical deposition techniques are utilized for the processing of ZnO thin films, which includes but may not be restricted to, chemical vapor deposition (CVD), sputtering techniques, plasma enhanced CVD, sol–gel process and pulsed laser deposition (PLD) [26]. Among these growth techniques magnetron sputtering has a lot of advantages such as its low cost, low thermal budget, simplicity, non-toxic and for desired properties, its ability to produce high quality thin films [27]. Sezen et al studied the optical properties of Dy_2O_3 and recorded the band gap of 3.90 eV through ab-initio calculations to give way for the experimental growth of these thin film in combination with different metal content such Cu, Cr etc. [28]. The current study, we report the deposition of a high purity Dy_2O_3 and Cu/Dy_2O_3 thin films by DC magnetron sputtering on silicon substrate at room temperature. Further, the structural, morphology, optical and magnetic properties of these thin films Dy_2O_3 and Cu/Dy_2O_3 are investigated for energy and memory storge devices applications.

EXPERIMENTAL DETAILS
Sample Preparation

Dy_2O_3 and Cu/Dy_2O_3 thin films were fabricated via well-known sputtering technique using magnetron sputtering (DaON 1000 S) system contains three sputtering guns, one for Radio Frequency (RF) and two Direct Current (DC) supply [29-30]. The silicon substrate was used for the deposition of Dy and Cu and the temperature of it was kept up to 300°C. Initially, for achieving the clear and content free environment inside the chamber; high vacuum with base pressure of 5×10^{-6} Torr was achieved in 30 minutes before starting the deposition process. The Oxygen and Argon (70:30) flow were

kept, but the flow rate was adjusted upto 5 mTorr. In the doping of Cu(10%) was controlled and calibrated by using STM (Sycon Thickness Monitor). The deposition of these films was carried out through DC sputtering keeping 300V and 100mA for Dy and 250V and 40mA for Cu respectively. Finally, thin films having thickness 117.14 nm & 258.30 nm for Dy_2O_3 and Cu/Dy_2O_3 respectively were collected after cooling the chamber to room temperature to avoid the deposited thin film from cracking down.

Sample Characterizations

The structure and crystallinity of the films were determined by an XRD (X'Pert) operating at 30 kV and 10 mA using Cu $K_{\alpha l}$ radiation (1.54 Å). The measurement was conducted at room temperature with $2\theta = 20^0$-70^0 incident angles. For morphological study of these thin films FESEM (FEI Nova 450) was used. The operating power of the FEI Nova 450 was 10 kV and 50kV respectively. The microscope was in the secondary electron mode at a working distance of 5.1 mm with lens detector. EDX spectrometry (Oxford Instruments Inca X-Act) built in with FEI Nova 450, was used for qualitative and quantitative compositions analysis of elements. Spectroscopic Ellipsometry (Alpha-SE Ellipsometer, J. A. Woollam) was used to get the thickness of thin films and absorption coefficient of thin films. Hysteresis loop for magnetization of the Dy_2O_3 and Cu/Dy_2O_3 thin films was obtained using a VSM (with low temperature 5K and at room temperature 300K) using Cryogen free measuring system (Cryogen Limited UK).

RESULTS AND DISCUSSION
Structural Analysis

Figure 1 shows crystallographic results i.e., XRD peaks and their miller indices of Dy_2O_3 and 10%-Cu substituted Dy_2O_3 thin films. For Dy_2O_3, two peaks are observed, one at 28.23^0 with miller indices (100) and other at 32.40^0 having Miller indices (101) as shown by Figure 1(a).
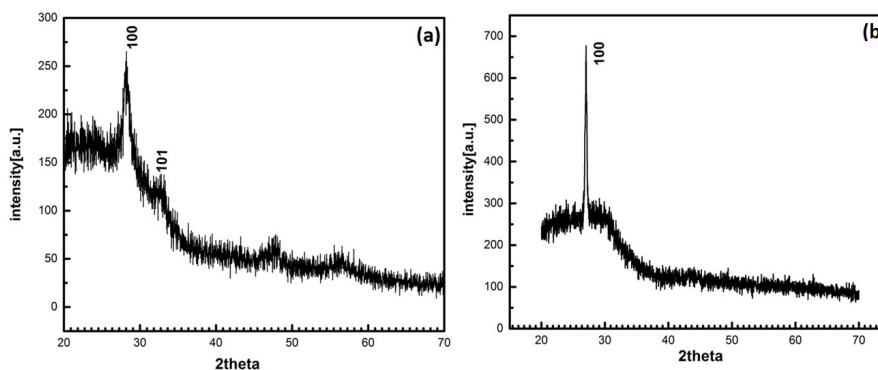
Figure 1. XRD pattern of (a) Dy_2O_3 and (b) Cu/Dy_2O_3 thin films

The comparison of Dy_2O_3 XRD data with the reference code 01-089-2926, confirm the hexagonal closed pack (hcp) structure and having space group P63/mmc and space number of 194. When 10%-Cu is co-deposited with Dy for the alloy thin film, only a single prominent, sharp peak has been observed, as in Figure 1(b). This peak is associated to Dy_2O_3, since having miller indices of (100) for 2θ value of 27.03.

It can be found that the presence of Cu has slightly adjusted the (100) peak to new 2θ value and no peak for Cu has been observed in the Cu/Dy_2O_3 thin film. It has been found for the case of Cu mixed ZnO thin films [31, 32] that the introduction of Cu adjusts the main peak of ZnO (002) to new values of 2θ and with no Cu peak. They have suggested that there is strong c-orientation preference with normal to the substrate and Cu atoms exist only on the interstitial sites. The same can be attributed in current scenario where Dy_2O_3 having close packing structure with maximum packing density does not allow Cu atoms to change/modify the base Dy_2O_3 structure, rather be present at the interstitial sites thus increasing the overall energy. Recalling the Cu standard pattern having reference No. 04-0836, there are three prominent peaks for copper, each at 43.30, 50.43 & 74.13 2θ values, but Figure 1(b) announces no peak (even smaller one) at the above-mentioned values for Cu.

Morphological studies and elemental analysis

FESEM micrographs of Dy_2O_3 and Cu/Dy_2O_3 thin films are shown in **figure 2(a-d)** (where a, b represents the Dy_2O_3 micrographs, and c, d show Cu/Dy_2O_3 images). It is clear from the micrographs of these thin films that growth of smooth and uniformly dispersed particles along with small grains on the silicon substrate, which can be due to the fact that both Dy_2O_3 and Cu/Dy_2O_3 are deposited simultaneously. Moreover, inclusion of Cu as dopant or co-dopant normally smoothens the ZnO thin film structure as can be found in many semiconductors' technologies-based materials [33].

The EDX spectra of pure and Cu substituted thin films were acquired by using 20 kV electron beam-energy are shown in Figure 3. The Cu, Dy and O intensities peaks in both thin films confirmed its high-purity and the presence of these acquired elements with their stoichiometric ratio. The table within figure 3 shows the wt% of each constituent elements with their stoichiometric-formulation.
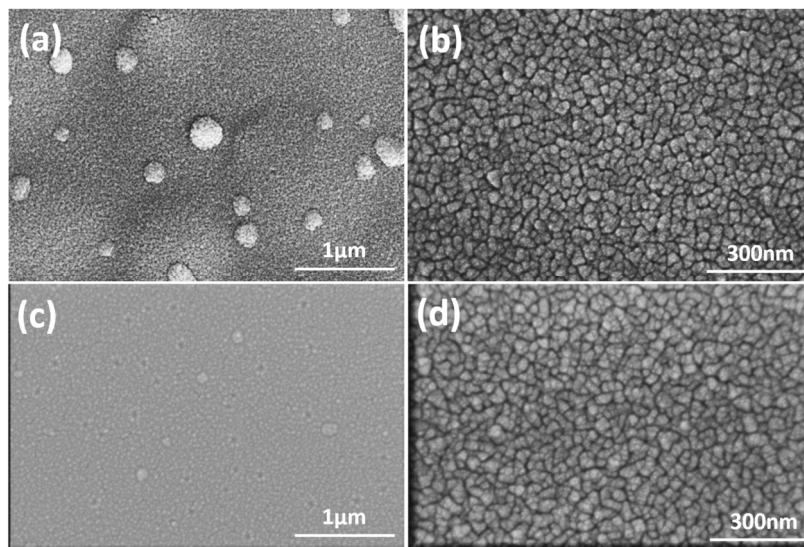
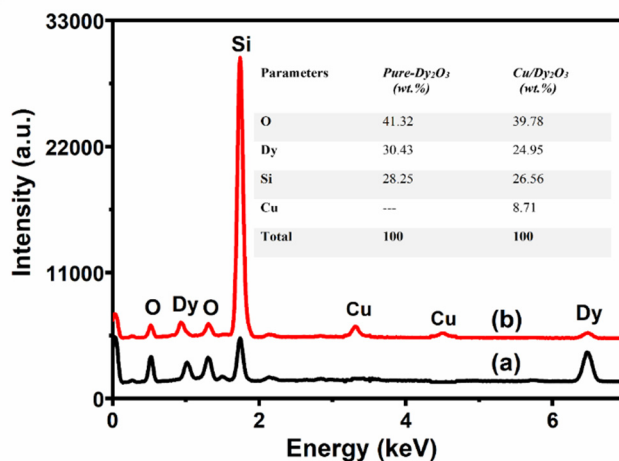**Figure 2.** FESEM micrographs at lower and higher magnification **(a, b)** Dy$_2$O$_3$, and **(c, d)** Cu/ Dy$_2$O$_3$ thin film

Figure 3: EDS spectra of thin films with their table of elements compositions wt.% where **(a)** shows Dy$_2$O$_3$ and **(b)** 10%-Cu doped Dy$_2$O$_3$ thin films compositions

Optical Studies

The absorption coefficient energy band gap curve obtained through ellipsometry and Tauc and Davis's plot respectively are shown in Figure 4.
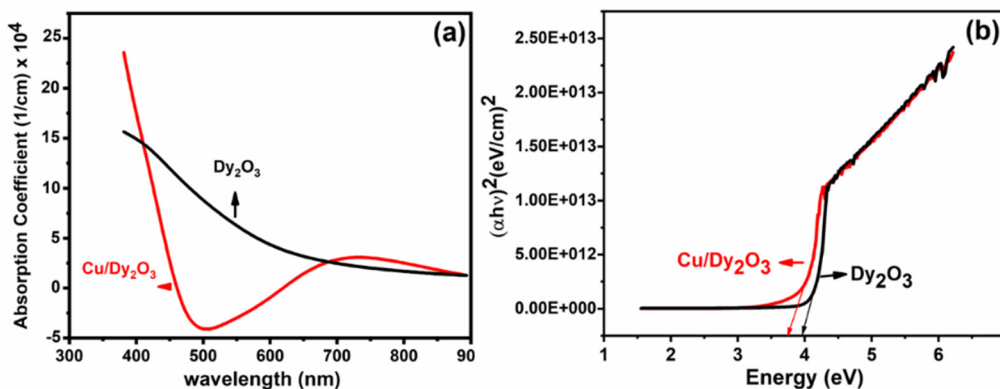

Figure 4: Optical properties measurement through ellipsometry **(a)** Absorption coeffient and **(b)** Energy band gap values for both thin films as plotted by the Tauc plot

The absorption coefficient value high at lower wavelength shows high value, but as the wavelength shifted towards the visible region that it decreases for both samples and finally a slight increase at the elevated wavelength as shown in

Figure 4(a). Which shows that these thin films are good observers at lower wavelength. Figure 4(b) represents the energy band gap value 3.8 eV for Dy_2O_3 and 3.9 eV for Cu/Dy_2O_3 thin films obtained from Tauc and Davis's plot in which the photon energy and absorption coefficient can be related in the absorbance region in a relation expressed as:

$$\alpha h v = A (h v - E_g)^n \qquad (1)$$

where "α" is the absorption coefficient, "hv" is photon energy, "A" is proportionality constant, "E_g" is optical band gap, "n" is an integer equal to 2 for an indirect and 1/2 for direct band gap in the above relation [34]. For the value of n=2 for Dy_2O_3 and Cu/Dy_2O_3 thin films, it states that an indirect band gap obtained for these structures. Similarly, energy band of Dy_2O_3 confirms the fact that valance shell electrons have the ability of absorbing energy, whereas value for second thin film Cu/Dy_2O_3 decrease which further enhances the chance for such materials to be used in electronic applications.

Magnetic Properties Studies

Figure 5 represents the magnetic hysteresis loops of Dy_2O_3 and Cu/Dy_2O_3 thin films at room temperature (300K) and low temperature 5K as presented in **figure 5**.
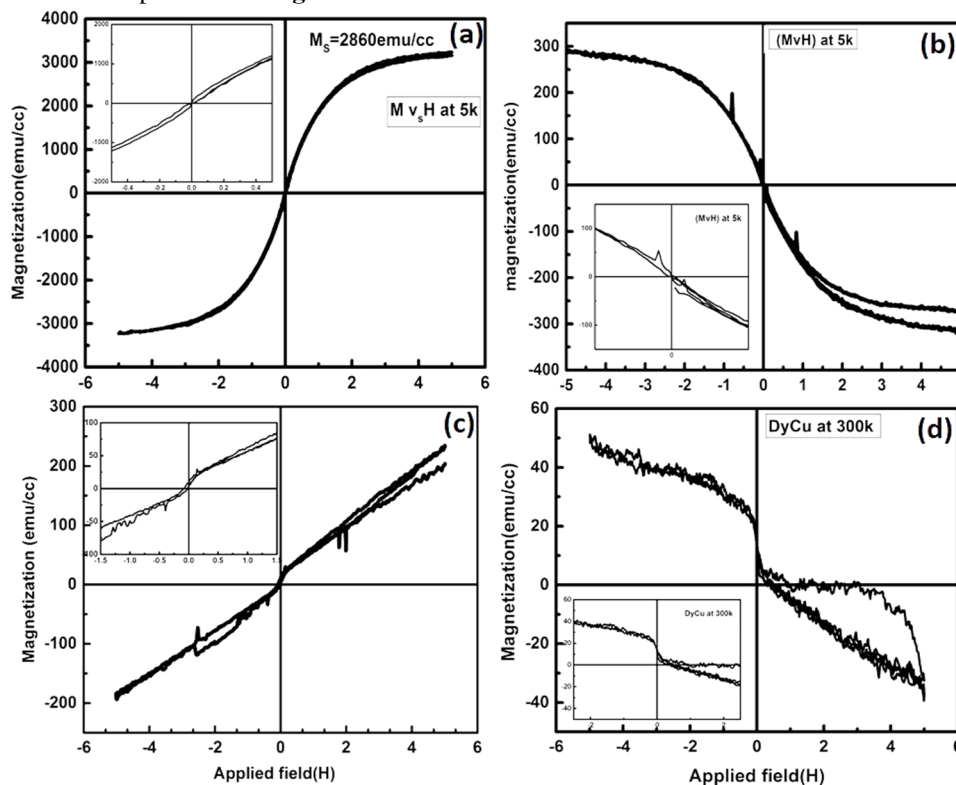
Figure 5. Shows M-H curves, here **(a)** presents Dy_2O_3 at 5k, **(b)** Cu/Dy_2O_3 at 300k, **(c)** Dy_2O_3 at 5k and **(d)** Cu/Dy_2O_3 at 300k, respectively

The ferromagnetic order in case of Dy_2O_3 at 5 K has been observed, since it behavior evaluates into anti-ferromagnetic ordering at above 85 K and further to paramagnetic nature at and above 179 K. The M_s value obtained for Dy_2O_3 thin film at low temperature is 2860 emu/cc. The inset of Figure 5(a) shows that the magnetization lines pass through the origin, announcing no remanent magnetization [35], a response typically related to pure ferromagnetic materials. Moreover, when magnetization for Dy_2O_3 thin film is measured at room temperature (Figure 5(c)), a paramagnetic type of behavior is observed, with much reduced saturation magnetization value and obviously no remanent magnetization as in the inset of this graph (Figure 5(c)).

A completely different response of the Cu/Dy_2O_3 thin film has been observed both at low and room temperature, with production of reverse hysteresis loop due to inclusion of Cu with Dy. The energy difference between the lowest doubly degenerate sublevels (formally corresponding to large J_z values of $\pm 11/2$ or $\pm 13/2$ for dysprosium) seems to be affected by the degree of longitudinal compression or elongation [36-37]. This behavior of the Cu/Dy_2O_3 thin film can be due to the effect of Cu diamagnetic nature, which drives Dy to behave diamagnetically and pronounces a small magnetization value. The difference above may be linked with the different local symmetry and the bond distances result in different ligand fields [38]. The behavior of Cu/Dy_2O_3 thin film has also the support of XRD data as presented above, with Cu atoms present at the interstitial sites, not affecting the structure, rather other physical properties of the thin film. For the case of Dy_2O_3 Figure 5(c) it is clear that dysprosium thin film transforms to paramagnetic nature with an improper saturation of the particles and a much-reduced saturation magnetization value. These results can be used for the tuning of magnetic properties of Dy based thin films for technological applications [15-20].

CONCLUSION

Thin films of Dy_2O_3 and Cu/Dy_2O_3 of thickness 17.14 nm and 258.30 nm respectively were prepared successfully by the magnetron sputtering method. It is suggested that Cu elements residing at the interstitial sites, not affecting the structure of the alloyed thin film, as confirmed by the XRD results but modify the other physical properties. Smooth behavior of the thin films is obtained by the FESEM micrographs along with no impurity shown by the elemental analysis through EDX. Further, by addition of Cu reveals a change in the optical properties, as well as diamagnetic response of the Cu compels Dy to produce negative hysteresis effect (by VSM) can be used for such material-based storage application.

ORCID

Muhammad Tauseef Qureshi, https://orcid.org/0000-0001-7388-8512

REFERENCES

[1] F. Schatz, M. Hirscher, G. Flik, and H. Kronmüller, Physica Status Solidi, **137**(1), 197 (1993). https://doi.org/10.1002/pssa.2211370117

[2] G. Flik, M. Schnell, F. Schatz, and M.B. Hirscher, in: *Proc. Actuator 94*, (Bremen, Germany, 1994), p. 232.

[3] J.Y. Kim, J. Appl. Phys. **74**, 2701 (1993). https://doi.org/10.1063/1.354664

[4] R. Jain, V. Luthra, and S. Gokhale, J. Mag. and Mag. Mater. **456**, 179 (2018). https://doi.org/10.1016/j.jmmm.2018.02.029

[5] H. Fernández-Morán, Physics, **53**, 445 (1965). https://doi.org/10.1073/pnas.53.2.445

[6] A. Paulson, N.M. Sabeer, and P.P. Pradyumnan, Mater. Sci. & Engi. B, **262**, 114745 (2020). https://doi.org/10.1016/j.mseb.2020.114745

[7] A. Bulatov, S. Goridov, M. Tikhonovskij, and S. Novikov, IEEE Trans. Mag. **28**, 509 (1992). https://doi.org/10.1109/20.119923

[8] R. Agustsson, P. Frigola, A. Murokh, O. Chubar, and V. Solovyov, in: *Proceedings of 2011 Particle Accelerator Conference*, (New York, USA, 2011). pp. 1256-1258.

[9] R. Agustsson, P. Frigola, A. Murokh, and V. Solovyov, in: *Proceedings of PAC09*, (Vancouver, Canada, 2009), WE5RFP077.

[10] Z.S. Shan, and D.J. Sellmyer, J. Appl. Phys. **64**, 5745 (1988). https://doi.org/10.1063/1.342245

[11] N.D. Subramanian, J. Moreno, J.J. Spivey, and C.S. Kumar, J. Phys. Chem. C, **115**, 14500 (2011). https://doi.org/10.1021/jp202215k

[12] Z.S. Shan, S. Nafis, K.D. Aylesworth, and D.J. Sellmyer, J. Appl. Phys. **63**, 3218 (1988).

[13] A.V. Trukhanov, K.A. Astapovich, V.A. Turchenko, M.A. Almessiere, Y. Slimani, A. Baykal, A.S.B. Sombra, *et al.*, J. Alloys Compounds, **841**, 155667 (2020). https://doi.org/10.1016/j.jallcom.2020.155667

[14] K. Dumesnil, C. Dufour, P. Mangin, G. Marchal, and H. Hennion, Phys. Rev. B, **54**, 6407 (1996). https://doi.org/10.1103/PhysRevB.54.6407

[15] K. Dumesnil, C. Dufour, P. Mangin, G. Marchal, and H. Hennion, Europhys. Let. **31**(1), 43 (1995). https://doi.org/10.1209/0295-5075/31/1/008

[16] M. Elisa, R. Stefan, I.C. Vasiliu, M.I. Rusu, B.A. Sava, L. Boroica, M. Sofronie, *et al.*, J. Non-cryst. Solids, **521**, 119545 (2019). https://doi.org/10.1016/j.jnoncrysol.2019.119545

[17] A.M. Henaish, O.M. Hemeda, E.A. Arrasheed, R.M. Shalaby, A.R. Ghazy, I.A. Weinstein, M.A. Darwish, *et al.*, J. Compos. Sci. **7**, 61 (2023). https://doi.org/10.3390/jcs7020061

[18] G. Ganesh, A. Sandeep, G. Chanti, R.S. Bose, M.S. Kumar, K.P. Kumari, T. Shekharam, *et al.*, Phys. Stat. solidi (a), **220**(9), 2200864 (2023). https://doi.org/10.1002/pssa.202200864

[19] G. Hussain, I. Ahmed, A.U. Rehman, M.U. Subhani, N. Morley, M. Akhtar, M.I. Arshad and H. Anwar, J. Alloys & Comp. **919**, 165743 (2022). https://doi.org/10.1016/j.jallcom.2022.165743

[20] T.H. Wu, J.C. Wu, B.M. Chen, and H.P.D. Shieh, J. Mag. Mag. Mater. **202**, 62 (1999). https://doi.org/10.1016/S0304-8853(99)00140-7

[21] S. Sugimoto, J. Phys. D: Appl. Phys. **44**, 064001 (2011). https://doi.org/10.1088/0022-3727/44/6/064001

[22] C.V. Mohan, and H. Kronmüller, J. Alloys Compounds, **267**, L9 (1998). https://doi.org/10.1016/S0925-8388(97)00524-0

[23] A.M. Tishin, and Y.I. Spichkin, *The Magnetocaloric Effect and its Applications*, (IOP Publishing Ltd., London, 2003).

[24] S. Zhang, K. Hongshan, S. Lin, L. Xin, S. Quan, X. Gang, W. Qing, *et al.*, Inorganic Chemistry, **55**, 3865 (2016). https://doi.org/10.1021/acs.inorgchem.5b02971

[25] V.P. Piskorskii, G.S. Burkhanov, O.G. Ospennikova, R.A. Valeev, I.S. Tereshina, and E.A. Davydova, Russian Metallurgy, 5, 442 (2010). https://doi.org/10.1134/S0036029510050150

[26] Y.S. Kim, H.J. Park, S.C. Mun, E. Jumaev, S.H. Hong, G. Song, J.T. Kim, *et al.*, Alloys & Comp. **797**, 834 (2019). https://doi.org/10.1016/j.jallcom.2019.05.043

[27] J. Kar, S. Kim, B. Shin, and J. Myong, Solid-State Electronics, **54**, 1447 (2010). https://doi.org/10.1016/j.sse.2010.07.002

[28] S. Horoz, S. Simsek, S. Palaz, A.M. Mamedov, E. Ozbay, International Journal of Scientific and Technological Research, **1**, 36 (2015). https://www.iiste.org/Journals/index.php/JSTR/article/view/23009/23526

[29] S.M. Ramay, A. Mahmood, H.M. Ghaithan, N.S. Al-Zayed, A. Aslam, A. Murtaza, N. Ahmad, *et al.*, J. Rare Earths, **37**, 989 (2019). https://doi.org/10.1016/j.jre.2018.12.002

[30] P. Salunkhe, M.A.V. Ali, and D. Kekuda, Mater. Res. Exp. **7**, 016427 (2020). https://doi.org/10.1088/2053-1591/ab69c5

[31] P.S. Shewale, V.B. Patil, S.W. Shin, J.H. Kim, and M.D. Uplane, Sens. Actuators B: Chem. **186**, 226 (2013). https://doi.org/10.1016/j.snb.2013.05.073

[32] X.B. Wang, D.M. Li, F. Zeng, and F. Pan, J. Phys. D: Appl. Phys. **38**, 4104 (2005). https://doi.org/10.1088/0022-3727/38/22/014

[33] H. Gonga, J.Q. Hua, J.H. Wang, C.H. Onga, F.R. Zhub, Sens. Actuators B: Chem. **115**, 247 (2006). https://doi.org/10.1016/j.snb.2005.09.008

[34] F.Y. Lo, Y.C. Ting, K.C. Chou, T.C. Hsieh, C.W. Ye, Y.Y. Hsu, M.Y. Chern, and H.L. Liu, J. Appl. Phys. **117**, 213911 (2015). https://doi.org/10.1063/1.4921979

[35] S.E. Harrison, L.J. Collins-McIntyre, S.L. Zhang, A.A. Baker, A.I. Figueroa, A.J. Kellock, A. Pushp, J. Phys. Condens. Matter. **27**, 245602 (2015). https://doi.org/10.1088/0953-8984/27/24/245602

[36] K. Niira, Phys. Rev. **117**, 129 (1960). https://doi.org/10.1103/PhysRev.117.129

[37] M. Morishita, T. Abe, H. Yamamoto, A. Nozaki, and S. Kimura, Thermoch. Act, **721**, 179410 (2023). https://doi.org/10.1016/j.tca.2022.179410

[38] L.I. Naumova, M.A. Milyaev, R.S. Zavornitsyn, T.P. Krinitsina, V.V. Proglyado, and V.V. Ustinov, Curr. Appl. Phys. **19**, 1252 (2019). https://doi.org/10.1016/j.cap.2019.08.012

[39] K.P. Belov, R.Z. Levitin, and S.A. Nikitin, Soviet Physics Uspekhi, **7**, 179 (1964). https://doi.org/10.1070/PU1964v007n02ABEH003660

ОПТИЧНИЙ ТА МАГНІТНИЙ ВІДГУК ЧИСТИХ ТА НАСИЧЕНИХ ІОНАМИ Cu ТОНКІХ ПЛІВОК ОКСИДУ ДИСПРОЗІЮ, ДЛЯ РІЗНИХ ЗАСТОСУВАНЬ

Мухаммад Таусеф Куреші
Факультет фундаментальних наук, Коледж підготовчого року, Університет Хаїль,
Хаїль, Королівство Саудівська Аравія

Тонкі плівки оксиду диспрозію (Dy_2O_3) і Cu/Dy_2O_3 товщиною 117,14 нм і 258,30 нм відповідно були успішно нанесені за допомогою добре відомого методу магнетронного напилення на постійному струмі. Автоемісійна скануюча електронна мікроскопія показала зростання однорідних і дрібних гранульованих частинок на кремнієвій підкладці. Гексагональна закрита структура пакування для обох тонких плівок спостерігалася за допомогою рентгенівського дифракційного аналізу, і було помічено, що завдяки включенню міді HCP-структура тонкої плівки зберігалася з невеликим зсувом головного піку. Зменшення ширини забороненої зони від 3,9 еВ до 3,8 еВ спостерігалося шляхом включення тонких плівок іонів міді Dy_2O_3. Петлі M-H, отримані за допомогою вібраційного магнітометра (VSM), показують, що тонка плівка Dy_2O_3 поводиться феромагнітно при низькій температурі зі значенням намагніченості насичення 2860 emu/cc і розвивається через температури фазового переходу та поводиться парамагнітно при кімнатній температурі. У випадку Cu/Dy_2O_3 діамагнітний відгук Cu домінує та створює петлю зворотного гістерезису при обох температурах, що робить його придатним кандидатом для додатків пристроїв зберігання енергії та пам'яті.

Ключові слова: *магнетронне розпилення; тонкі плівки; Dy_2O_3; Cu/Dy_2O_3; графік Таука; магнітні властивості; петля гістерезису*

STRUCTURAL AND OPTICAL PROPERTIES OF (ZnO/NiO) THIN FILMS MIXTURE[†]

Ali Amiar[a], Okba Belahssen[b], Mebrouk Ghougali[a], Mourad Mimouni[a], Ghani Rihia[a],
Mohammed Sadok Mahboub[a], Yamina Benkrima[c]

[a]LEVRES Laboratory, University of El Oued, B.P. 789, 39000 El Oued, Algeria
[b]Physics Laboratory of Thin Films and Applications (LPCMA), University of Biskra, B.P. 145 R.P 07000, Biskra, Algeria
[c]Ecole normale supérieure de Ouargla, 30000 Ouargla, Algeria
*Corresponding Author e-mail: b-amina1@hotmail.fr
Received May 10, 2023; revised June 8, 2023; accepted June 11, 2023

In this study, we prepared mixtures of nickel oxide (NiO) and zinc (ZnO) in different proportions as thin films on high-purity glass substrates, using pyrolysis spray technique. Where samples of mixtures were precipitated from two solutions of nickel nitrate $(Ni(NO_3)_2 \cdot 6H_2O)$ and zinc acetate $(C_4 H_6 O_4 Zn \cdot 2H_2O)$ mixed in different proportions. Then the optical and structural properties of the prepared samples were studied. The transmittance decreases with the increase in the percentage of nickel oxide, which means that increasing the zinc oxide improves the transmittance in all the studied spectral fields. Samples with higher zinc oxide (ZnO) have two energy gaps. Scanning electron microscopy (SEM) showed that the surface morphology of the films has a relatively homogeneous composition. Where it was observed that increasing the proportion of zinc oxide leads to the appearance of zinc oxide granules clearly.
Keywords: *Mixtures of NiO and ZnO; Thin films; Pyrolysis spray technology; Energy gap; Optical properties*
PACS: 73.20.At, 78.20.Ci

1. INTRODUCTION

ZnO and NiO thin films are among the most important films that have been scientifically and industrially exploited for their important applications in wide fields. Zinc oxide (ZnO) is a transparent n-type semiconductor with a wurtzite crystal structure. It has good potential in developing optoelectronic device technologies, mainly due to its outstanding physical properties, such as its high transparency in the visible spectrum and near infrared region [3, 4]. It has a bandgap ranging from (3.2-3.3) eV [5] and has a high binding energy [6, 7]. The outstanding optical and electrical properties of zinc oxide films have led to their use in many applications such as: solar cells [8, 9], gas sensors [10], piezoelectric sensors [11, 12], flat screens [13], acoustic devices [14], and optical waveguides [15], and laser diodes [16]. ZnO thin films can be produced by several techniques such as: spray pyrolysis [17, 18] hydrosol gel, thermal evaporation [19], and laser ablation (PLD) [20]. Nickel oxide (NiO) is a transparent p-type semiconductor that has a crystal structure (CFC) similar to that of sodium chloride (NaCl) and has a band gap between 3 and 4 eV [21].

Nickel oxide (NiO) is an attractive material due to its excellent chemical stability, good dynamic range and hardness, as well as its optical, electrical and magnetic properties [22]. Nickel oxide has important and extensive applications such as optical switching glass, antimagnetic materials, photoelectric display devices, lithium batteries, and functional layer materials for chemical gas sensors [23]. In addition, nickel oxide films oriented in the (111) direction can be used as dielectric layers that are deposited on oxide films of other orientations, such as C-oriented perovskite-type ferromagnetic films and superconducting films [00]. NiO films can be deposited using many different chemical and physical methods such as electrochemical deposition [24], thermal evaporation [25], ion beam deposition [26], laser ablation [27], spray pyrolysis [28] and gel coating by centrifugation [29].

In this work, we will prepare samples for mixtures of the aforementioned oxides in order to study their structural and optical properties in order to obtain the optimal mixture that has better properties than both oxides separately.

2. EXPRIMENTAL WORK

In this paper, mixtures of nickel oxide (NiO) and zinc oxide (ZnO) were prepared in the form of thin films on ultra-pure glass substrates using pyrolysis spray technique. Where two solutions were prepared from nickel nitrate $(Ni(NO_3)_2 \cdot 6H_2O)$ and zinc acetate $(C_4H_6O_4Zn \cdot 2H_2O)$ with the same molar concentration C=0.2 mol/L, by dissolving each mass of nickel nitrate and Zinc acetate in a volume of 12 ml of distilled water and add drops of chloride acid in order to facilitate the mixing process. To ensure complete dissolution of both solutions, a magnetic stirrer is used to mix each solution for 15 minutes at a temperature of 50ºC ensuring no sediment. Then, we prepare samples from the mixture consisting of nickel nitrate solution and zinc acetate solution in different proportions as shown in the table1.After preparing the precipitation mixture, preparing the glass substrates and preparing the spraying system, we start the precipitation process with the chemical spraying technique, which passes through several steps:

1- We put the spray nose at the vertical distance d = 30 cm.
2- We set the air compressor to a pressure of 2 bar.

3- The glass substrates are placed over the electric heater and set at a temperature of 500°C.

4- After heating, we do intermittent spraying for 5 seconds to keep the temperature of the glass substrate within 500°C. Where we obtained thin films with acceptable homogeneity and high adhesion strength on the substrate and with close thickness.

3. RESULTS AND DISCUSSIONS
3.1. Structural Properties

Figure 1 shows the XRD patterns of films of a mixture of nickel oxide (NiO) and zinc oxide (ZnO) prepared with different proportions of aforementioned oxides. In case of pure nickel oxide curve S_1 it can be seen two main diffraction peaks positioned at $2\theta \approx 37.296°$ and $43.272°$ assigned to the (111) and (200) crystal planes respectively.
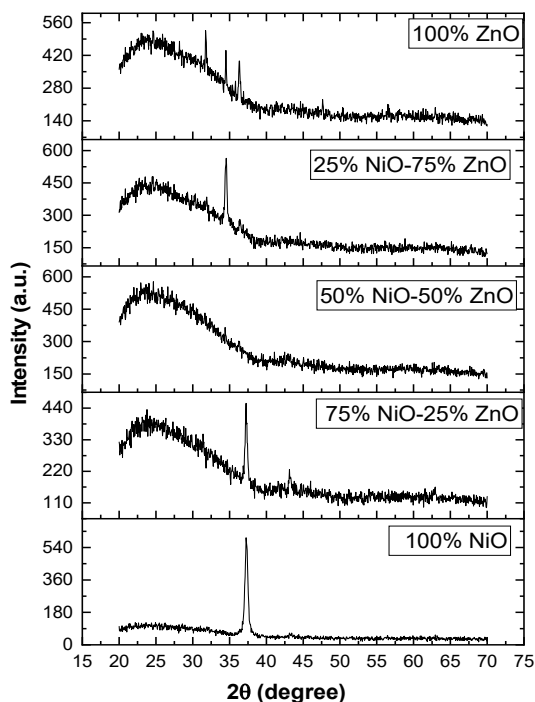
Figure 1. XRD patterns of the deposited ZnO/NiO thin films on glass substrate at different percentages

These peaks accurately correspond to the crystal structure of NiO (NaCl) with CFC crystal structure of which belongs to the space group Fm3m. The XRD patterns shows good agreement with JCPDS (47-1049) [1]. The presence of such peaks indicates that the films are polycrystalline in nature.

The same results can be deduced for sample S_2 where it is observed that three main peaks are identified in the angle range 2θ (37.247°, 43.197°, and 62.844°) corresponding to the following diffraction planes (111), (200) and (220), respectively. These results are consistent with the high percentage of nickel oxide present in this sample. In the case of equal proportions of oxides in the sample S_3, no diffraction peaks were observed, and the sample was amorphous. For sample S_4 two specific peaks appear at angles 2θ (34.515° and 36377°) corresponding to the diffraction levels (002) and (101) according to JCPDS (36-1451), which is consistent with a high percentage of ZnO in these sample. Sample S_5 showed three prominent main diffraction peaks (100), (002) and (101) corresponding to the angle (31.564°, 34.510° and 36.336°). These peaks correspond to the wurtzite hexagonal structure of pure ZnO. It is noted that there is a high compatibility with the international s showed three prominent main diffraction peaks (100), (002) and (101) corresponding to the angles 2θ (31.56°, 34.51° and 36.33°). These peaks correspond to the wurtzite hexagonal structure of pure ZnO. It is noted that there is a high compatibility with the international standard card JCPDS (36-1451).

In order to get more material structural information, we have studied different structural constants such as lattice constants a and c, grain size D, average stress ε and dislocation density δ for pure NiO and ZnO films as well as for the films of oxides mixtures. The lattice constant for the cubic structure phase of NiO films is calculated using the following equation [3]:

$$d_{hkl} = \frac{a}{\sqrt{h^2+k^2+l^2}} \qquad (1)$$

Where is the distance between the crystal structure and (h,k,l) are the Miller's coefficients.

The lattice constants a and c for the hexagonal structure phase of ZnO films is calculated using the following equation [4]:

$$\frac{1}{d^2} = \frac{4}{3}\left(\frac{h^2+hk+k^2}{a^2}\right) + \frac{l^2}{c^2} \qquad (2)$$

The grain size D of films is related to the physical and chemical properties of the material, where the Debye-Scherrer statement allowed estimating the size of the grains by X-ray diffraction, which is given by the following relationship [5]

$$D = \frac{0,9\lambda}{\beta \cos\theta} \qquad (3)$$

Where λ is the wavelength of X-rays (λ=1,540593), β is the value of the middle of the highest peak width (the value (FWHM) computed with the radial angle) andθ is the Bragg's angle.

Dislocation density δ represents the linear defect inside the crystal, and is calculated from Williamson and Smallman's relationship [6]:

$$\delta = \frac{1}{D^2} \qquad (4)$$

The average strain ε is the strain expresses the distortion in the network and is estimated by the following relationship [7]:

$$\varepsilon = \left(\frac{a-a_0}{a_0}\right) 100\% \tag{5}$$

Where a_0 is the theoretical lattice constant and a is the experimental lattice constant.

Table 1. Structural parameters of (ZnO/NiO) thin films mixture

Samples	Coding	2θ(°)	d (Å)	(hkl)	a (Å)	c (Å)	D (Å)	μ_ε	δ (Å⁻²)
100% NiO	S₁	37,296	2,411	111	4,176	------	3,32	0,104	0,091
		43,272	2,091	200					
75% NiO 25% ZnO	S₂	37,247	2,414	111	4,181	------	4,44	0,078	0,051
		43,197	2,094	200					
		62,844	1,479	220					
25% NiO 75% ZnO	S₄	34,515	2,600	002	3,24	5,200	5,59	0,062	0,036
		36,377	2,470	101					
100% ZnO	S₅	31,564	2,834	100	3,272	5,198	4,82	0,102	0,043
		34,510	2,599	002					
		36,336	2,472	101					

3.2. Morphological Properties

The surface morphology of the thin film was studied by scanning electron microscopy (SEM). For films of pure nickel oxide NiO and zinc oxide ZnO, as well as samples consisting of a mixture of NiO and ZnO in different proportions which have been sputtered onto glass substrates, where it appears that the deposited films have a composition and a relative homogeneity despite the preparation of homogeneous solutions for the samples because they contain pure grains and prepared under the same conditions. Hence the shape of the granules which does not appear clearly with a vertical growth on the surface of the film for samples S₁ and S₂which contain a higher percentage of nickel oxide. It should be noted that the higher the percentage of ZnO and this for samples S₃, S₄ and S₅ the more clearly the zinc grains appear on the surfaces of the thin films and the development of the skeleton with the random growth of islands in the middle and on the edges of the substrate.
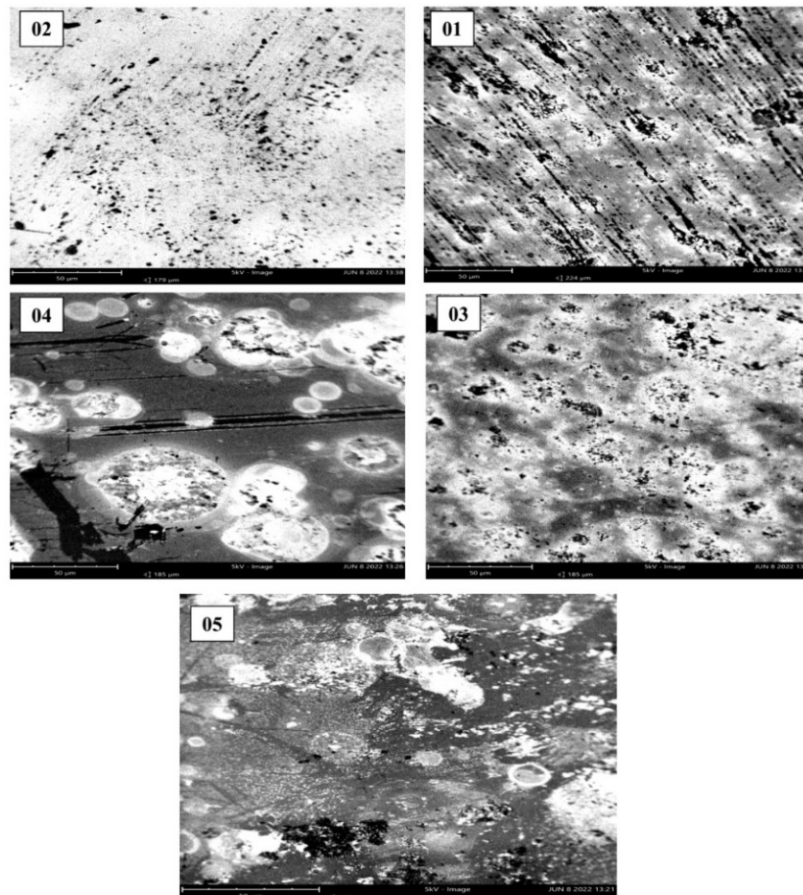
Figure 2. Images of samples S₁ – S₅ prepared by scanning electron microscopy (SEM)

3.3. Optical Properties

The absorbance and transmittance spectrum of all samples were studied in the ultraviolet, visible and near infrared rays. The values of the absorption coefficient, energy gap and Urbach energy are summarized in Table 2.

Figure3shows the transmittance changes with wavelength for all prepared samples. The results showed that the transmittance is as low in the ultraviolet region, i.e., in the short wavelength range of 300 to 380 nm. The low value of transmittance in this area is due to the fact that the absorption is high due to the proximity of the energy of the emitted photons to the energy of the basic absorption edge of these films [30]. The transmittance of the two samples S_1 and S_2 moves towards the blue spectrum, while the rest of the samples S_3, S_4 and S_5 moves towards the red spectrum. The transmittance increases significantly for all samples in the visible range, especially for samples that contain a higher percentage of zinc oxide, as it is close to 98% at the end of the visible range for samples S_3, S_4 and$S_5$and 88% for the two samples S_1 and S_2[31].

Table 2. Structural parameters of (ZnO/NiO) thin films mixture

Samples	Optical gap energy E_g(eV)		Urbach energy E_U (eV)
S_1	3.55		0.466
S_2	3.53		0.571
S_3	2.35	3.13	0.333
S_4	3	4.1	0.133
S_5	3.23	3.17	0.076

The optical band gap energy is one of the fundamental properties of electro-optical materials. The measurement of the gap energy depends on the material and its properties. The optical energy bandgap is defined as the lowest energy required to move an electron from the top of the valence band to the bottom of the conduction band. By determining the values of the absorption coefficient, it is possible to calculate the optical band gap of the permissible direct electronic transitions using Tauc's equation [32]:

$$(\alpha h\upsilon)^2 = A(h\upsilon - E_g). \qquad (6)$$

Where A is a constant, α is the absorption coefficient, $h\upsilon$ is the photon energy and E_g is the band gap energy.

Table 2 shows a significant difference in the band gap energy values of the thin films of the mixture of nickel and zinc. This difference can be attributed to the phase presence for both oxides, and since there is a clear difference between the nickel and zinc elements in chemical and physical properties, the strong presence of one of them means that the other plays a role doping, and therefore we notice a clear difference in the values of the energy gap, especially in the case of samples S_3, S_4 and S_5, where there is the largest presence of zinc oxide, and perhaps the appearance of a double energy gap is a clear indication of this.

It is noted that the energy gap of the thin layers of pure nickel oxide $S_1$and the mixture S_2 decreases to 2.35 eV, the decrease in the band gap energy is explained by the movement of the absorption front towards the lower energies, and this decrease can be explained by Roth effect because the impurities that make up the mixture have led to the formation of donor levels within the band gap near the conduction band and therefore to the absorption of low energy photons [35].

The Table 2 also shows for the samples S_3, S_4 and S_5 which contain a higher percentage of zinc oxide ZnO that they have two band gap energy and this is due to several reasons:
- This may be related to the formation of ZnO nanostructures on the bulk of the remaining ZnO thin film.
- This can also be explained by a defect in the composition and structure of our prepared sample [36].
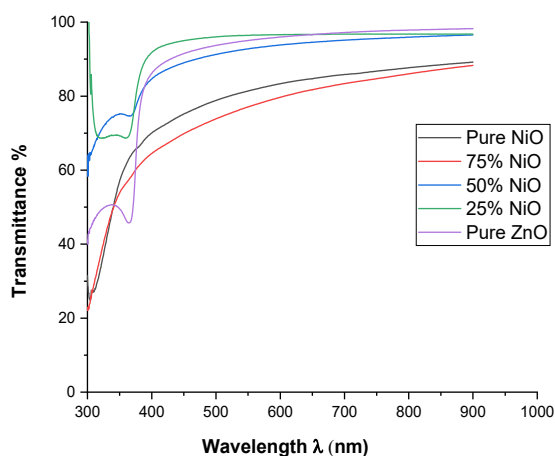- There are mixed phase or low crystallization [37].

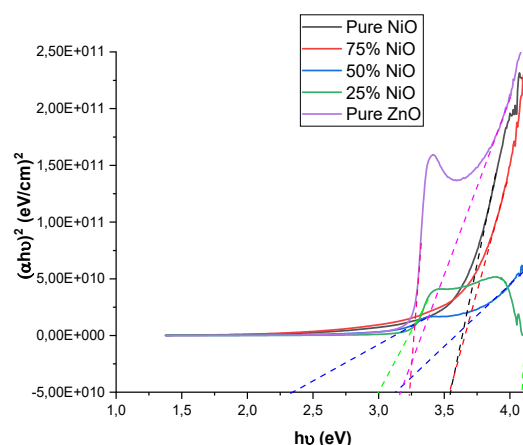**Figure 3.** Transmittance of ZnO/NiO thin films

Figure 4. Band gap energy of ZnO/NiO thin films

The Urbach energy is a physical quantity that characterizes the disorder of matter, since it is considered one of the important constants that characterize the optical properties of thin layers [36], since it relates to the absorption coefficient according to relationship [37]:

$$\alpha = \alpha_0 . e^{\left(\frac{h\nu}{E_u}\right)}. \tag{7}$$

It can be written:

$$ln\alpha = ln\alpha_0 + \left(\frac{h\nu}{E_u}\right). \tag{8}$$

Where α_0 is the absorption coefficient for which the absorption value is minimum and E_u is the Urbach energy.

The value of Urbach's energy (E_u) can be determined from the drawing of the curve of the changes of the linear function (lnα) in terms of photon energy (hν) shown in Figure5, where the inverse of the slope represents the Urbach energy. There is an increase in the Urbach energy values for the samples of pure nickel oxide $S_1$and S_2which contain a greater percentage of nickel oxide. For the samples (S_3, $S_4$and S_5), we find the opposite from what was obtained for the Urbach energy values for the first two samples. From the results of the Table2, we note that the optical behavior of the Urbach energy value changes inversely with the optical behavior of the energy interval.
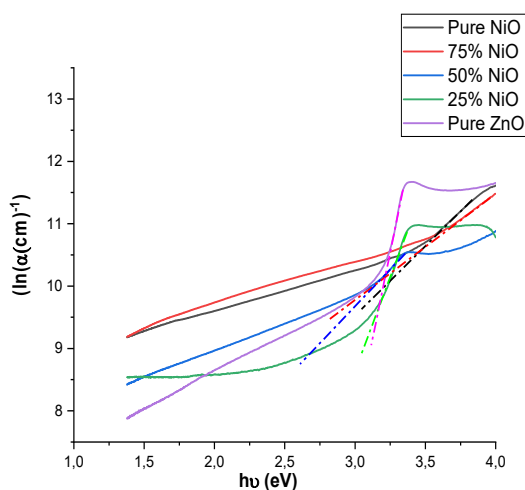
Figure 5. Urbach energy of ZnO/NiO thin films

4. CONCLUSIONS

In this study, we had the opportunity to prepare mixtures of different proportions of samples of nickel oxide (NiO) and zinc oxide (ZnO), which were deposited in the form of thin films on glass substrates, using pyrolysis spray technique at the same conditions.

The structure of the prepared mixtures, as well as the absorption and transmittance spectrum of all samples in the ultraviolet, visible, and near infrared, were studied. Where the values of the absorption coefficient, energy interval, and Urbach energy were summarized with the aim of deducing the relationship between these values and the prepared samples. Where the study showed:

- Samples that contain a higher percentage of nickel oxide (NiO) have the lowest possible transmittance in the ultraviolet region i.e., the short wavelength ranges from 300 to 380 nm while the absorption is high.

- The transmittance of samples with a higher percentage of NiO shifts towards the blue spectrum, while the transmittance of the remaining samples shifts towards the red spectrum.

- The transmittance increases dramatically for samples in the visible range, especially for samples that contain a greater percentage of zinc oxide, as it approaches 99% at the end of this range.

- Samples that contain a higher percentage of zinc oxide (ZnO) have two energy gaps.

- The optical behavior of the Urbach energy value changes inversely with the optical behavior of the energy gaps.

- The surface morphology of thin films has been studied by scanning electron microscopy (SEM), and it has been found to have a relatively homogeneous composition, where the shape of the granules does not appear clearly with a vertical growth on the surface of the film for the sample that contains a higher percentage of nickel oxide. It is noted that as the percentage of zinc oxide ZnO increases, the zinc granules appear on the surfaces of the thin films clearly, and the skeletal structure grows with the growth of random islands.

Through this general study it is clear that the determination of the optimal mixture depends on the application to which the mixture is directed. For example, in solar cell applications where we use transparent oxides as windows, the optimal mixture is one with greater transparency and an energy gap that fits the solar spectrum. In this case, sample S_4 is the best. Whereas in gas sensor applications where film morphology has a key role in optimal adsorption of gases with the film surface, in this case sample S_3 is ideal because the surface profile is more homogeneous and rougher.

ORCID

🟢**Ali Amiar,** https://orcid.org/0009-0008-6013-8542; 🟢**Okba Belahssen,** https://orcid.org/0000-0002-2770-4599
🟢**Mebrouk Ghougali,** https://orcid.org/0000-0003-0496-4555; 🟢**Mourad Mimouni,** https://orcid.org/0000-0002-4402-5918
🟢**Ghani Rihia,** https://orcid.org/0000-0002-5264-9480; 🟢**Mohammed Sadok Mahboub,** https://orcid.org/0000-0001-5495-5249
🟢**Yamina Benkrima,** https://orcid.org/0000-0001-8005-4065

REFERENCES

[1] N.E. Duygulu, A.O. Kodolbas, and A. Ekerim, "Influence of r.f. power on structural properties of ZnO thin films," Journal of Crystal Growth, **381**, 51 (2013). https://doi.org/10.1016/j.jcrysgro.2013.07.008

[2] Y. Wang, and Benli Chu, "Structural and optical properties of ZnO thin films on (111) CaF2 substrates grown by magnetron sputtering," Superlattices and Microstructures, **44**(1), 54 (2008). https://doi.org/10.1016/j.spmi.2008.01.024

[3] M.G. Tsoutsouva, C.N. Panagopoulos, D. Papadimitriou, I. Fasaki, and M. Kompitsas, "ZnO thin films prepared by pulsed laser deposition," Materials Science and Engineering: B, **175**(6), 480 (2011). https://doi.org/10.1016/j.mseb.2010.03.0591776

[4] C.W. Hsu, T.C. Cheng, C.H. Yang, Y.L. Shen, J.S. Wu, and S.Y. Wu, "Effects of oxygen addition on physical properties of ZnO thin film grown by radio frequency reactive magnetron sputtering," Journal of Alloys and Compounds, **509**(5), 1774 (2011). https://doi:10.1016/j.jallcom.2010.10.037

[5] L. Ding, M. Boccard, G. Bugnon, M. Benkhaira, S. Nicolay, M. Despeisse, F. Meillaud, and C. Ballif, "Hightly transparent ZnO bilayers by LP-MOCVD as front electrodes for thin-film micromorph silicon solar cells," Solar Energy Materials and Solar Cells, **98**, 331 (2012). https://doi.org/10.1016/j.solmat.2011.11.033

[6] H. Zhu, J. Hüpkes, E. Bunte, and S.M. Huang, "Study of ZnO:Al films for silicon thin film solar cells," Applied Surface Science, **261**(15), 268 (2012). https://doi.org/10.1016/j.apsusc.2012.07.159

[7] R. Mariappan, V. Ponnuswamy, P. Suresh, N. Ashok, P. Jayamurugan, and A.C. Bose, "Study of ZnO:Al films for silicon thin film solar cells," Superlattices and Microstructures, **71**, 238 (2014). https://doi.org/10.1016/j.spmi.2014.03.029

[8] J.P. Atanas, R.A. Asmar, A. Khoury, and A. Foucaran, "Optical and structural characterization of ZnO thin films and fabrication of bulk acoustic wave resonator (BAW) for the realization of gas sensors by stacking ZnO thin layers fabricated by e-beam evaporation and RF magnetron sputtering techniques," Sensors and Actuators A: Physical, **127**(1), 49 (2006). https://doi.org/10.1016/j.sna.2005.11.065

[9] E. Fortunato, P. Barquinha, A. Pimentel, A. Gonçalves, A. Marques, L. Pereira, and R. Martins, "Recent advances in ZnO transparent thin film transistors," Thin Solid Films, **487**(1–2), 205 (2005). https://doi.org/10.1016/j.tsf.2005.01.066

[10] T. Minami, J.I. Oda, J.I. Nomoto, and T. Miyata, "Effect of target properties on transparent conducting impurity-dopedZnO thin films deposited by DC magnetron sputtering," Thin Solid Films, **519**(1), 385 (2010). https://doi.org/10.1016/j.tsf.2010.08.007

[11] R. Serhane, S. Abdelli-Messaci, S. Lafane, H. Khales, W. Aouimeur, A. Hassein-Bey, and T. Boutkedjirt, "Pulsed laser deposition of piezoelectric ZnO thin films for bulk acoustic wave devices," Applied Surface Science, **288**, 572 (2014). https://doi.org/10.1016/j.apsusc.2013.10.075

[12] S.Y. Lee, E.S. Shim, H.S. Kang, S.S. Pang, J.S. Kang, "Fabrication of ZnO thin film diode using laser annealing," Thin Solid Films, **473**(1), 31 (2005). https://doi.org/10.1016/j.tsf.2004.06.194

[13] R. Jayakrishnan, K. Mohanachandran, R. Sreekumar, C.S. Kartha, and K.P. Vijayakumar, "ZnO thin films with blue emission grown using chemical spray pyrolysis," Materials Science in Semiconductor Processing, **16**(2), 326 (2013). https://doi.org/10.1016/j.mssp.2012.10.003

[14] P. Jongnavakit, P. Amornpitoksuk, S. Suwanboon, and T. Ratana, "Surface and photocatalytic properties of ZnO thin film prepared by sol-gel method," Thin Solid Films, **520**(17), 5561 (2012). https://doi.org/10.1016/j.tsf.2012.04.050

[15] S.F. Hasim, M.A.A. Hamid, R. Shamsudin, and A. Jalar, "Synthesis and characterization of ZnO thin films by thermal evaporation," Journal of Physics and Chemistry of Solids, **70**(12), 1501 (2009). https://doi.org/10.1016/j.jpcs.2009.09.013

[16] E. Fazio, A.M. Mezzasalma, G. Mondio, T. Serafino, F. Barreca, and F. Caridi, "Optical and structural properties of pulsed laser ablation", Applied Surface Science, **257**(6), 2298 (2011). https://doi.org/10.1016/j.apsusc.2010.09.092

[17] L. Ai, G. Fang, L. Yuan, N. Liu, M.W. Wang, C. Li, Q. Zhang, J. Li, and X. Zhao," Influence of substrate temperature on electrical and optical properties of p-type semitransparent conductive nickel oxide thin films deposited by radiofrequency sputtering," Applied Surface Science, **254**(8), 2401(2008). https://doi.org/10.1016/j.apsusc.2007.09.051

[18] H.L. Chen, Y.M. Lu, and W.S. Hwang, "Characterization of sputtered NiO thin films," Surface &Coating Technology, **198**, 138 (2005). https://doi.org/10.1016/j.surfcoat.2004.10.032

[19] H.L. Chen, and Y.S. Yang, "Effect of crystallographic orientation on electrical properties sputter-deposited nickel oxide thin films," Thin solid Films, **516**(16), 5590 (2008). https://doi.org/10.1016/j.tsf.2007.07.03

[20] Y. Lin, T. Xie, B. Cheng, B. Geng, and L. Zhang, "Ordered nickel oxide nanowire arrays and their optical absorption properties," Chemical Physics Letters, **380**, 521 (2003). https://doi.org/10.1016/j.cplett.2003.09.066

[21] B. Sasi, K. Gopchandran, P. Manoj, P. Koshy, P. Rao, and V.K. Vaidyan, "Preparation of transparent and semiconducting NiO films," Vacuum, **68**(8), 149 (2003). https://doi.org/10.1016/S0042-207X(02)00299-3

[22] J. Peng, Z. Xu, S. Wang, Q. Jie, and C. Chen, "Preparation and Performance of nickel oxide films by Ion beam sputtering deposition and oxidation annealing," Sensors and Materials, **22**(8), 409-416 (2010). https://doi.org/10.18494/SAM.2010.633

[23] S.Z. Khan, Y. Yuan, A. Abdolvand, M. Schmidt, P. Crouse, L. Li, Z. Liu, et al., "Generation and characterization of NiO nanoparticles by continuous wave fiber laser ablation in liquid", Journal Nanopart Research, **11**, 1421 (2009). https://doi.org/10.1007/s11051-008-9530-9

[24] P.S. Patil, and L.D. Kadam, "Preparation and characterization of spray pyrolyzed nickel oxide (NiO) thin films," Applied Surface Science, **199**, 211 (2002). https://doi.org/10.1016/S0169-4332(02)00839-5

[25] V. Patil, S. Pawar, M. Chougule, P. Godse, R. Sakhara, S. Sen, and P. Joshi, "Effect of annealing on structural, morphological, electrical and optical studies of nickel oxide thin films," Journal of surface engineered Materials and Advanced technology, **1,** 35 (2011). https://doi:10.4236/jsemat.2011.12006

[26] J. Wang, P. Yang, X. Wei, and Z. Zhou, "Preparation of NiO two-dimensional grainy films and their high-performance gas sensors for ammonia detection," Nanoscale Research Letters, **10**(1), 1 (2015). https://doi.org/10.1186/s11671-015-0807-5

[27] S. Ilican, Y. Caglar, M. Caglar, and F. Yakuphanoglu, "Electrical conductivity, optical and structural properties of indium-doped ZnO nanofiber thin film deposited by spray pyrolysis method," Physica E: Low-dimensional Systems and Nanostructures, **35**, 131 (2006). https://doi.org/10.1016/j.physe.2006.07.009

[28] H.L. Chen, Y.M. Lu, and W.S. Hwang, "Effect of film thickness on structural and electrical properties of sputter-deposited nickel oxide films," Materials Transactions, **46**(4), 872-879 (2005). https://doi.org/10.2320/matertrans.46.872

[29] Y. Aoun, B. Benhaoua, B. Gasmi, and S. Benramache, "Structural, optical and electrical properties of zinc oxide (ZnO) thin films deposited by a spray pyrolysis technique," Journal of Semiconductors, **36**(1), 013002 (2015). https://doi.org/10.1088/1674-4926/36/1/013002

[30] A.S. Riad, S.A. Mahmoud, and A.A. Ibrahim, "Structural and DC electrical investigations of ZnO thin films prepared by spray pyrolysis technique," Physica B: Condensed Matter, **296**(4), 319 (2001). https://doi.org/10.1016/S0921-4526(00)00571-8

[31] D.P. Padiyan, A. Marikani, and K.R. Murali, "Influence of thickness and substrate temperature on electrical and photoelectrical properties of vacuum-deposited CdSe thin films," Materials Chemistry and Physics, **78**(1), 51 (2003). https://doi.org/10.1016/S0254-0584(02)00211-0

[32] M. Mekhnache, A. Drici, L. Saad Hamideche, H. Benzarouk, A. Amara, L. Cattin, J.C. Bernède, and M. Guerioune, "Properties of ZnO thin films deposited on (glass, ITO and ZnO:Al) substrates," Superlattices and Microstructures, **49**(5), 510 (2011). https://doi.org/10.1016/j.spmi.2011.02.002

[33] S. Ilican, Y. Caglar, "Preparation and characterization of ZnO thin films deposited by sol-gel spin coating method," J. of optoelectronics and advanced materials, **10**(10), 2578-2583 (2008).

[34] E. Avendaño, L. Berggren, G.A. Niklasson, C.G. Granqvist, and A. Azens, "Electrochromic materials and devices: brief survey and new data on optical absorption in tungsten oxide and nickel oxide films," Thin Solid Films, **496**, 30 (2006). https://doi.org/10.1016/j.tsf.2005.08.183

[35] A. Rahal, S. Benramache, and B. Benhaoua, "Substracte Temperature Effect on Optical property of ZnO Thin Films," Engineering Journal, **18**(2), 81 **(**2013). https://doi.org/10.1016/j.tsf.2005.08.183

[36] E.S. Tüzemen, S. Eker, H. Kavak, and R. Esen, "Dependence of film thickness on the structural and optical properties of ZnO thin films," Appl. Surf. Sci. **255**(12), 6195 (2009). https://doi.org/10.1016/j.apsusc.2009.01.078

[37] A.U. Mane, and S.A. Shivashankar, "MOCVD of cobalt oxide thin films: dependence of growth, microstructure, and optical properties on the source of oxidation," J. Cryst. Growth, **254**(3-4), 368 (2003). https://doi.org/10.1016/S0022-0248(03)01156-4

СТРУКТУРНІ ТА ОПТИЧНІ ВЛАСТИВОСТІ ТОНКІХ ПЛІВОК ІЗ СУМІШІ (ZnO/NiO)

Алі Аміар[a], Окба Белахсен[b], Мебрук Гугалі[a], Мурад Мімуні[a], Гані Ріхі[a], Мохаммед Садок Махбуб[a], Яміна Бенкріма[c]

[a]Лабораторія LEVRES, Університет Ель-Уед, В.Р. 789, 39000 Ель-Уед, Алжир

[b]Фізична лабораторія тонких плівок і застосувань (LPCMA), Університет Біскри, В.Р. 145 R.P 07000 Біскра, Алжир

[c]Вища нормальна школа Уаргла, 30000 Уаргла, Алжир

У цьому дослідженні були підготовлені суміші оксиду нікелю (NiO) і цинку (ZnO) у різних пропорціях у вигляді тонких плівок на скляних підкладках високої чистоти за допомогою техніки піролізу. При цьому зразки сумішей осаджували з двох розчинів нітрату нікелю (Ni(NO₃)₂·6H₂O) і ацетату цинку C₄H₆O₄Zn·2H₂O), змішаних у різних пропорціях. Потім були досліджені оптичні та структурні властивості підготовлених зразків. Виявлено, що коефіцієнт пропускання зменшується зі збільшенням відсотка оксиду нікелю, що означає, що збільшення оксиду цинку покращує пропускання в усіх досліджуваних спектральних полях. Зразки з вищим вмістом оксиду цинку (ZnO) мають дві енергетичні щілини. Методом скануючої електронна мікроскопія (SEM) показано, що морфологія поверхні плівок має відносно однорідний склад, де спостерігалося, що збільшення частки оксиду цинку призводить до появи гранул оксиду цинку.

Ключові слова: *суміші NiO та ZnO; тонкі плівки; технологія піролізу; енергетична заборонена зона; оптичні властивості*

INVESTIGATION THE STRUCTURAL INFLUENCES OF SILVER OXIDE ADDITION IN THE BIOACTIVE PHOSPHATE GLASSES[†]

Ruqaya H. Hussian, **Dunia K. Mahdi***

Department of Physics, College of Science, University of Baghdad, Baghdad, Iraq
*Corresponding Author e-mail: dunia.mahdi@sc.uobaghdad.edu.iq
Received May 15, 2023; revised June 9, 2023; accepted June 10, 2023

This research investigates the impact of varying concentrations of silver oxide on the structure and morphology of phosphate bioactive glass (PBG). PBGs are gaining popularity as a potential replacement for traditional silicate glasses in biomedical applications due to their adjustable chemical resistance and exceptional bioactivity. Upon examination of the scanning electron microscope of the composites without Ag_2O, it was observed that the grains tended to merge together, and the surface particles appeared to be larger than those in composites with Ag_2O at concentrations of 0.25, 0.5, and 0.75 wt%. The study found that the diffraction pattern of phosphate bioactive glass composites sintered without Ag_2O showed the presence of Strontium di-phosphate and Calcium di-phosphate. The XRD pattern of these composites without Ag_2O revealed specific planes that corresponded to both types of di-phosphate. However, when Ag_2O was added, a new cubic phase was detected, and the intensity of the calcium and strontium diphosphate increased with higher Ag_2O content. The XRD pattern of the composites with Ag_2O displayed specific planes that corresponded to Ag_2O. In other words, the absence of Ag_2O in the composite material led to larger particle sizes and less distinct boundaries between grains. In addition, it has been found that, as the concentration of Ag_2O increased from 0 to 0.25, 0.5, and 0.75 wt%, the average crystallite size decreased from 36.2 to 31.7, 31.0, and 32.8 nm, respectively. These results suggest that the addition of Ag_2O can effectively reduce the average crystallite size of the composite materials. Also, as the concentration of Ag_2O increased from 0 g to 0.5 wt% within the composite material, the average lattice strain increased from $3.41 \cdot 10^{-3}$ to $4.40 \cdot 10^{-3}$. In simpler terms, adding Ag_2O to the composite material resulted in a slight increase in the average lattice strain.

Keywords: *phosphate bioactive glass (PBG); silicate glasses; Calcium di-phosphate; Silver oxide Strontium carbonate ($SrCO_3$)*
PACS: 81.05.-t, 81.05.Bx, 81.05.Je, 81.05.Kf

1. INTRODUCTION

Phosphate bioactive glasses (PBGs) have emerged as a promising alternative to conventional silicate glasses, thanks to their adjustable chemical resistance that can be customized to meet specific application requirements[1-3]. PBGs can be designed to degrade completely in a timeframe ranging from hours to years. This property, along with their demonstrated bioactivity, makes them an attractive material option for bone repair and reconstruction. Additionally, PBGs exhibit favorable thermal properties, as evidenced by the numerous studies on bioactive phosphate fibers conducted in recent years, suggesting a wider processing range[4-6].

The dissolution behavior of glasses in the $50P_2O_5$-$10Na_2O$-$(40-x)CaO$-$xSrO$ system was found to exhibit a minimum when half of the CaO was replaced with SrO [7]. The chemical resistance of the glass was observed to be influenced by its structure, with a reduction in the length of the phosphate chains resulting in increased chemical resistance. Additionally, the presence of SrO was found to enhance the proliferation and growth of gingival fibroblast cells, in contrast to the cell death observed with SrO-free glasses within 24 hours. The CaO-free glass displayed similar cell counts to those measured on the surface of the reference glass S53P4. The improved cell viability with SrO-containing glasses is partly attributed to the decreased initial dissolution rate, resulting from the replacement of CaO with SrO. The effect of strontium ions, both in the surrounding media and within the reactive layer of the glass, was also found to play a significant role [8, 9].

Metaphosphate glasses have shown promising results as potential biomaterials for bone repair and reconstruction. However, they exhibit a rapid initial dissolution rate, which can result in the late formation of a reactive layer. This can hinder the attachment and proliferation of cells during the first few days of culture, which is a crucial step in the healing process. The reactive layer may contain precipitates or other species that can interfere with cell adhesion and growth. This issue has been observed in previous studies, where fast-dissolving glasses were found to be unsuitable for promoting proper cell proliferation. Therefore, further research is required to address these challenges and optimize the performance of metaphosphate glasses as biomaterials [5].

The addition of metal ions, such as silver (Ag), copper (Cu), or cobalt (Co), to glass compositions can modify their physical and chemical properties and provide unique functionality for clinical applications. These metal ions are known to possess antimicrobial properties that can be useful in preventing or controlling infections [13-19]. For instance, silver ions are highly effective against a broad range of microorganisms, including bacteria, viruses, and fungi, by disrupting their cellular processes. Similarly, copper ions can damage the cell membranes of microorganisms, while cobalt ions not only have antibacterial properties but can also promote bone growth and enhance the mechanical strength of the glass.

Therefore, incorporating metal ions into glasses can expand their potential applications in the biomedical field and improve their functionality [17, 19].

Silver (Ag) is a widely used metal ion dopant in biomedical devices due to its effectiveness against various microbial growth and low toxicity to human cells, even at low concentrations. Ag ions in the form of nitrate or oxide are commonly employed in healthcare products such as Ag-coated catheters or wound dressings to prevent or control infections caused by microorganisms. Ag ions interact with the cellular structures of microbes, disrupt their metabolic processes, and eventually cause cell death, giving rise to their antimicrobial properties. Furthermore, Ag ions can promote tissue regeneration and wound healing, making them an excellent choice for biomedical applications[20]. Hence, the incorporation of Ag as a dopant in glass compositions can offer antimicrobial functionality, enhance the safety and efficacy of different medical devices, and improve patient outcomes[21]. Ag-based ointments have been traditionally used for treating wounds that are susceptible to bacterial infections. In the case of phosphate-based glasses (PBGs) doped with Ag, the metal ions are thought to be incorporated within the glass structure. Unlike silicate glasses, PBGs tend to dissolve congruently, which allows for the controlled release of Ag ions as the glass dissolves. Ahmed et al. conducted a study on silver-doped bioactive glasses by substituting Na_2O with Ag_2O up to 15 mol%, and found that the maximum antimicrobial effect was achieved in glasses containing 1 to 5 mol% of Ag_2O. The authors also examined the structure and properties of the silver-doped glasses. More recently, the antimicrobial properties of silver-doped phosphate glasses were investigated for glasses with 65 and 70 mol% of P_2O_5[22].

Previous studies have shown that an increase in the Ag content in phosphate glasses results in an increased antimicrobial effect, while increasing the phosphate content in Ag-free glasses has a similar effect. However, these studies were conducted with glasses having a phosphate content of 50 mol% or greater, which was found to inhibit growth and bone antigen expression due to the fast dissolution rate of the glass in the P_2O_5-CaO-Na_2O family[9]. On the other hand, glasses with slow solubility were found to promote cell proliferation. Despite a P_2O_5 content of 50%, previous research on Sr-containing bioactive glasses has demonstrated that gingival fibroblast cells can attach and proliferate. Therefore, it is important to investigate the impact of Ag doping on this glass composition and determine whether it is possible to obtain Ag-doped strontium-containing phosphate glasses with antimicrobial properties[8].

The objective of this study was to examine the impact of varying amounts of silver oxide on the structure and properties of a bioactive glass composed of metal-phosphate. The glass was synthesized using phosphor oxide, strontium carbonate, and calcium carbonate and subjected to characterization via X-ray diffraction (XRD), scanning electron microscopy (SEM), and atomic force microscopy (AFM). By analyzing the data obtained from XRD, AFM, and SEM, the researchers aimed to gain a better understanding of the physical and chemical characteristics of the glass, including its stability, reactivity, and biocompatibility. This would enable the optimization of its performance for diverse biomedical applications.

2. EXPERIMENTAL
2.1. Materials

Sodium carbonate was purchased from Shandong Yifengtuo Chemical Co., Ltd. Silver oxide Strontium carbonate ($SrCO_3$), and Calcium carbonate ($CaCO_3$) was purchased from Jinan Future Chemical Co., Ltd. Phosphor oxide was purchased from Hebei Ruisite Technology Co., Ltd.

2.2. Metal-Phosphate Bio-Active Glass

In order to prepare Metal-Phosphate Bio-Active Glass, the following steps were carried out: Firstly, the required amounts of different materials, including sodium carbonate (0.75g), phosphor oxide (1.5g), strontium carbonate (0.75g), calcium carbonate (0.427g), and varying amounts of Ag_2O (0g, 0.25g, 0.5g, or 0.75g), were accurately measured and mixed thoroughly using a mortar and pestle. This resulting mixture was then transferred to a mold, which had a diameter of 2 cm and a height of 0.5 cm. A pressure of 1000 psi (0.000445Ton) was applied to the mold using a hydraulic press for 2 minutes, following which the mold was sintered in a furnace at 780°C for a duration of 2 hours. Once the sintering process was completed, the mold was allowed to cool down to room temperature, following which the solidified glass was removed. These steps were undertaken to prepare the Metal-Phosphate Bio-Active Glass sample for further analysis.

To prepare Metal-Phosphate Bio-Active Glass, we followed the flowing steps: First, we measured out the required amounts of sodium carbonate (0.75g), phosphor oxide (1.5g), strontium carbonate (0.75g), calcium carbonate (0.427g), and Ag_2O (0g, 0.25g, 0.5g, or 0.75g). Mix these materials thoroughly in a mortar and pestle, and transfer the resulting mixture to a mold (2 cm in diameter and 0.5 cm with height). Apply a pressure of 1000 psi (0.000445 Ton) for 2 minutes using a hydraulic press, and then sinter the mold in a furnace at 780°C for 2 hours. After the sintering process is complete, allow the mold to cool to room temperature and then remove the solidified glass.

2.3. Characterization

Images of the current samples were captured by a JEOL/EO SEM (version 1.0). Platinum (Pt) coating was performed using an Auto fine coater-JEOL (JEC-3000 FC) for 60 seconds at 20 mA of operating current. The accompanying INCA x-act was used for the EDS analysis (Oxford instruments). Samples' EDS spectra were acquired at acceleration voltages of up to 10 keV.

To perform X-ray diffraction (XRD) analysis, the sintered compacted discs were first ground into powder and then analyzed using a Philips PW 1800 instrument. The instrument was set to a voltage of 40 kV and a current of 30 mA, and it used Cu–Kα radiation with a wavelength of 1.54 Å. XRD patterns were recorded in the range of $10° \leq 2\theta \leq 90°$ at a scanning rate of 2°/min for qualitative analysis.

Due to the limitations of SEM in revealing fine topological details, atomic force microscopy (AFM) was used to analyze the morphology of Metal-Phosphate Bio-Active Glass. Specifically, an NTEGRA Probe Nano Laboratory System manufactured by NT-MDT in Moscow, Russian Federation was used. The system was equipped with an NSG01 cantilever that had a tip with a resolution of 10 nm.

3. RESULTS AND DISCUSSION
3.1. Morphological Study

The morphology of powder samples sintered at 780°C for 2h with and without varying concentrations of Ag_2O (0, 0.25, 0.5 and 0.75g) is shown in Figure 1, evaluated using a field emission scanning electron microscopy image. Sintered sample powders are spherical with aggregation of particles, as can be seen plainly (Figure 1a).
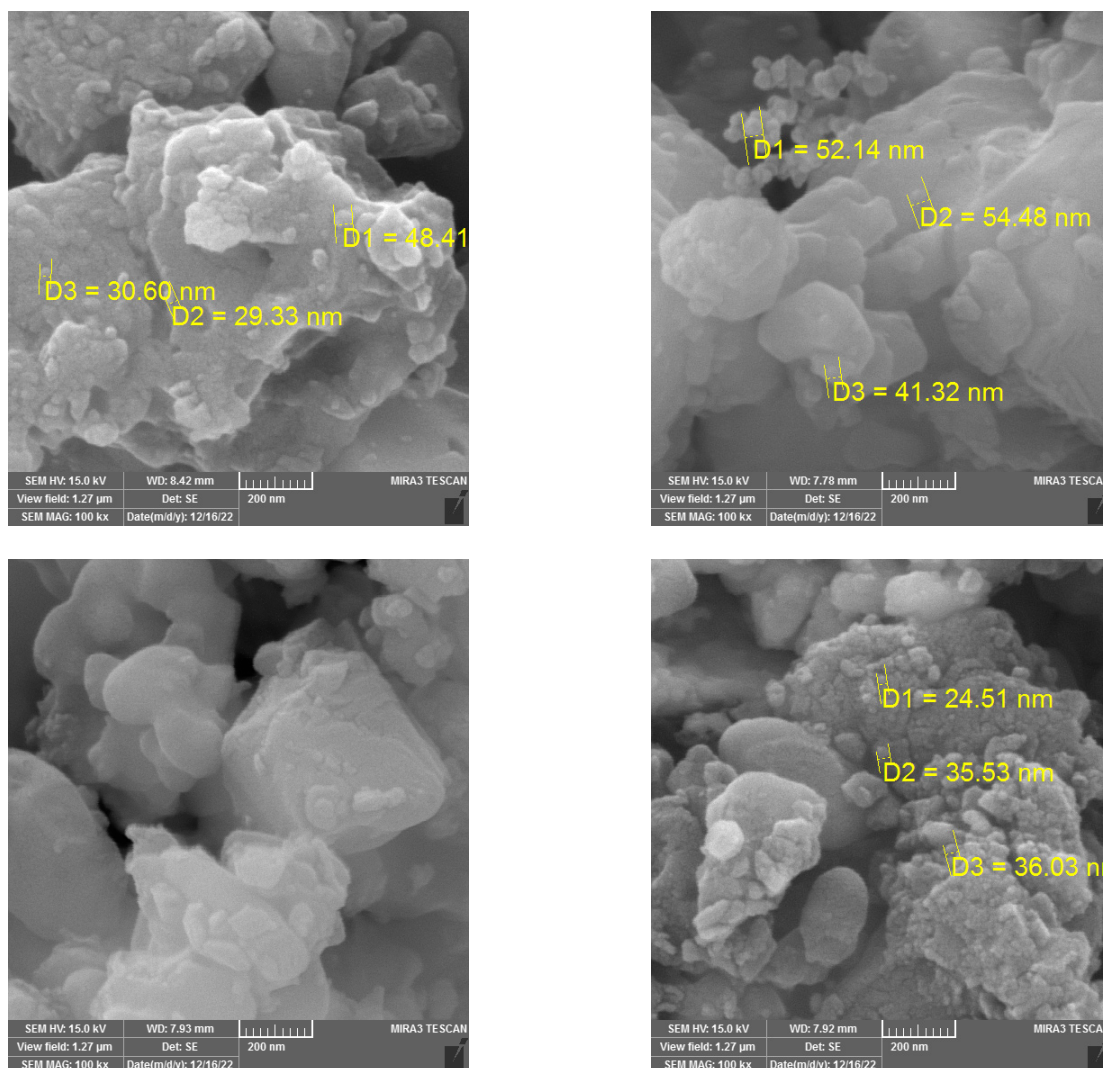
Figure 1. SEM Surface characteristics of calcium phosphate ceramic with (a) - 0 wt% Ag_2O, (b) - 0.25 wt% Ag_2O, (b) - 0.5 wt% Ag_2O, and (c) - 0. 75 wt% Ag_2O

Micrographs of Ag_2O-free composites show the grains coalescing and Surface particles are larger than Ag_2O (0.25, 0.5, and 0.75g) particles (Figure 1b-d). The results show that Ag_2O nucleation occurred on the surfaces of all the ceramics, and the Ag_2O-rich ceramics exhibited more particle growth. SEM examination leads us to the conclusion that adjusting the Ag_2O concentration in the bioactive glass can influence the rate at which the bioactive layer forms on its surface. In other words, the addition of Ag_2O leads to the depolymerization of $(PO_4)_3$ and the formation of a compact phosphate network.

In Figure 2a, it can be seen that, the composite without Ag_2O particles were formed as irregular dense block shapes with dispersion of agglomerates particles over the composite surface. Figures 2a-d manifest the interaction between the

ingredients including Ag_2O loaded on the surface of metal-phosphate bioactive glass which confirmed by EDS elemental analysis. Carbon, Oxygen, Nitrogen, Sodium, Phosphorus, Strontium, and Silver were all added to form the metal-phosphate composite bioactive glass that provided experimentally. Also, the SEM photos revealed that the addition of Ag_2O particles leads to form homogenous composites with effective attraction between the components to produce identity agglomeration shape. Increasing of Ag_2O to the composites contents leads to formation of smaller particles size as it appears in the external area of the SEM photography's. The surface pictures demonstrated that the P_2O_5 substrates with the $Ag_2O/CaCO_3/SrCo_3/Na_2CO_3$ had been successfully manufactured.
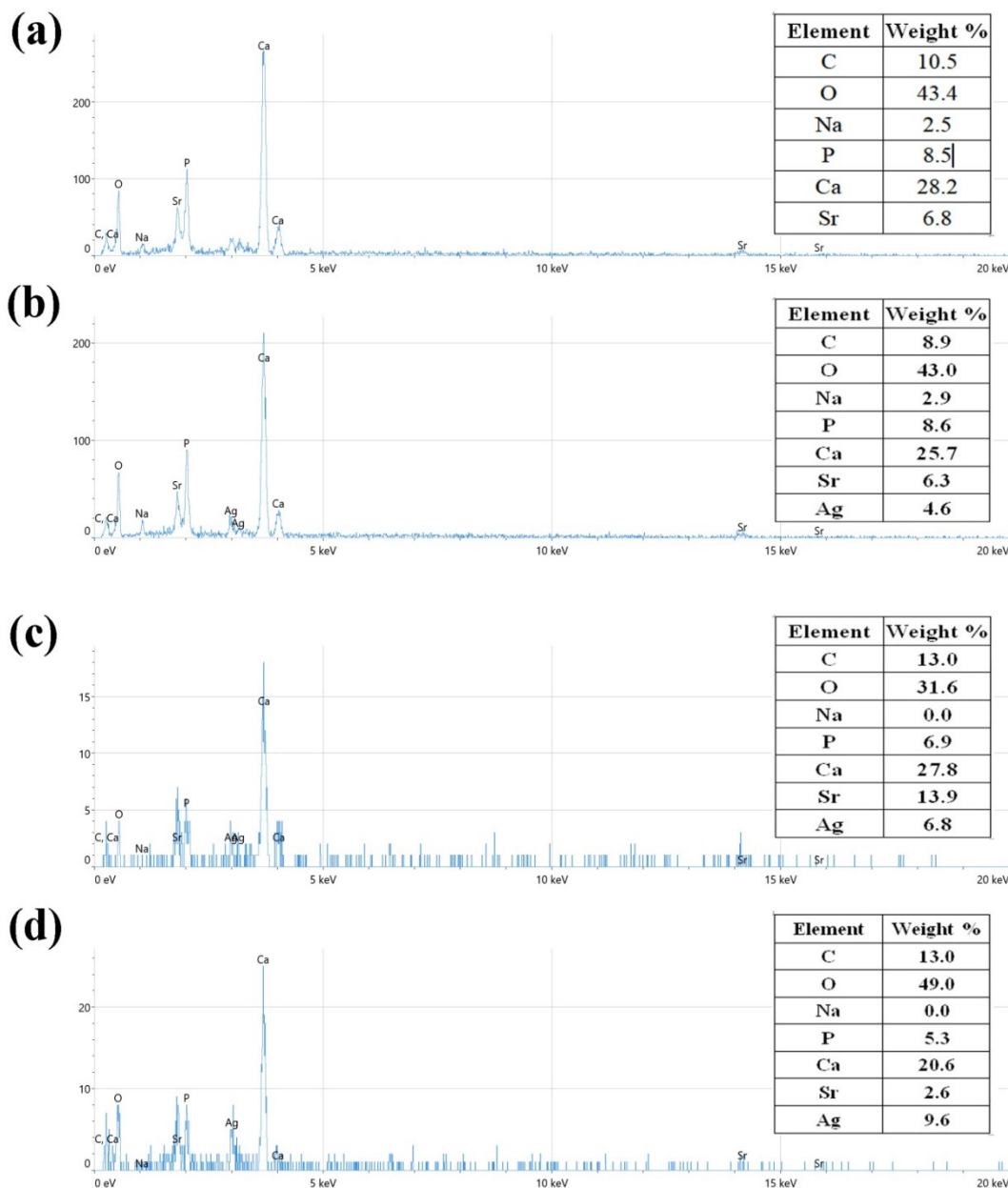
Figure 2. EDX analysis of calcium phosphate ceramic with (a) - 0 g Ag_2O, (b) - 0.25 g Ag_2O, (c) - 0.5 g Ag_2O, and (d) - 0. 75 g Ag_2O

3.2. X-ray diffraction

Figure 3 shows the XRD patterns of the samples sintered at 780 °C for 2h without and with different contents of Ag_2O (0. 0.25 ,0.5 and 0.75g). The diffraction pattern of the phosphate bio active glass composites sintered without Ag_2O displays the Strontium di-phosphate ($Sr_2O_7P_2$) ((orthorhombic - a=8.9459 Å b=5.4133 Å c=13.2114 Å) and the Calcium di-phosphate ((tetragonal - a=6.6858 Å c=24.1470 Å)) ($Ca_2O_7P_2$) (Figure 3). The reflections for phosphate bioactive glass composites without Ag_2O at 25.74°, 26.02°, 33.6947°, 36.3317°, 47.53°, 48.74° in the XRD pattern can be indexed to (210), (013), (204), (303), (322), and (413) planes of Strontium diphosphate, respectively. While the reflections at 26.94,

26.94, 27.89, 29.12, 29.68, 30.09, 32.11, 35.47, 38.51, 39.77, 43.48, 44.59, 45.43, 64.81, and 77.71 can be indexed to (201), (202), (023), (008), (121), (117), (125), (119), (223), (034), (035), (129), (337), and (1316) planes of calcium diphosphate, respectively. The appearance of a new phase relative to Ag$_2$O (cubic – a = 4.7600 Å) was detected after the addition of 0.25, 0.5 and 0.75 g Ag$_2$O (Figure 3b–d). At higher contents of Ag$_2$O (after 0.5 g Ag$_2$O), the intensity of calcium diphosphate and strontium diphosphate increased (Figure 3c–d). The reflections at 32.79°, 37.73° and 54.29° can be indexed to (111), (200) and (220) of Ag$_2$O, respectively.
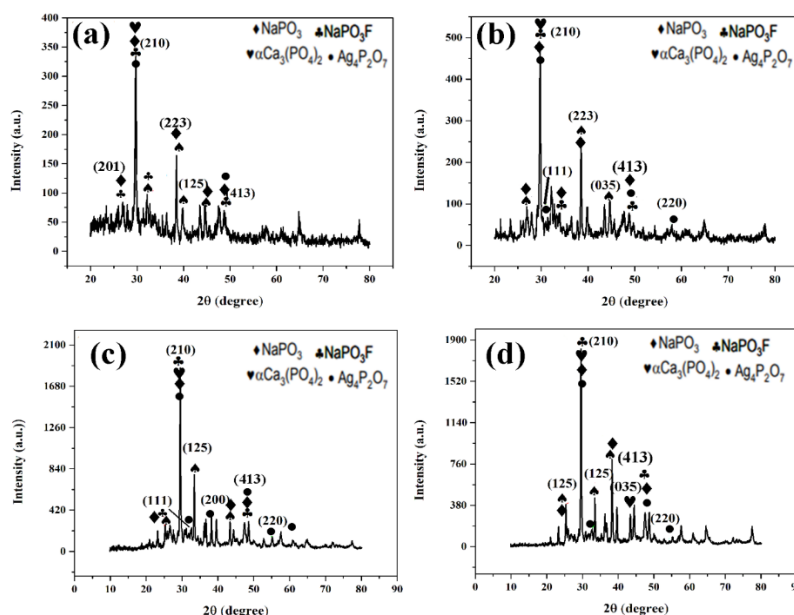
Figure 3. X-ray diffraction patterns of mixture of raw materials with different content of Ag$_2$O, (a) – 0 g Ag$_2$O, (b) - 0.25 g Ag$_2$O, (c) - 0.5 g Ag$_2$O, and (d) - 0.75 g Ag$_2$O.

In general, the increase in peak width in the X-ray diffraction and in the peak profile analysis as a result of dislocation growth is by reason of an increase in lattice strain and crystallite size, as a result of dislocation growth.
Equation (1) shows how to determine the size of a crystallite using the Scherrer formula, which is given below[23, 24]:

$$D = K\lambda/\beta \cdot \cos\theta \qquad (1)$$

where k is the shape factor (0.9), d is the crystallite size in nm, λ is the wavelength of X-ray (Cu K$_\alpha$ = 0.15406 nm), and β$_{hkl}$ is the full width at half maxima (FWHM) of an individual peak at 2θ.

Figure 4a and b show the average crystallite size and micro strain measurements for the phosphate bioactive glass composites with and without Ag$_2$O, respectively. The average crystallite size was decreased from 36.2 nm to 31.7, 31.0, and 32.8 nm with increased Ag$_2$O from 0 g to 0.25, 0.5, and 0.75 g within the composites, respectively.

The average lattice strain was increased from 4.41·10^{-3} to 4.40·10^{-3} with increased Ag$_2$O from 0 g to 0.5g within the composites (Figure 4b). Lattice strain is important because it can effect on the ceramic performance and full width at half maximum (FWHM: β$_{hkl}$) of X-ray diffraction peaks; in other word, lattice strain is a measure of the distribution of lattice constants arising from crystal imperfections, such as lattice disruptions and dislocations, in which crystallite size reduction can induces a large amount of strain.
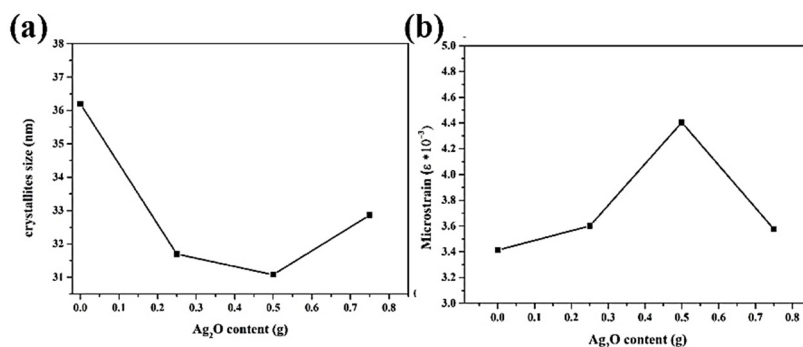
Figure 4. Average crystallites size and microstrain of phosphate bio active glass composites with different content of Ag$_2$O

3.3. Surface topography

AFM is used to measure the surface topography and roughness of materials [25, 26]. In this study, Metal-Phosphate bio-active glass has been prepared with different concentrations of silver oxide and tested its surface roughness using AFM. By analyzing the AFM data, the results show that the surface roughness decreased as the concentration of silver oxide increased up to a certain point, and then increased again at higher concentrations. This information can be useful in optimizing the composition of prepared glass material for specific applications where surface roughness is an important factor. Therefore, AFM is an important tool for characterizing and optimizing the properties of metal-phosphate Bio-active glass material.

The addition of silver oxide to Phosphate bio-active Glass can potentially affect the surface roughness of the resulting material, but the direction of this effect may depend on various factors, such as the concentration of silver oxide and the processing conditions.

In general, the addition of a foreign material to a glass matrix can introduce variations in the surface topography and roughness. Silver oxide is known to be a powerful nucleating agent, which can promote the formation of crystals or nanoparticles within the glass matrix [27]. These crystals or nanoparticles may alter the surface morphology of the glass, potentially increasing or decreasing its roughness, depending on their size, shape, and distribution. The decrease in surface roughness (Sq) observed in Figure 5 and Table 1 as the amount of silver oxide increased from 0g to 0.5g in the metal-phosphate Bio-active glass can be attributed to several factors. Firstly, silver oxide can act as a smoothing agent, filling in small surface irregularities and voids to reduce surface roughness. Secondly, the addition of silver oxide can inhibit crystal growth in the glass by interacting with the glass matrix and preventing the growth of crystalline phases that contribute to surface roughness [28]. Lastly, the presence of silver ions can promote the nucleation and growth of smaller particles during sintering, leading to a reduction in particle size and contributing to a smoother surface. In contrast, the increase in Sq observed as the concentration of silver oxide increased from 0.5g to 0.75g in the metal-phosphate Bio-active glass can be attributed to several factors. Firstly, there is a possibility of agglomeration or clustering of silver oxide particles during the sintering process at higher concentrations, leading to the formation of larger surface irregularities and voids. Secondly, the addition of a higher concentration of silver oxide may result in the formation of new phases in the glass, such as silver phosphate or silver strontium phosphate, which could contribute to an increase in surface roughness. Lastly, the higher concentration of silver oxide may lead to an increase in the crystallinity of the glass, which can also contribute to an increase in surface roughness.

Table 1. Surface roughness (Sq), average roughness (Sa), and maximum height of the surface (Sz) of metal-phosphate Bio-Active glass samples with varying silver oxide content.

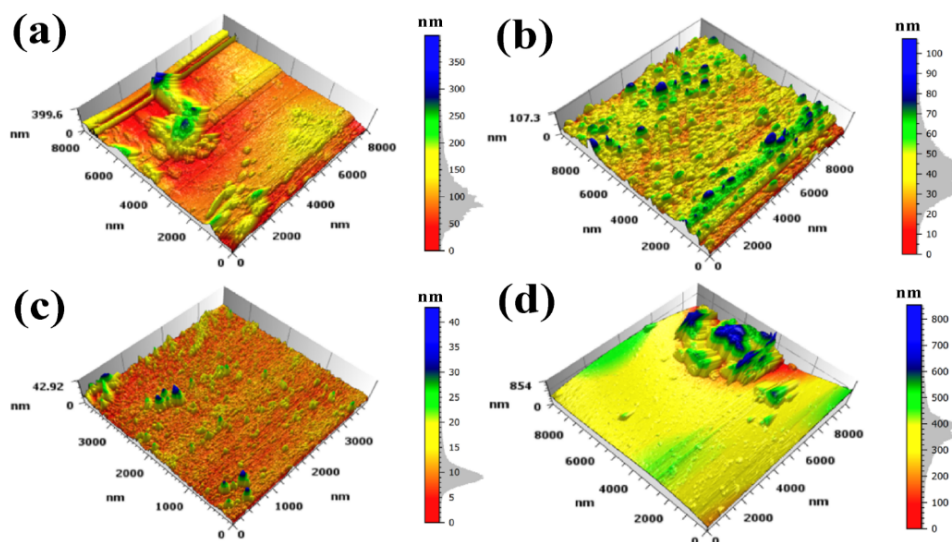| Surface roughness (nm)	Ag_2O content (g)			
	0	**0.25**	**0.5**	**0.75**
Sq	42.42	12.67	3.104	89.02
Sz	399.6	107.3	42.9	854.0
Sa	31.28	9.9	1.974	62.77

Figure 5. 3D topography of metal-phosphate Bio-Active glass samples with varying silver oxide content. (a) – 0 g Ag_2O, (b) - 0.25 g Ag_2O, (c) - 0.5 g Ag_2O, and (d) - 0.75 g Ag_2O

4. CONCLUSION

In this research, it has demonstrated that the concentration of silver oxide has a significant impact on the physical and structural properties of phosphate Bio-active glass. The addition of Ag_2O to the composite material led to smaller particle sizes and more distinct boundaries between grains, as well as a reduction in the average crystallite size. This

suggests that the incorporation of Ag$_2$O can improve the performance of the glass in various applications. Moreover, results showed a slight increase in the average lattice strain upon the addition of Ag$_2$O. These findings have important implications for the design and optimization of phosphate Bio-active glass for various biomedical and industrial applications. Further research is necessary to explore the specific mechanisms underlying these effects and to investigate the potential of these materials for specific applications.

ORCID

Ruqaya H. Hussian, https://orcid.org/0009-0006-0003-6988; **Dunia K. Mahdi,** https://orcid.org/0000-0002-0976-5531

REFERENCES

[1] Md.M. Pereira, A. Clark, and L. Hench, "Calcium phosphate formation on sol-gel-derived bioactive glasses in vitro," Journal of Biomedical Materials Research. **28**(6), 693-698 (1994). https://doi.org/10.1002/jbm.820280606

[2] R.F. Richter, T. Ahlfeld, M. Gelinsky, and A. Lode, "Composites consisting of calcium phosphate cements and mesoporous bioactive glasses as a 3D plottable drug delivery system," Acta Biomaterialia, **156**, 146-157, (2023). https://doi.org/10.1016/j.actbio.2022.01.034

[3] A. Obata, D.S. Brauer, and T. Kasuga, editors, *Phosphate and Borate Bioactive Glasses*, (Royal Society of Chemistry, 2022).

[4] D.S. Brauer, "Structure and Thermal Properties of Phosphate Glasses," in: *Phosphate and Borate Bioactive Glasses*, (CPI Group Ltd, Croydon, UK, 2022), pp.10-24.

[5] A. El-Ghannam, "Bone reconstruction: from bioceramics to tissue engineering," Expert review of medical devices, **2**(1), 87-101 (2005). https://doi.org/10.1586/17434440.2.1.87

[6] D.C.J. Cancian, E. Hochuli-Vieira, R.A.C. Marcantonio, and I.R. Garcia Jr., "Utilization of autogenous bone, bioactive glasses, and calcium phosphate cement in surgical mandibular bone defects in Cebus apella monkeys," International Journal of Oral & Maxillofacial Implants, **19**(1), 73-79 (2004), https://www.quintpub.com/journals/omi/full_txt_pdf_alert.php?article_id=1259

[7] J. Massera, L. Petit, T. Cardinal, J.-J. Videau, M. Hupa, and L. Hupa, "Thermal properties and surface reactivity in simulated body fluid of new strontium ion-containing phosphate glasses," Journal of Materials Science: Materials in Medicine, **24**, 1407-1416, (2013). https://doi.org/10.1007/s10856-013-4910-9

[8] J. Massera, A. Kokkari, T. Närhi, and L. Hupa, "The influence of SrO and CaO in silicate and phosphate bioactive glasses on human gingival fibroblasts," Journal of Materials Science: Materials in Medicine, **26**, 1-9 (2015). https://doi.org/10.1007/s10856-015-5528-x

[9] V. Salih, K. Franks, M. James, G. Hastings, J. Knowles, and I. Olsen, "Development of soluble glasses for biomedical use Part II: the biological response of human osteoblast cell lines to phosphate-based soluble glasses," Journal of Materials Science: Materials in Medicine, **11**, 615-620, (2000). https://doi.org/10.1023/A:1008901612674

[10] G. Kaur, O.P. Pandey, K. Singh, D. Homa, B. Scott, and G. Pickrell, "A review of bioactive glasses: their structure, properties, fabrication and apatite formation," Journal of Biomedical Materials Research Part A, **102**(1), 254-274 (2014). https://doi.org/10.1002/jbm.a.34690

[11] A. Shearer, M. Montazerian, J.J. Sly, R.G. Hill, and J.C. Mauro, "Trends and perspectives on the commercialization of bioactive glasses," Acta Biomaterialia, **160**(1), 14-31 (2023). https://doi.org/10.1016/j.actbio.2023.02.020

[12] L. Huang, W. Gong, G. Huang, J. Li, J. Wu, and Y. Dong, "The additive effects of bioactive glasses and photobiomodulation on enhancing bone regeneration," Regenerative Biomaterials, **10**, rbad024 (2023). https://doi.org/10.1093/rb/rbad024

[13] A. Mishra, J. Rocherullé, and J. Massera, "Ag-doped phosphate bioactive glasses: Thermal, structural and in-vitro dissolution properties," Biomedical glasses, **2**(1), 38-48 (2016). https://doi.org/10.1515/bglass-2016-0005

[14] J. Delben, O. Pimentel, M. Coelho, P. Candelorio, L. Furini, F. Alencar dos Santos, et al., "Synthesis and thermal properties of nanoparticles of bioactive glasses containing silver," J. Therm. Anal. Calorim. **97**(2), 433-436, (2009). https://doi.org/10.1007/s10973-009-0086-4

[15] U. Pantulap, M. Arango-Ospina, and A.R. Boccaccini, "Bioactive glasses incorporating less-common ions to improve biological and physical properties," J. Mater. Sci. Mater. Med. **33**, 1-41 (2022). https://doi.org/10.1007/s10856-021-06626-3

[16] R. Koohkan, T. Hooshmand, D. Mohebbi-Kalhori, M. Tahriri, and M.T. Marefati, "Synthesis, characterization, and in vitro biological evaluation of copper-containing magnetic bioactive glasses for hyperthermia in bone defect treatment," ACS Biomater. Sci. Eng. **4**(5), 1797-1811 (2018). https://doi.org/10.1021/acsbiomaterials.7b01030

[17] S. Chitra, P. Bargavi, M. Balasubramaniam, R.R. Chandran, and S. Balakumar, "Impact of copper on in-vitro biomineralization, drug release efficacy and antimicrobial properties of bioactive glasses," Mater. Sci. Eng. C. Mater. Biol. Appl. **109**, 110598 (2020). https://doi.org/10.1016/j.msec.2019.110598

[18] M. Azevedo, G. Jell, M. O'donnell, R. Law, R. Hill, and M. Stevens, "Synthesis and characterization of hypoxia-mimicking bioactive glasses for skeletal regeneration," J. Mater. Chem. **20**, 8854-8864 (2010). https://doi.org/10.1039/C0JM01111H

[19] N. Alasvand, S. Simorgh, M.M. Kebria, A. Bozorgi, S Moradi., V.H. Sarmadi, K. Ebrahimzadeh, et al., "Copper/cobalt doped strontium-bioactive glasses for bone tissue engineering applications," Open Ceramics, **14**, 100358 (2023). https://doi.org/10.1016/j.oceram.2023.100358

[20] M. Ebrahimi, S. Manafi, and F. Sharifianjazi, "The effect of Ag$_2$O and MgO dopants on the bioactivity, biocompatibility, and antibacterial properties of 58S bioactive glass synthesized by the sol-gel method," Journal of Non-Crystalline Solids, **606**, 122189 (2023). https://doi.org/10.1016/j.jnoncrysol.2023.122189

[21] S. Sánchez-Salcedo, A. García, A. González-Jiménez, and M. Vallet-Regí, "Antibacterial effect of 3D printed mesoporous bioactive glass scaffolds doped with metallic silver nanoparticles," Acta Biomaterialia, **155**, 654-666 (2023). https://doi.org/10.1016/j.actbio.2022.10.045

[22] A. Ahmed, A. Ali, D.A. Mahmoud, and A. El-Fiqi, "Study on the preparation and properties of silver-doped phosphate antibacterial glasses (Part I)," Solid State Sciences, **13**(5), 981-992 (2011). https://doi.org/10.1016/j.solidstatesciences.2011.02.004

[23] B.D. Cullity, *Elements of X-ray Diffraction*, (Addison-Wesley Publishing, 1956).

[24] A. Guinier, *X-ray diffraction in crystals, imperfect crystals, and amorphous bodies*, (Dover Publication, Inc., New York,, 1994).

[25] B. Stuart, G. Stan, A. Popa, M. Carrington, I. Zgura, M. Necsulescu, and D.M. Grant, "New solutions for combatting implant bacterial infection based on silver nano-dispersed and gallium incorporated phosphate bioactive glass sputtered films: A preliminary study," Bioactive Materials, **8**, 325-340 (2022). https://doi.org/10.1016/j.bioactmat.2021.05.055

[26] D. Chioibasu, L. Duta, G. Popescu-Pelin, N. Popa, N. Milodin, S. Iosub, et al. "Animal origin bioactive hydroxyapatite thin films synthesized by RF-magnetron sputtering on 3D printed cranial implants," Metals, **9**(12), 1332 (2019). https://doi.org/10.3390/met9121332

[27] N.T. Lo, "Second harmonic generation in germanotellurite glass ceramics doped with silver oxide," Th. Doct.: Université de Bordeaux : Universidade de Lisboa, 2015, https://tel.archives-ouvertes.fr/tel-01363649

[28] S. Aravindan, and V. Rajendran, and N. Rajendran, "Influence of Ag₂O on crystallisation and structural modifications of phosphate glasses," Phase Transitions, **85**(7), 630-649 (2012). https://doi.org/10.1080/01411594.2011.639013

ДОСЛІДЖЕННЯ СТРУКТУРНОГО ВПЛИВУ ОКСИДУ СРІБЛА В БІОАКТИВНОМУ ФОСФАТНОМУ СКЛІ

Рукайя Х. Хусан, Дунья К. Махді

Факультет фізики, Науковий коледж, Багдадський університет, Багдад, Ірак

Досліджено вплив різних концентрацій оксиду срібла на структуру та морфологію фосфатного біоактивного скла (PBG). PBG набувають популярності як потенційна заміна традиційному силікатному склу у біомедичних застосуваннях завдяки їх регульованій хімічній стійкості та винятковій біоактивності. При дослідженні за допомогою скануючого електронного мікроскопу композитів без Ag₂O було виявлено тенденцію до злиття зерен, а поверхневі частинки виявилися більшими, ніж у композитах з Ag₂O при концентраціях 0,25, 0,5 і 0,75 мас.%. Дослідження показало, що дифракційна картина фосфатних біоактивних скляних композитів, спечених без Ag₂O, показала присутність дифосфату стронцію та дифосфату кальцію. Рентгенограма цих композитів без Ag₂O виявила специфічні площини, які відповідали обом типам дифосфату. Однак, коли додавали Ag₂O, була виявлена нова кубічна фаза, і інтенсивність дифосфату кальцію та стронцію зростала з вищим вмістом Ag₂O. Рентгенограма композитів з Ag₂O відображала специфічні площини, які відповідали Ag2O. Іншими словами, відсутність Ag₂O в композиційному матеріалі призвела до більших розмірів частинок і менш чітких меж між зернами. Крім того, було виявлено, що при збільшенні концентрації Ag₂O від 0 до 0,25, 0,5 і 0,75 мас.% середній розмір кристалітів зменшився з 36,2 до 31,7, 31,0 і 32,8 нм відповідно. Ці результати свідчать про те, що додавання Ag₂O може ефективно зменшити середній розмір кристалітів композитних матеріалів. Крім того, у міру збільшення концентрації Ag₂O від 0 г до 0,5 мас.% у композиційному матеріалі середня деформація решітки збільшилася з $3,41 \cdot 10^{-3}$ до $4,40 \cdot 10^{-3}$. Простіше кажучи, додавання Ag₂O до композитного матеріалу призвело до незначного збільшення середньої деформації решітки.

Ключові слова: *фосфатне біоактивне скло (ФБС); силікатне скло; дифосфат кальцію; оксид срібла, карбонат стронцію (SrCo₃)*

EFFECTS OF QUANTUM CONFINEMENT ENERGY ON THE TRANSMITTANCE OF CADMIUM TELLURIDE (CdTe) WITHIN THE NEAR INFRARED REGION (700-2500NM)†

Ali Hussein Hammad Asal*, **Saeed Naif Turki Al-Rashid‡**

College of Education for Pure Sciences, University of Anbar, Ramadi, Iraq
Corresponding Author e-mail: ali21u3013@uoanbar.edu.iq ‡E-mail: esp.saeedn.turkisntr2006@uoanbar.edu.iq

This study investigates how the energy of quantum confinement affects the transmittance of cadmium telluride, because of the importance of this substance, as it crystallizes in the form of cubes as thin films that are used in solar cells and liquid crystal imaging devices, as well as in infrared optics [1]. The MATLAB computer program version (2012a) was used, which is based on the characteristic matrix theory and Brus model, in addition to the quantum confinement energy equation. We found that the transmittance value of the nano CdTe thin film at normal incidence reaches 96.4% at a quantum confinement energy E_{co} = 2.7eV and at a particle size P_S =2.6nm, while the value reaches 73.6% at a quantum confinement energy E_{co} = 0.01eV and at a particle size of P_S=50nm.
Keywords: *Transmittance; Energy gap; Quantum confinement Energy; Brus model; The characteristic matrix*
PACS: 73.22.f, 78.66.w, 78.67.n

I. INTRODUCTION

Reducing the size of semi-conducting materials to the nano-scale leads to a significant change in their physical properties, so they acquire unique properties that differ from those found in bulk materials [2]. In addition, the mechanical properties are considered at the top of the list of properties benefiting from the small size of the nanoparticles, with the presence of large numbers of atoms of the material on their outer surfaces. The hardness values of these materials will also increase, by reducing the dimensions of the particles of the material. And controlling the arrangement of its atoms [3]. This difference in material properties is due to the increase in surface area compared to volume, and to the of quantization of the energy levels of electrons within a specific dimension. This is known as quantum confinement [4]. Quantum confinement occurs when the particle dimensions of a material are equal to or smaller than the Bohr radius of an electron or hole, and quantum confinement is one of the direct effects of reducing the size of a material to the nanoscale as the energy levels of matter become discrete, its effect is shown by the change in the density of states and the energy gap of the material, thus the optical, electronic and electrical properties of materials become confinement scale dependent [5,6]. Quantum confinement can be in one dimension, that is, electrons or holes are allowed to spread in only one dimension, and their movement is restricted in the other two dimensions, and it is known as quantum wires. And it can be two-dimensional, that is, it allows electrons or holes to spread in two dimensions, and their movement is restricted in the third dimension, and it is known as a quantum energy well, but in the case of quantum dots, the system is described as zero dimensions [7].

II. THE EFFECT OF PARTICLE SIZE ON QUANTUM CONFINEMENT ENERGY

Quantum confinement energy mainly deals with the trapping of electrons .This energy is observed when there is an increase in the energy gap. It is very important because it determines the emission energy of the quantum dot [8]. Quantum dots can be described as semiconductor nanoparticles in which electrons are bound in all three directions. The process of trapping charge carriers in quantum dots leads to volume quantization, and this has important implications for the absorption and emission spectra that shift to short a wavelength as the size of the quantum dot decreases, this means that large quantum dots produce red a light while small quantum dots produce blue light thus the energy gap is tunable by changing the size of the quantum dots (QDs) based on the quantum confinement effect [9]. The equation for the quantum confinement energy for the ground state of quantum dots is given [10]:

$$E_{con} = \frac{\hbar^2\pi^2}{2r_{ps}^2} \left[\frac{1}{m_e^*} + \frac{1}{m_h^*}\right],\tag{1}$$

where r_{ps} is the radius of a spherical quantum dot, and m_e, m_h are the effective mass of the electron and hole.

By using the Brus model we obtain, the change in the energy gap with the change in particle size due to the effect of quantum confinement. It is an important theoretical model that considers both the effective masses' values of an electron and a hole, the quantum dot energy gap variation value (ΔE_g) is given according to this model in the following equation [11].

$$\Delta E_g = \frac{\hbar^2\pi^2}{2r_{ps}^2}\left[\frac{1}{m_e^*} + \frac{1}{m_h^*}\right] - \frac{1.786\,e^2}{\varepsilon\,r_{ps}} - \frac{0.124e^4}{h^2\varepsilon^2}\left[\frac{1}{m_e^*} + \frac{1}{m_h^*}\right]^{-1}.\tag{2}$$

And also

$$\Delta E_g = E_g^{nano}(r_{ps}) - E_g^{bulk}.$$

With which equation (2) takes the form [12]:

$$E_g^{nano}(r_{ps}) = E_g^{bulk} + \frac{\hbar^2\pi^2}{2r_{ps}^2}\left[\frac{1}{m_e^*} + \frac{1}{m_h^*}\right] - \frac{1.786\,e^2}{\varepsilon\,r_{ps}} - \frac{0.124e^4}{\hbar^2\varepsilon^2}\left[\frac{1}{m_e^*} + \frac{1}{m_h^*}\right]^{-1}. \tag{3}$$

The energy gap is inversely proportional to r_{ps}^2, as shown by the second component on the right-hand side of equation (3), Because the third and final terms are so small in comparison to the second term, they can be overlooked. Then equation (3) becomes.

$$E_g^{nano}(r_{ps}) = E_g^{bulk} + \frac{\hbar^2\pi^2}{2r_{ps}^2}\left[\frac{1}{m_e^*} + \frac{1}{m_h^*}\right]. \tag{4}$$

III. THE CHARACTERISTIC MATRIX

When electromagnetic radiation strikes a single thin film with two dividing borders that has been produced on the substrate material as shown in Fig1. Using the characteristic matrix which connects the optical permittivity of the system for any polarization and for both vertical and oblique incidence [13], the continuous tangential elements of the magnetic and electrical fields entering and leaving the system, and it is provided as the following equation [14].

$$\begin{bmatrix} B \\ C \end{bmatrix} = \begin{bmatrix} cos\delta & isin\delta/\eta_1 \\ i\eta_1 sin\delta & cos\delta \end{bmatrix} \begin{bmatrix} 1 \\ \eta_{sub} \end{bmatrix}. \tag{5}$$

The matrix's elements, which stand in for the electric and magnetic fields, are represented by the letters (B, C). The membrane's optical permittivity is represented by the number η_1, and the substrate's optical permittivity is represented by the number η_{sub}.
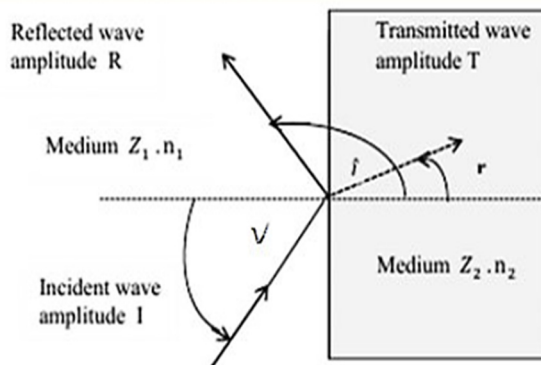
Figure (1) shows the geometry of a plane electromagnetic wave incident on a plane surface [15]

The reflectivity and transmittance value of the electromagnetic beam falling on a surface separating two different media is given by Fresnel's equations [16,15]

$$R = \left(\frac{\eta_\circ - \eta_1}{\eta_\circ + \eta_1}\right)^2, \tag{6}$$

$$T = \frac{4\eta_\circ\eta_1}{(\eta_\circ + \eta_1)^2}, \tag{7}$$

where η_1 and $\eta_\circ$ denote the appropriate effective refractive index for the incidence and penetration modes, respectively.

The value of the optical permittivity of the medium in for the vertical incidence of the wave is equal to the real part of the refractive index [17]:

$$\eta = y = n\,\vartheta = n, \tag{8}$$

where n is the real part of the refractive index of the medium, and ϑ is the admittance of free space. Its value may be neglected because it is very small ($2.65 \times 10^{-3}S$)

Since we use a thin film, the absorbance will be neglected because the thickness of the film is very small, so the reflectivity and transmittance become complementary to each other[4].

IV. ENERGY GAP

A semiconductor atom has a number of electrons in its outer shell, which are distributed into close energy levels as a result of the Pauli exclusion principle, which states that each energy level can accommodate two different electrons in the spin direction [18]. As a result of the convergence of atoms, the individual levels of atoms of matter form a continuous

set of energy levels known as energy bands, which represent the entire system when the temperature is zero (T = 0K). In a semiconductor these bands are either fully filled with electrons and known as the valence band, or they are empty known as the conduction band, the valence band is separated from the conduction band by the energy gap, and represents the energy difference between the top of the valence band and the bottom of the valence band delivery [19]. In a direct energy gap semiconductor, the electrons at the top of the valence band have the same momentum (k) as the holes below the conduction band, as shown in the figure (2) where the probability of electron transfer between the two bands is high and the momentum is conserved (Δk = 0) [20]. The energy gap is closely related to the refractive index, and many attempts have been made to find mathematical equation that link the refractive index with the energy gap, perhaps the most important of which is the equation presented by Ravindra in 1979, which is given in the following equation [21]:

$$n = \alpha + \beta E_g \tag{9}$$

As: (α = 4.048) and (β = −0.62 eV^{-1})this equation is independent of the temperature, and we notice that the value of the refractive index decreases with the increase of the energy gap
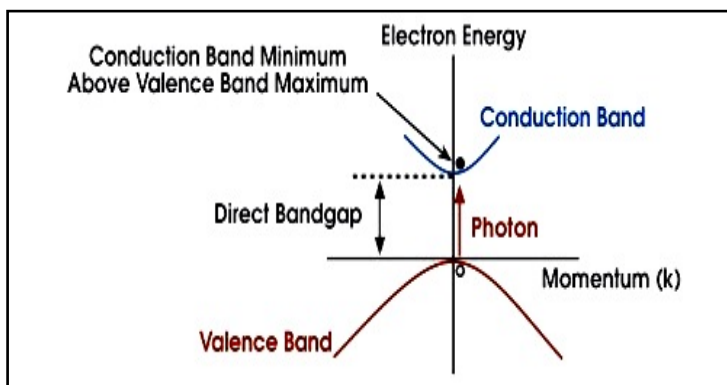
Figure 2. The direct energy gap in the semiconductor material [22]

V. RESULTS AND DISCUSSION

The transmittance change was studied as a function of the change in the quantum confinement energy of cadmium telluride (CdTe) to find out the highest value and the lowest value of the transmittance at which the material reaches as a result of the effect of quantitative confinement on the particle size. We use the MATLAB program version (2012a) which is based on the characteristic matrix and the Brus model in addition to the quantum confinement energy equation.

Fifteen optional incremental values for the radius of the material particles were determined (r_{ps} = 1.3nm to 25nm), through the relationship ($P_S = 2r_{ps}$), we noticed that the material behaves naturally similar to its behavior in the natural state at large size (i.e. bulk material). But with a gradual reduction in size, it was found that there is a wide change in the transmittance of the material, in addition to a wide change in the energy gap, as a result of the effect of quantum confinement on matter.

Table 1. The quantum confinement energy changes with the change of particle size and its effect on the energy gap and transmittance

particle size(nm)	Confinement Energy(eV)	Energy gap(eV)	Transmittance (%) at normal incidence
2.6	2.6587	4.1587	96.3843
2.8	2.2925	3.7925	93.3258
3	1.997	3.497	90.6656
4	1.1233	2.6233	82.7385
5	0.7189	2.2189	79.2631
6	0.4992	1.9992	77.4514
7	0.3668	1.8668	76.3864
8	0.2808	1.7808	75.7063
10	0.1797	1.6797	74.918
12	0.1248	1.6248	74.4949
14	0.0917	1.5917	74.2415
22	0.0371	1.5371	73.8269
30	0.02	1.52	73.6972
40	0.0112	1.5112	73.6313
50	0.0072	1.5072	73.6008
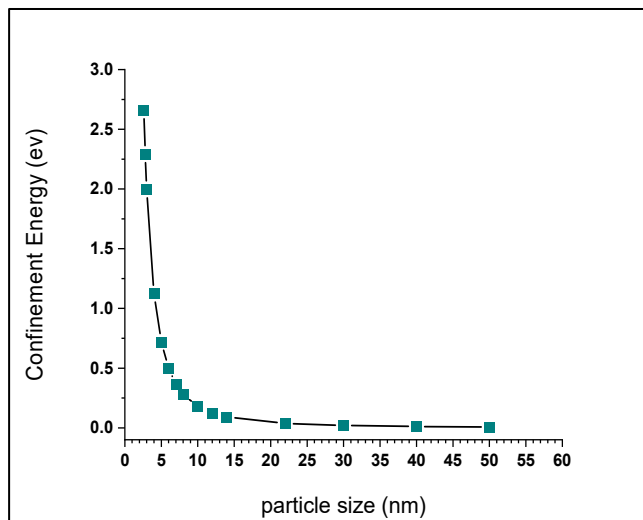
Figure 3. The quantum confinement energy of cadmium telluride (CdTe) as a function of the particle size

We notice from the Figure (3) above that the quantum confinement energy has high values at small nanoscales because the effect of quantum confinement is large when the size of the nanoparticle becomes smaller or equal to the Bohr radius of the natural exciton. while the quantum confinement energy value is low at large nanoscales.

We note from Figure 4&5 that the transmittance at normal incidence increases with the increase in the quantum confinement energy at small nanoscales and begins to decrease when the quantum confinement energy decreases at the large nanoscales. Where it was observed that the transmittance value of the nano CdTe thin film reaches (96.4%) at a quantum confinement energy (E_{co} = 2.7eV) and at a size (P_S = 2.6nm) and at an energy gap (E_g = 4.2eV), while at a size (PS = 50nm) it reaches the transmittance value to (73.6%) at a quantum confinement energy (E_{co}=0.01eV) and at an energy gap (E_g = 1.5eV), This can be explained when the particle size becomes smaller or equal to the Bohr diameter of the natural exciton, the effect of quantum confinement is large, and therefore the energy gap will increase at small sizes, and since the energy gap is inversely proportional to the refractive index as shown in equation (9), its increase It leads to a decrease in the refractive index, a decrease in the refractive index leads to an increase in the transmittance. But when the value of the energy gap decreases when the effect of quantum confinement on the material decreases, then the transmittance value begins to decrease at large sizes.
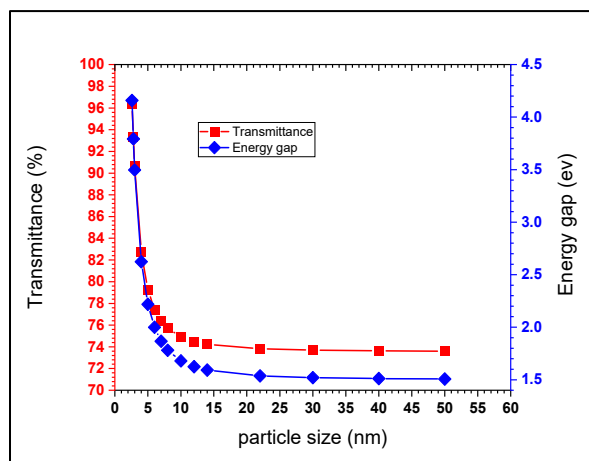
Figure (4) The transmittance at normal incidence and energy gap for cadmium telluride (CdTe)as function of particle size at the nanoscale
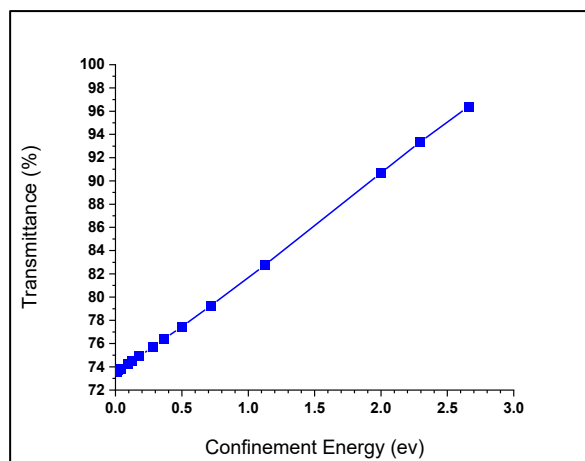
Figure (5) The transmittance of cadmium telluride (CdTe) at normal incidence as a function of the quantum confinement energy

VI. CONCLUSION

It was found that the transmittance at normal incidence of the nano CdTe thin film at the smallest particle size P_S = 2.6nm is as high as 96.4% because the confinement energy is high in the small sizes, while the transmittance at the largest particle size P_S =50nm is low to 73.6% because the quantum confinement energy is low or almost non-existent in the large sizes. The increase in transmittance because the particle size becomes smaller or equal to the normal Bohr diameter of the exciton, the quantum confinement effect increases, and thus the energy gap increases. An increase in the energy gap leads to an increase in the transmittance, while the lower transmittance of the nano CdTe thin film is due to a decrease in the energy gap at these volumes because the quantum confinement effect is very small.

ORCID
Ali Hussein Hammad Asal, https://orcid.org/0009-0000-6855-4577
Saeed Naif Turki Al-Rashid, https://orcid.org/0000-0002-7622-1526

REFERENCES

[1] S. Adachi, *Optical constants of crystalline and amorphous semiconductors: numerical data and graphical information*, (Springer Science & Business Media, 2013).

[2] S. Suresh, "Semiconductor Nanomaterials, Methods and Applications: A Review," Nanoscience and Nanotechnology, **3**, 62-74 (2013). http://www.sapub.org/global/showpaperpdf.aspx?doi=10.5923/j.nn.20130303.06

[3] O. El-Kady, and A. Fathy, "Effect of SiC particle size on the physical and mechanical properties of extruded Al matrix nanocomposites," Materials and Design, **54**, 348-353 (2013). https://doi.org/10.1016/j.matdes.2013.08.049

[4] A. Al-Azzawi, *Light and Optics: Principles and Practices*, (CRC Press, Boca Raton, 2007).

[5] Scaff, Introduction to Nanotechnology (Science, Engineering & Applications) Series of Strategic and Advanced Techniques, Arabic Compendium of Translation, INSB: 139789953824437, (2011);

[6] G. Cao, *Nanostructures and Nanomaterials: Synthesis, Properties, and Applications*, (Imperial College Press, 2004).

[7] L. Banyai, and S.W. Koch, *Semiconductor Quantum Dots*, (World Scientific Publishing Co. Pte. Ltd, 1993).

[8] S.T. Harry, and M.A. Adekanmbi, "Confinement energy of quantum dots and the brus equation," *International Journal of Research-Granthaalayah*, **8**(11), 318-323 (2020). https://doi.org/10.29121/granthaalayah.v8.i11.2020.2451

[9] H.I. Ikeri, A.I. Onyia, and O.J. Vwavware, "The dependence of confinement energy on the size of quantum dots," Int. J. Sci. Res. Phys. Appl. Sci. **7**, 27-30 (2019). https://doi.org/10.26438/ijsrpas/v7i2.2730

[10] A. Irshad, et al., "Comparative energy bandgap analysis of zinc and tin based chalcogenide quantum dots," Revista Mexicana de Física, **68**(4), 041601 (2022). https://doi.org/10.31349/RevMexFis.68.041601

[11] H.A. Abid,, and S.N.T. Al-Rashid, "Study of the effect of nanoparticle size on the dielectric constant and concentration of charge carriers of Si and CdS materials," Chalcogenide Lett. **17**, 623-629 (2020). https://chalcogen.ro/623_AbidHA.pdf

[12] Z.L. Wang, Y. Liu, and Z. Zhang, *Handbook of nanophase and nanostructured materials II*, (Kluwer Academic Plenum, 2003).

[13] A.J. Ghazai, J.Thi-Qar Sci. **1**(2), 79-86 (2008). https://www.iasj.net/iasj/article/19431

[14] H.A. Macleod, *Thin-Film Optical Filters*, Fourth Edition, (CRC Press, Taylor & Francis Group, LLC, 2010).

[15] S.M. Abed, and S.N.T. Al-Rashid, "Study of effect the particle size on CdS optical properties as solar cell," https://www.researchgate.net/publication/335753749_Study_of_effect_the_particle_size_on_CdS_optical_properties_as_solar_cell

[16] Bass, Michael, et al, eds. *Handbook of optics*. Vol. 2. New York, McGraw-Hill, 1995);

[17] J.J. Zhong, A.R.L. Travis, F.P. Payne, and J.R. Moore, *The Antireflection Coating for a Wedge Flat Panel Projection Display*, (Convention Centre, San Jose, California, 2001).

[18] M. Di Ventra, S. Evoy, and J.R. Heflin, Jr., *Introduction to Nanoscale Science and Technology*, (Springer Science and Business Media, Inc, 2004).

[19] B.E.A. Saleh, and M.C. Teich, *Fundamentals of photonics*, (John Wiley & Sons, Inc, 1991).

[20] A. Goetzberger, J. Knobloch, and B. Vob, *Crystalline silicon solar cells*, (John Wiley & Sons Ltd, (1998).

[21] A. Ramizy, Z. Hassan, K. Omar, Y. Al-Douri, and M.A. Mahdi, "New optical features to enhance solar cell performance based on porous silicon surfaces," Applied Surface Science, **257**(14), 6112-6117 (2011). https://doi.org/10.1016/j.apsusc.2011.02.013

[22] H.S. Nalwa, *Photodetectors and Fiber Optics*, (Academic Press, 2001).

ВПЛИВ ЕНЕРГІЇ КВАНТОВОГО ОБМЕЖЕННЯ НА ПРОПУСКАННЯ ТЕЛЛУРИДУ КАДМІЮ (CdTe) В БЛИЖНІЙ ІНФРАЧЕРВОНІЙ ОБЛАСТІ (700-2500 нм)
Алі Хусейн Хаммад Асал, Саїд Наїф Туркі Аль-Рашид
Коледж освіти чистих наук, Університет Анбара, Рамаді, Ірак

В роботі досліджено, як енергія квантового обмеження впливає на пропускну здатність телуриду кадмію через важливість цієї речовини, оскільки вона кристалізується у формі кубів у вигляді тонких плівок, які використовуються в сонячних елементах і рідкокристалічних пристроях для зображення, а також в інфрачервоній оптиці [1]. Була використана версія комп'ютерної програми MATLAB (2012a), яка базується на теорії характеристичних матриць і моделі Брюса, на додаток до квантового рівняння енергії розміру. Ми виявили, що коефіцієнт пропускання тонкої плівки наноCdTe при нормальному падінні досягає 96,4% при енергії квантового обмеження $E_{co} = 2,7$ еВ і при розмірі частинок PS = 2,6 нм, тоді як значення досягає 73,6% при енергії квантового обмеження $E_{co} = 0,01$ еВ і при розмірі частинок P_s=50 нм.

Ключові слова: *пропускна здатність; енергетича щілина; енергія квантового обмеження; модель Бруса; характеристична матриця*

CURRENT STATUS OF SILICON STUDIES WITH Ge$_x$Si$_{1-x}$ BINARY COMPOUNDS AND POSSIBILITIES OF THEIR APPLICATIONS IN ELECTRONICS[†]

Nurulla F. Zikrillaev, Giyosiddin A. ugli Kushiev*, Sergey V. Koveshnikov, Bakhromjon A. Abdurakhmanov, Ugiloy K. Qurbonova, Abdujalol A. Sattorov
Tashkent State Technical University, Tashkent, Uzbekistan
*Corresponding Author e-mail: giyosiddinkushiev@gmail.com
Received May 17, 2023; revised June 12, 2023; accepted June 13, 2023

The paper determines the technological regimes for obtaining Ge$_x$Si$_{1-x}$ alloys by introducing germanium atoms into single-crystal silicon by the diffusion method. From the results of the study, it was found that the fundamental parameters of the formed Ge$_x$Si$_{1-x}$ alloys differ from the fundamental parameters of the original silicon, in particular, the energy values of the silicon band gap change. Elemental analysis of the surface of the samples showed that the concentration of silicon (in atomic percent) was ~70.66%, germanium ~29.36%. It was assumed that on the silicon surface and in the front part, a thin layer of an alloy of a compound with a composition of approximately Ge$_{0.3}$Si$_{0.7}$ (0.5÷2 μm) would be formed. Analysis of the spectra (p shows that the spectrum contains peaks ~303 cm^{-1} and ~406 cm^{-1}, corresponding to the Ge-Ge and Si-Ge bonds, respectively. It was also shown that Ge$_x$Si$_{1-x}$ binary compounds are a new material for modern electronics, the possibility of creating properties on their basis in electronics was shown. It is proposed on their basis to create devices with new functionality and highly efficient solar cells.
Keywords: *Diffusion; Germanium; Silicon; Solubility; Concentration; Binary complexes*
PACS: 41.50.+h, 61.05.C−,71.18.+y, 68.43.Jk, 68.47.Fg

INTRODUCTION

Today, special attention is paid to obtaining new materials with clusters of impurity atoms on the surface and in the bulk of a semiconductor, which is one of the main directions in the development of technology and physics of semiconductor materials [1–3]. In this case, one of the important tasks is the creation of a simple and cheap technology for the formation of clusters (clusters) of impurity atoms in the bulk of a crystal, which makes it possible to create nanoscale structures that change the properties of the base material. The methods of molecular beam epitaxy used to obtain such nanosized structures require expensive equipment.

Obtaining clusters of germanium (quantum dots) in a silicon lattice allows you to significantly expand the spectral region of sensitivity of photodetectors, solar cells. Germanium nanostructures in a solid solution of the Ge$_x$Si$_{1-x}$ type can be obtained on the basis of single-crystal silicon by the diffusion method. It is known [4] that germanium forms stable solid solutions in silicon up to a germanium concentration of 1650 K from 80%. At the same time, the maximum solubility of germanium in silicon reaches $1 \cdot 10^{22}$ at/cm^{-3}% at a temperature of 1430°C [5].

Upon cooling, the solid solution of germanium in silicon decomposes, and an excess of germanium forms accumulations (clusters) containing mainly germanium (the solubility of silicon in germanium at a temperature of 1550 K is less than 50% [6].

In this regard, the purpose of research is the development of a diffusion technology for obtaining germanium clusters in the volume of a silicon lattice and the study of the electrical parameters of these materials.

TECHNIQUE AND EXPERIMENTAL

Single-crystal p- and n-type silicon with resistivity of 10 and 100 Ohm·cm was chosen as the starting material. The size of all silicon samples was the same $8 \times 4 \times 1$ mm^3.

The diffusion technology for obtaining Ge$_x$Si$_{1-x}$ solid solutions with different ratios of components, although of great interest, is technologically unacceptable. This is mainly due to the very small diffusion coefficient of germanium atoms in silicon (D$_0 \sim 10^{-14}$ cm^2/s) [7], which requires a long diffusion time (Table 1) to obtain layers with a high concentration of germanium. Here x is the depth at which the concentration of germanium drops by a factor of e, the diffusion time is 20 hours.

We managed to solve the problem of a low diffusion coefficient due to the technology of low-temperature diffusion alloying of silicon with germanium. The technology of two-stage diffusion was used, which makes it possible to obtain a noticeable increase in diffusion coefficients [8-10]. Initial samples of silicon and diffusant - powdered germanium grade GES-1 were placed in quartz ampoules, after which evacuation was performed (residual pressure in the ampule p~ 10^{-5} mm Hg). The ampoules were placed in a diffusion furnace of the Vacuum Tube Furnace 1700°C brand at T = 300K.

Table 1. Diffusion coefficient and displacement length of germanium atoms in silicon

Temperature, °C	1250	1200	1150	1050	950
D, cm^2/s	$4 \cdot 10^{-13}$	$8 \cdot 10^{-14}$	$6.6 \cdot 10^{-15}$	$6 \cdot 10^{-17}$	$7 \cdot 10^{-19}$
x, µm	3.6·	3.12·	2.12·	1.42	1.6

The amount of diffusant was determined by calculation based on the volume of the ampoule and the required vapor pressure (concentration of atoms) of the diffusant at the diffusion temperature.

The furnace temperature was gradually increased at a rate of 5°C/min to a temperature of T = (900÷940) °C. Then the samples were kept t = (20÷25) min at this temperature, after which they continued heating at a rate of 150÷200°C/min to the final diffusion temperature. At this temperature, the samples were kept for t = 20 hours, after which the quartz ampoules were removed from the furnace and cooled at a rate of about 200°C/sec. Diffusion annealing of the obtained samples was carried out at the final diffusion temperature T = 1050; 1150; 1250 °C for t = 5 hours

DISCUSSION OF EXPERIMENTAL RESULTS

The electrical parameters of the samples were measured on an ECOPIA HMS-3000 Van der Pauw setup. The distribution profiles of the electrical parameters of the samples were studied by mechanical removal of layers (by 1 µm), measurement on the Van der Pauw installation, and further calculation of the profiles of resistivity, mobility, and concentration of carriers). The chemical composition of individual points of the samples was studied by energy dispersive X-ray microanalysis on a JSM-IT 200 SEM.
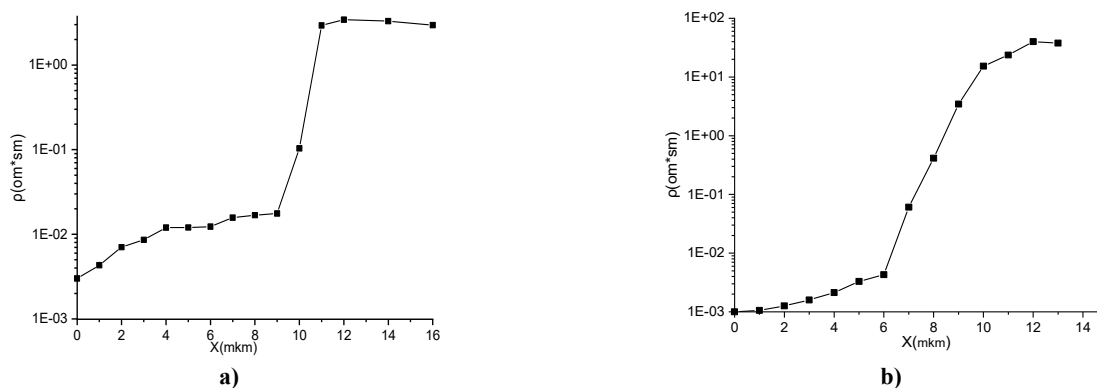
Figure 1. Changes in silicon resistivity with Ge$_x$Si$_{1-x}$ binary compounds a) sample of no. 2, b) sample of no. 3.

It is known that Raman spectroscopy is an accurate method for studying the bond states and symmetries of binary compounds of impurity atoms in semiconductors, which depend on the various local modes of vibrations of atoms and molecules formed in the crystal structure. Raman spectroscopy is also widely used to diagnose various structures formed in the bulk of silicon [11-13]. The measurements were carried out using a Raman spectrometer in the spectral range from 100 cm^{-1} to 3400 cm^{-1}. The spectra were determined using a diode laser with a wavelength of λ = 785 nm. During the measurement, a diffraction grating with a period of 1200 lines/mm was used. To clarify the presence and composition of new phases in the samples, X-ray phase analysis was performed on a Shimadzu XRD-100 diffractometer.

The results of (Fig. 1) the study of surface resistance showed that after diffusion, the surface resistance of the sample decreased by 5 orders of magnitude, which indicates a strong doping of the surface layer with antimony contained in germanium.
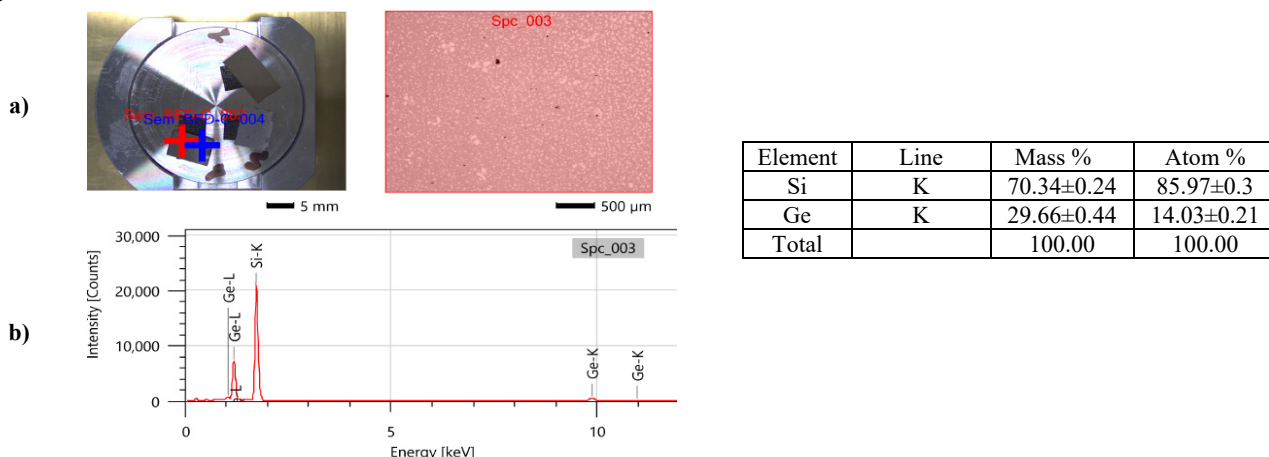

Element	Line	Mass %	Atom %
Si	K	70.34±0.24	85.97±0.3
Ge	K	29.66±0.44	14.03±0.21
Total		100.00	100.00

Figure 2. a) Topography of the surface of a silicon sample after doping with germanium atoms (sample no. 3).
b) X-ray energy-dispersive microanalysis of silicon samples doped with impurity germanium atoms

Figure 2a shows the topography of the surface of a silicon sample doped with germanium atoms, obtained on a JSM-IT 200 SEM in the secondary electron mode. The X-ray spectrum obtained at point 3 (Fig. 1,b) showed that the concentration of silicon atoms was 86%, germanium atoms - 14%, which corresponds to the composition of the $Ge_{0.14}Si_{0.86}$ solid solution.

From the literature data [14,15], it is known that it is impossible to obtain an equilibrium solid solution of germanium in silicon with a germanium concentration of more than 90%. The result obtained can be explained by the quenching of the solution due to the rapid cooling of the samples after diffusion.

Figure 3 shows an enlarged image of the sample area near point 4 and the elemental composition of the surface.

a)

b)

Element	Line	Mass %	Atom %
Si	K	5.59±0,09	13.28±0,2
Ge	K	94.41±0,68	86.72±0,63
Total		100.00	100.00
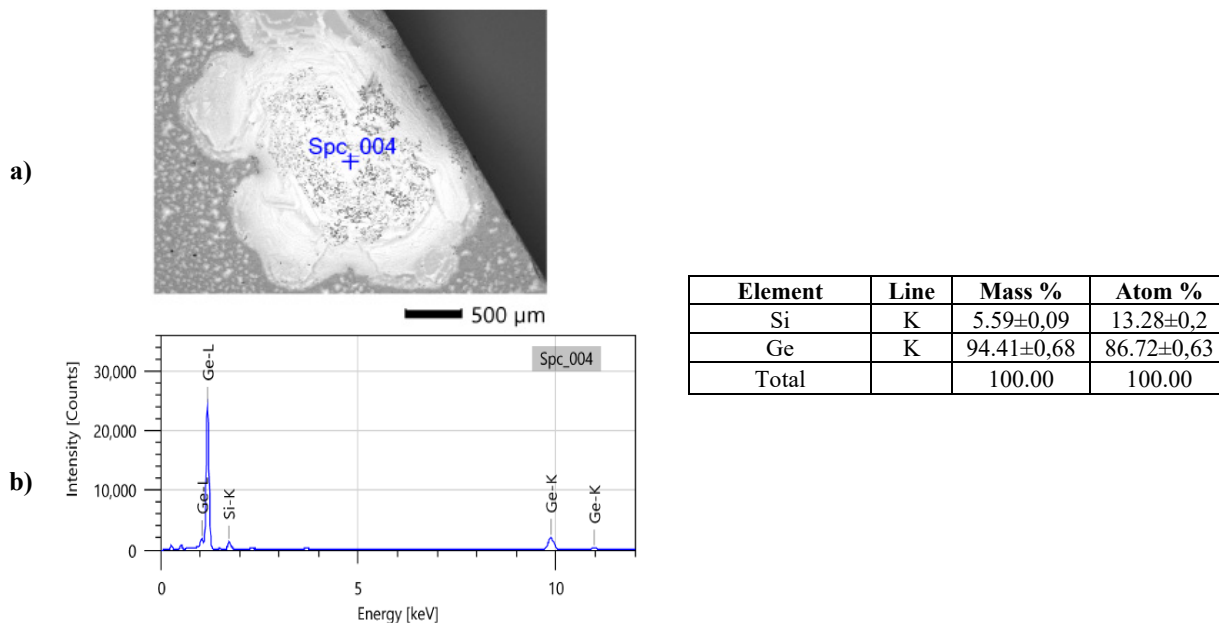
Figure 3. a) Topography of the annealed sample
b) X-ray energy-dispersive microanalysis of silicon samples doped with impurity germanium atoms

Judging by the appearance, at this point there is a drop of germanium that has adhered to the surface and has dissolved a significant amount of silicon. The composition corresponds to a solid solution of silicon in germanium $Ge_{0.87}Si_{0.13}$. This shows the possibility of obtaining germanium clusters containing a relatively small amount of silicon.

In order to reveal the presence of bonds of the Si-Ge and Ge-Ge type, the samples were studied by Raman spectroscopy. Figure 4 shows the spectrum of Raman scattering in samples of the original silicon (a) and silicon doped with germanium. The spectral measurement range is from 100 cm^{-1} to 3400 cm^{-1}. The spectra were determined using a diode laser with a wavelength of $\lambda = 785$ nm.
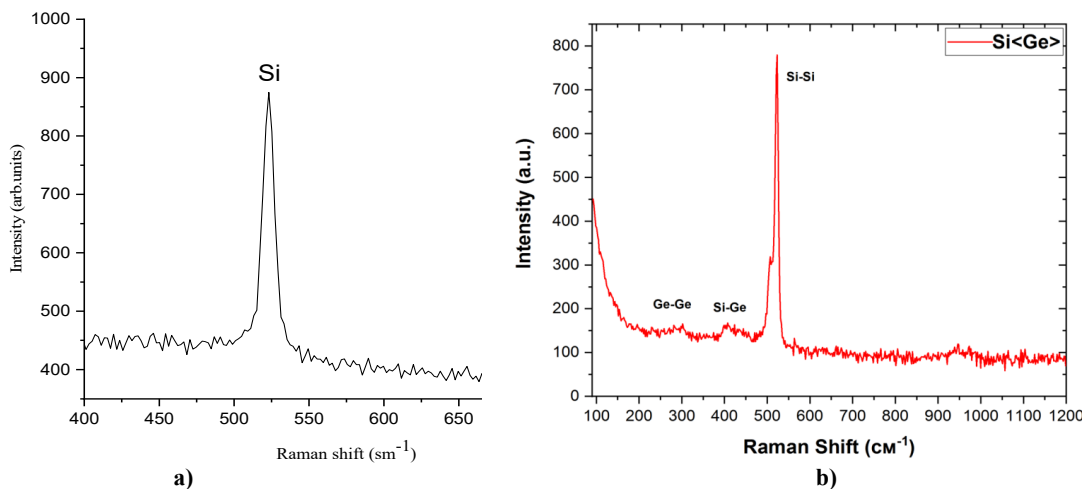
Figure 4. Raman spectrum: a) initial silicon (SEP-100); b) silicon doped with Ge (no. 3)

Analysis of the spectra (Fig. 3b) shows that the spectrum contains peaks of ~303 cm^{-1} and ~406 cm^{-1}, corresponding to the Ge-Ge and Si-Ge bonds, respectively. These results are in good agreement with the data presented in [16, 17]. The amplitude of these peaks is small, and the width is large, which indicates a low volume concentration of these bonds and a significant inhomogeneity of the samples, apparently associated with the "diffusion" inhomogeneity of the composition,

and, consequently, mechanical stresses in the samples. To test this assumption, the samples were annealed at a temperature of 1050 °C degrees for 5 hours. Figure 5 shows the Raman spectrum of this sample. There is no Si-Ge peak in the spectrum, and the Ge-Ge peak is noticeably narrower and higher. This indicates the decomposition of the solid solution with the formation of a new germanium phase containing an insignificant amount of silicon.
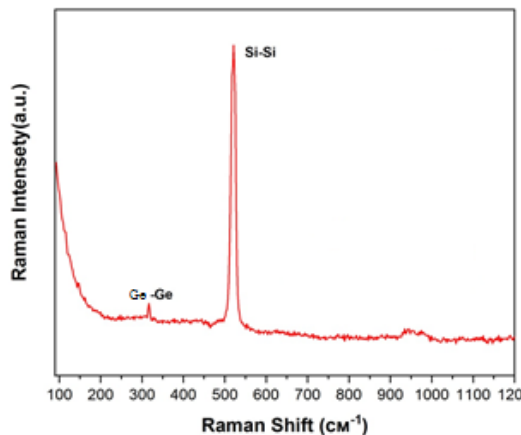

Figure 5. Raman spectrum of the annealed sample.

Figure 6 (a,b) shows the diffraction spectra obtained with a step of 0.05° at a scanning speed of 2°/min in the range of scanning angles of 10°-70°.
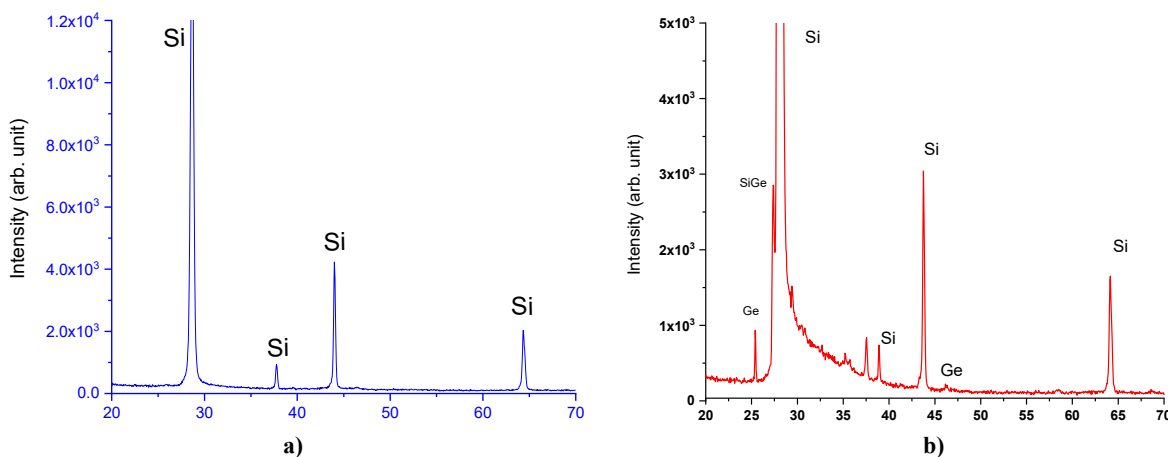
Figure 6. X-ray diffraction pattern: a) initial silicon [18]; b) silicon doped with germanium (no.3)

The diffraction spectra confirm the formation of germanium clusters during the diffusion treatment and the presence of inhomogeneities in the lattice parameter
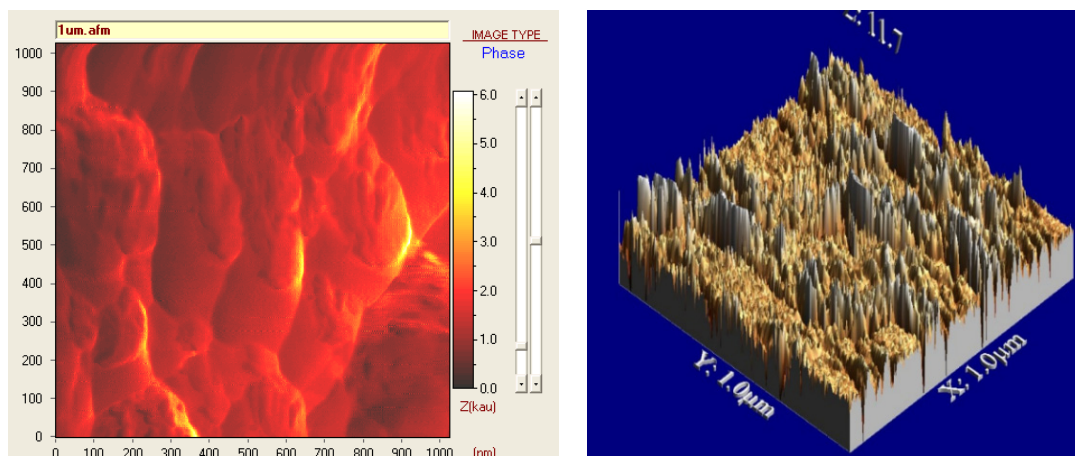
Figure 7. AFM images of the silicon surface doped with impurity germanium atoms

As can be seen from Figure 7, the formation of islands on the silicon surface doped with germanium impurity atoms leads to an increase in the average roughness size. This indicates the formation on the silicon surface of binary compounds Ge_xSi_{1-x}, the electric potential of which is higher than that of the initial silicon

An analysis of the experimental results showed the formation of binary compounds of the Ge_xSi_{1-x} type in the lattice of single-crystal silicon.

Studies of the state of germanium atoms in diffusion-doped silicon according to the developed technology showed that under diffusion conditions a solid mixture of the Ge_xSi_{1-x} type is formed in silicon [19-21]. It has been established that germanium impurity atoms in the silicon lattice create monoclusters with a certain composition in the formed binary cell.

CONCLUSION

From the analysis of the spectra obtained by the Raman spectrometer and X-ray diffraction analysis, it can be said that binary silicon-germanium (Ge_xSi_{1-x}.) compounds are formed in the silicon crystal lattice, the concentration of which will increase from the diffusion conditions and heat treatment (temperatures, time). Comparison of the results obtained with the available literature data established that binary compounds of the Ge_xSi_{1-x} type are formed in the lattices of single-crystal silicon. In addition, the results obtained show that silicon atoms enriched with germanium atoms lead to a change in the fundamental parameters of the initial silicon. Changing the fundamental parameters of the original silicon allows you to control the electrical, photoelectric and optical parameters of silicon, which makes it possible to obtain a new material with unique photoelectric and optical properties.

ORCID

Nurulla F. Zikrillaev, https://orcid.org/0000-0002-6696-5265; **Giyosiddin A. ugli Kushiev,** https://orcid.org/0009-0006-5847-6601

REFERENCES

[1] M. Tomassini, J. Veirman, R. Varache, et al., J. Appl. Phys. **119**, 084508 (2016). https://doi.org/10.1063/1.4942212

[2] A.S. Saidov, A.Sh. Razzakov, D.V. Saparov, Press Technical Physics Letters, **28**(11), 927-928 (2002). https://doi.org/10.1134/1.1526886

[3] J. Lindroos, D.P. Fenning, D.J. Backlund, E. Verlage, A. Gorgulla, S.K. Estreicher, H. Savin, and T. Buonassisi, J. Appl. Phys. **113**(20), 204906 (2013). https://doi.org/10.1063/1.4807799

[4] B. Cook, Energies, **15**(8), 2957 (2022). https://doi.org/10.3390/en15082957

[5] M. Ogino, Phys. Stat. Sol. (a), **72**, 535 (1982). https://doi.org/10.1002/pssa.2210720214

[6] T. Walthera, C. Humphreys, A.G. Cullis, Appl. Phys. Lett. **71**, 729 (1997). https://doi.org/10.1063/1.119627

[7] F.A. Trumbore, Bell System Technical Journal, **309**(1), 205 (1960). https://doi.org/10.1002/j.1538-7305.1960.tb03928.x

[8] N.F. Zikrillaev, S.V. Koveshnikov, S.B. Isamov, B.A. Abdurahmonov, and G.A. Kushiev, Semiconductors, **56**(1), 29-31 (2022). https://doi.org/10.1134/S1063782622020191

[9] R. Duffy, V.C. Venezia, J. Loo, M.J.P. Hopstaken, M.A. Verheijen, J.G.M. van Berkum, G.C.J. Maas, Y. Tamminga, T. Dao, C. Demeurisse, Appl. Phys. Lett. **86**, 081917 (2005). https://doi.org/10.1063/1.1869540

[10] M.I. Alonso, K. Winer, Raman spectra of c-Si1-xGex alloys, Physical Review B, **39**(14) 10056 (1989). https://doi.org/10.1103/PhysRevB.39.10056

[11] A. Picco, E. Bonera, E. Grilli, and M. Guzzi, Physical Review, **82**(11), 115317 (2010). https://doi.org/10.1103/PhysRevB.82.115317

[12] D. Rouchon, M. Mermoux, F. Bertin, J.M. Hartmann, Journal of Crystal Growth, **392**, 66 (2014). https://doi.org/10.1016/j.jcrysgro.2014.01.019

[13] A.R. Toshev, B.A. Abdurakhmanov, Kh.M. Iliev, S.A. Tachilin, and B.E. Egamberdiev, Surface Engineering and Applied Electrochemistry, USA, **46**(5), 505 (2010). https://doi.org/10.3103/S1068375510050170

[14] U. Schmid, N.E. Christensen, M. Cardona, Solid State Communications, **75**(1), 39 (1990). https://doi.org/10.1016/0038-1098(90)90154-4

[15] D. Duveau, B. Fraisse, F. Cunin, L. Monconduit, Chem. Mater. **27**(9), 3226 (2015). https://doi.org/10.1021/cm504413g

[16] H.-S. Tsai, Y.-Z. Chen, H. Medina, T.-Y. Su, T.-S. Chou, H.-S. Tsai, Y.-Z. Chen, et al., Physical Chemistry Chemical Physics, **17**(33), 21389 (2015). https://doi.org/10.1039/C5CP02469B

[17] E. Onaran, M.C. Onbasli, A. Yesilyurt, H.Y. Yu, A.M. Nayfeh, and A.K. Okyay, Optics Express, **20**(7), 7608 (2012). https://doi.org/10.1364/OE.20.007608

[18] J. Ghosh, S.K Chattopadhyay, A.K. Meikap, and S.K. Chatterjee Indian Academy of Sciences, **29**(4), 385 (2006). https://doi.org/10.1007/BF02704140

[19] D. Duveau, B. Fraisse, F. Cunin, and L. Monconduit, Chemistry of Materials, **27**(9), 3226 (2015). https://doi.org/10.1021/cm504413g

[20] A.S. Risbaev, J.B. Khujaniyazov, I.R. Bekpulatov, A.M. Rakhimov, J. Surf. Investig. **11**, 994 (2017). https://doi.org/10.1134/S1027451017050135

[21] N.F. Zikrillaev, G.A. Kushiev, S.B. Isamov, B.A. Abdurakhmanov, O.B. Tursunov, J. Nano- Electron. Phys. **15**, 01021 (2023). https://doi.org/10.21272/jnep.15(1).01021

ПОТОЧНИЙ СТАН ДОСЛІДЖЕНЬ КРЕМНІЮ З БІНАРНИМИ СПОЛУКАМИ Ge_xSi_{1-x} ТА МОЖЛИВОСТІ ЇХ ЗАСТОСУВАННЯ В ЕЛЕКТРОНІЦІ

Нурулла Ф. Зікріллаєв, Гійосіддін А. углі Кушієв, Сергій В. Ковешніков, Бахромджон А. Абдурахманов, Угілой К. Курбонова, Абдуджалол А. Сатторов

Ташкентський державний технічний університет, Ташкент, Узбекистан

Визначено технологічні режими отримання сплавів GexSi1-x шляхом введення атомів германію в монокристалічний кремній дифузійним методом. За результатами дослідження встановлено, що фундаментальні параметри сформованих сплавів Ge_xSi_{1-x} відрізняються від фундаментальних параметрів вихідного кремнію, зокрема змінюються енергетичні значення ширини забороненої зони кремнію. Елементний аналіз поверхні зразків показав, що концентрація кремнію (в атомних відсотках) становила ~70,66%, германію ~29,36%. Передбачалося, що на поверхні кремнію і в лицьовій частині утворюється тонкий шар сплаву сполуки складу приблизно $Ge_{0.3}Si_{0.7}$ (0,5÷2 мкм). Аналіз спектрів (р) показує, що спектр містить піки ~303 cm^{-1} and ~406 cm^{-1}, що відповідають зв'язкам Ge-Ge і Si-Ge відповідно. Також було показано, що бінарні сполуки Ge_xSi_{1-x} є нових матеріалів для сучасної електроніки, показано можливість створення на їх основі властивостей в електроніці, на їх основі запропоновано створювати прилади з новою функціональністю та високоефективними сонячними елементами.

Ключові слова: *дифузія; германій; кремній; розчинність; концентрація; бінарні комплекси*

STUDY THE EFFECT OF HYDROFLUORIC (HF) CONCENTRATION ON THE TOPOGRAPHY OF THE POROUS SILICON LAYER PREPARED BY SUNLIGHT PHOTOCHEMICAL ETCHING (SLPCE)[†]

Hassan A. Kadhem[a], Abdul Hakim Sh. Mohammed[b], Issa Z. Hassan[b], Rosure Borhanalden Abdulrahman[c]*

[a]*Ministry of Education, Open Educational College, Kirkuk Center, Iraq*
[b]*Department of Physics, college of Education for pure sciences, University of Kirkuk, Kirkuk, Iraq*
[c]*Department of Physics, College of Science, University of Kirkuk, Kirkuk, Iraq*
Corresponding Author: rbadulrahman@uokirkuk.edu.iq

Silicon nanocrystals have a vast range of potential applications, from improving the efficiency of solar cells and optoelectronic devices to biomedical imaging and drug delivery, wastewater treatment, and antibacterial activities. In this study a photochemical etching technique was used to create layers of porous silicon on a donor silicon wafer with orientation (111) and resistivity equal to 1-10 ohm·cm. The process involved focusing sunlight onto the samples using a telephoto lens with a suitable focal length of 30cm and a diameter of 90 mm, which provided sufficient energy to complete the chemical etching. By using a constant etching time of 60 minutes and different concentrations of hydrofluoric acid (ranging from 25% to 40%), layers with varying properties were obtained. The resulting surfaces were studied using the atomic force microscope (AFM), revealing the formation of different nanostructures and particles with varying shapes, sizes, and thicknesses depending on the preparation conditions. The average size of the particles was found to be 90.43nm at a concentration of 40% acid, while decreasing to 48.7nm at a concentration of 25% HF acid.
Keywords: *Photochemical Etching; Porous silicon; Morphology studies; Sunlight photochemical; AFM; SLPCE*
PACS: 81.65.Cf, 81.05.Rm, 61.72.uf, 68.37.Ps, 73.63.Bd

INTRODUCTION

Silicon nanocrystals are a class of nanomaterials that have gained significant attention due to their unique properties [1,2]. These particles are incredibly small, typically in the nanometer range, and possess both optical and electronic properties desirable for various applications in biomedicine [3,4], optoelectronics [5–7], and energy storage [8,9]. The fabrication of silicon nanocrystals can be achieved through several methods such as thermal decomposition of silane [10], green synthesis [11], plasma-enhanced chemical vapor deposition [12], dry/wet laser ablation [13,14], and thermally induced phase separation [15]. The size and surface chemistry of silicon nanocrystals can be tuned to control their properties, making them highly customizable for specific applications [16,17].

Silicon nanocrystals exhibit the quantum confinement effect, which results from the confinement of electrons and holes within the particles, leading to discrete energy levels [18,19]. This effect is influenced by the size of the particle and the Bohr radius. Manipulating the size and surface chemistry of silicon nanocrystals enables precise tuning of their optical and electronic properties, particularly their absorption and emission spectra within the visible and near-infrared regions of the electromagnetic spectrum [20,21]. Porous silicon nanocrystals possess unique optical and electronic properties, which arise from their porous structure. This structure increases their surface area, allowing them to interact with a broader range of molecules [22].

Silicon nanocrystals have a wide range of potential applications that can enhance the efficiency of different devices and technologies. In the field of photovoltaics, they can increase light absorption and reduce recombination losses, thereby improving the efficiency of solar cells [23]. Silicon nanocrystals can also serve as the active element in light-emitting diodes and other optoelectronic devices [24]. Additionally, they can be utilized as an anode material in lithium-ion batteries [25]. Moreover, silicon nanocrystals can be functionalized with biomolecules, making them valuable in biomedical imaging [26] and drug delivery [27]. They can also be used to remove heavy metal ions from wastewater applications [28]. Additionally, silicon nanocrystals exhibit antibacterial activity by generating reactive oxygen species, which can damage the cell membranes of bacteria [29].

To investigate how photochemical etching affects the surface topography of silicon wafers, researchers examine how the process modifies the physical and chemical characteristics of the surface [30,31]. This investigation can be accomplished using different techniques, including microscopy, spectroscopy, and profilometry [32–34]. By analyzing the alterations in surface topography, researchers can gain knowledge about how to optimize the process to attain particular outcomes, such as enhanced surface roughness or specific surface characteristics [30,35]. Such studies can be valuable for the development of novel technologies in fields such as microelectronics [36], optoelectronics [7], and photovoltaics [37].

The article discusses the photochemical etching of silicon wafer, which employs a light through sun light photochemical etching (SLPCE) process to dissolve particular regions of a silicon surface, leading to the creation of unique patterns or structures. The study employs a novel and straightforward approach that utilizes natural sunlight instead of traditional light sources such as lasers, halogen lamps, and tungsten lamps that are commonly used for preparing materials in the microelectronics industry. The photochemical etching method is extensively utilized in the industry to develop complex patterns or structures on silicon wafers utilized in electronic devices and integrated circuits.

MATERIALS AND METHODS

To conduct the experiment, a single side polished silicon wafer with a (111) orientation and resistivity ranging from 1-10 ohm·cm was utilized. The material was sliced into small pieces measuring 0.5×0.5 cm and subsequently cleaned using distilled water and ethanol. Afterward, the samples were immersed in a diluted hydrofluoric acid solution (10%) for 5 minutes to eliminate the oxide layer from the surfaces of the crystalline silicon.

The system comprises a Teflon container with a 7 cm inner diameter 3 cm tall on the inside, and 4 cm tall on the outside. The Teflon container's interior is designed as a U-shaped sample holder to accommodate the samples. Hydrofluoric acid of varying concentrations (40%, 35%, 30%, and 25%) is poured into the Teflon container, covering the sample's upper surface by a few millimeters. A lens with a suitable focal length is used to focus sunlight on the sample. The lens has a 9 cm diameter and a 30 cm focal length, and its inclination angle is adjusted by mounting it on an iron stand that allows free movement. This ensures that the sunlight spot is focused on the polished front side of the sample, as shown in Figure 1.

(a)   (b)

Figure 1: (a) The setup of the system for preparing nanoporous silicon samples, (b) the Teflon container

The optical power and intensity of illumination per cm^2 on the lens surface can be calculated using the average radiation intensity at the top of the Earth's atmosphere, which is approximately 1361 W/m^2. For the experiment, a digital light meter (Lutron LX-103) was used to measure the sun's light intensity, and 1000 W/m^2 was considered a realistic average value for working conditions, which translates to 100 mW/cm^2. The power was calculated by multiplying the lens area by the solar radiation falling on each centimeter of the lens, resulting in 6360 mW. This light energy, when focused on a sample measuring 1 cm^2, produces an intensity of 6360 mW/cm^2 or 6.36 W/cm^2, which is sufficient to complete the photochemical etching process. If the same energy is focused on a sample measuring 25 cm^2, the intensity increases fourfold to 25.44 W/cm^2.

The first sign that the photochemical dissolution process has begun is the appearance of some bubbles on the samples' surfaces. These bubbles are made of hydrogen and are the product of chemical reactions [38] that dissolve silicon. Another sign that the porous layer has formed on the sample surface is the short-term change in surface color, which eventually turns buffish-brown (like iron corrosion). As stated in this work, this procedure continues for a set period of time of 60 minutes. The samples are meticulously taken out of the Teflon container using specialized forceps in order to preserve the surface and get them ready for analysis. The samples are then put in plastic receptacles with methanol in them to prevent oxidation.

Atomic force microscopy was used to examine the surface topography of the generated samples, including the particle size, dispersion, thickness of the porous layer, and roughness.

RESULTS AND DISCUSSION

Figure 2 shows an AFM image at the nanoscale, in which 3D images are displayed when scanning at about 2×2 μm for porous silicon layers. The Root Mean Square (RMS) roughness were 3.47 nm, 4.46 nm, 10.6 nm, and 4 nm at hydrofluoric acid etching concentrations of 40%, 35%, 30%, and 25%, respectively. When silicon is treated in diluted hydrofluoric acid, a condensation of Si-OH groups is formed due to rapid exchange of Si-F with water molecules followed by Si-O-Si bridges formation and oxide nuclei appear [39]. Strain and altered surface topography led to a changed rate of the logarithmic oxide growth. The oxide formation is accompanied by a slight corrosive attack of water molecules, leading to roughening of the surface [38]. At low concentrations of hydrofluoric acid, the silicon ions may not be fully removed

from the surface and can undergo a redeposition process, leading to a rougher surface. However, when the concentration of hydrofluoric acid is further reduced, the etching rate becomes slower, and the amount of silicon ions formed on the surface is also reduced. Therefore, the redeposition process is less likely to occur, resulting in a smoother surface and a decrease in RMS roughness [17,40]. Figure 3 shows the consistency between the roughness and thickness of the samples, where they are proportional to each other [41]. These images illustrated that porous silicon exhibited a sponge-like structure with high homogeneity and densely branching pores.

(a)

(b)

(c)

(d)
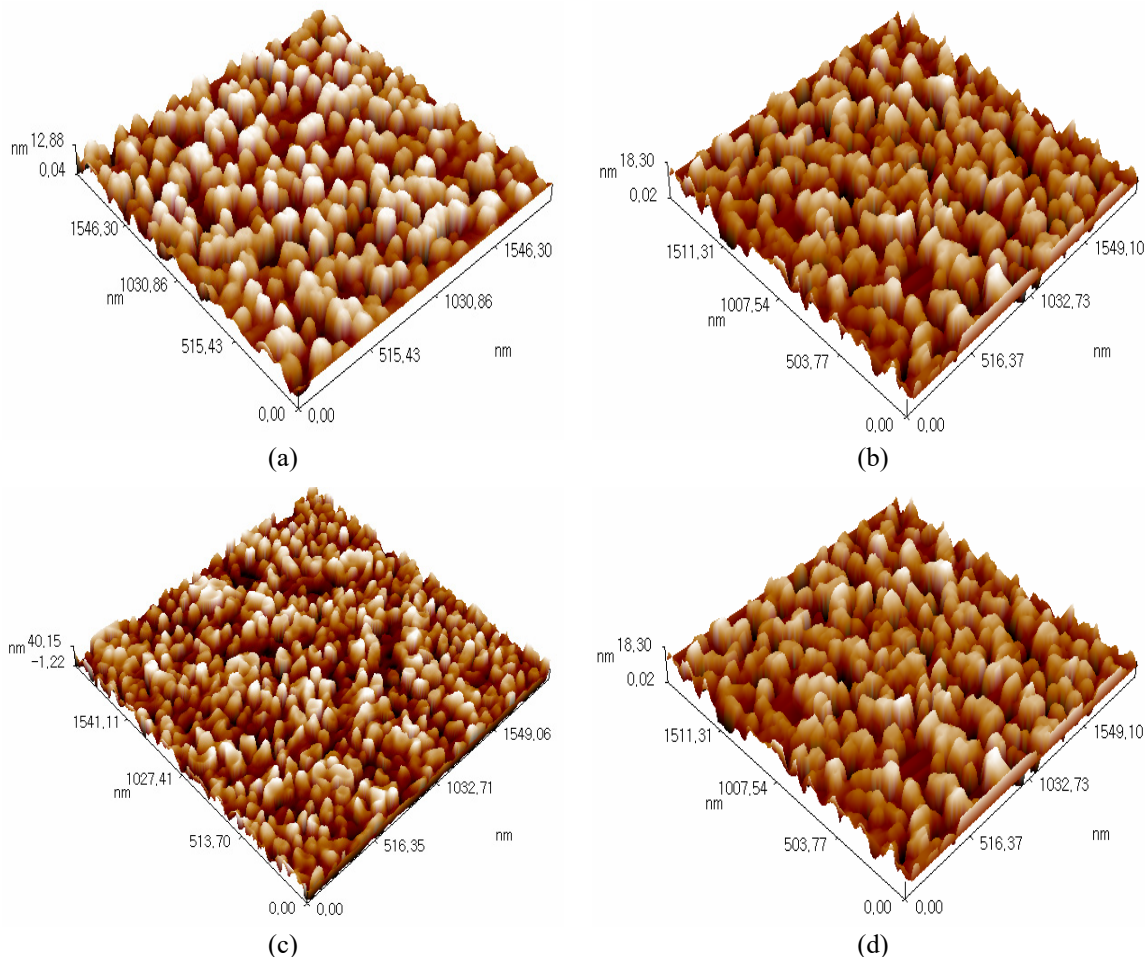
Figure 2. AFM image of silicon wafer at hydrofluoric acid etching concentrations of (a) 40%, (b) 35%, (c) 30%, and (d) 25%
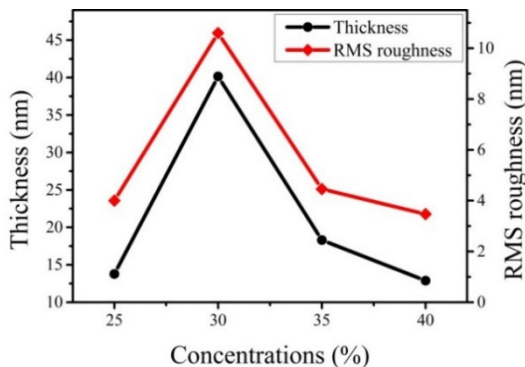
Figure 3. The roughness and thickness of the samples at each concentration.

Figure 4 illustrates the statistical measures (surface skewness and surface kurtosis) of the sample surface, demonstrating a comprehensive understanding of the etching process on the surface. The asymmetry of the surface height distribution about its mean (surface skewness) reveals that the surfaces of the samples treated with 40% and 35% concentrations contain more low valleys than high peaks, whereas those treated with 30% and 25% concentrations have more high peaks than low valleys. The sharpness of the surface height distribution relative to a Gaussian distribution (surface kurtosis) reveals that the surfaces have more high peaks and low valleys than a Gaussian distribution and they exhibit a platykurtic distribution because the kurtosis value is less than 3 for all samples [42].
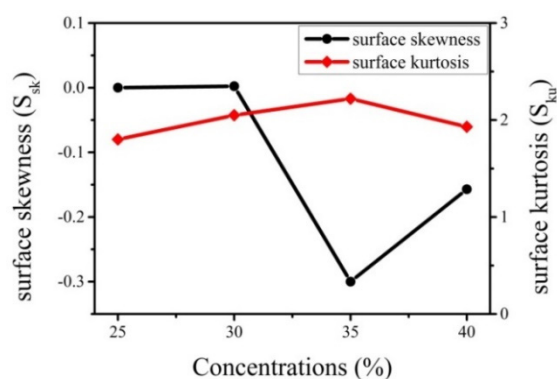
Figure 4. The statistical measures of the silicon surface: surface skewness (black line) and surface kurtosis (red line) for different hydrofluoric acid etching concentrations treatments

The samples have been characterized by means of equivalent diameter distribution through digital image processing of AFM pictures. In Figure 5, the percentage of the total volume occupied by these particles as well as the percentage cumulation of particles that fall within a certain size range are shown. The average nanostructure diameters were 90.43 nm, 75.55 nm, 67.45 nm, and 48.70 nm at hydrofluoric acid etching concentrations of 40%, 35%, 30%, and 25%, respectively as shown in Figure 6. These parameters can provide valuable insights into the distribution and size of surface features, which can be useful in many applications, such as materials science, nanotechnology, and biophysics.
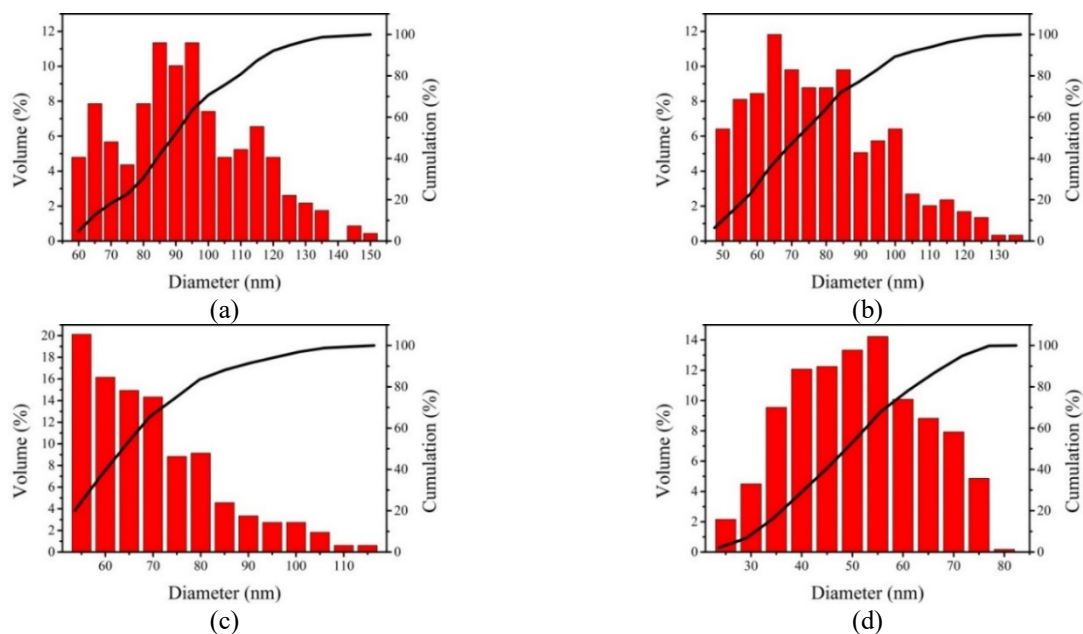
Figure 5. Equivalent diameter volume percentage (histogram in red) and cumulation percentage (black line) distributions at (a) 40%, (b) 35%, (c) 30%, and (d) 25% hydrofluoric acid etching concentrations
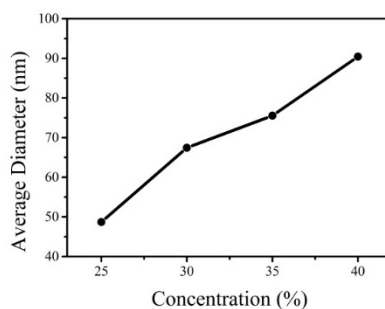
Figure 6. The average diameters of the samples at each concentration.

CONCLUSIONS

The photochemical etching method by focusing sunlight can be considered one of the approved methods for producing porous silicone layers. The preparation parameters for each experiment led to the production of layers of porous

silicon with different structures and properties. In this work, results showed that reducing the concentration of hydrofluoric acid when the other parameters (luminous intensity, etching time, and the type and resistivity of the silicon wafer) were constant led to a reduction in the size of the nanoparticles. The formation of a porous layer depleted of charges on bulk silicon, which is of the donor type, leads to the formation of a junction between them that can be used as a basis for the manufacture of diodes, photodetectors, gas sensors, and other electronic applications. Therefore, according to the finding more smaller nanoparticles can be obtain with lower hydrofluoric acid concentrations such as 20%, 15%, 10%, and 5%, while keeping other experimental constants.

ORCID

Rosure Borhanalden Abdulrahman, https://orcid.org/0000-0003-3439-5672

REFERENCES

[1]   Z. Ni, S. Zhou, S. Zhao, W. Peng, D. Yang, X. Pi, "Silicon nanocrystals: unfading silicon materials for optoelectronics," Mater. Sci. Eng. Reports, **138**, 85-117 (2019). https://doi.org/10.1016/j.mser.2019.06.001

[2]   R.B. Abdulrahman, A.S. Alagoz, T. Karabacak, "Enhanced Light Trapping in Periodic Aluminum Nanorod Arrays as Cavity Resonator," MRS Proc. **1566**, mrss13-1566-ii09-06 (2013). https://doi.org/10.1557/opl.2013.878

[3]   M.B. Gongalsky, N.V Pervushin, D.E. Maksutova, U.A. Tsurikova, P.P. Putintsev, O.D. Gyuppenen, Y.V Evstratova, O.A. Shalygina, G.S. Kopeina, A.A. Kudryavtsev, B. Zhivotovsky, L.A. Osminkina, "Optical Monitoring of the Biodegradation of Porous and Solid Silicon Nanoparticles," Nanomaterials, **11**, (2021) 2167. https://doi.org/10.3390/nano11092167

[4]   S.H. Anastasiadis, K. Chrissopoulou, E. Stratakis, P. Kavatzikidou, G. Kaklamani, A. Ranella, "How the Physicochemical Properties of Manufactured Nanomaterials Affect Their Performance in Dispersion and Their Applications in Biomedicine: A Review," Nanomaterials, **12**, 552 (2022). https://doi.org/10.3390/nano12030552

[5]   M.S. Abo Ghazala, H.A. Othman, L.M. Sharaf El-Deen, M.A. Nawwar, A.E.B. Kashyout, "Fabrication of Nanocrystalline Silicon Thin Films Utilized for Optoelectronic Devices Prepared by Thermal Vacuum Evaporation," ACS Omega, **5**, 27633-27644 (2020). https://doi.org/10.1021/acsomega.0c04206

[6]   Y. Li, Y. Wang, L. Yin, W. Huang, W. Peng, Y. Zhu, K. Wang, D. Yang, and X. Pi, "Silicon-based inorganic-organic hybrid optoelectronic synaptic devices simulating cross-modal learning," Sci. China Inf. Sci. **64**, 162401 (2021). https://doi.org/10.1007/s11432-020-3035-8

[7]   I.K. Jassim, and A.Y. Khudair, "Preparation of porous silicon Wafers using sun light photo chemical etching (SLPCE)," Tikrit J. Pure Sci. **23**, 78–84 (2018).

[8]   Y. An, Y. Tian, C. Wei, Y. Zhang, S. Xiong, J. Feng, and Y. Qian, "Recent advances and perspectives of 2D silicon: Synthesis and application for energy storage and conversion," Energy Storage Mater. **32**, 115-150 (2020). https://doi.org/10.1016/j.ensm.2020.07.006

[9]   L.C. Loaiza, L. Monconduit, and V. Seznec, "Si and Ge-Based Anode Materials for Li-, Na-, and K-Ion Batteries: A Perspective from Structure to Electrochemical Mechanism," Small, **16**, 1905260 (2020). https://doi.org/10.1002/smll.201905260

[10] F. Kunze, S. Kuns, M. Spree, T. Hülser, C. Schulz, H. Wiggers, and S.M. Schnurre, "Synthesis of silicon nanoparticles in a pilot-plant-scale microwave plasma reactor: Impact of flow rates and precursor concentration on the nanoparticle size and aggregation," Powder Technol. **342**, 880-886 (2019). https://doi.org/10.1016/j.powtec.2018.10.042

[11] S.D. Karande, S.A. Jadhav, H.B. Garud, V.A. Kalantre, S.H. Burungale, and P.S. Patil, "Green and sustainable synthesis of silica nanoparticles," Nanotechnol. Environ. Eng. **6**, 29 (2021). https://doi.org/10.1007/s41204-021-00124-1

[12] T. Sun, D. Li, J. Chen, Y. Wang, J. Han, T. Zhu, W. Li, J. Xu, and K. Chen, "Enhanced Electroluminescence from a Silicon Nanocrystal/Silicon Carbide Multilayer Light-Emitting Diode," Nanomaterials, **13**, 1109 (2023). https://doi.org/10.3390/nano13061109

[13] A. Fronya, S. Antonenko, N. Karpov, N. Pokryshkin, A. Eremina, A. Kharin, V.G. Yakunin, et al., Pulsed laser deposition in He-N₂ gaseous mixtures for the synthesis of photoluminescent Si and Ge nanoparticles for bioimaging," in: *Nanoscale Quantum Mater. From Synth. Laser Process. to Appl. SPIE*, (2023), p. 32. https://doi.org/10.1117/12.2655137

[14] M. Martínez-Carmona, and M. Vallet-Regí, "Advances in Laser Ablation Synthesized Silicon-Based Nanomaterials for the Prevention of Bacterial Infection," Nanomaterials, **10**, 1443 (2020). https://doi.org/10.3390/nano10081443

[15] L.J. Richter, U. Ross, M. Seibt, and J. Ihlemann, "Excimer Laser Surface Patterning for Photoluminescence Enhancement of Silicon Nanocrystals, Photonics," **10**, 358 (2023). https://doi.org/10.3390/photonics10040358

[16] S. Dutta, S. Chatterjee, K. Mallem, Y.H. Cho, and J. Yi, "Control of size and distribution of silicon quantum dots in silicon dielectrics for solar cell application: A review," Renew. Energy, **144**, 2-14 (2019). https://doi.org/10.1016/j.renene.2018.06.078

[17] M.F. Abdullah, and R.B. Abdulrahman, "The Electrical and Optical properties of Copper Oxide Nanostructures fabricated by Hot Deionized Water Copper Treatment," Eurasian J. Physics, Chemistry Math. **9**, 45-53 (2022). https://geniusjournals.org/index.php/ejpcm/article/view/2098

[18] M. Zacharias, and P.C. Kelires, "Temperature dependence of the optical properties of silicon nanocrystals," Phys. Rev. B, **101**, 245122 (2020). https://doi.org/10.1103/PhysRevB.101.245122

[19] M. Bürkle, M. Lozac'h, C. McDonald, M. Macias-Montero, B. Alessi, D. Mariotti, V. Švrček, "Tuning the Bandgap Character of Quantum-Confined Si–Sn Alloyed Nanocrystals," Adv. Funct. Mater. **30**, 1907210 (2020). https://doi.org/10.1002/adfm.201907210

[20] C. Samanta, S. Bhattacharya, A.K. Raychaudhuri, and B. Ghosh, "Broadband (Ultraviolet to Near-Infrared) Photodetector Fabricated in n-ZnO/p-Si Nanowires Core–Shell Arrays with Ligand-Free Plasmonic Au Nanoparticles," J. Phys. Chem. C, **124**, 22235-22243 (2020). https://doi.org/10.1021/acs.jpcc.0c06080

[21] K.E. González-Flores, J.L. Frieiro, P. Horley, S.A. Pérez-García, L. Palacios-Huerta, M. Moreno, J. López-Vidrier, S. Hernández, B. Garrido, A. Morales-Sánchez, Ultraviolet, visible and near infrared photoresponse of SiO2/Si/SiO2 multilayer system into a MOS capacitor, Mater. Sci. Semicond. Process. 134 (2021) 106009. https://doi.org/10.1016/j.mssp.2021.106009

[22] M. alsaalihiu, G. Al Nuaimi, Study of Electrical Properties of Silver Nanoparticles on Porous Silicon, J. Educ. Sci. 30 (2021) 28–36. https://doi.org/10.33899/edusj.2021.129664.1147

[23] M. Otsuka, Y. Kurokawa, Y. Ding, F.B. Juangsa, S. Shibata, T. Kato, T. Nozaki, Silicon nanocrystal hybrid photovoltaic devices for indoor light energy harvesting, RSC Adv. 10 (2020) 12611–12618. https://doi.org/10.1039/D0RA00804D

[24] Ghosh, Shirahata, All-Inorganic Red-Light Emitting Diodes Based on Silicon Quantum Dots, Crystals. 9 (2019) 385. https://doi.org/10.3390/cryst9080385

[25] J. Li, J.-Y. Yang, J.-T. Wang, S.-G. Lu, A scalable synthesis of silicon nanoparticles as high-performance anode material for lithium-ion batteries, Rare Met. 38 (2019) 199–205. https://doi.org/10.1007/s12598-017-0936-3

[26] C.J.T. Robidillo, J.G.C. Veinot, Functional Bio-inorganic Hybrids from Silicon Quantum Dots and Biological Molecules, ACS Appl. Mater. Interfaces. 12 (2020) 52251–52270. https://doi.org/10.1021/acsami.0c14199

[27] C.G. França, T. Plaza, N. Naveas, M.H. Andrade Santana, M. Manso-Silván, G. Recio, J. Hernandez-Montelongo, Nanoporous silicon microparticles embedded into oxidized hyaluronic acid/adipic acid dihydrazide hydrogel for enhanced controlled drug delivery, Microporous Mesoporous Mater. 310 (2021) 110634. https://doi.org/10.1016/j.micromeso.2020.110634

[28] C. Zamora-Ledezma, D. Negrete-Bolagay, F. Figueroa, E. Zamora-Ledezma, M. Ni, F. Alexis, V.H. Guerrero, Heavy metal water pollution: A fresh look about hazards, novel and conventional remediation methods, Environ. Technol. Innov. 22 (2021) 101504. https://doi.org/10.1016/j.eti.2021.101504

[29] A. Nastulyavichus, S. Kudryashov, N. Smirnov, I. Saraeva, A. Rudenko, E. Tolordava, A. Ionin, Y. Romanova, D. Zayarny, Antibacterial coatings of Se and Si nanoparticles, Appl. Surf. Sci. 469 (2019) 220–225. https://doi.org/10.1016/j.apsusc.2018.11.011

[30] Q. Wang, G. Yuan, S. Zhao, W. Liu, Z. Liu, J. Wang, J. Li, Metal-assisted photochemical etching of GaN nanowires: The role of metal distribution, Electrochem. Commun. 103 (2019) 66–71. https://doi.org/10.1016/j.elecom.2019.05.005

[31] A.-R.N. Abed, F.A. Khammas, R.N. Abed, Improvement the efficiency of the solar cells using nanosizing process (photochemical etching), in: AIP Conf. Proc., American Institute of Physics, 2020: p. 020109. https://doi.org/10.1063/5.0000315

[32] A.K.K. Soopy, Z. Li, T. Tang, J. Sun, B. Xu, C. Zhao, A. Najar, In(Ga)N Nanostructures and Devices Grown by Molecular Beam Epitaxy and Metal-Assisted Photochemical Etching, Nanomaterials. 11 (2021) 126. https://doi.org/10.3390/nano11010126

[33] Y. Xing, Z. Guo, M.A. Gosálvez, G. Wu, X. Qiu, Characterization of anisotropic wet etching of single-crystal sapphire, Sensors Actuators A Phys. 303 (2020) 111667. https://doi.org/10.1016/j.sna.2019.111667

[34] T.S. Wilhelm, I.L. Kecskes, M.A. Baboli, A. Abrand, M.S. Pierce, B.J. Landi, I. Puchades, P.K. Mohseni, Ordered Si Micropillar Arrays via Carbon-Nanotube-Assisted Chemical Etching for Applications Requiring Nonreflective Embedded Contacts, ACS Appl. Nano Mater. 2 (2019) 7819–7826. https://doi.org/10.1021/acsanm.9b01838

[35] Z. Shao, Y. Wu, S. Wang, C. Zhang, Z. Sun, M. Yan, Y. Shang, E. Song, Z. Liu, All-sapphire-based fiber-optic pressure sensor for high-temperature applications based on wet etching, Opt. Express. 29 (2021) 4139. https://doi.org/10.1364/OE.417246

[36] M.H. Kareem, A.M. Abdul Hussein, H.T. Hussein, Effect of current density on the porous silicon preparation as gas sensors **, J. Mech. Behav. Mater. 30 (2021) 257–264. https://doi.org/10.1515/jmbm-2021-0027

[37] X. Zhang, Y. Liu, C. Yao, J. Niu, H. Li, C. Xie, Facile and stable fabrication of wafer-scale, ultra-black c -silicon with 3D nano/micro hybrid structures for solar cells, Nanoscale Adv. 5 (2023) 142–152. https://doi.org/10.1039/D2NA00637E

[38] D. Gräf, M. Grundner, R. Schulz, Reaction of water with hydrofluoric acid treated silicon(111) and (100) surfaces, J. Vac. Sci. Technol. A Vacuum, Surfaces, Film. 7 (1989) 808–813. https://doi.org/10.1116/1.575845

[39] A.M.E. Ibrahim, H.A. Kadhem, Study the effect resistivity slide and the time of etching on silicon surfaces morphology of producing photovoltaic method, Tikrit J. Pure Sci. 21 (2016) 152–161.

[40] O. V Sukhova, V.A. Polonskyy, Peculiarities in the Structure Formation and Corrosion of Quasicrystalline Al65Co20Cu15 Alloy in Neutral and Acidic Media, East Eur. J. Phys. (2021) 49–54. https://doi.org/10.26565/2312-4334-2021-3-07

[41] Tae Hun Kim, Hyuck In Kwon, Jong Duk Lee, Byung-Gook Park, Thickness measurements of ultra-thin films using AFM, in: Dig. Pap. Microprocess. Nanotechnol. 2001. 2001 Int. Microprocess. Nanotechnol. Conf. (IEEE Cat. No.01EX468), Japan Soc. Appl. Phys, 2001: pp. 240–241. https://doi.org/10.1109/IMNC.2001.984179

[42] A. Rehman, M.A. Ehsan, A. Afzal, A. Ali, N. Iqbal, Aerosol-assisted nanostructuring of nickel/cobalt oxide thin films for viable electrochemical hydrazine sensing, Analyst. 146 (2021) 3317–3327. https://doi.org/10.1039/D1AN00222H

ДОСЛІДЖЕННЯ ВПЛИВУ КОНЦЕНТРАЦІЇ ФТОРВОДНЮ (HF) НА ТОПОГРАФІЮ ШАРУ ПОРИСТОГО КРЕМНІЮ, ПІДГОТОВЛЕНОГО ФОТОХІМІЧНИМ ТРАВЛЕННЯМ СОНЯЧНИМ СВІТЛОМ (SLPCE)

Хасан А. Кадхем[a], Абдул Хакім Ш. Мохаммед[b], Ісса З. Хасан[b], Росуре Борханалден Абдулрахман[c]
[a]Міністерство освіти, відкритий освітній коледж, Кіркук-Центр, Ірак
[b]Кафедра фізики, освітній коледж чистих наук, університет Кіркука, Кіркук, Ірак
[c]Кафедра фізики наукового коледжу університету Кіркука, Кіркук, Ірак

Кремнієві нанокристали мають широкий спектр потенційних застосувань, від підвищення ефективності сонячних елементів і оптоелектронних пристроїв до біомедичної візуалізації та доставки ліків, очищення стічних вод і антибактеріальної діяльності. У цьому дослідженні метод фотохімічного травлення використовувався для створення шарів пористого кремнію на донорній кремнієвій пластині з орієнтацією (111) і питомим опором, рівним 110 Ом·см. Процес передбачав фокусування сонячного світла на зразках за допомогою телеоб'єктива з відповідною фокусною відстанню 30 см і діаметром 90 мм, що забезпечувало достатню енергію для завершення хімічного травлення. Використовуючи постійний час травлення 60 хвилин і різні концентрації фтористоводневої кислоти (від 25% до 40%), були отримані шари з різними властивостями. Отримані поверхні досліджували за допомогою атомно-силового мікроскопа (АСМ), виявляючи утворення різних наноструктур і частинок різної форми, розміру та товщини залежно від умов підготовки. Було встановлено, що середній розмір частинок становив 90,43 нм при концентрації 40% кислоти, а при концентрації 25% HF кислоти зменшувався до 48,7 нм.

Ключові слова: *фотохімічне травлення; пористий кремній; морфологічні дослідження; фотохімічні сонячні промені; АСМ; SLPCE*

THE EFFECT OF DOPING ON THE ELECTRICAL CONDUCTIVITY OF VANADIUM OXIDE (V₂O₅) FILMS DOPED WITH NICKEL OXIDE (NiO) PREPARED VIA PULSED LASER DEPOSITION (PLD)†

Sadon Hassan Hamad*, Huda Saadi Ali#

Department of Physics, College of Education for Pure Sciences, Tikrit University, Salahuddin, Iraq
Corresponding Author e-mail: sadon.h.hamad@st.tu.edu.iq
#*e-mail: huda.wahbi@tu.edu.iq*
Received June 3, 2023; revised July 15, 2023; accepted August 5, 2023

In this research, the focus was on examining thin films of vanadium oxide (abbreviated as V_2O_5) with different levels of doping using nickel oxide (NiO) (X = 0, 6, 8)%. The films were created through pulsed laser deposition (PLD) method. The thin films were made and subjected to annealing at 450°C for a duration of one hour. The structural properties of the films were examined using the XRD diffraction technique, whereby the films' composition was found to be polycrystalline, featuring an orthorhombic structure. Notably, the films displayed a prominent alignment along the (111) plane, manifesting at an angle measuring approximately 27.889°. The FE-SEM technology was utilized to explore and evaluate the surface morphology of the thin films. This showed a nanotube-to-spherical shape transformation. Following the implementation of EDX x-ray technique, it was determined that the films comprised the elemental components of vanadium (V), nickel (Ni), and oxygen (O), consistent with the doping ratios. The assessment of the films' optical properties was carried out through the utilization of UV–visible spectrophotometer, demonstrating decreased absorbance and absorption coefficient, as well as an increased energy gap from 2.32 eV to 2.93 eV. The electrical conductivity results indicated a decrease in direct current conductivity ($\sigma_{d.c}$) with increasing doping ratio, while the activation energy (E_a) increased. Consequently, these films can be utilized in thermoelectric generators.
Keywords: *Thin films; Vanadium oxide (V₂O₅); Pulsed laser deposition (PLD); Annealing; Electrical properties*
PACS: 68.55.-a, 73.25.+I, 74.62.Dh, 78.20.Ci.

1. INTRODUCTION

The technological advancement in various fields such as electro-optics, magnetism, and optics heavily relies on the thin film technology. The fundamental characteristics of thin films encompass their crystalline structure, membrane thickness, and other distinctive properties not present in bulk materials. The composition of thin films primarily depends on the preparation technique and can exist in the form of random polycrystalline or single-crystal membranes. Furthermore, the electrical and optical properties of the films exhibit variations. This is in view of two pieces of evidence. Firstly, the crystalline structure in addition to the presence or absence of impurities. In general, thin films belong to the solid-state category, allowing for their classification based on their crystalline composition or atomic arrangement. Researchers have employed diverse deposition techniques including spray deposition [1], electron beam evaporation [2], sol-gel [3], thermal evaporation [4], pulsed laser deposition (PLD) [5], and so forth.

Vanadium pentoxide, chemically represented as V_2O_5, is an inorganic compound commonly known as vanadium oxide. It is a solid material with a yellowish crystalline structure, and when precipitated from an aqueous solution, it appears dark orange [1,6]. The pentavalent state of vanadium in Vanadium pentoxide stands out as the most stable oxide showing the ultimate level of oxidation compared to other oxides. The lattice parameters of vanadium pentoxide are as follows: a = 11.516 Å (length along the "a" axis), b = 3.565 Å (length along the "b" axis), and c = 4.372 Å (length along the "c" axis). These parameters determine the dimensions of the crystal structure [7,8]. The layered structure of V_2O_5 consists of chains of shared square pyramids (VO_5) at the edges, linking these chains together through corner sharing. Vanadium pentoxide is considered a n-type semiconductor material with multiple valence states, displaying wide energy bandgap transitions that span two values starting from 2.2 eV reaching 2.3 eV [9,10]. With its transformation into a thin film, the material experiences fluctuations in its electrical properties, rendering it an effective catalyst because of its interconnected electrical and optical characteristics. Consequently, it holds promising prospects for diverse applications across multiple domains [11,12], such as microelectronics, optoelectronic devices, solar cells, electrical appliances, electronic switches, and optics, among others [13].

Nickel (II) oxide, with the chemical formula NiO, is a chemical compound that possesses exceptional physical and chemical properties. It holds significant importance in advanced research disciplines and has emerged as one of the few metal oxides of type P with promising prospects in various applications [14]. NiO has a bandgap ranging from 4.3 eV to 3.6 eV. Distinguished by its inherent chemical stability, minimal toxic levels, remarkable resilience, and elevated ionization potential, the material possesses a valuable assemblage of attributes. Moreover, it can be manufactured at low costs, making it economically viable. Additionally, NiO possesses distinct characteristics such as excellent electrical, optical, and magnetic properties [15]. Functioning as a proficient sensor for gas and exemplifying a prototype for semiconductor materials, it demonstrates its aptitude in both aspects. This can be fabricated using a range of physical and chemical methods [16].

The investigation of Nio's particular structural characteristics as well as the optical, and electrical ones was carried out utilizing the PLD method in this study.

2. Practical Part
2.1 Preparation of powder substances and discs

High-purity vanadium oxide (V$_2$O$_5$) with a purity of (99.0%) was used, prepared by the German company Merck, and high-purity nickel oxide (NiO) with a purity of (99.9%) was prepared by the American company Sky Spring Nanomaterials. The powders were weighed using a sensitive electronic balance (Mettler. A.K-160) with a sensitivity of 10^{-5} gm. After weighing the powders, vanadium oxide (V$_2$O$_5$) and nickel oxide (NiO) were mixed in different weight ratios (X=0.6, 8)% to obtain a sample weighing 3g. The physical mixing method was used to achieve high homogeneity between pure vanadium oxide particles and the samples doped with nickel oxide. The powders were ground using a ceramic mortar for half an hour. Subsequently, the mixed powders were compressed with a pressure of 3 tons in a special mound made of stainless steel, measuring 1.5cm in diameter and a thickness of 0.5cm, using an American hydraulic press manufactured by Across International.

2.2- Glass Substrate Preparation

Glass substrates with geometric dimensions of 75mm×25mm×0.2mm were used for thin film deposition. The substrates were of AFCO type and were cleaned prior to the deposition process. The following steps were followed:
- The glass substrates were washed with distilled water to remove dirt and impurities from their surfaces.
- After washing with distilled water, the glass substrates were immersed in a glass container containing 96% ethanol for 20 minutes.
- The glass substrates were dried using a soft cloth and stored in dedicated holders.

2.3- Sedimentation system

The application of a Nd:YAG Laser System was observed in the course of depositing thin films onto glass substrates. The system consists of a computer-controlled power supply, an internal cooling system, and a manually adjustable laser beam path on the target. The laser beam has a wavelength of $\lambda = 1064$nm, an energy of 800 mJ, a frequency of 6 Hz, and a pulse duration of 10ns. A precise positioning of the laser beam is achieved as it is directed at a fixed15cm from the target material. This is placed inside a cylindrical quartz chamber with low-pressure air (10^{-3}mbar) at room temperature. The glass slide is positioned 3cm above the target material and is subjected to the laser beam at an incident angle of 45°. A total of 800 pulses are used to obtain the desired thin films. The deposition and growth of thin films are facilitated through the PLD interacting with the target material.

2.4- Annealing

The annealing process is used to improve the properties of thin films, where the surface is subjected to a controlled heating process for a specific duration. The purpose of annealing is to eliminate stresses in the material, facilitate the diffusion and arrangement of impurities, increase electrical efficiency, and minimize structural defects resulting from manufacturing. The prepared thin films were annealed using an electric furnace (MUFFLE FURNACE, model MF-12). The thin films are subjected to a temperature of 450°C for a duration of one hour, after which they undergo natural cooling inside the furnace. This process renders the films ready for the to perform the following checks:

2.4.1- Measuring thickness of films

Measuring the thickness of films was performed utilizing the optical interferometer method. For the experimentation, we employed a helium-neon laser operating at a wavelength of 632 nm. The laser beam was directed towards the film at an inclination of 45 degrees. The reflected beam passed through a converging lens and was projected onto a screen to observe interference fringes, as depicted in (Figure 3).
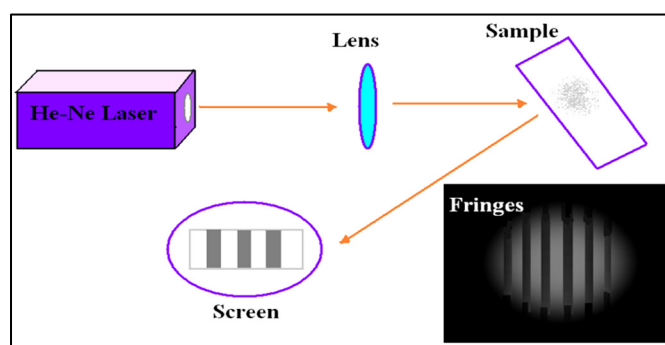

Figure 3. Schema of optical interferometer technique for quantifying the thin films'level of thickness. The fabricated films exhibited an estimated thickness of (500 ± 50)nm.

By measuring the width of the bright fringes (x) and the dark fringes (Δx), The determination of the film thickness can be achieved by applying the following correlation

$$t = \frac{\Delta x}{x} \times \frac{\lambda}{2}. \tag{1}$$

2.4.2- Structural Measurements

To conduct structural evaluations, the films were subjected to XRD using a Shimadzu X-ray machine (model PW1730) produced by Shimadzu in Japan. The XRD instrument employed a wavelength measured at 1.541874 Å [Cd Kα radiation], operated at 40 kV and 30 mA [voltage, current], and encompassing 80˚-10˚ [scanning range]. The calculation of the average grain size (specifically crystallite) of the thin films utilized the Debye-Scherrer relationship.

$$G.S = \frac{K\lambda}{\beta\cos\theta}, \tag{2}$$

where K is a constant parameter with a precise numerical value of 0.94, β corresponds to the peak's width at half of its maximum intensity (FWHM), θ designates the angle of diffraction, indicating the angle at which X-rays are dispersed by the crystal lattice, λ represents the specific wavelength of the X-ray employed for the analysis, specifically Cu Kα with a value of 1.5405 Å. [17,18].

Furthermore, the surface morphology of the membranes was investigated by field-emission scanning electron microscopy FE-SEM and energy dispersive X-ray spectroscopy EDX attached to the FE-SEM device using a (model ZEISS SIGMA VP) device manufactured by Carl Zeiss Microscopy in United States, field emission FE-SEM produces clearer, less electrostatically distorted images with spatial resolution down to 1 1/2 nanometers.

2.4.3- Optical Measurements

A UV-Vis was employed to analyze the optical characteristics of the aforementioned films. The model used was (model 1900) manufactured by SHIMADZU in Japan, located at the College of Pure Science, Department of Physics, Tikrit University. The absorbance spectrum was obtained, and the absorbance range served as the basis for the calculation of the absorbance coefficient of the prepared films. The following formula was adopted [19,20]:

$$\alpha = 2.303\frac{A}{t}. \tag{3}$$

The absorbance coefficient (α) is a parameter that quantifies the level of light absorption exhibited by a material. The absorbance (A) is a measure of the amount of light that the material absorbs. On the other hand, the film thickness (t) provides valuable information regarding the physical dimensions of the film.

The determination and calculation of the lowest-energy transition value for the thin films were performed for the allowed direct transitions using the following equation

$$\alpha(h\upsilon) = A'(h\upsilon - E_g)^r, \tag{4}$$

Where: E_g – energy gap, α – absorption coefficient, A' – proportionality constant, r – exponential coefficient [21].

2.4.4- Measurements‡Electrical

By utilizing a versatile multimeter (Fluke-8846A), the electrical resistance (R) of the thin films was measured across a temperature range, enabling the investigation of their electrical properties. The resistance value of the film ® was recorded for a specific range of temperature variations, with an increment of 10˚C.

The electrical conductivity depends on two main factors: the density level of charge carriers and its mobility as influenced by the electric field. These factors vary with temperature, doping ratios, and preparation conditions. The direct current electrical conductivity (σ_{dc}) is the reciprocal of the specific electrical resistivity (ρ), as shown in the following equation [22]:

$$\boldsymbol{\rho = R\frac{A}{L}} \quad \boldsymbol{where}\{A = b.t\}, \tag{5}$$

$$\boldsymbol{\sigma_{dc} = \frac{1}{\rho}}, \tag{6}$$

Where:

σ_{dc}: continuous electrical conductivity with units of $(\Omega.cm)^{-1}$, ρ: specific resistivity, R: electrical resistance of the film measured practically in (Ω), L: distance between the aluminum electrodes in (cm), A: cross-sectional area for electron movement through the film, b: electrode width (cm), t: film thickness in nm, converted to (cm)

Semiconductors typically exhibit a negative temperature coefficient of resistance, and their conductivity generally follows an exponential pattern that is influenced by temperature. Consequently, an equation can be formulated to describe the nature of connection that electrical conductivity displays in relation to temperature, enabling the determination of the activation energy. This equation bears resemblance to the well-known Arrhenius equation [23]:

$$\sigma_{dc} = \sigma_o exp\left(\frac{-E_a}{K_B T}\right)$$

.(7)

In the present study, the following variables are considered:

E_a: representing the activation energy for electrical conduction measured in eV and corresponding to the difference between Ec and E$_F$ [24], σ_o: denoting the minimum metallic conductivity, T: the absolute temperature in Kelvin, k$_B$: the Boltzmann constant equal to (k$_B$ = 1.38×10^{-23} J/K = 0.086×10^{-3} eV/K).

By employing Equation (7), a plot of (ln σ_{dc}) against (1000/T) is generated. The slope of the resulting straight line is equal to (-E$_a$/k$_B$), allowing for the determination of the activation energy E$_a$ in units of eV [25]:

$$E_a = -slope \times k_B \times 1000$$

(8)

3- RESULTS AND DISCUSSION
3.1- X-Ray diffraction

The XRD examination performed has revealed that the pure vanadium oxide (V$_2$O$_5$) and nickel oxide (NiO) and films of V$_2$O$_5$ were doped using varying levels of dopants (X =0,6,8)% possess a crystalline structure of the orthorhombic phase. The diffraction peaks were observed at angles (12.12°, 15.390°, 18.366°, 26.342°, 27.889°, 29.033°, 30.665°,37.305°, 43.348°, 63.017°) corresponding to the planes (101), (002), (100), (011), (111), (301), (220), (200), (111) as depicted in (Figure 4). These findings are in agreement with the International Centre for Diffraction Data (JCPDS Card No: PDF-85-2422), indicating that the (111) plane is the dominant growth direction for both pure and NiO-doped V$_2$O$_5$ films. The dominant direction (111), corresponding to the angle (2θ = 27.889°), remained unchanged after doping. Additionally, with an increase in the doping level, there was a corresponding reduction in the how intense the diffraction peaks get, which suggests that doping reduces the grain size of V$_2$O$_5$ [26]. In the case of the 8% doping ratio, the grain was measured at 29.293 nm. The grain size of the doped V$_2$O$_5$ films exhibited a significant reduction when compared to the grain size of the pure V$_2$O$_5$ films. (55.536 nm) as shown in Table 1. These findings are consistent with previous studies [27-29].
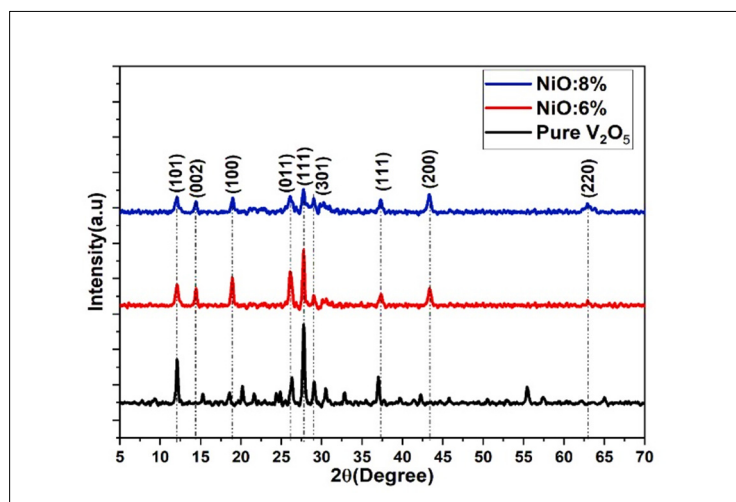
Figure 4. (XRD) patterns of (V$_2$O$_5$) films, including both the pure films and the films doped with (NiO)

Table 1. X-ray examination results of pure and Nickel oxide -doped vanadium pentoxide films

Sample	2θ exp (Deg)	2θ std (Deg)	d exp (Å)	d Std (Å)	FWHM	hkl	G.S (nm)
Pure V$_2$O$_5$	27.889	27.882	3.195	3.197	0.145	111	55.536
V$_2$O$_5$ +NiO(6%)	27.780	27.882	3.208	3.197	0.236	111	34.130
V$_2$O$_5$ +NiO(8%)	27.729	27.882	3.213	3.197	0.275	111	29.293

3.2- Field emission scanning electron microscope (FE-SEM)

As can be seen in Figure 5, the assessment of the surface morphological properties of the thin films, specifically focusing on the influence of doping, utilizing (FE-SEM). Images of both (Pure V$_2$O$_5$) and (NiO) films were captured using (FE-SEM). Nanoparticles with a nanotube structure and an average size of 89.32 nm were observed in (Figure a).

However, the introduction of doping caused agglomeration as a result of secondary growth on the film surface. This resulted in spherical particles [30,31]. This doping-induced transformation reduced the nanoparticle size to an average range of 37.96 - 24.56 nm in (Figures b, c), while concurrently enhancing surface smoothness through recrystallization. This interesting phenomenon is compatible with various medical applications in the future, including in the field of biomedicine, where vanadium oxide was used because of its strong effect as an inhibitor of blood vessels, as well as in disease resistance and chemotherapy [32].
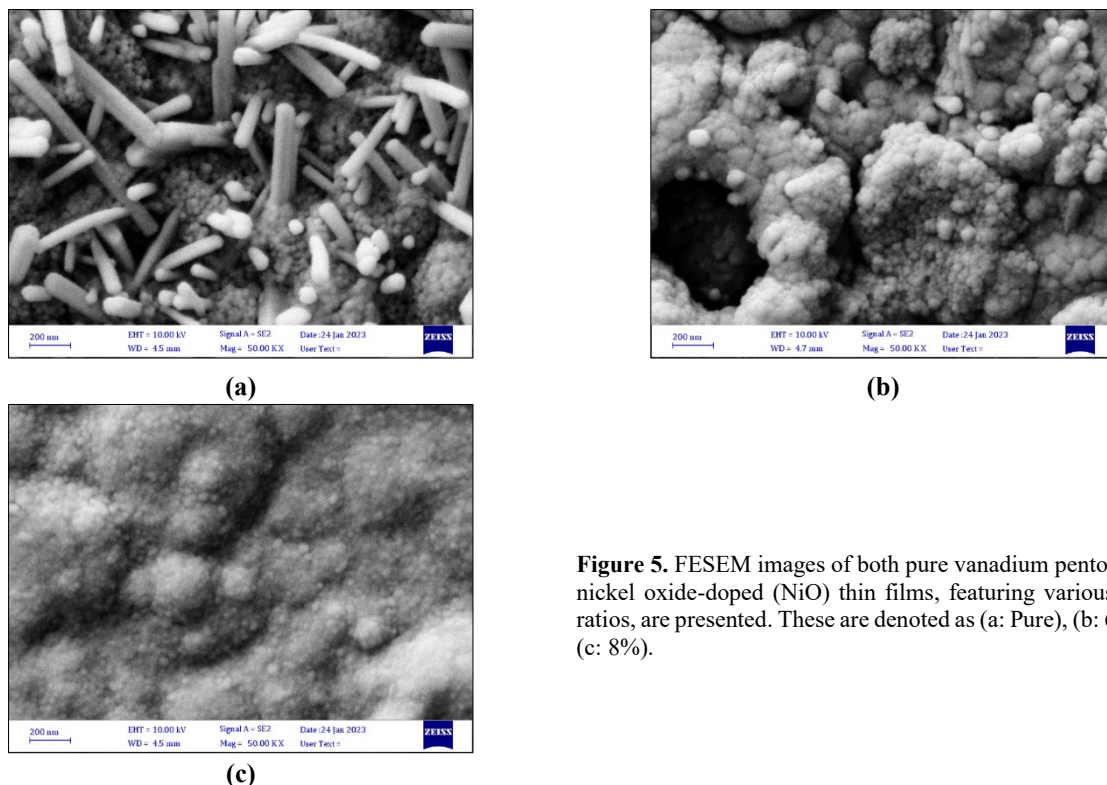
(a)

(b)

Figure 5. FESEM images of both pure vanadium pentoxide and nickel oxide-doped (NiO) thin films, featuring various doping ratios, are presented. These are denoted as (a: Pure), (b: 6%), and (c: 8%).

(c)

3.3- X-ray energy dispersive spectroscopy (EDX)

Figure 6 showcases the EDX results. It can be noted that there are multiple peaks corresponding to different elements in the thin film samples. As regards (Pure: 0%), the noticed peaks indicate the presence of vanadium (V = 90.3 wt%) and oxygen (O = 9.7 wt%), along with gold (Au) from the sample coating used for examination purposes. In the first doping ratio of 6% nickel oxide, the peaks of vanadium (V = 76.2 wt%) and oxygen (O = 8.5 wt%) are observed, along with trace amounts of nickel (Ni = 15.3 wt%), confirming its incorporation as an impurity within the crystal structure of vanadium pentoxide. In the second doping ratio of 8% nickel oxide, the peaks of vanadium (V = 51.3 wt%) and oxygen (O = 5.4 wt%) are detected, along with significant peaks of nickel (Ni = 43.3 wt%). Notably, the peak corresponding to gold, present in the coated films for examination purposes, is not observed. No other elements associated with impurities or contamination were detected, reaffirming the purity of the studied films in this research.

(a)

(b)

(c)
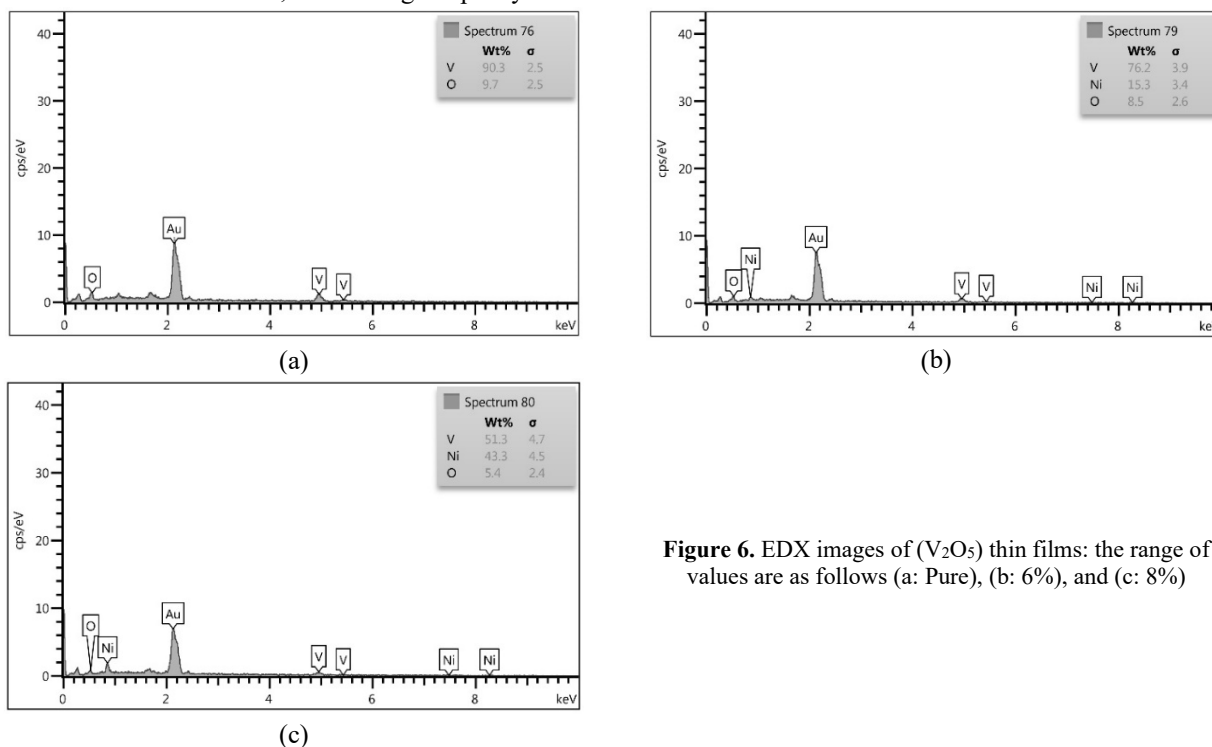
Figure 6. EDX images of (V_2O_5) thin films: the range of values are as follows (a: Pure), (b: 6%), and (c: 8%)

3.4- Optical Properties
3.4.1- Absorbance (A)

The examination of the optical characteristics of the thin films involved analyzing the absorption spectra within the extended wavelength range of 400 nm to 1000 nm. This analysis enabled the determination of the optical constants. It was observed that the absorbance slightly decreases in the high-wavelength region, while A substantial enhancement in absorbance is observed within the area of shorter wavelengths, as shown in (Figure 7). The absorption edge for pure vanadium oxide occurs at 430 nm [33]. Of particular importance is the observation that the absorbance diminishes as the doping ratios increase, primarily as a consequence of a reduction in particle size and an elevation in the optical energy bandgap caused by the presence of nickel oxide (NiO) impurities within the bandgap.

3.4.2- Absorption Coefficient (α)

In a comparable manner to absorbance, the absorption coefficient exhibits a decrease as doping ratios increase, owing to the creation of impurity levels within the energy bandgap, as visually depicted in (Figure 8). At lower levels of photon energy, the absorption coefficient remains minimal, indicating a limited likelihood of electronic transitions. Nevertheless, as the absorption edge is approached towards higher energy levels, the absorption coefficient experiences an increment [34].
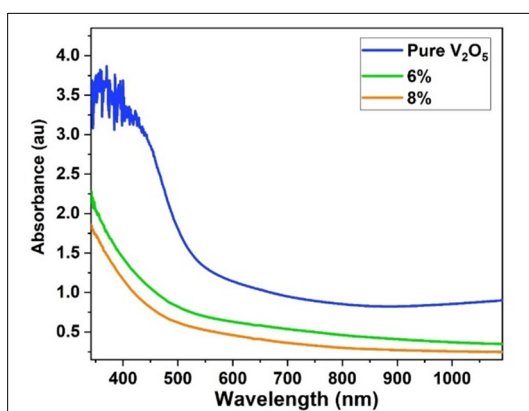
Figure 7. It is clear Absorbance change as a function of wavelength
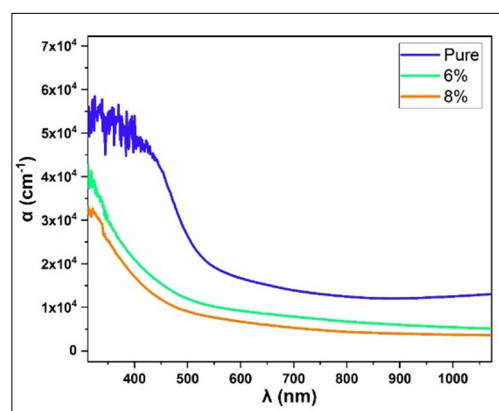
Figure 8. provides a visual representation showcasing the changes in the absorption coefficient as a function of photon energy

3.4.3- The Optical Energy Gap (E_g)

The direct bandgap semiconductors known as V_2O_5 membranes possess an approximate energy gap of 2.3 eV. Upon introducing nickel oxide (NiO) as a dopant, equation (4) was employed to compute the optical energy gap value for permissible direct transitions. The plotted relationship between $(\alpha h v)2$ and photon energy (hv) is depicted in (Figure 9), highlighting that the optical energy gap exhibits a conspicuous amplification in its magnitude as the doping ratio increases. This augmentation in the value of the energy gap can be ascribed to the emergence of levels within the energy gap caused by NiO, consequently resulting in the narrowing of said levels [35]. In its pure form, vanadium oxide (V_2O_5) exhibits an energy gap of 2.32 eV. However, when doped with nickel oxide at a rate of 6%, the energy gap amplifies to 2.84 eV. Similarly, at an 8% NiO doping ratio, the energy gap is measured at 2.93 eV.
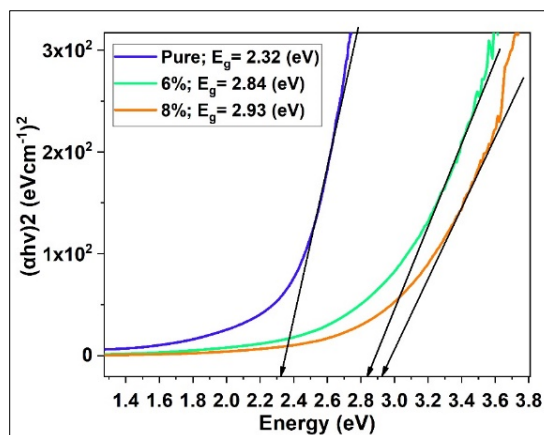

Figure 9. illustrates the variation in the energy gap for the allowed direct transition as a function of photon energy.

3.5- Electrical properties
Continuous conductivity calculation (DC)

By utilizing Equation (6) based on Equation (5), the temperature-dependent electrical conductivity $\sigma_{d.c}$ was determined in the temperature range of 313K-373K. It was observed in (Figure 10.a) that, for a single sample, the electrical resistivity of all the prepared membranes exhibits an inverse relationship with increasing temperature, which is a characteristic behavior of semiconductors. In contrast to conductors, semiconductors exhibit a negative temperature coefficient of resistivity, indicating that the electrical conductivity increases with rising temperature across all membranes. Furthermore, (Figure 10.b) also notes that an increase in the nickel oxide NiO doping ratio is accompanied by a corresponding increase in electrical resistivity, resulting in a decline in electrical conductivity. This decline can be explained as a result of the formation of trap levels near the conduction band's energy gap, leading to an augmentation in defect concentrations within the membrane. The heightened concentration of defects subsequently raises the energy barriers that charge carriers (electrons) must overcome during the conduction process [35]. These findings are consistent with measurements of optical properties, crystal structure distortion, and XRD. The widening of the energy gap arises from a decrease in the abundance of majority charge carriers (electrons) and the emergence of new energy states within the band gaps. Consequently, this decrease leads to diminished electrical conductivity as the nickel oxide doping ratio increases, accompanied by an elevated energy gap value in the doped membrane, as confirmed through energy gap measurements. Consequently, the space for electron mobility expands, necessitating electrons to possess greater energy to transition to the conduction band. Additionally, there is a decrease in the concentration of charge carriers [36,37].

In the evaluation of all membranes, we subtracted the energy level of the Fermi level E_F from the energy level of the conduction band Ec, hence the activation energy Ea was computed.

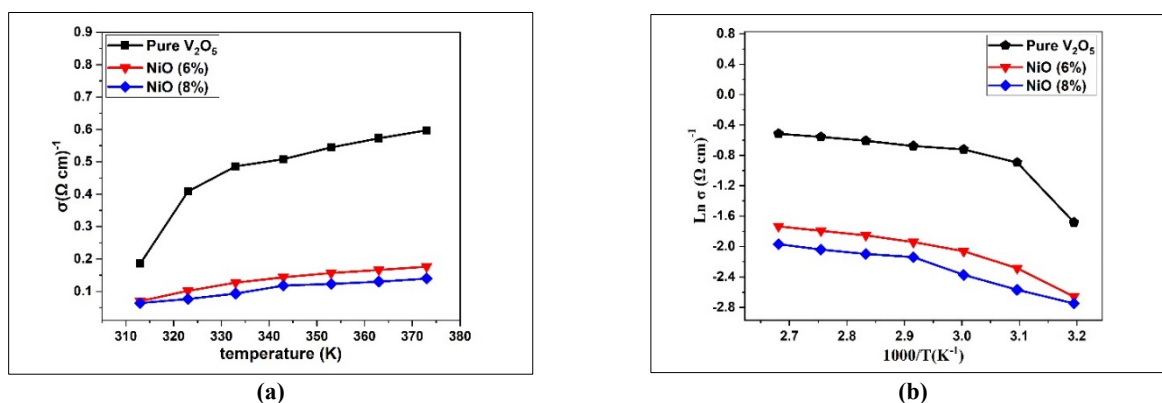**(a)**   **(b)**

Figure 10. a – Continuous Conductivity ($\sigma_{d.c}$) as a function of temperature change for pure and doped membranes
b - Continuous Conductivity (Ln $\sigma_{d.c}$) as a function of temperature change (1000/T) for pure and doped membranes.

The thin membranes that were prepared possess two distinct activation energy values. The first activation energy is observable within the lower temperature range 313K-343K, characterized by conduction through a hopping mechanism where charge carriers energetically leap from one neutral atom to another within the same energy level in the energy gap. This hopping process takes place within confined energy levels amidst the energy gap, predominantly occurring at grain boundaries, where charge carriers lack the necessary energy to overcome voltage barriers. Consequently, conduction transpires by exciting charge carriers in localized states present within the forbidden energy gap, facilitated by phonons. (Table 2) provides a visual representation, specifying the corresponding temperature intervals for each activation energy. The existence of two activation energies aligns with the XRD examinations conducted on all membranes and the electrical conductivity mechanisms found in polycrystalline semiconducting materials. Regarding the second activation energy E_{a2} or the alternative conduction mechanism, which was computed within the temperature range of 343K-373K, electronic transitions occur due to either thermal excitation or thermionic emission. At elevated temperatures, carriers possess sufficient energy to surmount the voltage barriers arising from grain boundaries and increased potential energy barriers, thereby transitioning into extended states situated above the electron conduction levels Ec. Consequently, grains, grain boundaries, and energy barriers play a pivotal role in determining the electrical characteristics of polycrystalline materials [35,38]. These findings are consistent with the XRD analysis, which demonstrates that the activation energy exhibits an increase alongside the augmentation of the nickel oxide doping ratio. In simpler terms, as the doping ratio rises, the excitation energy required for electrons to reach the conduction band also escalates. These outcomes find support in prior investigations [38]. Within (Table 2), one can find the values denoting direct current conductivity $\sigma_{d.c}$ and activation energy E_a.

Table 2. Continuous Conductivity and Activation Energy Values for Pure and Doped Membranes

Sample	$\rho(\Omega cm)$	$(\sigma_{d.c})_{RT}$ $(\Omega.cm)^{-1}$	$E_{a1}\times10^{-4}$(eV) at Range (313-343)K	$E_{a2}\times10^{-4}$ (eV) at Range (343-373)K
Pure V_2O_5	2.44	0.472	0.434	0.592
V_2O_5+NiO(6%)	8,139	0.135	3.21	2.68
V_2O_5+NiO(8%)	10.13	0.106	4.97	3.65

CONCLUSIONS

In light of the research conducted, it is evident that the polycrystalline nature of all membranes is revealed through X-ray diffraction (XRD) analysis, wherein the size of crystallites diminishes as doping levels rise. By employing field-emission scanning electron microscopy (FE-SEM), the impact of doping on the nanostructure of vanadium oxide is observed, resulting in the transformation from nanotubes to nanosized particles and a subsequent reduction in particle size. This transformation has consequential effects on the optical properties, leading to an escalation in the value of the energy gap. To affirm the reliability and purity of the findings, energy-dispersive X-ray spectroscopy (EDX) yields conclusive and uncontaminated results. Pertaining to the electrical properties, it is noted that the membrane's resistance exhibits an increment with fluctuations in temperature, whereas conductivity experiences a decline as the first activation energy at low temperatures and the second activation energy at high temperatures increase. As a result, these findings hold promise for the development of thermoelectric generators, facilitating the capture and conversion of heat energy into electrical power.

ORCID
Sadon Hassan Hamad, https://orcid.org/0009-0002-9160-7256; **Huda Saadi Ali,** https://orcid.org/0000-0003-4115-3591

REFERENCES

[1] H.M.R. Giannetta, C. Calaza, D.G. Lamas, L. Fonseca, and L. Fraigi, "Electrical transport properties of V$_2$O$_5$ thin films obtained by thermal annealing of layers grown by RF magnetron sputtering at room temperature," Thin Solid Films, **589**, 730-734 (2015). https://doi.org/10.1016/j.tsf.2015.06.048

[2] Z. Zheng et al., "The Optical Properties of V$_2$O$_5$ Films Deposited on Single Crystal Diamond Under Homogenizing Preparation Technology," Integrated Ferroelectrics, **235**(1), 100-105 (2023). https://doi.org/10.1080/10584587.2023.2192674

[3] S. Senapati, and S. Panda, "Effect of aging of V$_2$O$_5$ sol on properties of nanoscale films," Thin Solid Films, **599**, 42-48 (2016). https://doi.org/10.1016/j.tsf.2015.12.045

[4] B. Priya, P. J. Arunima, and T. Kumar, "Structural, morphological and optical properties of V2O5 thin films for," Growth And Characterization Of Semiconductor Nanostructure For Device Applications, p. 106, 2023.

[5] J. Huotari, J. Lappalainen, J. Eriksson, R. Bjorklund, E. Heinonen, I. Miinalainen, J. Puustinen, et al., "Synthesis of nanostructured solid-state phases of V$_7$O$_{16}$ and V$_2$O$_5$ compounds for ppb-level detection of ammonia," Journal of Alloys and Compounds, **675**, 433-440 (2016). https://doi.org/10.1016/j.jallcom.2016.03.116

[6] R. Moskalyk, and A.M. Alfantazi, "Processing of vanadium: a review," Minerals Engineering, **16**(9), 793-805 (2003). https://doi.org/10.1016/S0892-6875(03)00213-9

[7] H. Khmissi, S.A. Mahmoud, and A.A. Akl, "Investigation of thermal annealing effect on the microstructure, morphology, linear and non-linear optical properties of spray deposited nanosized V$_2$O$_5$ thin films," Optik, **227**, 165979 (2021). https://doi.org/10.1016/j.ijleo.2020.165979

[8] Y. Yue, L. Ma, J. Sun, H.-K. Jeong, and H. Liang, "Super-hierarchical Ni/porous-Ni/ V$_2$O$_5$ nanocomposites," RSC Adv. **7**(64), 40383-40391 (2017). https://doi.org/10.1039/C7RA06446B

[9] S.F. Cogan, N.M. Nguyen, S.J. Perrotti, and R.D. Rauh, "Optical properties of electrochromic vanadium pentoxide," Journal of Applied Physics, **66**(3), 1333-1337 (1989). https://doi.org/10.1063/1.344432

[10] K. Schneider, "Optical properties and electronic structure of V$_2$O$_5$, V$_2$O$_3$ and VO$_2$," Journal of Materials Science: Materials in Electronics, **31**(13), 10478-10488 (2020). https://doi.org/10.1007/s10854-020-03596-0

[11] V.S. Vijay, R. Varghese, A. Sakunthala, S. Rajesh, and B.J.V. Vidhya, "Highly crystalline V$_2$O$_5$ and V$_6$O$_{13}$ thin films by PLD and a study on morphology transition of V$_2$O$_5$ by post annealing," Vacuum, **187**, 110097 (2021). https://doi.org/10.1016/j.vacuum.2021.110097

[12] M. Zou, "Deposition Methods and Thermoresistive Properties of Vanadium Oxide and Amorphous Silicon Thin Films," M.Sc. Thesis, University of Dayton, 2015. http://rave.ohiolink.edu/etdc/view?acc_num=dayton1446477859

[13] H. Lv, X. Tian, M.Y. Wang, and D. Li, "Vibration energy harvesting using a phononic crystal with point defect states," Appl. Phys. Lett. **102**(3), 034103 (2013). https://doi.org/10.1063/1.4788810

[14] M. Bonomo, "Synthesis and characterization of NiO nanostructures: a review," Journal of Nanoparticle Research, **20**(8), 222 (2018). https://doi.org/10.1007/s11051-018-4327-y

[15] H. Xuemei, S. Yukun, and B. Bai, "Fabrication of cubic pn heterojunction-like NiO/In V$_2$O$_3$ composite microparticles and their enhanced gas sensing characteristics," Journal of Nanomaterials, **2016**, 7589028 (2016). https://doi.org/10.1155/2016/7589028

[16] A.N. Mohsin, B.H. Adil, H.Q. Khaleel, R.A. Al-Ansari, and I.R. Swadi, "Non-Thermal Plasma Effect Of Li Doped Nio Thin Films Prepared By The Spray Pyrolysis Technique For Sensor Applications," International Journal of Applied Sciences and Technology, **4**(1), 80-97 (2022). http://dx.doi.org/10.47832/2717-8234.10.8

[17] A.S. Fathima, I.K. Punithavthy, A. Rajeshwari, A. Sindhya, and A. Muthuvel, "Structural, Optical and Electrical Properties of V$_2$O$_5$ Thin films at different Molarities by Spray pyrolysis method," Journal of the Nigerian Society of Physical Sciences, **4**(4), 1050 (2022). https://doi.org/10.46481/jnsps.2022.1050

[18] B. Priya, P. Jasrotia, I. Sulania, D.K. Chaudhary, R. Gupta, A.S. Verma, R. Kumar, *et al*., "Tuning of Structural and Morphological Characteristics of V$_2$O$_5$ Thin Films Using Low Energy 16 keV N+ for Optical and Wetting Applications," ECS Advances, **2**(2), 021002 (2023). https://doi.org/10.1149/2754-2734/accafc

[19] Y.S. Thakur, A.D. Acharya, and S. Sharma, and Bhawna, "Reinforcement of V$_2$O$_5$ nanoparticle in polyaniline to improve the optical and UV-shielding properties," Results in Optics, **11**, 100400 (2023). https://doi.org/10.1016/j.rio.2023.100400

[20] R. Ramadan, M. Ahmed, and M.M. El-Masry, "PVDF-based (V$_2$O$_5$)$_x$(Mn$_{0.4}$Fe$_{2.6}$O$_4$)$_{(2−x)}$, x=[0.2, 0.4, 0.6, 0.8, and 1] nanocomposites for tailoring the optical and nonlinear optical properties of PVDF," Polym. Bull. 1436-2449 (2023). https://doi.org/10.1007/s00289-023-04850-1

[21] M. Abdelrazek, A.E. Hannora, R.M. Kamel, I. Morad, M.J.O. El-Desoky, and Q. Electronics, "Effect of lanthanum doping on the structure and optical properties of nanocrystalline vanadium pentoxide films prepared by sol-gel method," **55**(6), 491 (2023). https://doi.org/10.21203/rs.3.rs-2461694/v1

[22] Y. Xia, C. Calahoo, B. P. Rodrigues, K. Griebenow, L. Graewe, and L. Wondraczek, "Structure and properties of cerium phosphate and silicophosphate glasses," Journal of the American Ceramic Society, **106**(5), 2808-2819 (2023). https://doi.org/10.1111/jace.18936

[23] N. Komal, M. A. Mansoor, M. Mazhar, M. Sohail, Z. Malik, and M. Anis-ur-Rehman, "Effect of (Sm, In) Doping on the Electrical and Thermal Properties of Sb_2Te_3 Microstructures," ACS Omega, **8**(11), 9797-9806 (2023). https://doi.org/10.1021/acsomega.2c05859

[24] N. Bhardwaj, and S. Mohapatra, "Structural, optical and gas sensing properties of $Ag-SnO_2$ plasmonic nanocomposite thin films," Ceramics International, **42**(15), 17237-17242 (2016). https://doi.org/10.1016/j.ceramint.2016.08.017

[25] R.K. Jain and A. Khanna, "Structural, optical and electrical properties of crystalline V_2O_5 films deposited by thermal evaporation and effects of temperature on UV–vis and Raman spectra," Optik, **144**, 271-280 (2017). https://doi.org/10.1016/j.ijleo.2017.06.104

[26] Y.Z. Zheng, H. Ding, E. Uchaker, X. Tao, J.F. Chen, Q. Zhang, and G. Cao, "Nickel-mediated polyol synthesis of hierarchical V_2O_5 hollow microspheres with enhanced lithium storage properties," J. Mater. Chem. A, **3**(5), 1979-1985 (2015). https://doi.org/10.1039/C4TA05500D

[27] P. Hu, P. Hu, T.D. Vu, M. Li, S. Wang, Y. Ke, X. Zeng, et al., "Vanadium Oxide: Phase Diagrams, Structures, Synthesis, and Applications," Chem. Rev. **123**(8), 4353-4415 (2023). https://doi.org/10.1021/acs.chemrev.2c00546

[28] T.K. Le, M. Kang, V.T. Tran, and S.W. Kim, "Relation of photoluminescence and sunlight photocatalytic activities of pure V_2O_5 nanohollows and V_2O_5/RGO nanocomposites," Materials Science in Semiconductor Processing, Materials Science in Semiconductor Processing, **100**, 159-166 (2019). https://doi.org/10.1016/j.mssp.2019.04.047

[29] T.K. Le, M. Kang, and S.W. Kim, "Room-temperature photoluminescence behavior of α-V2O5 and mixed α-β phase V_2O_5 films grown by electrodeposition," Materials Science in Semiconductor Processing, **94**, 15-21 (2019). https://doi.org/10.1016/j.mssp.2019.01.026

[30] Y. Vijayakumar, P. Nagaraju, T. Sreekanth, U. Rushidhar, P.S. Reddy, "Effect of precursor volume on chemically sprayed V_2O_5 thin films for acetaldehyde detection," Superlattices and Microstructures, **153**, 106870 (2021). https://doi.org/10.1016/j.spmi.2021.106870

[31] H. Liu, X. Liang, T. Jiang, Y. Zhang, S. Liu, X. Wang, X. Fan, *et al*., "Analysis of structural morphological changes from 3DOM V_2O_5 film to V_2O_5 nanorods film and its application in electrochromic device," **238**, 111627 (2022). https://doi.org/10.1016/j.solmat.2022.111627

[32] P. Deepika, H. Vinusha, B. Muneera, N. Rekha, and K. S. Prasad, "Vanadium oxide nanorods as DNA cleaving and anti-angiogenic agent: novel green synthetic approach using leaf extract of Tinospora cordifolia," Current Research in Green and Sustainable Chemistry, vol. 1, pp. 14-19, 2020. https://doi.org/10.1016/j.crgsc.2020.04.001

[33] C.K.P. Neeli, V.S.P. Ganjala, V. Vakati, K. Seetha, R. Rao, and D R. Burri, "V_2O_5/SBA-15 nanocatalysts for the selective synthesis of 2,3,5-trimethyl-1, 4-benzoquinone at room temperature," New J. Chem. **40**(1), 679-686 (2016). https://doi.org/10.1039/C5NJ02399H

[34] M. Thirumoorthi, and J.T.J. Prakash, "A study of Tin doping effects on physical properties of CdO thin films prepared by sol–gel spin coating method," Journal of Asian Ceramic Societies, **4**(1), 39-45 (2016). https://doi.org/10.1016/j.jascer.2015.11.001

[35] L.K. Emhjellen, X. Liu, J.M. Polfus, and R. Haugsrud, "Native point defects and polaron transport in zirconium pyrovanadate," Solid State Ionics, **386**, 116033 (2022). https://doi.org/10.1016/j.ssi.2022.116033

[36] A. Qasrawi, N.M. Gasanly, "Temperature effect on dark electrical conductivity, Hall coefficient, space charge limited current and photoconductivity of $TlGaS_2$ single crystals," Semiconductor Science and Technology, **20**(5), 446 (2005). https://doi.org/10.1088/0268-1242/20/5/021

[37] S.K. Sinha, "Effect of temperature on structural, optical and electrical properties of pulsed-laser deposited W-doped V_2O_5 thin films," Superlattices and Microstructures, **125**, 88-94 (2019). https://doi.org/10.1016/j.spmi.2018.10.029

[38] Z. Zhang, C. Yin, L. Yang, J. Jiang, Y. Guo, "Optimizing the gas sensing characteristics of Co-doped SnO_2 thin film based hydrogen sensor," Journal of Alloys and Compounds, **785**, 819-825 (2019). https://doi.org/10.1016/j.jallcom.2019.01.244

ВПЛИВ ЛЕГУВАННЯ НА ЕЛЕКТРОПРОВІДНІСТЬ ПЛІВОК ОКСИДУ ВАНАДІЮ (V_2O_5), ЛЕГОВАНИХ ОКСИДОМ НІКЕЛЮ (NiO) ПІДГОТОВЛЕНИХ ІМПУЛЬСНИМ ЛАЗЕРНИМ ОСАДЖЕННЯМ (ІЛО)

Садон Хасан Хамад, Худа Сааді Алі

Факультет фізики, Освітній коледж чистих наук, Університет Тікріту, Салагуддін, Ірак

У цьому дослідженні основна увага була зосереджена на дослідженні тонких плівок оксиду ванадію (скорочено V_2O_5) з різними рівнями легування оксидом нікелю (NiO) (X = 0, 6, 8)%. Плівки були створені методом імпульсного лазерного осадження (PLD). Тонкі плівки виготовляли та піддавали відпалу при 450°C протягом однієї години. Структурні властивості плівок досліджували за допомогою дифракційного методу XRD, за допомогою якого було виявлено, що склад плівок є полікристалічним, що має орторомбічну структуру. Примітно, що плівки показали помітне вирівнювання вздовж площини (111), що проявляється під кутом приблизно 27,889˚. Технологія FE-SEM була використана для дослідження та оцінки морфології поверхні тонких плівок. Це показало трансформацію форми нанотрубки в сферичну. Після застосування рентгенівського методу EDX було визначено, що плівки містять елементарні компоненти ванадію (V), нікелю (Ni) і кисню (O), що відповідає співвідношенням легування. Оцінку оптичних властивостей плівок проводили за допомогою УФ-видимого спектрофотометра, який продемонстрував зниження абсорбції та коефіцієнта поглинання, а також збільшення енергетичної забороненої зони з 2,32 еВ до 2,93 еВ. Результати електричної провідності вказують на зменшення провідності постійного струму (σd.c) зі збільшенням коефіцієнта легування, тоді як енергія активації (Ea) зростає. Отже, ці плівки можуть бути використані в термоелектричних генераторах.

Ключові слова: *тонкі плівки; оксид ванадію (V_2O_5); імпульсне лазерне осадження (PLD); відпал; електричні властивості*

EFFECT OF CALCINATION TEMPERATURE ON STRUCTURAL AND OPTICAL PROPERTIES OF NICKEL ALUMINATE NANOPARTICLES†

Katrapally Vijaya Kumar[a,*], Sara Durga Bhavani[b]

*ªDepartment of Physics, JNTUH University College of Engineering Rajanna Sircilla,
Agraharam, Rajanna Sircilla-District, 505302, TS, India*
ᵇDepartment of Chemistry, Government Degree College, Rajendra Nagar, Hyderabad, 500001, TS, India.
*Corresponding Aythor e-mail: kvkumar@jntuh.ac.in, kvkphd@gmail.com
Received May 19, 2023; revised June 30, 2023; accepted June 30, 2023

Nickel aluminate ($NiAl_2O_4$) nanoparticles were synthesized using sol-gel method with auto-combustion. The prepared nanoparticles were made into four parts and calcinated at 700, 900, 1100 and 1300°C and taken up for the present study. The taken-up nanoparticles were characterized using powder X-Ray Diffraction (XRD), Scanning Electron Microscopy (SEM), Energy Dispersion X-Ray Spectroscopy (EDS), Fourier Transform and Infrared (FT-IR) spectroscopy and UV-Vis spectroscopy techniques. The X-ray diffraction patterns confirmed the spinel structure and Fd3m space group. Scherrer formula was used to calculate the crystallite size and found in the range 5.78 to 20.55 nm whereas the lattice parameter was found in the range of 8.039 to 8.342 Å. The average grain size was found in the range 142.80 to 187.37 nm whereas interplanar spacing was found in the range of 2.100 to 2.479 Å. The FTIR spectroscopy showed six absorption bands in the range 400 to 3450 cm^{-1} and confirmed the spinel structure. The optical band gap (E_g) was decreased with calcination temperature and found in the range 4.2129-4.3115eV.
Keywords: *Nickel Aluminate nanoparticles; Sol-Gel Auto-Combustion method; Calcination Temperature; Crystallite size; Grain size; Elemental analysis; IR and UV-Vis spectroscopy*
PACS: 75.50.Gg, 61.05.cp, 68.37.Hk, 78.40.Fy, 33.20.Ea, 42.70.Qs

INTRODUCTION

Since few years, the usage of composite materials has significantly increased in various applications due to their exceptional properties when compared with metals, ceramics and polymers. The composite materials containing spinel phase are stable at high temperatures, chemically resistant, abrasion resistant and exhibit high hardness [1-3]. The composite oxides such as mixed spinels have been attracted the scientists due to their significance behaviour in magnetic properties [4], catalytic properties [5], luminescent properties [6], sensing properties [7], lithium batteries [8] etc. The composite oxides having chemical formula AB_2O_4, where A, represents divalent metal ion residing tetrahedral sites and B, represents trivalent metal ion residing octahedral sites [9, 10]. In the recent days, spinel oxides having chemical formula MCr_2O_4, where M represents a divalent metal ion such as Ni, Cu, Zn, Co, Mg, Fe have attracted several researchers because of their upgraded properties [11]. These materials at the nanoscale range are gained importance because of their small size and large surface area with their upgraded properties compared to their counter bulk materials. Especially, $ZnCr_2O_4$ mixed spinels have become important functional materials due to their humidity sensing properties [12], optical and photocatalytic properties [13], electrical and magnetic properties [13-14]. The properties of these materials would depend on the synthesis process and reaction conditions. Many synthesis processes were found in the literature to synthesize $ZnCr_2O_4$ nanoparticles such as ball milling method [15], solid-state reaction method [16], micro emulsion method [17], precipitation method [18], auto-combustion method [19] etc. Few of the synthesis processes give the product material of low quality with existence of impurities, require high temperature and consume more energy, require involvement of organic solvents which makes the process costly. Kumar et al [20] investigated structural properties of $ZnCr_2O_4$ nanoparticles prepared by sol-gel method with auto combustion as it gives the product material of high purity, good homogeneity at low processing temperature. Expecting an interesting study on calcination temperature dependent physical and optical properties, the nickel aluminate ($NiAl_2O_4$) spinel nanoparticles were considered for investigation and prepared by using sol-gel method with auto combustion.

EXPERIMENTAL

Nickel aluminate ($NiAl_2O_4$) spinel nanoparticles were prepared by sol-gel method with auto-combustion [21] following the procedure shown in flowchart (Fig. 1). The materials such as nickel nitrate ($Ni(NO_3)_2·6H_2O$) and aluminium nitrate ($Al(NO_3)_2·6H_2O$) were used as starting materials. The citric acid and ammonia of analytical grade (AR) were also used in the required quantity in the synthesis process. A solution was prepared using the raw materials in their stoichiometry by dissolving in a deionized water. The molar ratio of citric acid and the total moles of nitrate ions was adjusted to 1:3 and added to the arranged solution to chelate Ni^{2+}, Al^{3+} and Fe^{3+} ions in the solution. The prepared solution was made neutralized by maintaining the pH value 7 by the addition of ammonia (NH_3) to the solution in required proportion. The final neutralized solution was then heated at about 100°C on a hot plate with constant stirring till the

viscous state was reached which led to form a viscous gel. There onwards, the temperature was increased to ~ 200°C to burn the gel entirely in a self-propagating combustion manner to turn into a loose powder [22, 23]. The prepared powder was divided into four parts and calcinated at 700, 900, 1100 & 1300°C for 8 h.
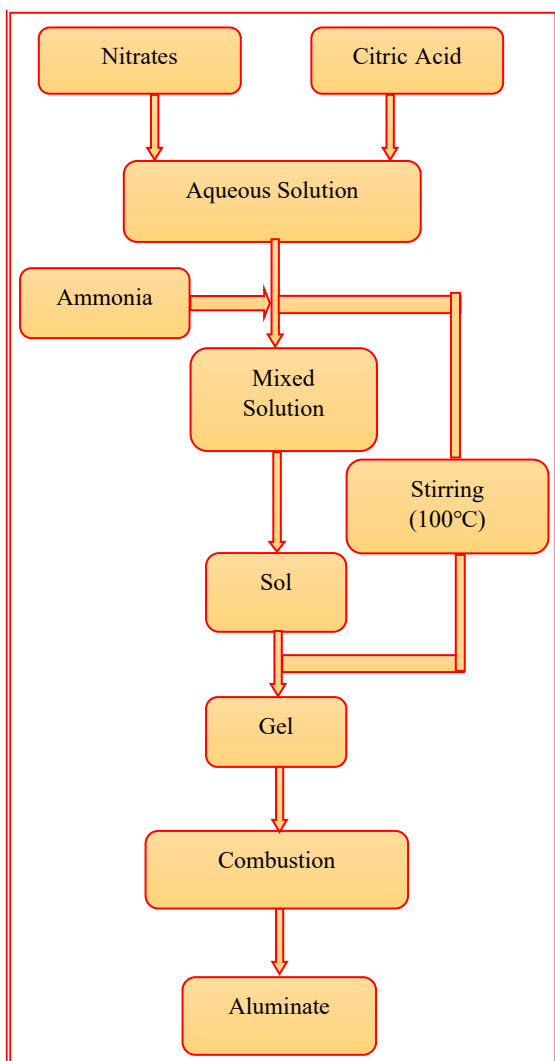

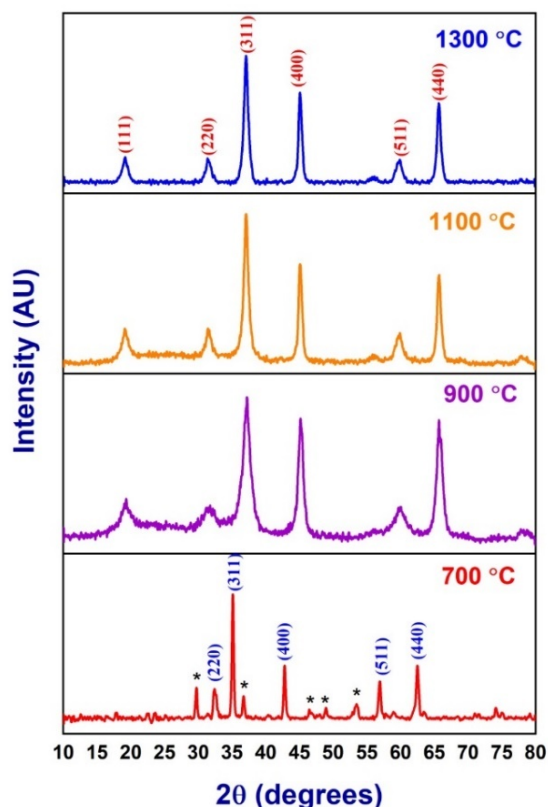**Figure 1.** Flowchart of the sol-gel auto combustion method

Figure 2. XRD patterns of $NiAl_2O_4$ nanoparticles calcinated at 700, 900, 1100 & 1300°C

Using Phillips Expert Diffractometer, the X-Ray diffraction (XRD) measurements were carried out at room temperature in the range of 20°-80° whereas ZEISS EVO 18, Special Edition was used to bring out the micro structural studies and elemental analysis of the prepared samples. Using Shimadzu FTIR spectrometer (Model: FTIR-8400 S), Fourier transform infrared spectroscopic studies were carried out within a range of 300-4000 cm^{-1}. Using, SYSTRONICS DOUBLE BEAM UV-VIS Spectrophotometer: 2202, UV-Vis spectra studies were recorded in the range 200-800 nm.

RESULTS AND DISCUSSION
XRD Analysis

XRD plots of the nickel aluminate ($NiAl_2O_4$) spinel nanoparticles calcinated at 900, 1100 and 1300°C are shown in Fig. 2. They clearly exhibited the prominent peaks for the crystal planes of Miller indices (1 1 1), (2 2 0), (3 1 1), (4 0 0), (5 1 1), (4 4 0) and they confirmed the establishment of single-phase spinel structure with space group of Fd3m [24]. But, in the XRD pattern of the sample calcinated at 700°C the crystal planes of Miller indices (1 1 1) were missed. Few extra peaks were observed in all the XRD plots and they were marked with star symbol. Hence, it was clearly understood that the crystal phase was formed perfectly in all the samples [25-27] except in the sample calcinated at 700°C. Using Scherrer formula [28] shown in equation (1), the crystallite size was calculated for all the prominent peaks and the same furnished in the Table 1 along with Miller indices, FWHM, 2θ and d-spacing values.

$$t = \frac{0.89\,\lambda}{\beta\,Cos\,\theta}$$

(1)

Table 1. (hkl), 2θ, FWHM, crystallite size, Interplanar spacing of NiAl$_2$O$_4$ nanoparticles calcinated at 700, 900, 1100 & 1300°C

Calcination Temperature (°C)	Average FWHM (Radians)	Average Crystallite Size (nm)	Lattice Parameter (Å)	Unit Cell Volume (Å^3)	Average Interplanar spacing (Å)	Average Grain Size (nm)
700	0.45	20.55	8.342	580.64	2.100	142.80
900	1.80	5.78	8.039	519.54	2.472	145.29
1100	1.05	9.21	8.042	520.34	2.479	159.75
1300	0.90	10.38	8.058	523.17	2.479	187.37

Where, t is known as crystallite size, λ is known as X-ray wavelength (1.54 Å), θ is angle of diffraction and β is known as full width at half maximum (FWHM). The average crystallite size of all the samples was found in the range 5.78 nm-20.55 nm and the same furnished in the Table 2.

Table 2. Interplanar spacing, average grain size, reciprocal lattice of NiAl$_2$O$_4$ nanoparticles calcinated at 700, 900, 1100 & 1300°C

Calcination Temperature (°C)	(h k l)	2θ (Degrees)	FWHM (Radians)	Crystallite Size (nm)	d (spacing) (Å)
700	220	32.40	0.62	13.34	2.76
	311	**35.12**	**0.32**	**26.04**	**2.558**
	400	42.8	0.35	24.82	2.113
	511	56.9	0.46	19.65	1.617
	440	62.48	0.48	19.36	1.486
900	111	19.3	2.29	3.52	4.608
	220	31.76	2.9	2.85	2.416
	311	**37.20**	**1.3**	**6.45**	**2.416**
	400	45.14	0.95	9.05	2.006
	511	59.96	2.3	3.99	1.543
	440	65.68	1.07	8.84	1.420
1100	111	19.12	1.42	5.67	4.628
	220	31.38	1.26	6.55	2.837
	311	**37.08**	**0.82**	**10.22**	**2.423**
	400	45.12	0.66	13.03	2.009
	511	59.80	1.46	6.28	1.558
	440	65.70	0.70	13.51	1.421
1300	111	19.16	1.06	7.60	4.632
	220	31.38	1.00	8.25	2.840
	311	**37.08**	**0.76**	**11.02**	**2.425**
	400	45.06	0.60	14.33	2.010
	511	59.84	1.32	6.94	1.547
	440	65.66	0.67	14.11	1.421

Though, the phase is not formed completely for the sample calcinated at 700°C, the crystallite size was observed highest, i.e., 20.55 nm where as for the sample calcinated at 900°C, the crystal phase was formed perfectly and the crystallite size was observed lowest, i.e., 5.78 nm. Further, the crystallite size was found increased for the samples calcinated from 900 to 1300°C [29]. The calculated lattice parameter values were found in the range of 8.039 to 8.342 Å. In the similar lines to the crystallite size, the lattice parameter was found highest, i.e., 8.342 Å for the sample calcinated at 700°C where as it is found lowest, i.e., 8.039 Å, for the sample calcinated at 900°C. Further, the lattice parameter was increased with the calcinated from 900 to1300°C.

The bond lengths between cations and oxygen located at A and B sites were measured along with ionic radii of cations furnished in Table 3. The bond lengths of A site-oxygen and B site-oxygen were found maximum in case of the sample calcinated at 700°C where as they were found minimum for the sample calcinated at 900°C.

Table 3. Bond lengths and ionic radii in NiAl$_2$O$_4$ nanoparticles calcinated at 700, 900, 1100 & 1300°C

Calcination Temperature (°C)	Bond length of A site-O (^{0}A)	Bond length of B site-O (^{0}A)	Ionic radius(r_A) (^{0}A)	Ionic radius(r_B) (^{0}A)
700	1.898	1.984	0.4796	0.4855
900	1.829	1.913	0.4076	0.4132
1100	1.830	1.914	0.4084	0.4141
1300	1.834	1.918	0.4120	0.4177

Further they were found increased with the calcination temperature. In the similar lines, the ionic radii at A and B sites were found maximum in case of the sample calcinated at 700°C where as they were found minimum for the sample calcinated at 900°C. Further they were found increased with the calcination temperature. Hence, it can be concluded that the effect of calcination temperature on all the calculated parameters from the XRD data was clearly observed.

SEM Analysis

The SEM micrographs of the nickel aluminate ($NiAl_2O_4$) spinel nanoparticles calcinated at 900, 1100 and 1300°C are shown in Fig. 3. It is clearly observed that the size and shape of the grains were appeared as non-uniform flakes [30] with several pores and voids. The calculated average grain size was found in the range 142.80 to 187.82 nm and the same furnished in the Table 2. The grain size was found minimum for the sample calcinated at 700°C and it was found gradually increased with the calcination temperature [31].

At 700°C

b) At 900°C

At 1100°C
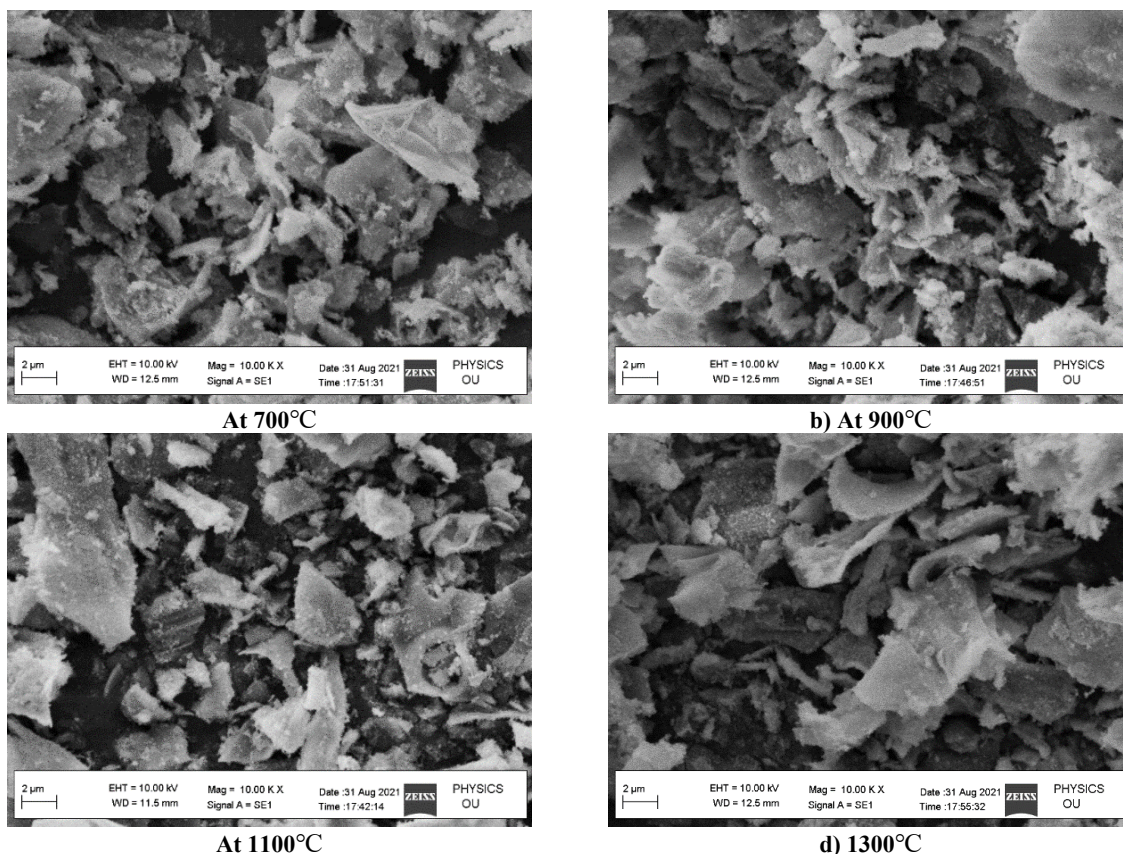
d) 1300°C

Figure 3. SEM images of $NiAl_2O_4$ nanoparticles calcinated at 700, 900, 1100 & 1300°C

EDS Analysis

The Energy Dispersive X-ray Spectra of all the nickel aluminate ($NiAl_2O_4$) spinel nanoparticles are shown in Fig. 4. It was clearly observed that the presence of Ni, Al and O without any impurities and the atomic percentages are furnished in Table 4.

Table 4. Elemental percentage of $NiAl_2O_4$ nanoparticles calcinated at 700, 900, 1100 & 1300°C

Calcination Temperature (°C)	Element	Atomic %
700	Ni	4.93
	Al	8.05
	O	25.44
	C	61.58
900	Ni	14.23
	Al	28.40
	O	57.36
1100	Ni	14.78
	Al	25.78
	O	59.43
1300	Ni	14.37
	Al	28.30
	O	57.34

It was clearly noticed that the theoretical and experiential atomic percentages of nickel, aluminium and oxygen are in close agreement in case of all the taken-up samples [32]. It was clearly observed that no impurities were traced in all the samples except in the sample calcinated at 700°C as an impurity of carbon was found in a considerable quantity. Further, it was also clearly noticed that there was no loss of any fundamental elements during the synthesis process.

a)700°C

b) 900°C

c)1100°C
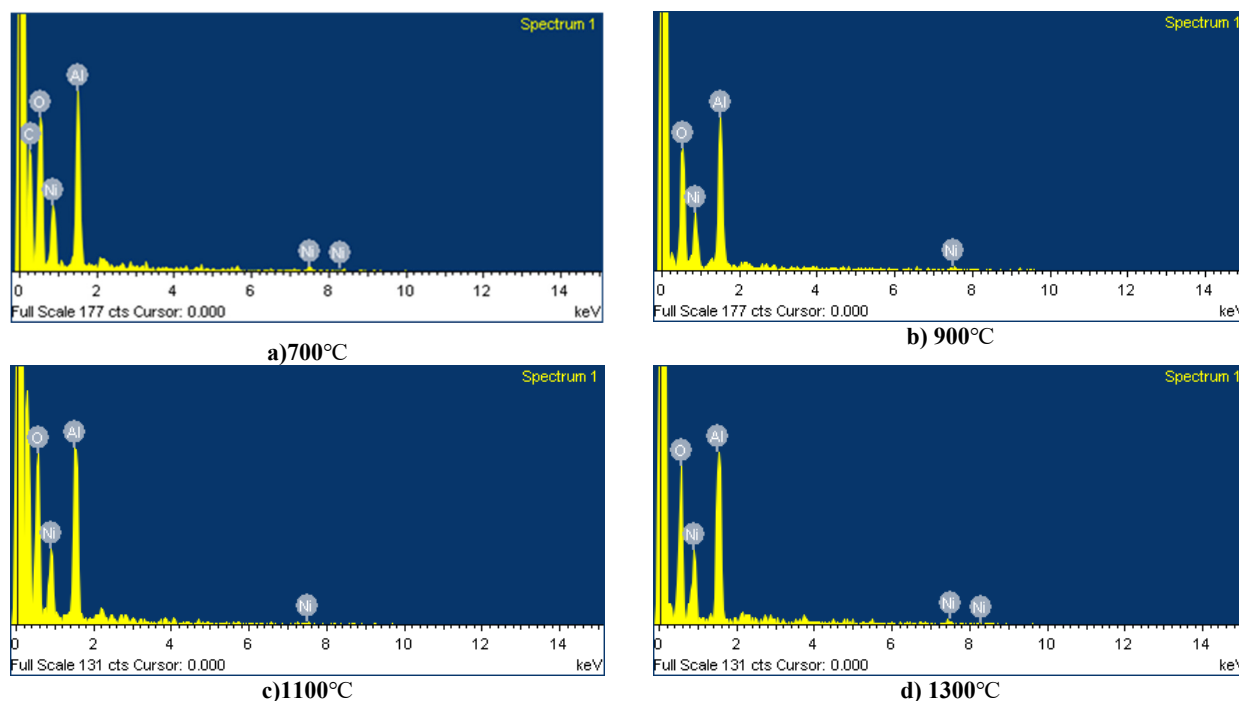
d) 1300°C

Figure 4. EDS spectra of NiAl$_2$O$_4$ nanoparticles calcinated at 700, 900, 1100 & 1300°C

FTIR Spectroscopy

Fourier transform infrared (FTIR) spectra of all the nickel aluminate (NiAl$_2$O$_4$) spinel nanoparticles are presented in Fig. 5.
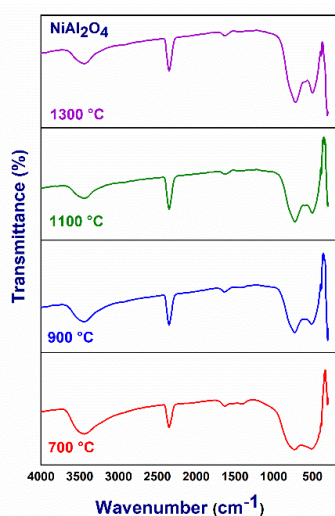
Figure 5: FTIR patterns of NiAl$_2$O$_4$ nanoparticles calcinated at 700, 900, 1100 & 1300°C

The FTIR spectra showed a categorization of absorption peaks in the range of 300-4000 cm^{-1} and the concerned frequencies are furnished in Table 5. Based on the absorption peaks, the functional groups that are existing were appraised for all the samples. The characteristic frequencies in the range 499-730 cm^{-1} may be attributed to characteristic metal-oxygen vibrations indicating the establishment of single phase NiAl$_2$O$_4$ [33]. The peaks observed in the frequency range 499-730 cm^{-1} can be assigned to Ni-O, Al-O, and Ni-O-Al bonds. The peaks observed in the frequency range of 499.5-511.1 cm^{-1} can be attributed to Al-O stretching vibrations whereas the peaks observed in the frequency range 719.4-729.1 cm^{-1} can be attributed to Ni-O stretching vibrations. The peaks observed in the frequency range 1400-1413 cm^{-1} represent the stretching vibrations in CH2 and CH3 [34]. The peaks observed in the frequency range 1630-1632 cm^{-1} can be assigned to the deformative vibration of water molecules which would be most possibly due to water absorption during the pressing of the powder samples with KBr. The strong peak observed at the frequency 2349 cm^{-1} originates from the mode of CO$_2^{3-}$ ion. The presence of this CO$_2$ would be either because of the presence of aerial CO$_2$ or may be due to the presence of CO$_2$ inside the grains of powders [35]. The peaks observed in the frequency range 3441-3143 cm^{-1} denoted for the -OH stretching vibration of free hydrogen bonded hydroxyl groups [32]. For the nanosized grains, the atomic orientations along the boundaries very much differed from those of bulk crystals with regard to coordination number and bond lengths and showed some extent of disorder [36, 37]. And it can be concluded that impurity phase was not detected in FTIR spectra which agrees with the results attained by XRD.

Table 5. The Characteristic wavenumbers of NiAl$_2$O$_4$ nanoparticles calcinated at 700, 900, 1100 & 1300°C

Calcination Temperature (°C)	ν_1 (cm^{-1})	ν_2 (cm^{-1})	ν_3 (cm^{-1})	ν_4 (cm^{-1})	ν_5 (cm^{-1})	ν_6 (cm^{-1})
700	511.1	729.1	1413	1630	2349	3441
900	509.2	729.1	1400	1632	2349	3443
1100	501.5	725.3	-	1632	2349	3443
1300	499.5	719.4	-	1630	2349	3441

UV-Visible Spectroscopy

Optical absorption properties of all the nickel aluminate (NiAl$_2$O$_4$) spinel nanoparticles were studied in the wavelength region 200-800 nm at room temperature using UV-Visible spectroscope. Fig. 6 shows the UV-Visible absorbance spectra of all the samples and observed two prominent absorption peaks in the wavelength range 230-360 nm and few peaks thereafter.

a) 700°C

(b) 900°C

(c) 1100°C
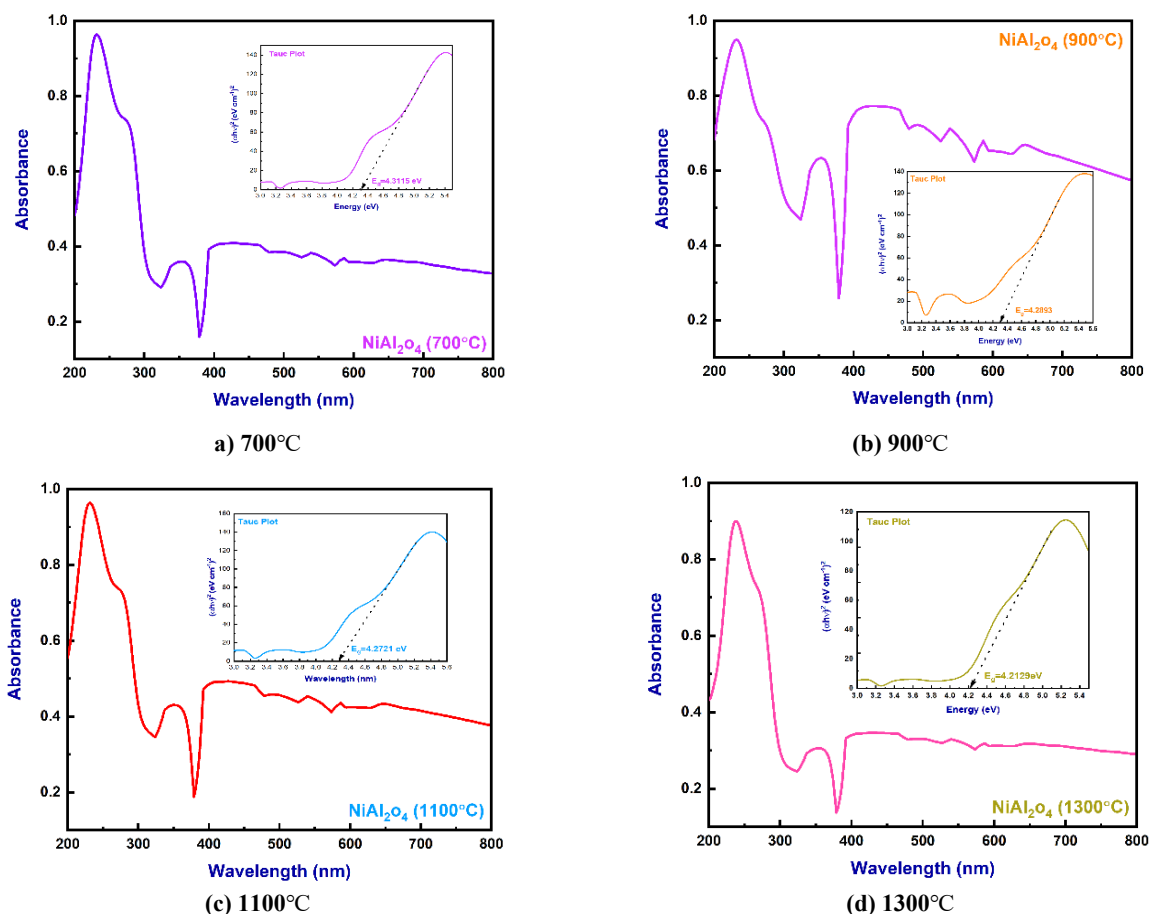
(d) 1300°C

Figure 6. UV-Vis patterns of NiAl$_2$O$_4$ nanoparticles calcinated at 700, 900, 1100 & 1300°C

The first peak can be assigned to the O^{2-} → Ni^{2+} charge transfer process while the second peak to the O^{2-} → Ni^{3+} charge transfer [38]. The energy-level diagram for Ni^{2+} (3d7 configurations) in both octahedral and tetrahedral sites presents few spin-allowed transitions. Regarding Ni^{2+} in a tetrahedral site, it was detected a peak recognized to the [^{4}A$_2$ (F) → ^{4}T$_1$ (P)] transition at around ~ 426 nm (red region), 538 nm (green region), ~ 586 nm (yellow-orange region) and ~646 nm which gives rise to the red coloration. These peaks can be accredited to a Jahn-Teller distortion of the tetrahedral structure [39, 40]. From the literature [41], the absorption peak at 540-650 nm can be attributed to the spin electronic transition ^{3}T$_1$(F) →^{3}T$_1$(p) assigned to tetrahedrally coordinated Ni^{2+}, the peak at 630-800 nm was due to spin transition ^{3}A$_{2g}$(F) → ^{3}T$_{1g}$(F) assigned to octahedrally coordinated Ni^{2+} and the peaks at 230-360 nm and 360-540 nm can be assigned to the charge transfer.

The band gap can be determined by extrapolation to the energy axis of the linear plots of (αhν)^n as a function of the photon energy (hν) as shown in Fig. 6 (Tauc plot). To determine the type of transition, we have used equation (2) which is known as Tauc formula [42]:

$$(\alpha h\nu)^{1/n} = A \, (h\nu - E_g). \qquad (2)$$

Where, α is known as absorption coefficient, A is known as proportional constant, E$_g$ is known as optical band gap of the material and exponent, n represents the nature of electronic transition (2 for a direct transition and 1/2 for an indirect transition). The optical band gap (E$_g$) value for all the samples is calculated, found in the range 4.2129-4.3115eV and furnished in Table 6.

Table 6. The band gap values of NiAl$_2$O$_4$ nanoparticles calcinated at 700, 900, 1100 & 1300°C

Calcination Temperature (°C)	Band gap (E$_g$) (eV)
700	4.3115
900	4.2893
1100	4.2721
1300	4.2129

It can be observed that the optical band gap was found minimum (E_g= 4.2129 eV) for the sample calcinated at 700℃, further it was increased with calcination temperature and found maximum (E_g= 4.3115 eV) for the sample calcinated at 1300℃. In the case of Rahman et al, the optical energy gap for the undoped ZnO and zinc aluminate spinel nanoparticles were found 2.82 and 2.84 eV respectively [43] and they found that it is increased to 3.07 eV with aluminium concentration. Suresh et al. found, the higher optical energy gap of 4.11 eV in case of zinc aluminate [44]. The increase in band gap is due to formation of $ZnAl_2O_4$ spinel phase in $ZnO–Al_2O_3$ system and can be explained on the basis of the Burstein-Moss effect [45]. The optical band gap of nickel aluminate spinel nanoparticles in the present work was observed in the range 4.6270-4.7330 eV. It can be understood that the Fermi level would move close to the conduction band when the carrier concentration was increased, therefore the lower energy transitions were blocked and the optical band gap would be increased. This was also found in good agreement to the quantum confinement effect of the nanoparticles [46].

CONCLUSIONS

1. The prepared nickel aluminate ($NiAl_2O_4$) nanoparticles were divided into four parts and calcinated at 700, 900, 1100 and 1300℃.
2. The X-Ray diffraction patterns authorize the establishment of single-phase cubic spinel structure with space group Fd3m for all the samples except the sample calcinated at 700℃.
3. The average crystallite size and lattice parameter were found maximum in case of the sample calcinated at 700^0C. Both the parameters were found to be increased with the calcination temperature from 900 to 1300℃.
4. The average grain size was found increased with calcination temperature and it was found in the range of 142.80-187.82 nm.
5. The average grain size was found in the range 142.80-187.37 nm whereas interplanar spacing was found in the range of 2.100-2.479 Å. Both the parameters were found to be increased with calcination temperature.
6. The two absorption peaks related to octahedral and tetrahedral sites, in the range 499.5-511.1 and 719.4-729.1 cm^{-1} which confirmed the spinel cubic crystal structure and in good agreement with XRD results.
7. The value of optical band gap (E_g) was found in the range 4.2129-4.3115eV, and the band gap was increased with the calcinated temperature.

ORCID
Katrapally Vijaya Kumar, https://orcid.org/0000-0001-6160-8632
Sara Durga Bhavani, https://orcid.org/0000-0001-9854-0061

REFERENCES
[1] Z. Yin, C. Huang, B. Zou, H. Liu, H. Zhu, and J. Wang, Ceramic International, **40**(2), 2809 (2014). https://doi.org/10.1016/j.ceramint.2013.10.033
[2] J.B. Wachtman, *Mechanical Properties of Ceramics*, (Wiley, New York, 1996)
[3] K. Konopka, M. Maj, and K.J. Kurzydłowski, Mater. Charact. **51**, 335 (2003). https://doi.org/10.1016/j.matchar.2004.02.002
[4] C.C. Huang, C.C. Mo, T.H. Hsiao, G.M. Chen, S.H. Lu, Y.H. Tai, H.H. Hsu, *et al.*, Results in Materials, **8**, 100150 (2020). https://doi.org/10.1016/j.rinma.2020.100150
[5] D.C. Kim, and S.K. Ihm, Env. Sci. Tech. **35**(1), 222 (2001). https://doi.org/10.1021/es001098k
[6] C. Chaves, S.J.G. Lima, R.C.M.U. Araujo, M.A. Maurera, E. Longo, P.S. Pizani, L.G.P. Simões, *et al.*, J. Solid-State Chem. **179**, 985 (2006). https://doi.org/10.1016/j.jssc.2005.12.018
[7] K. Ahn, B.W. Wessels, and S. Sampath, Sensor Actuators B, **107**(1), 342 (2005). https://doi.org/10.1016/j.snb.2004.10.020
[8] P. Lavela, J.L. Tirado, and C.V. Abarca, Electrochimica Acta, **52**(28), 7986 (2007). https://doi.org/10.1016/j.electacta.2007.06.066
[9] Y. Fan, X. Lu, H. Zhang, L. Zhao, J. Chen, and C. Sun, Environ. Sci. Technol. **44**(8), 3079 (2010). https://doi.org/10.1021/es9031437
[10] S. Chen, Y. Wu, P. Cui, W. Chu, X. Chen, and Z. Wu, J. Phys. Chem. C, **117**(47), 25019 (2013). https://doi.org/10.1021/jp404984y
[11] J. Ma, B. Zhao, H. Xiang, F.Z. Dai, Y. Liu, R. Zhang, and Y. Zhou, J. Adv. Cer. **11**, 754 (2022). https://doi.org/10.1007/s40145-022-0569-3
[12] S. Pokhrel, B. Jeyaraj, and K.S. Nagaraja, Mater. Lettrs. **57**(22-23), 3543 (2003). https://doi.org/10.1016/S0167-577X(03)00122-8
[13] C. Peng, and L. Gao, J. Amer. Cer. Soc. **91**(7), 2388 (2008). https://doi.org/10.1111/j.1551-2916.2008.02417.x
[14] R.J. Harrison, and A. Putnis, Surv. in Geophys. **19**, 461 (1998). https://doi.org/10.1023/A:1006535023784
[15] Z.V. Marinkovic, L. Mancic, P. Vulic, and O. Milosevic, J. Euro. Cer. Soc. **25**, 2081 (2005). https://doi.org/10.1016/j.jeurceramsoc.2005.03.085
[16] Yunasfi, A. Mulyawan, Mashadi, D.S. Winatapura, and A.A. Wisnu, Applied Phys. A, **127**, 763 (2021). https://doi.org/10.1007/s00339-021-04907-w
[17] X. Niu, W. Du, and W. Du, Sensor Actuators B, **99**, 405 (2004). https://doi.org/10.1016/j.snb.2003.12.007
[18] C. Jagadeeshwaran, and R. Murugaraj, J. Supercondu. and Novel Magn. **33**, 1765 (2020). https://doi.org/10.1007/s10948-020-05427-z

[19] K.R. Krishna, K.V. Kumar, and D. Ravinder, Adv. in Mater. Phys. and Chem. **2**(3), 185 (2012). http://dx.doi.org/10.4236/ampc.2012.23028

[20] K.V. Kumar, and C.H.S. Chakra, Asian J. of Phys. and Chem. Sci. **2**(2), 1 (2017). https://doi.org/10.9734/AJOPACS/2017/34683

[21] K. Vijaya Kumar, R. Sridhar, D. Ravinder, Int. J. of Nanopart. Res., **2**(6), 1 (2018). https://escipub.com/Articles/IJONR/IJNR-2018-01-0302

[22] L.J. Berchmans, R.K. Selvan, and C.O. Augustin, Mater. Lettrs. **58**(12), 1928 (2004). https://doi.org/10.1016/j.matlet.2003.12.008

[23] Z. Yue, J. Zhou, L. Li, X. Wang, and Z. Gui, Mater. Sci. and Eng. B, **86**(1), 64 (2001). https://doi.org/10.1016/S0921-5107(01)00660-2

[24] N.M. Deraz, Int. J. Electrochem. Sci. **8**, 5203 (2013). http://electrochemsci.org/papers/vol8/80405203.pdf

[25] A. Yamakawa, M. Hashiba, and Y. Nurishi, J. Mater. Sci. **24**, 1491 (1989). https://doi.org/10.1007/BF02397091

[26] N.M. Deraz, Ceramic International, **38**, 511 (2012). https://doi.org/10.1016/j.ceramint.2011.07.036

[27] N.M. Deraz, Int. J. Electrochem. Sci. **7**, 4596 (2012). http://www.electrochemsci.org/papers/vol7/7054596.pdf

[28] A. Becheri, M. Durr, P. Lo Nostro, and P. Baglioni, J. Nanopart. Res. **10**, 679 (2008). https://doi.org/10.1007/s11051-007-9318-3

[29] J. Jacob, and M.A. Khadar, J. Appl. Phys. **107**(11), 114310 (2010). https://doi.org/10.1063/1.3429202

[30] Y.B. Kannan, R. Saravanan, N. Srinivasan, and I. Ismail, J. Magn. and Magn. Mat. **423**, 217 (2017). https://doi.org/10.1016/j.jmmm.2016.09.038

[31] D. Venkatesh, K.V. Ramesh, and C.V.S.S. Sastry, AIP Conference Proceedings, **1859**, 020035 (2017). https://doi.org/10.1063/1.4990188

[32] F. Meyer, R. Hempelmann, S. Mathurband, and M. Veith, J. Mater. Chem. **9**, 1755 (1999). https://doi.org/10.1039/A900014C

[33] Giedrė Nenartavičienė, Darius Jasaitis, and Aivaras Kareiva, Acta Chim. Slov. **51**, 661 (2004). https://acta-arhiv.chem-soc.si/51/51-4-661.pdf

[34] M. Chroma, J. Pinkas, I. Pakutinskiene, A. Beganskiene, and A. Kareiva, Ceramic International, **31**(8), 1123 (2005). https://doi.org/10.1016/j.ceramint.2004.11.012

[35] J.J. Vijaya, L.J. Kennedy, G. Sekaran, and K.S. Nagaraja, Materials Research Bulletin, **43**, 473 (2008). https://doi.org/10.1016/j.materresbull.2007.02.030

[36] S. Angappan, L.J. Bechermans, and C.O. Augustin, Mater. Lett. **58**, 2283 (2004). https://doi.org/10.1016/j.matlet.2004.01.033

[37] Z. Chen, E. Shi, W. Li, Y. Zheng, N. Wu, and W. Zhong, J. Am. Ceram. Soc. **85**, 2949 (2002). https://doi.org/10.1111/j.1151-2916.2002.tb00561.x

[38] M. Llusar, A. Forés, J.A. Badenes, J. Calbo, M.A. Tena, and G. Monrós, J. Eur. Ceram. Soc. **21**(8), 1121 (2001). https://doi.org/10.1016/S0955-2219(00)00295-8

[39] A.A. Verberckmoes, B.M. Weckhuysen, and R.A. Schoonheydt, Micropor. Mesopor. Mater. **22**(1-3), 165 (1998). https://doi.org/10.1016/S1387-1811(98)00091-2

[40] F. Matteucci, G. Cruciani, M. Dondi, G. Gasparotto, and D.M. Tobaldi, J. Solid State Chem. **180**(11), 3196 (2007). https://doi.org/10.1016/j.jssc.2007.08.029

[41] P. Jeevanandam, Yu. Koltypin, and A. Gedanken, Mater. Sci. Eng. B, **90**(1-2), 125 (2002). https://doi.org/10.1016/S0921-5107(01)00928-X

[42] M. Jestl, I. Maran, A. Köck, W. Beinsting, and E. Gornik, Opt. Lett. **14**(14), 719 (1989). https://doi.org/10.1364/OL.14.000719

[43] A. Rahman, M.S. Charoo, and R. Jayaganthan, Materials Technology Adv. Perf. Mater. **30**(3), 1 (2015). https://doi.org/10.1179/1753555714Y.0000000211

[44] S.K. Sampath, D.G. Kanhere, and R. Pandey, J. Phys. Condens. Matter, **11**, 3635 (1999). https://doi.org/10.1088/0953-8984/11/18/301

[45] S. Suwanboon, T. Ratana, and T. Ratana, J. Sci. Technol. **4**(1), 111 (2007). https://wjst.wu.ac.th/index.php/wjst/article/view/129/111

[46] T. Takagahara, and K. Takeda, Phys. Rev. B, **46** 15578 (1992). https://doi.org/10.1103/PhysRevB.46.15578

ВПЛИВ ТЕМПЕРАТУРИ КАЛЬЦИНАЦІЇ НА СТРУКТУРНІ ТА ОПТИЧНІ ВЛАСТИВОСТІ НАНОЧАСТИНОК АЛЮМІНАТУ НІКЕЛЮ

Катрапалі Віджая Кумар[a], Сара Дурга Бхавані[b]

[a]Кафедра фізики, Інженерний коледж університету JNTUH Rajanna Sircilla,
Аграхарам, район Раджанна Сірчілла, 505302, TS, Індія
[b]Кафедра хімії, Державний коледж, Раджендра Нагар, Хайдарабад, 500001, TS, Індія

Наночастинки алюмінату нікелю (NiAl$_2$O$_4$) синтезовано золь-гель методом з автоспалюванням. Підготовлені наночастинки були розділені на чотири частини та прожарені при 700, 900, 1100 і 1300°C і використані для цього дослідження. Захоплені наночастинки були охарактеризовані за допомогою порошкової рентгенівської дифракції (XRD), скануючої електронної мікроскопії (SEM), енергетичної дисперсійної рентгенівської спектроскопії (EDS), перетворення Фур'є та інфрачервоної (FT-IR) спектроскопії та спектроскопії UV-Vis. Рентгенівські дифрактограми підтвердили структуру шпінелі та просторову групу Fd3m. Формула Шеррера була використана для розрахунку розміру кристалітів і було знайдено розмір в діапазоні від 5,78 до 20,55 нм, тоді як параметр решітки був знайдений в діапазоні від 8,039 до 8,342 Å. Середній розмір зерна знаходився в діапазоні від 142,80 до 187,37 нм, тоді як міжплощинний відстань знаходилася в діапазоні від 2,100 до 2,479 Å. Спектроскопія FTIR показала шість смуг поглинання в діапазоні від 400 до 3450 см$^{-1}$ і підтвердила структуру шпінелі. Ширина забороненої зони (Eg) зменшувалася з температурою прожарювання і знаходилася в діапазоні 4,2129 - 4,3115 еВ.

Ключові слова: *наночастинки алюмінату нікелю; метод золь-гель автозгоряння; температура прожарювання; розмір кристаліту; розмір зерен; елементний аналіз; ІЧ та УФ-видима спектроскопія*

X-RAY DIFFRACTION AND RAMAN SPECTROSCOPY ANALYSES OF GaSb-ENRICHED Si SURFACE FORMED BY APPLYING DIFFUSION DOPING TECHNIQUE[†]

Xalmurat M. Iliyev[a], Vladimir B. Odzhaev[b], Sobir B. Isamov[a], Bobir O. Isakov[a,*], Bayrambay K. Ismaylov[a], Kutub S. Ayupov[a], Shahzodbek I. Hamrokulov[a], Sarvinoz O. Khasanbaeva[a]

[a]*Tashkent state technical university, Uzbekistan, 100095, Tashkent, University St., 2.*
[b]*Belarusian State University, 4220030 Minsk, Republic of Belarus*
Corresponding Author e-mail: bobir6422isakov@gmail.com

The paper studies the properties of surface and near-surface region of a single crystalline silicon sample doped with atoms of Ga (A^{III}) and Sb (B^{V}). n-type single-crystal Si wafers were chosen as substrates, and samples were size of $8 \times 10 \times 0.5$ mm^3. For diffusion into silicon, Ga and Sb impurities were used with a purity of 99.999 and 99.998, respectively. The authors propose that a new heterostructure might form in the near-surface region of silicon that could be engineered by applying a relatively cheap diffusion method. The experimental and analysis results show that the composition and absorption spectrum of silicon start manifest certain changes, and can be used in the future as a functional material for solar cells. The result showed that randomly located islands with an average diameter of 1–15 μm are formed on the substrate surface. X-ray diffraction analysis was carried out using a Rigaku diffractometer to study the crystallographic parameters of islands formed with the participation of Ga and Sb atoms on the silicon surface. The energy spectrum was studied on Nanofinder High End Raman spectrometer (LOTIS TII) in order to determine the presence of complexes of Ga and Sb atoms within islands formed as a result of diffusion. The optical emission spectra in the new structure were studied using a Lambda 950 spectrophotometer. The measurements 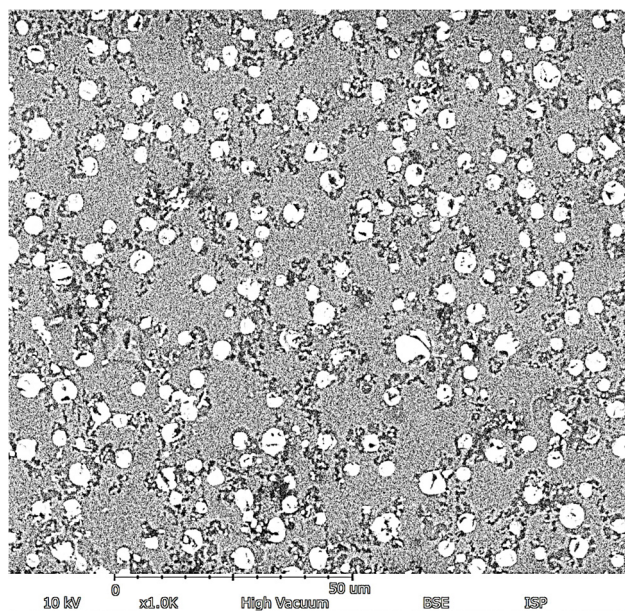were carried out at room temperature, i.e., at 300°K. Having studied the results of X-ray analysis, Raman spectroscopy, and optical spectroscopy, the authors have revealed that Ga and Sb atoms form new Si$_{0.44}$(GaSb)$_{0.56}$ and Si$_{0.75}$(GaSb)$_{0.25}$-type binary compounds on Si surface.

Keywords: *Silicon, Gallium; Antimony; Doping; Diffusion; Microsized islands*
PACS: 61.72.uf, 68.43.Jk

1. INTRODUCTION

It is well known that silicon tends to be the main semiconductor material most commonly used in the field of electronics. Despite a number of advantages such as the abundance of silicon raw material on earth, the availability of a standard production technology, nevertheless, the main parameters of silicon, such as the band gap, charge carrier mobility, energy band structure, cannot meet the requirements of the current rapidly developing field of electronics [1-3]. Therefore, today it is of certain scientific and practical importance to study the effect of binary compounds on the crystal lattice, leading to a substantial alteration in the properties of silicon [4-5]. GaSb layers were obtained on various substrates by the authors [6-7] using the modern technique of molecular beam epitaxy, while their properties were studied by X-ray diffraction analysis [8], Raman spectroscopy [9], transmission electron microscopy (TEM) [10-11]. The possibilities of manufacturing high-precision electronic devices [12–14] and manufacturing infrared sensors [15–16] are shown. Previously unknown nanoscale effects have been discovered in GaSb-based structures [17–19], where layers are limited across one, two, or even three dimensions. However, the modern method of molecular beam epitaxy, which is currently used to obtain nanosized structures, requires the availability of expensive equipment and complex technological processes [20].

While growing thin layers, the quality of crystallization strongly depends on the crystallographic parameters of the base material, which means that the lattice constants of the substrate and growing crystals should be close to each other [21]. An analysis of the literature shows that, in most cases, the degree of interaction between the resulting GaSb layer and the substrate was not taken into account [22–24]. In this paper, we demonstrate that diffusion technology can be used to form thin layers of GaSb transferred onto a Si substrate, and the parameters of the obtained samples are given (Si and GaSb ~12% lattice mismatch).

2. MATERIALS AND METHODS

A Czochralski-grown n-type single-crystal Si wafer was chosen as the substrate, and several samples were made for further cutting using a Machine STX-402 (diamond wire cutting machine STX-402) brand. Samples were cut out with a size of $8 \times 10 \times 0.5$ mm^3. For diffusion into silicon, Ga and Sb impurities were used with a purity of 99.999 and 99.998, respectively.

Before diffusion, the substrate surface was subjected to standard cleaning and degreasing with HF-acid at 1-2 minutes intervals. The diffusion process was carried out inside AOT-GLS-1750X-type Vacuum Tube Furnace for

---

Laboratory Material Burning. The diffusion process lasted for 5 hours and started from room temperature (30°C) up to 1200°C, then it was carried out in a gas-phase medium of impurity atoms at this temperature. The image of the silicon surface after diffusion was obtained using a DJ-SEM-type 150D-ST scanning electron microscope.

The result showed that randomly located islands with an average diameter of 1–15 µm are formed on the substrate surface. X-ray diffraction analysis was carried out using a Rigaku diffractometer to study the crystallographic parameters of islands formed with the participation of Ga and Sb atoms on the silicon surface. The energy spectrum was studied on Nanofinder High End Raman spectrometer (LOTIS TII) in order to determine the presence of complexes of Ga and Sb atoms within islands formed as a result of diffusion. The optical emission spectra in the new structure were studied using a Lambda 950 spectrophotometer. The measurements were carried out at room temperature, i.e., at 300°K.

Figure 1. SEM image of the surface of Si doped with Ga and Sb

3. RESULTS AND DISCUSSION
3.1. XRD analysis

The Figure 2 illustrates the comparative analysis of X-ray diffraction data of Si sample in which Ga and Sb atoms were diffusely embedded and the values extracted from COD crystallographic open database. The spectrogram of X-rays reflected from the surface of a silicon sample after diffusion shows 17 main peaks (Fig. 2-*a*). To identify the resulting peaks, the lines were superimposed corresponding to 2 theta angles (Fig. 2-*b*, *c*) from the International Open Crystallographic Database for GaSb and Si materials.
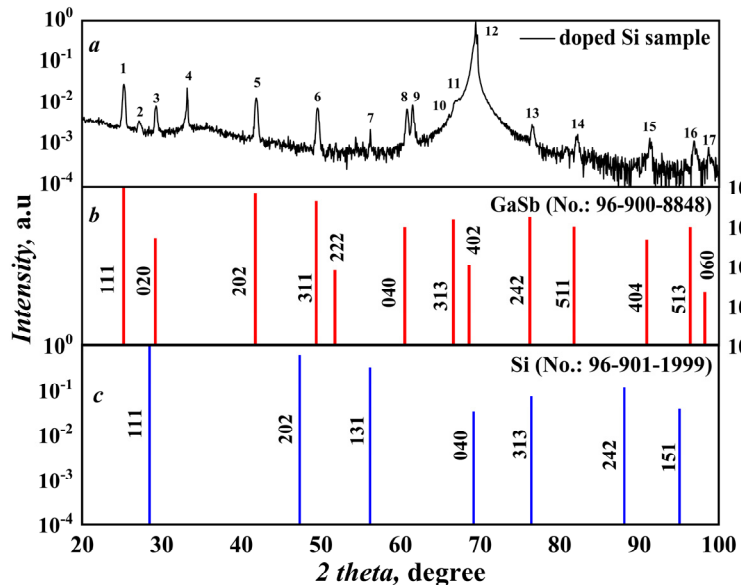
Figure 2. X-ray pattern: *a* – Si sample doped with Ga and Sb atoms; *b* and *c* – GaSb and Si semiconductor crystal databases from the COD (Crystallography Open Database) No: 96-900-8848 and No: 96-901-1999 respectively

One can judge that GaSb form on Si surface that is reflected by revealing peaks 25.25, 29.35, 41.89, 49.58, 60.78, 66.05, 67.5, 76.55, 82.25, 91.32, 96.82, 98.71, corresponding to crystallographic directions (111), (020), (202), (311), (040), (313), (402), (242), (511), (404), (513), (060). In the general spectrum in Figure 2-a, of course, there are peaks 56.23, 69.41, 76.55, related to Si, corresponding to crystallographic planes (131), (040), (313). Peak analysis showed that there were peaks No. 2, No. 9, which do not belong to either GaSb or Si. It's known that lattice constants of GaSb and Si are a=6,09 Å, a=5,34 Å respectively [25-26].

The peaks of GaSb (242) in Figure 2-*b* and Si (313) in Figure 2-*c* overlap. The authors of [27] indicate that peak No.4 belongs to Si (020). But since the No.2 and No.9 peaks are located between the GaSb 2 theta=25.25 (111) and Si 2 theta=28.45 (111) and GaSb 2 theta = 60.51 (040) and Si 2 theta = 69.25 (040) peaks, respectively, we can assume that that the detected peaks No.2 (111) and peak No.9 (040) probably belong to the new $Si_{l-x}GaSb_x$ structure. Using these results, the lattice constant (a) and diffraction lattice constant (d_{hkl}) of the GaSb binary compound formed on Si and its surface were calculated using the following expressions 1 and 2, respectively (Table 1)

$$a = d_{hkl} \cdot \sqrt{h^2 + k^2 + l^2} \ . \tag{1}$$

$$d_{hkl} = \frac{\lambda}{2 \cdot \sin\theta}, \tag{2}$$

where θ is Bragg's angle and λ=0.15402 nm (wavelength of Cu - Kα).

Table 1. Values of the lattice constant and diffraction lattice constant of new crystals formed in the sample, calculated based on the experimental results.

Crystal	Peak No.	2 theta	h	k	l	d_{hkl}, Å	a_{hkl}, Å
GaSb	1	25.25	1	1	1	3.52	6.10
	3	29.35	0	2	0	3.04	6.08
	5	41.89	2	0	2	2.15	6.09
	6	49.58	3	1	1	1.84	6.09
	8	60.78	0	4	0	1.52	6.09
	10	66.05	3	1	3	1.41	6.16
	11	67.5	4	0	2	1.39	6.19
	13	76.55	2	4	2	1.24	6.09
	14	82.25	5	1	1	1.17	6.08
	15	91.32	4	0	4	1.08	6.09
	16	96.82	5	1	3	1.03	6.09
	17	98.71	0	6	0	1.01	6.09
Si	4	33.21	0	2	0	2.69	5.39
	7	56.23	1	3	1	1.63	5.42
	12	69.41	0	4	0	1.35	5.41
	13	76.55	3	1	3	1.24	5.42
$Si_{1-x}(GaSb)_x$	2	27.19	1	1	1	3.28	5.67
	9	61.55	0	4	0	1.50	6.02

3.2. Analysis of Raman spectroscopy

Raman spectrometry is the most useful method available for studying lattice vibrations and their interactions with other excitations. Changes after implantation of type III-V semiconductors with ions were considered based on the study of Raman spectra [28-30]. When Raman spectra are obtained at room temperature while samples were exposed to Ar laser with a wavelength of 5145 Å, the light penetration depth happened to be 1000 Å [28-30]. Therefore, it is possible to estimate the properties of the near-surface structure using the Raman spectrometry analysis [28-30]. Given that the Ga and Sb atoms in silicon are located at the sites of the crystal lattice [28-30], we can expect changes in lattice vibrations. Detecting such changes by studying the Raman spectra is of both scientific and practical importance. Therefore, during the study of Si samples doped with Ga and Sb atoms, the Raman spectrum was obtained at 3 different points depending on the areas on the image of the sample surface (Fig. 3).

Figures 3-*b, d, f* represents an image of the surface of the sample, and also show the areas where laser light with a wavelength of 532 nm and a power of 20 MW is incident. As seen in the pictures, the main surface is gray with white islands and black closed-type curves. These three regions, which differ from each other, were chosen for exposer to laser beam. A graphical representation of each selected point of the Raman spectrum is shown in Figures 3-*a, c, e*, respectively. Analysis of the Raman spectrum obtained in the main gray area in Figure 3-*a* showed the presence of one peak at 519 cm^{-1}, the intensity of which was very high (intensity = 15000 a.u.). The fact that this peak belongs to Si has been confirmed in literature [30]. However, figure 3-*c* shows the spectrum obtained at one of the points on the surface of the white island. As can be seen from the figure, one peak was found in the spectrum at 225 cm^{-1} (intensity = 7000 a.u.), and it turned out that this peak belongs to GaSb (LO) crystal. Figure 3-*e* shows the spectrum obtained above the black line, in this case 2 completely different peaks were obtained. When comparing the peak values with the data given in the literature, it was found that the peak at 222.1 cm^{-1} refers to GaSb, and the peak at 519 cm^{-1} to Si. From the latest results obtained, we can assume that the region with a black closed curve is a crystal with the composition Si(GaSb).
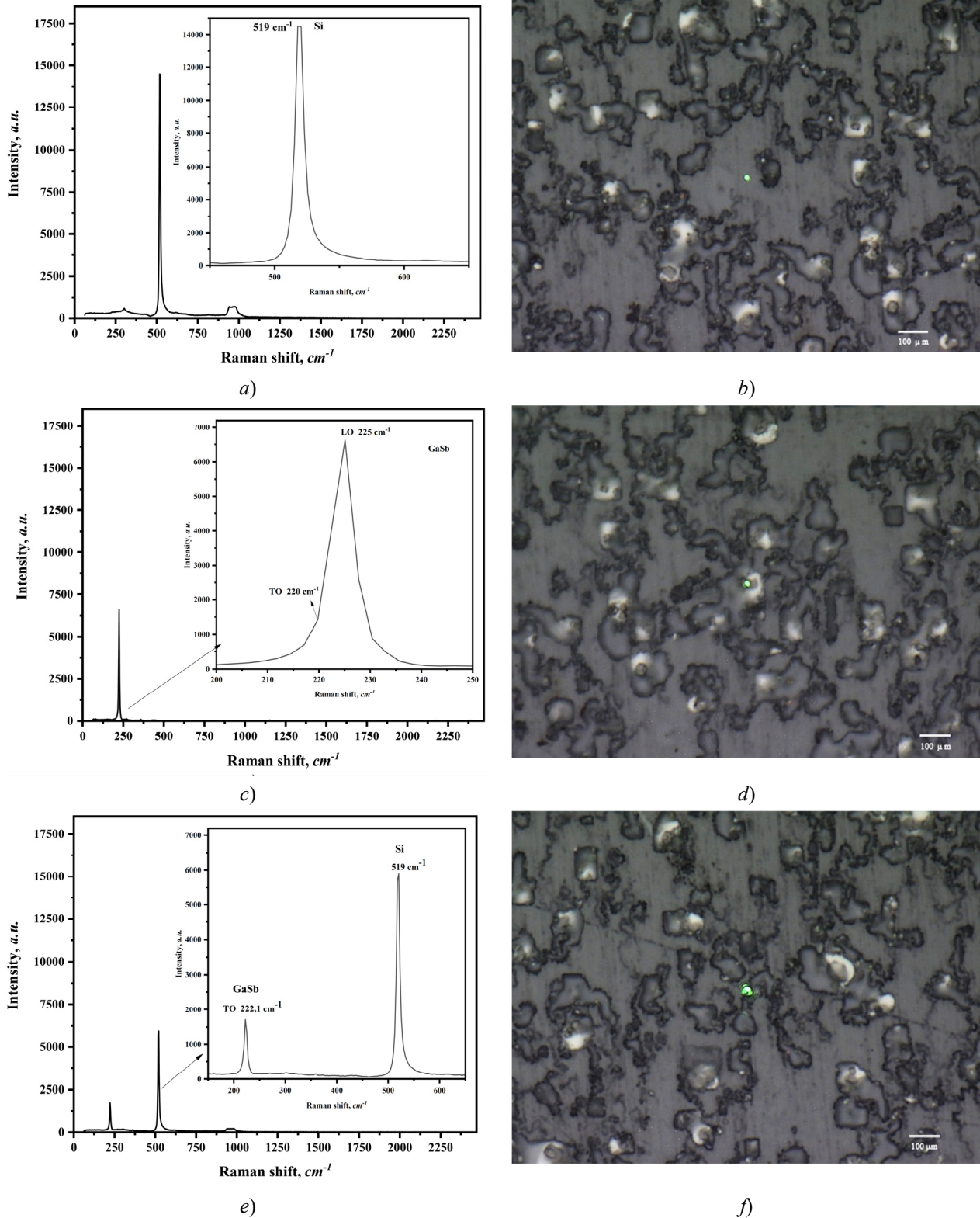
Figure 3. Raman spectrum and image of Si sample surface doped with Ga and Sb impurity atoms

3.3. Spectroscopic analysis

It is known that the band gap of GaSb binary compound and Si semiconductor material is E_g=0.726 eV, E_g=1.12 eV (at T=300 K), respectively. The band gap of semiconductors with complex compounds can theoretically be calculated using Vegard's law (expression 7)

$$E_{g,A_{(1-x)}B_x} = (1-x) \cdot E_{g,A} + x \cdot E_{g,B} \tag{7}$$

Where $E_{g,A}$ is the band gap of material A, $E_{g,B}$ is the band gap of material B, $E_{g,A_{(1-x)}B_x}$ is the band gap of the compound material, x is the fraction of the material. Using expression 7, the band gap of the $Si_{(1-x)}(GaSb)_x$ compound was calculated. The results of the study showed that the band gap of $Si_{(1-x)}(GaSb)_x$ compound can be in the range of $0.726 \div 1.12$ eV.

A Si sample doped with Ga and Sb atoms was characterized by light reflection using a Perkin-Elmer Lambda 950-type UV-visible spectrophotometer, available at the laboratory of the Solar Energy Institute at EGE University (Fig. 5).
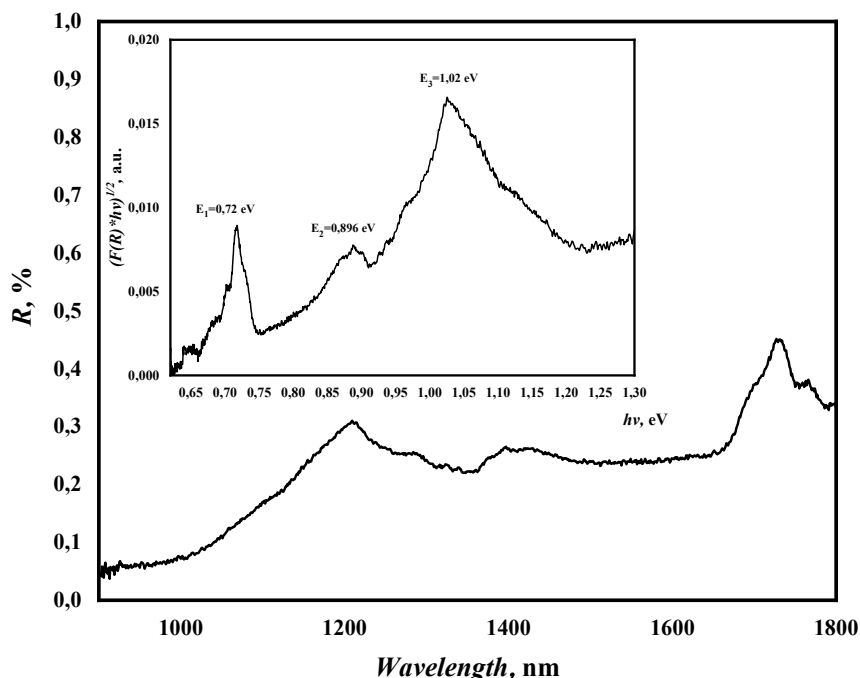
Figure 5. Reflective characteristic of a Si sample doped with Ga and Sb atoms

The Figure 5 shows the energies $E_1=0.72$ eV, $E_2=0.896$ eV and $E_3=1.02$ eV. The energy E_1 is the band gap of the GaSb semiconductor material, E_2 and E_3 are the band gap values of the material with $Si_{(1-x)}(GaSb)_x$ compounds. Having determined the ratio of Si and GaSb using the inverse calculation of Vegard's law (formula 7) and taking into consideration that $E_2=0.892$ eV is the band gap Eg of the material $Si_{(1-x)}(GaSb)_x$, we calculate it in GFA as follows.

$$E_{g,Si_{(1-x)}(GaSb)_x} = (1-x) \cdot E_{g,Si} + x \cdot E_{g,GaSb}$$

if we substitute the energy values E_2, $E_{g,Si}$, $E_{g,GaSb}$ into this equation, we get the following linear equation with one unknown

$$0.896 = (1-x) \cdot 1.12 + x \cdot 0.726$$

This equation shows that $x = 0.56$. Thus, we can say that E_2 corresponds to energy of $Si_{0.44}(GaSb)_{0.56}$ newly formed structure. Similarly, E_3 corresponds to the energy of $Si_{0.75}(GaSb)_{0.25}$ structure.

3.4. Discussion

In times of diffusion of more than one type of impurity element atoms into silicon, under certain thermodynamic conditions, the formation of complex compounds can theoretically be predicted. In this work, to study diffusion into silicon of elements with similar diffusion parameters, solubility, and diffusion coefficient, such as Ga and Sb, were chosen as impurities. In addition, GaSb itself is a semiconductor material, the crystal parameters of which are fundamentally different from those of Si. Its cost is 1.5 times greater than the cost of Si. The formation of GaSb crystals on the silicon surface by diffusion of atoms of the elements Ga and Sb in Si without the use of a priori GaSb material was confirmed by X-ray diffraction analysis.

The results of the experiments revealed the formation of a new type of crystal, consisting not only of GaSb crystals, but also of components of Si and GaSb crystals. This is of great scientific and practical importance, since a new Si-based material can be obtained by simple diffusion process. It can be assumed that the properties of the material might reflect new previously unknown properties of Si and GaSb semiconductor materials. The graph of the comparative XRD and Raman spectra shows the formation of a new peak. Based on the calculation results, we assumed that the newly formed compound contains SiGaSb, and its lattice constant was equal to 5.67 Å and 6.02 Å. The properties of the new crystal further expand the scope of Si, differing from the fundamental parameters of Si. Based on the results obtained, it can be concluded that Si can also be widely used in optoelectronics.

4. CONCLUSION

The formation of a new $Si_{0.44}(GaSb)_{0.56}$ and $Si_{0.75}(GaSb)_{0.25}$ -type crystal structures on the surface of a Si sample doped by the diffusion method with impurity Ga and Sb atoms, was confirmed using three modern spectroscopic methods: X-ray phase analysis, Raman spectroscopy, and UV-VIS-NIR spectroscopy. The results of the experiments showed that a new crystal structure containing GaSb on the Si surface can be formed using an inexpensive and widely used diffusion doping technology. The crystallographic parameters of the new crystal were presented for the first time on the basis of experimental results.

ORCID
Sobir B. Isamov, https://orcid.org/0000-0001-5669-9306; **Bobir O. Isakov,** https://orcid.org/0000-0002-6072-3695
Bayrambay K. Ismaylov, https://orcid.org/0000-0002-5880-4568; **Kutub S. Ayupov,** https://orcid.org/0000-0002-2521-3921

REFERENCES
[1]   Y. Yin, J. Li, Y. Xu, H.K. Tsang, and D. Dai, "Silicon-graphene photonic devices," Journal of Semiconductors, **39**(6), 061009/1-8 (2018). https://doi.org/10.1088/1674-4926/39/6/061009

[2]   W. Yang, Y. Li, F. Meng, H. Yu, M. Wang, P. Wang, G. Luo, et al., "III–V compound materials and lasers on silicon," Journal of Semiconductors, **40**, 101305 (2019). http://doi.org/10.1088/1674-4926/40/10/101305

[3]   M. Levinshtein, S. Rumyantsev, and M. Shur, editors, *Semiconductor parameters. Handbook series on semiconductor parameters.* (World Scientific Publishing, 1996). Vol. 1.

[4]   A.A.M. Monzur-Ul-Akhir, M. Mori, and K. Maezawa, "Heteroepitaxial growth of InGaSb on GaSb/Si(111)–√3×√3-Ga surface phase with a two-step growth method to investigate the impact of high-quality GaSb buffer layer," Phys. Status Solidi B, **254**(2), 1600528 (2017). https://doi.org/10.1002/pssb.201600528

[5]   A.A.M. Monzur-Ul-Akhir, M. Mori, and K. Maezawa, "An investigation of the crystalline nature for GaSb films on Si(111) at varied growth temperature and growth rate," Japanese Journal of Applied Physics, **58**, (SIIA17) (2019). https://doi.org/10.7567/1347-4065/ab23f8

[6]   N. Bertru, M. Nouaoura, J. Bonnet, and L. Lassabatere, "GaSb molecular beam epitaxy growth on vicinal surfaces studied by RHEED," Journal of Crystal Growth. **160**, 1-6 (1996). https://doi.org/10.1016/0022-0248(95)00435-1

[7]   R. Machida, K. Akahane, I. Watanabe, S. Hara, S. Fujikawa, A. Kasamatsu, and H.I. Fujishiro, "Advantage of heteroepitaxial GaSb thin-film buffer and GaSb dot nucleation layer for GaSb/AlGaSb multiple quantum well structure grown on Si(1 0 0) substrate by molecular beam epitaxy," Journal of Crystal Growth, **507**, 357-361 (2019). https://doi.org/10.1016/j.jcrysgro.2018.11.026

[8]   J.B. Rodriguez, K. Madiomanana, L. Cerutti, A. Castellano, E. Tournié, "X-ray diffraction study of GaSb grown by molecular beam epitaxy on silicon substrates," Journal of Crystal Growth, **439**, 33-39 (2016). http://dx.doi.org/10.1016/j.jcrysgro.2016.01.005

[9]   M. Yano, H. Furuse, Y. Iwai, K. Yoh, and M. Inoue, "Raman scattering analysis of InAs/GaSb ultrathin-layer superlattices grown by molecular beam epitaxy," Journal of Crystal Growth, **127**, 807-811 (1993). https://doi.org/10.1016/0022-0248(93)90737-H

[10] A. Guivarc'h, Y. Ballini, Y. Toudic, M. Minier, P. Auvray, B. Guenais, J. Caulet, et al., "ErSb/GaSb(OQl) and GaSb/ErSb/GaSb(OOl) heterostructures and [ErSb,GaSb] superlattices: Molecular beam epitaxy growth and characterization," Journal of Applied Physics, **75**, 2876-2883 (1994). https://doi.org/10.1063/1.356181

[11] K. Krishnaswami, S.R. Vangala, H.M. Dauplaise, L.P. Allen, G. Dallas, D. Bakken, D.F. Bliss, and W.D. Goodhue, "Molecular beam epitaxy on gas cluster ion beam-prepared GaSb substrates: Towards improved surfaces and interfaces," Journal of Crystal Growth, **310**, 1619-1626 (2008). https://doi.org/10.1016/j.jcrysgro.2007.11.225

[12] Y.H. Kim, Y.K. Noh, M.D. Kim, J.E. Oh, K.S. Chung, "Transmission electron microscopy study of the initial growth stage of GaSb grown on Si (001) substrate by molecular beam epitaxy method," Thin Solid Films, **518**, 2280-2284 (2010). https://doi.org/10.1016/j.tsf.2009.09.120

[13] Y.H. Kim, J.Y. Lee, Y.G. Noh, M.D. Kim, J.E. Oh, "High-resolution transmission electron microscopy study on the growth modes of GaSb islands grown on a semi-insulating GaAs (001) substrate," Applied Physics Letters, **90**, 241915 (2007). https://doi.org/10.1063/1.2747674

[14] R.D. Wiersma, J.A.H. Stotz, O.J. Pitts, C.X. Wang, M.L.W. Thewalt, and S.P. Watkins, "Electrical and optical properties of carbon-doped GaSb," Physical Review B, **67**, 165202 (2003). https://doi.org/10.1103/PhysRevB.67.165202

[15] M.R. Kitchin, J.P. Hagon, and M. Jaros, "Models of GaSb/InAs type-II infrared detectors at very long wavelengths: band offsets and interface bonds," Semiconductor Science and Technology, **18**, 225-233 (2003). https://doi.org/10.1088/0268-1242/18/4/306

[16] R. Hao, S. Deng, L. Shen, P. Yang, J. Tu, H. Liao, Y. Xu, and Z. Niu, "Molecular beam epitaxy of GaSb on GaAs substrates with AlSb/GaSb compound buffer layers," Thin Solid Films, **519**, 228-230 (2010). https://doi.org/10.1016/j.tsf.2010.08.001

[17] R. Pathak, U. Dadwal, and R. Singh, "Study of hydrogen implantation-induced blistering in GaSb for potential layer transfer applications," Journal of Physics D: Applied Physics, **50**, 285301 (2017). https://doi.org/10.1088/1361-6463/aa7522

[18] M.A. Kamarudin, M. Hayne, Q.D. Zhuang, O. Kolosov, T. Nuytten, V.V. Moshchalkov, and F. Dinelli, "GaSb quantum dot morphology for different growth temperatures and the dissolution effect of the GaAs capping layer," Journal of physics D: Applied physics, **43**, 065402 (2010). http://iopscience.iop.org/0022-3727/43/6/065402

[19] M. Tornberg, E.K. Mårtensson, R.R. Zamani, S. Lehmann, K.A. Dick, and S.G. Ghalamestani, "Demonstration of Sn-seeded GaSb homoand GaAs–GaSb heterostructural nanowires," Nanotechnology, **27**, 175602 (2016). https://doi.org/10.1088/0957-4484/27/17/175602

[20] M.K. Bakhadyrkhanov, Kh.M. Iliev, K.S. Ayupov, B.A. Abdurakhmonov, P.Yu. Krivenko, and R.L. Kholmukhamedov, "Self-Organization of Nickel Atoms in Silicon," Inorganic Materials, **47**(9), 962-964 (2011). https://doi.org/10.1134/S0020168511090020

[21] S.G. Konnikov, T.B. Popova, S.A. Ruvimov, M.M. Sobolev, L.M. Sorokow, I.L. Shulpina, V.E. Umanse, "The Influence of Lattice Mismatch upon Defects Generation and Luminescent Characteristics of Heterostructures in the Gap-InP System," Crystal Research and Technology, **16**(2), 169-174 (1981). https://doi.org/10.1002/CRAT.19810160209

[22] M.R. Calvo, J.-B. Rodriguez, L. Cerutti, M. Ramonda, G. Patriarche, and E. Tournié, "Molecular-beam epitaxy of GaSb on 6-offcut (0 0 1) Si using a GaAs nucleation layer," Journal of Crystal Growth, **529**, 125299 (2020). https://doi.org/10.1016/j.jcrysgro.2019.125299

[23] I. Lucci, S. Charbonnier, L. Pedesseau, M. Vallet, L. Cerutti, J.-B. Rodriguez, E. Tournié, et al., "Universal description of III-V/Si epitaxial growth processes," Physical review materials, **2**, 06040 (2018). https://doi.org/10.1103/PhysRevMaterials.2.060401

[24] A. Ponchet, G. Patriarche, J. B. Rodriguez, L. Cerutti, and E. Tournie, "Interface energy analysis of III–V islands on Si (001) in the Volmer-Weber growth mode," Applied Physics Letters, **113**, 191601(2018). https://doi.org/10.1063/1.5055056

[25] H. Aharoni, "Measurement of the lattice constant of Si-Ge heteroepitaxial layers grown on a silicon substrate," Vacuum, **28**(12), 571-578 (1978). https://doi.org/10.1016/0042-207X(78)90014-3

[26] A. Sasaki, M. Nishiuma, and Y. Takeda, "Energy Band Structure and Lattice Constant Chart of III-V Mixed Semiconductors, and AlGaSb/AlGaAsSb Semiconductor Lasers on GaSb Substrates," Japanese Journal of Applied Physics, **19**(9), 1695-1702 (1980). https://doi.org/10.1143/JJAP.19.1695

[27] Y. Meng, G. Liu, A. Liu, H. Song, Y. Hou, B. Shi, and F. Shan, "Low-temperature fabrication of high-performance indium oxide thin film transistors," The Royal Society of Chemistry. RSC Adv. **2015**(5), 37807-37813 (2015). https://doi.org/10.1039/c5ra04145g

[28] Y.K. Su, K.J. Gan, J.S. Hwang, and S.L. Tyan, "Raman spectra of Si-implanted GaSb," J. Appl. Phys. **68**, 5584-5587 (1990). https://doi.org/10.1063/1.346994

[29] S.G. Kim, H. Asahi, M. Seta, J. Takizawa, S. Emura, R.K. Soni, and S. Gonda, and H. Tanoue, "Raman scattering study of the recovery process in Ga ion implanted GaSb," Journal of Applied Physics, 74, 579-585 (1993). https://doi.org/10.1063/1.355270

[30] T. Toda, Y. Jinbo, and N. Uchitomi, "Structural and optical characterization of GaSb layers on Si (001) substrates," Phys. Stat. Sol. (c) **3**(8), 2693-2696 (2006). https://doi.org/10.1002/pssc.200669553

АНАЛІЗ РЕНТГЕНОВСЬКОЇ ДИФРАКЦІЇ ТА РАМАНІВСЬКА СПЕКТРОСКОПІЯ ПОВЕРХНІ Si, ЗБАГАЧЕНОЇ GaSb, СФОРМОВАНОЇ ШЛЯХОМ ЗАСТОСУВАННЯ МЕТОДУ ДИФУЗІЙНОГО ЛЕГУВАННЯ

Халмурат М. Ілієв[a], Володимир Б. Оджаєв[b], Собір Б. Ісамов[a], Бобір О. Ісаков[a], Байрамбай К. Ісмайлов[a], Кутуб С. Аюпов[a], Шахзодбек І. Хамрокулов[a], Сарвіноз О. Хасанбаева[a]

[a]*Ташкентський державний технічний університет, Узбекистан, 100095, м. Ташкент, вул. Університетська, 2.*
[b]*Білоруський державний університет, 4220030 Мінськ, Республіка Білорусь*

Досліджено властивості поверхневої та приповерхневої області зразка монокристалічного кремнію, легованого атомами Ga (AIII) та Sb (BV). Як підкладки були обрані пластини монокристалічного кремнію n-типу, розмір зразків 8×10×0,5 мм³. Для дифузії в кремній використовували домішки Ga і Sb з чистотою 99,999 і 99,998 відповідно. Автори припускають, що нова гетероструктура може утворитися в приповерхневій області кремнію, яку можна створити шляхом застосування відносно дешевого методу дифузії. Результати експерименту та аналізу показують, що склад і спектр поглинання кремнію на початку зазнають певних змін і можуть використовуватися в майбутньому як функціональний матеріал для сонячних елементів. Результат показав, що на поверхні підкладки утворюються хаотично розташовані острівці із середнім діаметром 1-15 мкм. Рентгеноструктурний аналіз проводили на дифрактометрі Rigaku для дослідження кристалографічних параметрів острівців, утворених за участю атомів Ga та Sb на поверхні кремнію. Енергетичний спектр досліджували на спектрометрі Nanofinder High End Raman (LOTIS TII) з метою визначення наявності комплексів атомів Ga і Sb в острівцях, утворених в результаті дифузії. Спектри оптичної емісії в новій структурі досліджувалися на спектрофотометрі Lambda 950. Вимірювання проводили при кімнатній температурі, 300°К. Вивчивши результати рентгенівського аналізу, спектроскопії комбінаційного розсіювання та оптичної спектроскопії, виявлено, що атоми Ga та Sb утворюють нові бінарні сполуки типу $Si_{0,44}(GaSb)_{0,56}$ та $Si_{0,75}(GaSb)_{0,25}$ на поверхні Si.

Ключові слова: *кремній, галій; сурма; легування; дифузія; мікроострови*

IMPACT OF CRYSTALLITE SIZE ON STRUCTURAL, OPTICAL AND MAGNETIC CHARACTERISTICS OF La0.7Sr0.15Ca0.15MnO3 NANOCRYSTALLINE[†]

Mohd Abdul Shukur[a,b], Katrapally Vijaya Kumar[a,*], Gade Narsinga Rao[c]

[a]Department of Physics, JNTUH University College of Engineering Rajanna Siricilla,
Agraharam, Rajanna Siricilla District, 505302, Telangana, India
[b]Department of Physics, SRR Government Arts & Science College (Autonomous), Karimnagar, 505001, Telangana, India
[c]Department of Physics. Marri Laxman Reddy Institute of Technology and Management, Dundigal, Hyderabad, Telangana, India
*Corresponding Author e-mail: kvkphd@gmail.com, kvkumar@jntuh.ac.in

Nanocrystalline La0.7Sr0.15Ca0.15MnO3 (LSCMO) manganites were prepared by the combustion process and heated to various annealing temperatures (T_A) to get various sized crystallites. The X-ray diffraction (XRD) patterns provided evidence that a Rhombohedral structure with space group $R\bar{3}c$ was formed. Additionally, an increase in the size of the crystallites was observed, from 15.64 to 36.78nm, as the temperature (T_A) increased from 700°C to 1300°C. The FESEM micrographs revealed that homogeneous with porosity. The FTIR spectra showed five absorption peaks. The Optical energy gap of LSCMO nanocrystalline is decreased from 3.51 to 3.28 eV as annealed temperature raised, reveals that the LSCMO nanoparticles are semiconductor in nature. Room temperature Raman spectra of LSCMO nanoparticles demonstrate a notable reliance on annealing temperature. When the Raman modes were analysed with respect to T_A, it was observed that the Raman vibrational phonon mode below 200cm^{-1} (A_{1g}) and four modes (E_g) in the range 200-800cm^{-1} displayed significant displacements and widening, which were associated with oxygen sublattice distortion. Considerable changes were observed in both the intensity and full width half maximum (FWHM) of the five Raman modes as the annealing temperature increased. Magnetic behaviour using M-H loop at room temperature were measured by the Vibrating sample magnetometer revealed that gradation of saturation magnetization as the function of annealing temperature. Hence there is a remarkable crystallite size effect on optical and magnetic properties of LSCMO nanocrystallites.

Keywords: *Crystallite size; Optical band gap; FTIR spectra; M-H loop; Raman vibrational phonons*
PACS: 61.46. +w; 75.50. Gg; 7840.-q; 78.30.-j

INTRODUCTION

Colossal magnetoresistance (CMR) materials are a highly important research topic in the scientific field due to their exceptional properties in terms of structure, optical, and magnetism when compared to ordinary magnetic materials. These materials have a wide range of applications, including magnetic recording, flash memory technologies, hyperthermia, bioimaging, biosensor applications, and designing of semiconductor devices. Additionally, they can be utilized to create cooling systems that are highly efficient in terms of cooling while being environmentally friendly, producing minimal noise, and emitting no greenhouse gases [1,2].

Lanthanum doped perovskite manganite oxides with divalent alkaline earth ion substitution display interesting properties such as drastically change of electrical resistance with the magnetic field response, which is called as colossal magnetoresistance (CMR) and metal to insulating behaviour [3-7]. Substituting a divalent ion into La sites causes Mn^{+3} ions to transform into Mn^{+4}, resulting in magnetic exchange (Double Exchange) arises between Mn^{+3} and Mn^{+4} ions having in different oxidation states with electronic configurations of (3d^4, t$^3_{2g}\uparrow$e$^1_g \uparrow$, S=2) and (3d^3, t$^3_{2g}\uparrow$e$^0_g \uparrow$, S=3/2) respectively. The double exchange consequences the materials, whether they are ferromagnetic, antiferromagnetic or shows spiral magnetism. The magnetic properties of perovskite manganites are significantly influenced by the Mn+3/Mn+4 ratio, Mn-O bond length, and Mn-O-Mn bond angles, as they impact the double exchange interaction [8]. This behaviour can be altered through the introduction of suitable ions at A and B sites, resulting in a significant change in the characteristic behaviour of these manganites [9-14]. The method of preparation, magnitude, orientation of the unit cell, dopant, etc., all have an impact on the structural features of manganites. [15-17]. Manganite's transport and magnetic properties are affected by their crystalline size [18,19]. The size of the grains can be impacted by the annealing temperature, hence raising the T_A should result in the growth of the grains. [20,21]. The MI transition in La$_{1-x}$Sr$_x$MnO$_3$ can be attributed to the double exchange (DE) interaction, which explains the high bandwidth [22,25]. Similarly, the DE mechanism explains the small bandwidth of Metal Insulator transition and colossal magneto-resistance effect in La$_{1-x}$Ca$_x$MnO$_3$[26,27]. Perovskite-type manganites doped with lanthanum are fascinating materials with unique characteristics that make them highly sought after. To gain a thorough understanding of the complex properties of rare-earth manganites, it is essential to examine the interrelationship between their structural, optical, and magnetic properties. As electronic devices become increasingly integrated and miniaturized, these perovskite manganites are being produced at the nanoscale level. In recent years, research on perovskite manganites with nanoscale particle sizes has expanded significantly, driven by their intriguing properties, such as a significant ratio between surface area and volume and surface effects. Different

optical and magnetic properties are obtained by combining $La_{1-x}Sr_xMnO_3$ with $La_{1-x}Ca_xMnO_3$ in the appropriate ratio. Calcium doped Strontium – Lanthanum manganite exhibit remarkable properties as a high magnetocaloric material among divalent ions [28]. Raman spectroscopy is a widely recognized method that employs vibrational state data to offer insights into the chemical and structural properties of various compounds. The Raman spectra of La0.7Ca0.15Sr0.15MnO3 can provide insight into its vibrational modes, which are related to the material's structure and properties. The spectra would display peaks at different wavenumbers corresponding to the different vibrational modes of the material. Compared to bulk materials, nanoscale manganites exhibit novel characteristics that vary with particle size. Among several investigations using $La_{1-x}Sr_xMnO_3$ and $La_{1-x}Ca_xMnO_3$ only a handful had revealed coexisting Ca and Sr systems.

In this study, the combustion preparation method was employed to create La0.7Sr0.15Ca0.15MnO3 (LSCMO) nanoparticles due to its affordability, convenience, and ability to produce nanocrystals at modest annealing temperatures. Additionally, this method enables the production of LSCMO nanoparticles in large quantities, down to a few tenths of a gram. Various analytical tools were utilized to examine the structural, optical, and magnetic properties of the LSCMO nanoparticles, and the results showed that these nanocrystals exhibited typical properties.

EXPERIMENTAL

We prepared $La_{0.7}$ $Sr_{0.15}Ca_{0.15}MnO_3$ (LSCMO) nanocrystallites using high-purity nitrate precursors of $La(NO_3)_3.6H_2O$, $Sr(NO_3)_2$, $Ca(NO_3)_2.4H_2O$ and $Mn(NO_3)_2.4H_2O$. The nitrate compounds were dissolved in de-ionised water based on their stoichiometry and mixed to form a precursor solution. To this solution, citric acid ($C_6H_8O_7$) was added in a 1:3 molar ratio to the total moles of nitrate ions. The solution was stirred continuously until a white precipitate was formed. Ammonia was then gradually added neutralize the pH of 7, resulting in a thick, brown solution. The mixture was then heated at 60°C with continuous stirring for three hours, and ethylene glycol was added. The gelation agent was ethylene glycol, and the chelating agent was citric acid. The resulting solution was heated at 100°C until it turned into a gel, and then heated to 300°C until it was completely burned, resulting in a free dark powder [29]. The powder was then finely ground and divided into four parts, each of which was annealed separately at 700, 900, 1100, and 1300°C (sample code LSCMO7, LSCMO9, LSCMO11, LSCMO13) for four hours to produce nanocrystallites of various sizes.

The crystal structure, crystallite size, and phase identification of LSCMO nanocrystalline were identified using the X-ray powder diffraction method with CuKα (λ = 1.5418Å) radiation using a Rigaku (Miniflex-II) diffractometer with 0.02°step size. Field Emission Scanning Electron Microscopy (FESEM) (CARLZESIS - Ultra 55) and Energy Dispersive Spectroscopy (EDS) (OXFORD-INCAx-act) were used to evaluate the surface morphology, nanostructure, and elemental composition. Fourier transform infrared spectroscopy (FTIR) (SHIMADU), UV-Vis spectroscopy (SYSTRONICS DOUBLE BEAM), and Raman spectrometry (Lab RAM HR, HORIBA, France) were used to assess the optical characteristics. The resolution of the FTIR measurements, which ranged from 400 to 4000cm^{-1}, was 4cm^{-1}. To acquire the optical absorbances, ultrasonic assisted dispersing of a small quantity of sample in distilled water was performed, and the data was captured in the range of 100-800nm. Raman spectroscopic studies were carried out using laser light of λ = 532nm as the 1% illumination source with 1cm^{-1} resolution, and the slit was adjusted to obtain data in the range of 100-800nm.

RESULT AND DISCUSSION
XRD, FESEM and EDS Analysis

In Figure 1, the X-ray powder diffraction (XRD) pattern of LSCMO7, LSCMO9, LSCMO11, and LSCMO13 nanocrystallites at room temperature is presented. The JCPDS# 51-0409 and Rietveld by Full Prof software were used to match the XRD patterns as shown in the Figure 2, confirming the formation of pure and single-phase Rhombohedral structure with space group $R\overline{3}c$. The intensity of the prominent peak observed at around 32.8° for LSCMO13 perovskite structure was substantially higher than that of the other samples, which can be attributed to the large crystalline size and high electron density.
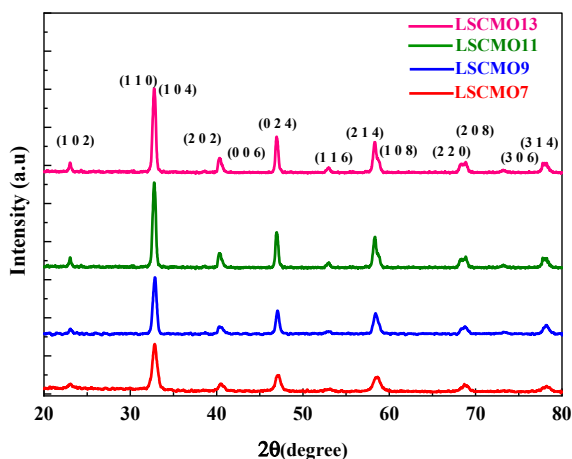

Figure 1. X-ray diffraction patterns of LSCMO7, LSCMO9, LSCMO11, and LSCMO13 nanocrystallites
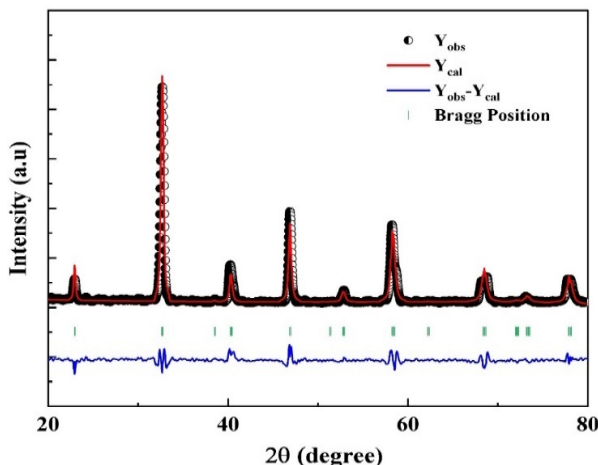
Figure 2. Rietveld refinement of LSCMO13 nanocrystallite

The average crystallite size $\langle D \rangle$ relates to full width half maximum of Bragg's peaks at different annealing temperatures were calculated using Scherrer formula (1) [30].

$$\langle D \rangle = \frac{K\,\lambda}{\beta\cos\theta} \tag{1}$$

Where K is the shape factor which is equal to 0.9.

It was observed that average crystallite size values were increased from 15.64 to 36.78 nm as a function of T_A which were shown in Figure 3. The structural parameters and crystallite sizes are depicted in Table 1.

FESEM images of the prepared LSCMO7, LSCMO9, LSCMO11, and LSCMO13 samples were shown in Figure 4. The fluffy nature and voids powder can be ascribed to the significant amount of gases released during the reaction. The average particle size changed from 42.23 nm to 327.5 nm as the annealing temperature was increased. The particles seemed to be cluster together with no apparent shape at low annealing temperature. The crystal grains entirely solidified at 1100 and 1300°C, generating homogeneous and independent nanoparticles. Better crystalline structure and very well symmetry were reported at 1300°C. as a result, from the morphological studies, the crystal growths were consistent with the XRD data.
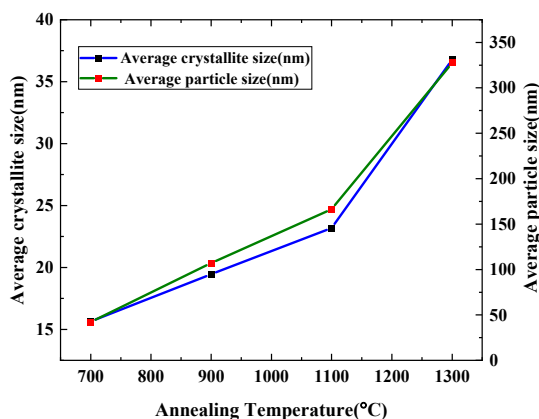
Figure 3. Variation of Crystallite Size as function of Annealing temperature of LSCMO7, LSCMO9, LSCMO11, and LSCMO13 nanocrystallites
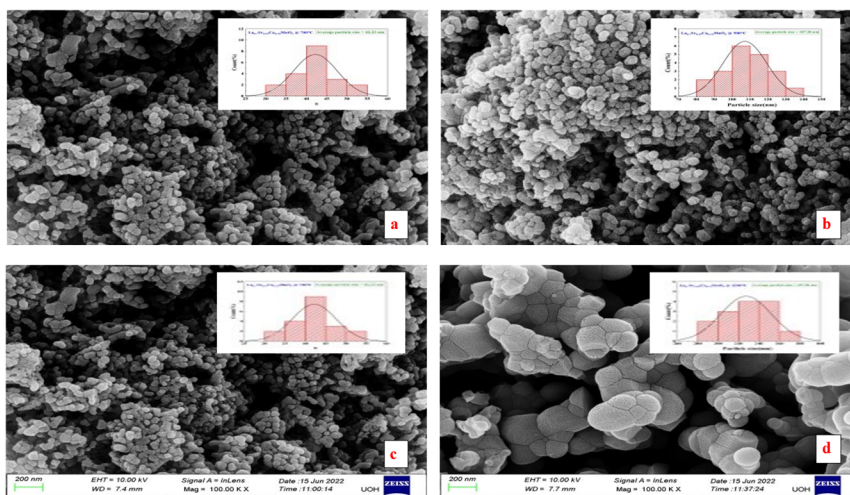
Figure 4. FESEM micrographs of (a) LSCMO7, (b) LSCMO9, (c) LSCMO11, and (d) LSCMO13 nanocrystallites

Table 1. Structural parameters of LSCMO7, LSCMO9, LSCMO11, and LSCMO13 nanocrystallites

Sample code	LSCMO7	LSCMO9	LSCMO11	LSCMO13
Lattice Parameter (a, b) (nm)	0.54764	0.54896	0.54935	0.55944
Lattice Parameter (c) (nm)	1.33502	1.33333	1.33395	1.3442
Volume of Unit Cell (Å^3)	346.74	347.98	348.81	348.93
Crystallite Size D (nm)	15.64	19.46	23.18	36.78
Average particle size(nm)	42.23	107.20	166.44	327.5

To better understand the distribution of individual surface elements, EDX analysis of post annealed samples were illustrated the results in Figure 5 and atomic percentages of individual elements were Table 2. The EDX revealed the uniform distribution concerned elements on the nanostructure surfaces. This accurately depicts the stoichiometric quantities utilized in the experiment.
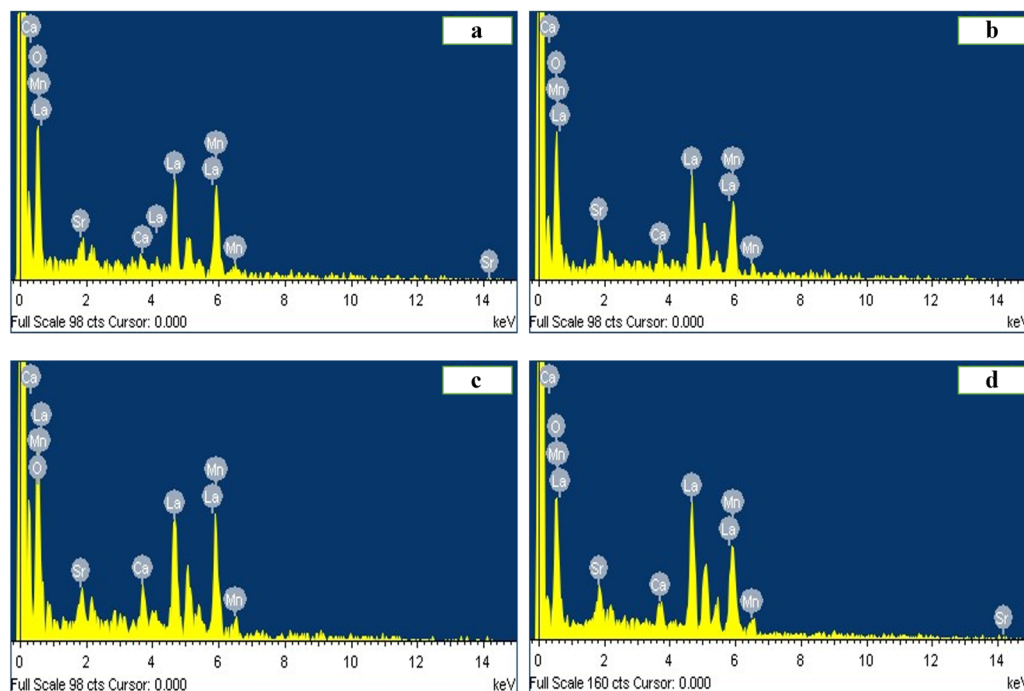
Figure 5. EDX patterns of (a) LSCMO7, (b) LSCMO9, (c) LSCMO11, and (d) LSCMO13 nanocrystallites

Table 2. Atomic percentage of LSCMO7, LSCMO9, LSCMO11, and LSCMO13 nanocrystallites from EDX.

Sample code	La	Sr	Ca	Mn	O
LSCMO7	14.75	1.83	1.79	21.53	60.1
LSCMO9	16.11	3.84	2.31	17.93	59.81
LSCMO11	13.04	1.66	3.4	18.88	63.02
LSCMO13	21.04	2.28	3.12	20.78	52.78

FTIR Spectra Analysis

The lattice phonon vibrations of LSCMO7, LSCMO9, LSCMO11, and LSCMO13 after annealing were analyzed using Fourier Transform Infrared (FTIR) spectroscopy and shown in the Figure 6.
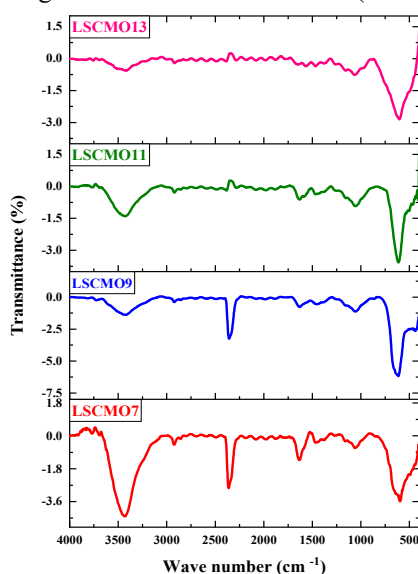
Figure 6. FTIR patterns of LSCMO7, LSCMO9, LSCMO11, and LSCMO13 nanocrystallites

Mn-O bond stretching vibration mode was observed in all the prepared LSCMO samples, which was attributed to the JT effect, and a strong absorption peak was seen at $597 cm^{-1}$[31]. The stretching vibration mode frequency of metal-oxygen bond shifted towards high wave numbers (blue shift) as the annealing temperature increased to 1300℃, indicating additional deformation of the MnO_6 octahedron [32]. The absorption peak at $1059 cm^{-1}$ confirmed the presence of carbonate and decreased with increasing annealing temperature [33]. The C=O bond symmetric stretching vibration peak around $1631 cm^{-1}$ and the C=C bond antisymmetric stretching vibration peak at $1360 cm^{-1}$ also decreased with increasing annealing temperature. [34,35]. The O-H stretching vibration mode was confirmed by the wide band observed at $3600 cm^{-1}$, which originated from the ethylene glycol solvent used in nanoparticle synthesis [34]. LSCMO13 showed less intense peaks at 1059, 1360, 1631, and $3600 cm^{-1}$ due to weak vibrations, indicating the formation of pure crystallinity. The presence of stretching and bending modes in the transmission spectra confirmed the formation of the LSCMO perovskite structure, which was consistent with the XRD results.

UV-Vis Spectroscopic Analysis

The optical characteristics of LSCMO7, LSCMO9, LSCMO11, and LSCMO13 nanocrystals are defined by their energy gap and refractive index as the main physical features. To investigate these properties, UV-Vis absorption spectroscopy was conducted on the prepared samples and variation of absorption peaks with wavelength were shown in Figure 7. A clear absorption edge was observed in the ultraviolet to visible range, with wavelengths ranging from 447 to 468nm for all samples.
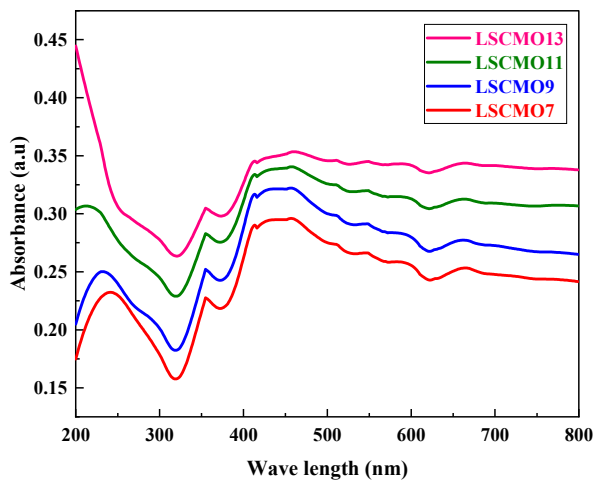
Figure 7. UV-Vis absorbance spectra of LSCMO7, LSCMO9, LSCMO11, and LSCMO13 nanocrystallites
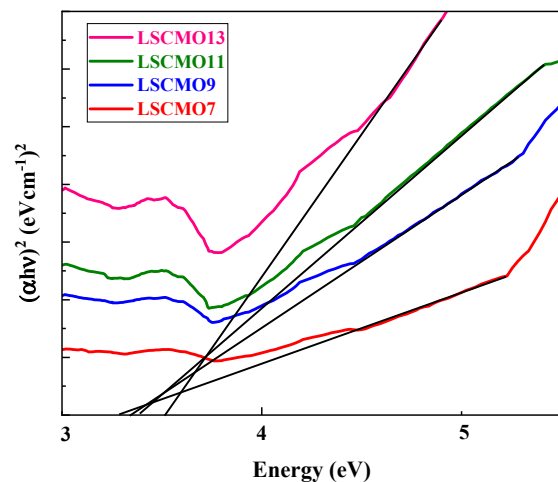

Figure 8. UV-Vis absorbance -Tauc plot: Variation of $(\alpha h\nu)^2$ versus photon energy "hv" of LSCMO7, LSCMO9, LSCMO11, and LSCMO13 nanocrystallites

The absorption coefficient (α) was calculated using equations (2), (3), and (4) [36,37].

$$I = I_0 e^{\alpha t} \tag{2}$$

$$A = log \frac{I_0}{I} \tag{3}$$

$$\alpha = \frac{2.303\,A}{t} \tag{4}$$

where 'A' and 't' are the absorbance and thickness of sample respectively.

The band gap of LSCMO7, LSCMO9, LSCMO11, and LSCMO13 nanocrystallites was determined using Tauc's relation (5) and resulting Tauc plots [38].

$$(\alpha h\nu)^n = A(h\nu - E_g) \tag{5}$$

Equation (5) relates the band gap (E_g), frequency (ν), and refractive index (n) to the absorption coefficient (α), Planck's constant (h), and photon energy (hv). Different values of n (1/2, 1, 3/2, and 2) were used to plot $(\alpha h\nu)^n$ against photon energy. Variation of $(\alpha h\nu)^2$ versus photon energy "hv" of LSCMO7, LSCMO9, LSCMO11, and LSCMO13 nanocrystallites is shown Figure 8 and a linear relationship was observed over a wide range of energy, indicating a direct transition from higher to lower energy levels. The optical bandgap values for LSCMO7, LSCMO9, LSCMO11, and LSCMO13 nanocrystallites were obtained by extending the linear section of the graph on the 'hv' axis. These values, presented in Table 3, show that the optical band gap decreases from 3.51 eV to 3.28 eV with increasing annealing temperature (T_A), due to increase in crystallite size as confirmed by XRD analysis. These results suggest that the prepared nanocrystallites may be useful in photocatalytic applications based on their band gap energy values [39].

Table 3. Optical parameters of LSCMO7, LSCMO9, LSCMO11, and LSCMO13 nanocrystallites

Sample code	LSCMO7	LSCMO9	LSCMO11	LSCMO13
Absorption peak(nm)	447.2	448.7	448.9	468.8
Band gap (eV)	3.51	3.39	3.34	3.28
Refractive Index (By Moss Relation)	2.2680	2.2776	2.2974	2.3128
Refractive Index (By Herve and Vandamme)	2.2074	2.2396	2.2520	2.2682
Static dielectric constant (ε_o)	7.4628	7.6476	8.0172	8.2944
High frequency dielectric constant (ε_α)	5.1438	5.1874	5.2780	5.3490

The refractive index of prepared LSCMO nanoparticles were measured by Moss relation (6) as well as Herve and Vandamme relation (7) [40-43].

$$E_g n^4 = 95 eV \tag{6}$$

$$n = \sqrt{1 + \left(\frac{A}{E_g + B}\right)^2} \tag{7}$$

A=13 .6 eV, B=3.4eV represents the hydrogen ionization energy constants. The static dielectric constant (ε_o) and high frequency dielectric constant (ε_α) of all samples are determined using the following relation (8) and (9) [44].

$$\varepsilon_o = 18.52 - 3.08E_g \tag{8}$$

$$\varepsilon_\alpha = n^2 \tag{9}$$

The theoretically measured values of n, ε_o, ε_α for LSCMO7, LSCMO9, LSCMO11, and LSCMO13 were posted in Table 3, reveals that the refractive index rises as the annealing temperature rises and rate of rise appears to be depending on the models utilized. The static dielectric constant (ε_o) and high frequency dielectric constant (ε_α) were also increased with T_A.

Raman Spectroscopic Analysis

Several recent articles have argued that optical properties of perovskite type manganites were affected by "the Mn-O bond length and symmetry of MnO_6, which establishing the link between the optical phonon mode and Jahn Teller mode" [45]. The Jahn-Teller effect impacts on the rhombohedral structure of manganite. In this structure, the dynamic and incoherent distortion of MnO_6 is influenced by six identical Mn-O bond lengths. Despite this distorted configuration, only five Raman-active modes related to the vibration and stretching of oxygen vibrations of MnO6 can typically be observed [46,47]. $La_{0.7} Sr_{0.3}MnO_3$ nanocrystallites possess a rhombohedral structure with space group $D_{3d}^6(R\bar{3}c)$ and Jahn-Teller phenomenon is a crucial factor in controlling "the dynamic and non-coherent deformation of MnO_6". In the rhombohedral distorted structure, only five Raman-active modes ($1A_{1g} + 4E_g$) can be observed, which are associated with MnO_6 vibrations and stretching oxygen vibrations [46]. Among these modes, two ($1A_{1g} + 1E_g$) "correspond to rotational or tilt stretching mode, while one Eg mode is associated with the bending mode. The other two E_g modes are related to the anti-stretching of the MnO6 octahedra and the vibration of A ions" [48]. "Previous studies have indicated that the Raman spectra of La0.7 Sr0.3MnO3 nanoparticles exhibit two weak modes at 180 and 425cm-1, with the former being an A_{1g} symmetry mode associated with an out-of-phase rotation, and the latter being an Eg symmetry mode related to the bending mode of the MnO6 octahedra" [49].

The Raman spectra at room temperature of LSCMO7, LSCMO9, LSCMO11, and LSCMO13 nanocrystallites were obtained in the spectrum of wave number 50-1500 cm^{-1} and presented in Figure 9, shows that five vibration modes were observed in the range 100-800cm^{-1} for the all the samples, which correspond to the phonons of the rhombohedral structure with space group D_{3d}^6, Z = 2. "This particular structure can be derived from a simple cubic perovskite by rotating the neighbouring MnO_6 octahedra in opposite directions along the$[111]_c$ cubic direction"[50].
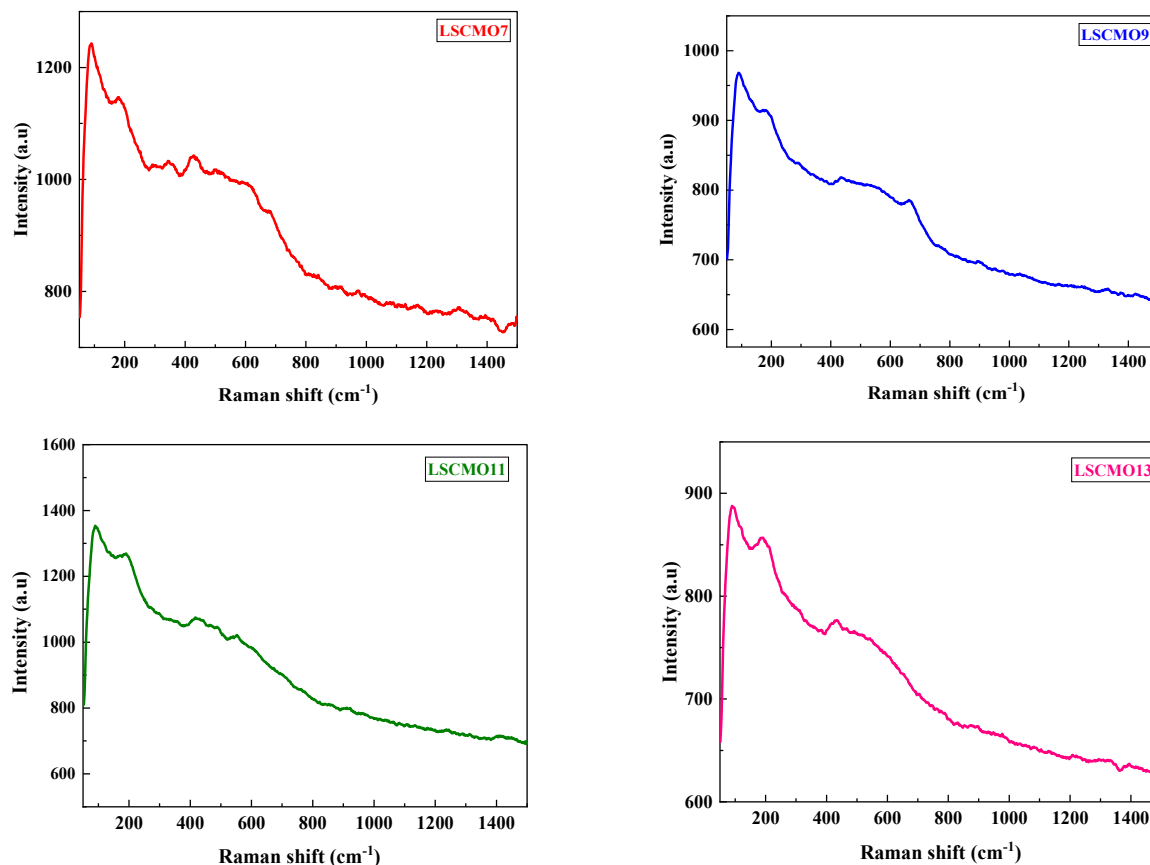

Figure 9. Room temperature Raman spectrum of LSCMO7, LSCMO9, LSCMO11, and LSCMO13 nanocrystallites

The position of peaks in the Raman spectra can be identified clearly by deconvolution of peaks using by the Lorentz fitting, and five vibration modes were observed for all samples, which were shown in the Figure 10.

The positions of vibration modes of LSCMO7, LSCMO9, LSCMO11, and LSCMO13 nanocrystallites were shown in Table 4. The vibration mode at lower frequencies occurs around 177, 184, 189, and 190 cm^{-1} for LSCMO7, LSCMO9, LSCMO11, and LSCMO13 nanocrystallites respectively, which shows. The A_{1g} phonon mode is associated with the primary distortion of A-site cations (such as La, Sr, Na, or Ca) and the strength of the electron-phonon coupling [51, 52]. The peaks located at 343 and 430 cm^{-1} correspond to the E_g symmetry mode, which represents an internal mode (i.e., bending of the MnO_6 octahedra). Moreover, the two highest peaks located at 550cm^{-1} for LSCMO11 and at 613, 662, and 655 cm^{-1} for LSCMO7, LSCMO9, and LSCMO13 nanocrystallites are attributed to the E_g bands, which are related to the vibration of oxygen in the MnO_6 octahedra. [53].
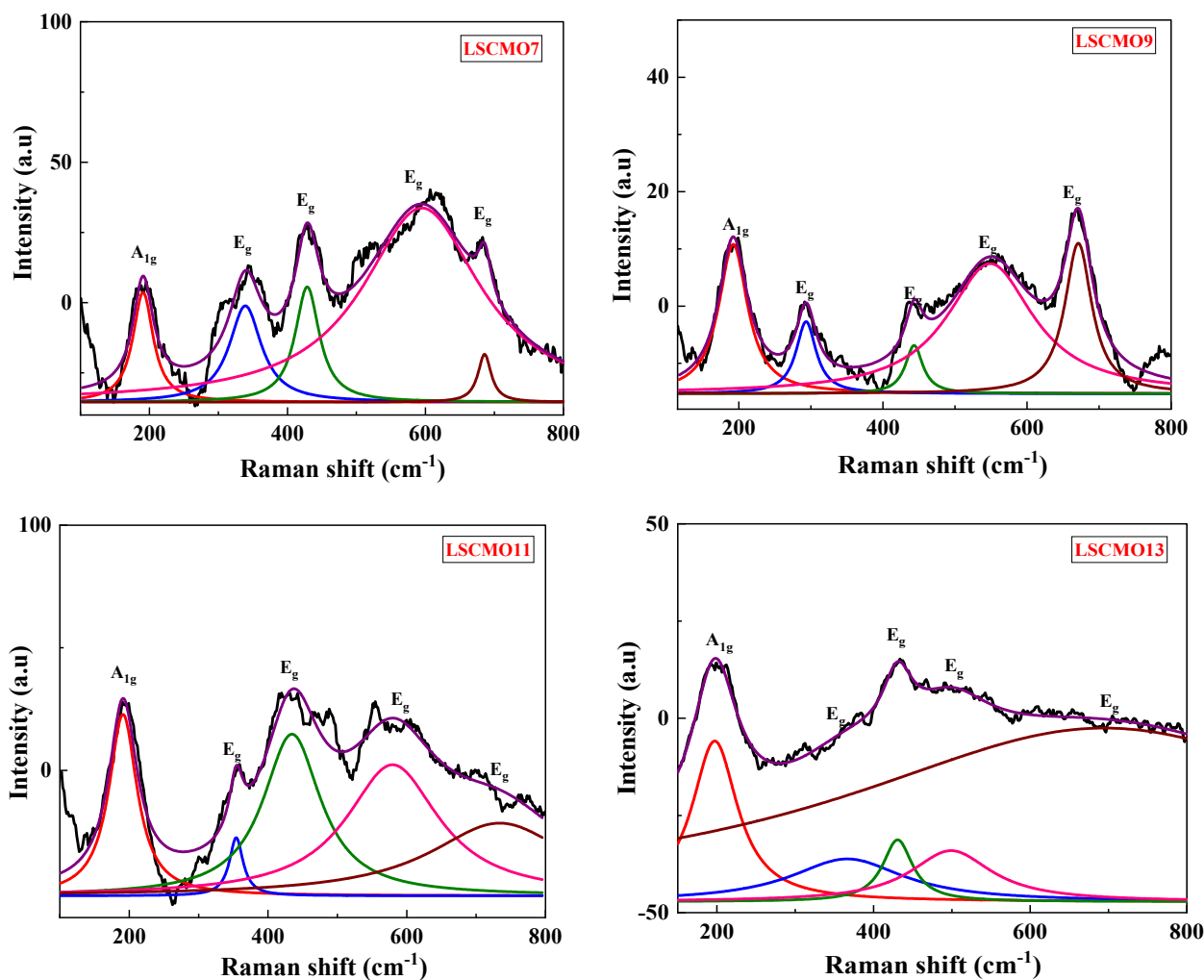
Figure 10. Deconvolution fitting of Raman spectra of LSCMO7, LSCMO9, LSCMO11, and LSCMO13 nanocrystallites

Table 4. Raman vibrational modes of LSCMO7, LSCMO9, LSCMO11, and LSCMO13 nanocrystallites.

Raman modes	LSCMO7	LSCMO9	LSCMO11	LSCMO13
A_{1g}(cm^{-1})	177	184	189	190
E_g(cm^{-1})	293	291	298	213
E_g(cm^{-1})	343	343	335	310
E_g(cm^{-1})	428	437	417	433
E_g(cm^{-1})	613	662	600	655

The position of Raman modes of all samples changes with annealing temperature can be observed from the Figure 11 and clearly shows that the A_{1g} mode is shifted from 177 to 190cm^{-1} (blue shift) with increase of annealing temperature from700 to 1300°C and no significant change were observed for E_g symmetry modes (around 343 and 430 cm^{-1}). However, inverse effect was observed for the samples LSCMO11, and LSCMO13 in the E_g bands around 298 and 600cm^{-1}. From the Figure 11, it is evident that the Raman active phonon modes are greatly influenced by crystallite size.
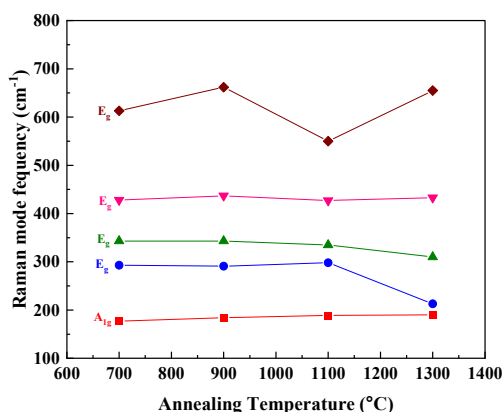
Figure 11. Annealing temperature dependence of Active Raman mode frequencies of La$_{0.7}$Sr$_{0.15}$Ca$_{0.15}$MnO$_3$ nanocrystallites
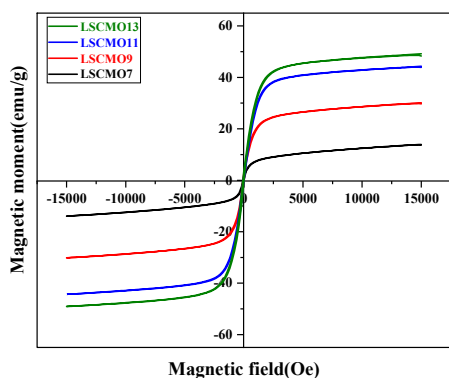
Magnetic Behaviour Analysis

Figure 12. Variation of magnetic moment as function of Magnetic field of LSCMO7, LSCMO9, LSCMO11, and LSCMO13 nanocrystallites
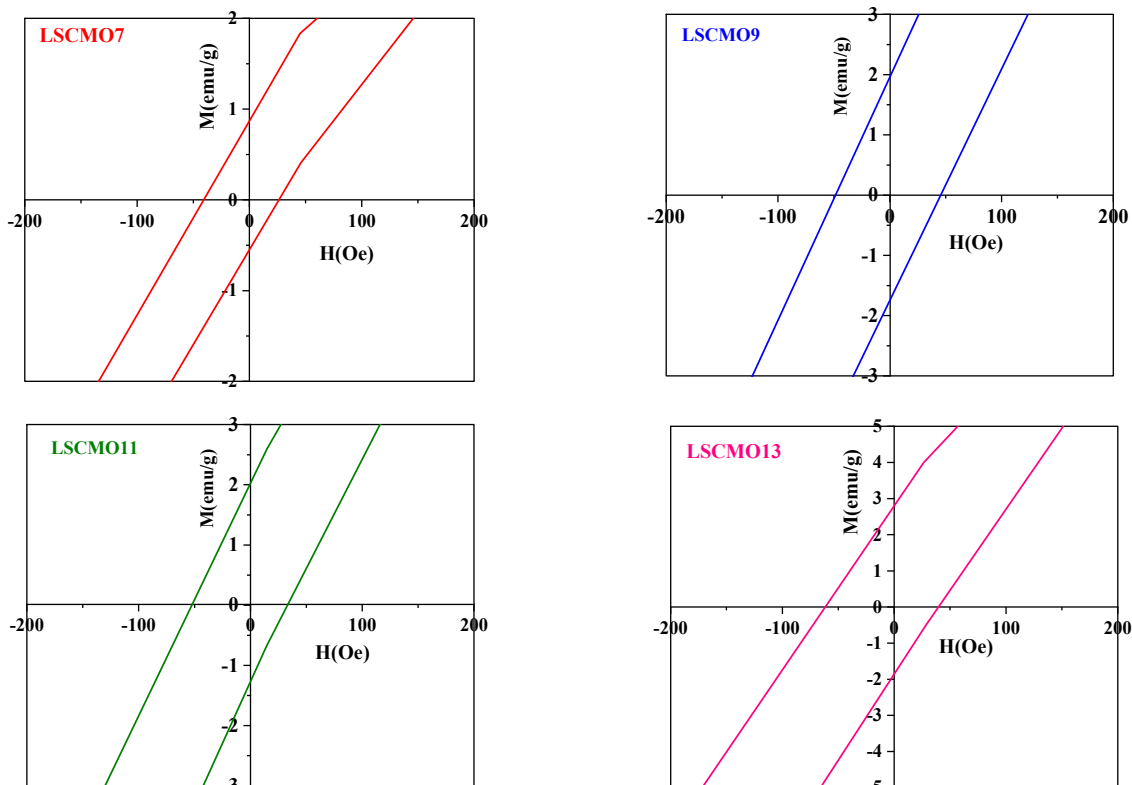
Vibration sample magnetometer was used to measure the magnetic field dependence of magnetization of LSCMO7, LSCMO9, LSCMO11, and LSCMO13 nanocrystallites at room temperature, ranging from -1.5 to 1.5T, and corresponding local M-H hysteresis loops were displayed in Figure 12.

Figure 13 shows enlarged curves of M-H loops of all samples gives the values of the saturation magnetization (Ms), remanent magnetization (Mr), and coercive field (Hc) and observed that all samples exhibit ferromagnetic behaviour. Table 5 displays the characteristic parameters obtained from the local M-H hysteresis loops. The saturation magnetization (Ms), remanent magnetization (Mr), and coercive field (Hc) of all samples increase with the annealing temperature, indicating that the magnetic response increases with the increase in crystallite size.

Figure 13. Enlarged curves of M-H loops of LSCMO7, LSCMO9, LSCMO11, and LSCMO13 nanocrystallites

Table 5. Magnetic parameters of LSCMO7, LSCMO9, LSCMO11, and LSCMO13 nanocrystallites.

Magnetic parameters	LSCMO7	LSCMO9	LSCMO11	LSCMO13
Saturation magnetization (M_s) (emu/g)	13.875	30.166	44.210	49.168
Remanent magnetization (M_r) (emu/g)	0.862	1.974	2.003	2.761
Coercive field (H_c) (Oe)	40.584	48.609	52.804	62.380

CONCLUSIONS

$La_{0.7}Sr_{0.15}Ca_{0.15}MnO_3$ nanocrystalline were effectively produced through combustion method and annealed at different temperatures to obtain various sizes of crystals and endorsed the phase formation of rhombohedral ($R\bar{3}c$) with no evidence of impurity peaks. The annealing temperature resulted in an increase in lattice parameters and crystalline size. The morphology and element composition were confirmed by SEM and EDX. FTIR main absorption band verified the presence of around 597cm^{-1} showed that LSCMO nanoparticles form a perovskite structure. This frequency shifted towards higher wave number to 613cm^{-1}(blue-shift) as the annealing temperature was increased, suggested that additional deformation of the MnO_6 octahedron. The results of the UV-vis spectroscopic analysis indicated that the LSCMO nanocrystallites were semiconductors with a broad band gap. As the size of the particles increased, the values of the optical band gap decreased from 3.51 eV to 3.25 eV. The Raman spectra of LSCMO showed that five vibration modes are formed around. The A_{1g} mode is shifted from 177 to 190 cm^{-1} (blue shift) with increase of annealing temperature from 700 to 1300°C. LSCMO nanocrystallites presents ferromagnetic properties, show increasing response with annealing temperature. Hence, the structural, optical, and magnetic properties of $La_{0.7}Sr_{0.15}Ca_{0.15}MnO_3$ nanocrystalline are significantly affected by the crystallite sizes.

ORCID

Mohd Abdul Shukur, https://orcid.org/0000-0003-3506-412X
Katrapally Vijaya Kumar, https://orcid.org/0000-0001-6160-8632
Gade Narsinga Rao, https://orcid.org/0000-0002-8229-8992

REFERENCES

[1] V. Franco, J.S. Blazqee, J.J. Ipus, J.Y. La, L.M. Moreno, and A. Conde, Prog. Mater, Sci. **93,** 112 (2018), https://doi.org/10.1016/j.pm atsci.2017.10.005

[2] V.K. Pecharsky, and K.A. Gschneidner Jr, J. Magn. Mag. Mater. **200,** 44 (1999), http://doi.org/10.1016/S0304-8853(99)00397-2

[3] T.D. Thanh, L.H. Nguyen, D.H. Manh, N.V. Chien, P.T. Phong, N.V. Khiem, L.V. Hong, and N.X. Phuc, Physica B: Condensed Matter. **407,** 145 (2012), https://doi.org/10.1016/j.physb.2011.10.006

[4] A. Gaur, and G.D. Varma, J Phys: Condens Matter. **18,** 8837 (2006), http://dx.doi.org/10.1088/0953-8984/18/39/014

[5] S. Zhao, X.-J. Yue, and X. Liu, Ceram. Int. **43,** 13240 (2017), http://dx.doi.org/10.1016/j.ceramint.2017.07.021

[6] U. Shankar, and A.K. Singh, The Journal of Physical Chemistry C, **119,** 28620 (2015), http://dx.doi.org/10.1021/acs.jpcc.5b08381

[7] W. Xia, L. Li, H. Wu, P. Xue, and X. Zhu, Ceram Int. **43,** 3274 (2017), http://dx.doi.org/10.1016/j.ceramint.2016.11.160

[8] N. Zaidi, S. Mnefgui, A. Dhahri, J. Dhahri, and E.K. Hlil, J. Alloys Compd. **616,** 378 (2014), https://doi.org/10.1016/j.jallcom.2014.07.113

[9] H. Nakatsugawa, M. Saito, and Y. Okamoto, Journal of Electronic materials, **46,** 3262 (2017), http://dx.doi.org/10.1007/s11664-017-5366-3

[10] Y. Tokura, Reports on Progress in Physics. **69**, 797 (2006), http://dx.doi.org/10.1088/0034-4885/69/3/R06

[11] C.B. Larsen, S. Samothrakitis, A.D. Fortes, A.O. Ayas, M. Akyol, A. Ekicibil, and M. Laver, Journal of Magnetism and Magnetic Materials, **498**, 166193 (2020), http://dx.doi.org/10.1016/j.jmmm.2019.166192

[12] M. K. Verma, N.D. Sharma, S. Sharma, N. Choudhary, and D, Singh, Materials Research Bulletin.**125,** 10813(2020), http://dx.doi.org/10.1016/j.materresbull.2020.110813

[13] S. Biswas, and S. Keshri, Journal of Materials Science: Materials in Electronics. **31**, 21896(2020). http://dx.doi.org/10.1007/s10854-020-04694-9

[14] L. Joshi, S. Rajput, and S. Keshri, Phase Transitions. **83**, 482 (2010), http://dx.doi.org/10.1080/01411594.2010.492466

[15] R.V. Helmholt, J. Wecker, and B. Holzapfel, Phys. Rev. Lett. **71**, 2331 (1993), https://doi.org/10.1103/PhysRevLett.71.2331

[16] K. Chahara, T. Ohno, and M. Kasai, Appl. Phys. Lett. **63**, 1990 (1993), https://doi.org/10.1063/1.110624

[17] S Jin, T.H. Tiefel, M. McCormack, R.A. Fastnacht, R.Ramesh, and L.H. Chen, Science, **264**, 413 (1994), https://doi.org/10.1126/science.264.5157.413

[18] D.H. Manh, P.T. Phong, T.D. Thanh, D.N.H. Nam, L.V. Hong, and N.X. Phuc, J Alloy Compd. **509,** 1373 (2011), https://doi.org/10.1016/j.jallcom.2010.10.104

[19] K. Navin, R. Kurchania, Ceram Int. **44,** 4973 (2018), http://dx.doi.org/10.1016/j.ceramint.2017.12.091

[20] M. Oumezzine, O. Pena, T. Guizouarn, R. Lebullenger, and M. Oumezzine, J. Magn. Magn. Mater. **324**, 2821 (2012), http://dx.doi.org/10.1016/j.jmmm.2012.04.017

[21] M. Rosic, L. Kljaljevic, D. Jordanov, M. Stoiljikovic, V. Kusigerski, V. Spasojevic, and B. Matovic, Ceram. Int. **41,** 14964 (2015), http://dx.doi.org/10.1016/j.ceramint.2015.08.041

[22] R. Von Helmolt, J. Wecker, B. Holzapfel, L. Schultz, and K. Samwer, Phys. Rev. Latt. **71**(14), 2331 (1993), https://doi.org/10.1103/PhysRevLett.71.2331

[23] M. Yamanaka, and N. Nagaosa, Phys B, **28**, 237 (1997), https://doi.org/10.1016/S0921-4526(97)00034-3

[24] Q.L. Fang, J.M. Zhang, and K.W. Xu, J. Magn. Magn. Mater. **349**,104 (2014), https://doi.org/10.1016/j.jmmm.2013.08.030

[25] A. Sundaresan, J.L. Tholence, A. Maignan, B. Raveau, E. Suard, and P. Border, J. Magn. Magn. Mater. **226-230**(1), 777 (2001), https://doi.org/10.1016/S0304-8853(00)01323-8

[26] G. Alejandro, M. Tovar, A. Butera, A. Caneiro, M.T. Causa, F. Prado, and R. Sánchez, Phys. B. **284-288(2),** 1408 (2000), https://doi.org/10.1016/S0921-4526(99)02571-5

[27] G.C. Rout, Nilima Parhi, and S.N. Behera, Phys. B. **404**, 2315 (2009), https://doi.org/10.1016/j.physb.2009.04.036

[28] M.H. Phan, S.C. Yu, and N.H. Hur, Appl. Phys. Lett. **86**, 072504 (2005), https://doi.org/10.1063/1.1867564

[29] W. Xia, K. Leng, Q. Tang, L. Yang, Y. Xie, Z. Wu, and X. Zhu, AIP Advances, **11**, 035007 (2021). https://doi.org/10.1063/5.0036723

[30] N.D. Lipham, G.M. Tsoi, and L.E. Wenger, IEEE Transactions on Magnetics, **43**, 3088 (2007). https://doi.org/10.1109/TMAG.2007.893850

[31] H. Wang, Z. Zhao, C.M. Xu, and J. Liu, Catal. Lett. **102**, 251 (2005). http://dx.doi.org/10.1007/s10562-005-5864-4

[32] W. Xia, H. Wu, P. Xue, and X. Zhu, Nanoscale Res. Lett. **13**, 135 (2018). https://doi.org/10.1186/s11671-018-2553-y

[33] S. Kumar, G. D. Dwivedi, S. Kumar, R. B. Mathur, U. Saxena, A. K. Ghosh, A. G. Joshi, H. D. Yang, and S. Chatterjee, Dalton Trans. **44,** 3109 (2015). https://doi.org/10.1039/C4DT03452J

[34] M.P. Reddy, R.A. Shakoor, and A.M.A. Mohamed, Mater. Chem. Phys. **177,** 346 (2016), https://doi.org/10.1016/j.matchemphys.2016.04.038

[35] Y. Liu, T. Sun, G. Dong, S. Zhang, K. Chu, X. Pu, H. Li, and X. Liu, Ceram. Int. **45,** 17467 (2019), https://doi.org/10.1016/j.ceramint.2019.05.308

[36] H.M. Pathan, J.D. Desai, and C.D. Lokhande, Appl. Surf. Science, **202**, 47 (2002), https://doi.org/10.1016/S0169-4332(02)00843-7

[37] M. Srivastava, A.K. Ojha, S. Chaubey, and A. Materny, Journal of Alloys and Compounds, **481**,515 (2009), https://doi.org/10.1016/j.jallcom.2009.03.027

[38] U. Kumar, D. Yadav, A.K Thakur, K.K. Srivastav, and S. Upadhyay, J. Therm. Anal. Calorim. **135**, 1987 (2018), https://doi.org/10.1007/s10973-018-7432-3

[39] F.R. Afje, and M. Ehsani, Materials Research Express, **5**, 045012 (2018), https://doi.org/10.1088/2053-1591/aaba51

[40] T.S. Moss, Proc. Phys. Soc. London, Sect. B, **63**, 167 (1950), https://doi.org/10.1088/0370-1301/63/3/302

[41] T.S. Moss, Phys. Status Solidi B, **131,** 415 (1985), https://doi.org/10.1016/1350-4495(94)90026-4

[42] P. Herve, and L.K.J. Vandamme, Infrared Phys. Technol. **35,** 609 (1994), https://doi.org/10.1016/1350-4495(94)90026-4

[43] W. Wang, and S.P. Jiang, Solid State Ionics. **177,** 1361 (2006), http://hdl.handle.net/20.500.11937/10875

[44] A.O. Turky, M.M. Rashid, A.M. Hassan, E.M. Elnaggard, and M. Bechelanyc, Phys. Chem. Chem, Phys. **19,** 6878 (2017), http://doi.org/10.1039/c6cp07333f

[45] V. Dediu, C. Ferdeghini, F.C. Matacotta, P. Nozar, and G. Ruani, Phys. Rev. Lett. **84,** 4489 (2000). https://doi.org/10.1103/PhysRevLett.84.4489

[46] L.M. Carr´on, A. de Andr´es, M.J. Mart´ınez-Lope, M.T. Casais, and J.A. Alonso, Phys. Rev. B. **66,** 174303 (2002). https://doi.org/10.1103/PhysRevB.66.174303

[47] X. Kong, J. Wang, Z. Zou, F. Long, and Y. Wu, J. Supercond. Novel Magn. **31,** 373 (2018), https://doi.org/10.1007/s10948-017-4217-z

[48] P.T. Phong, S.J. Jang, B.T. Huy, Y.I. Lee, and I.J. Lee, J. Mater. Sci. Mater. Electron. **24,** 2292 (2013), https://doi.org/10.1007/s10854-013-1092-7

[49] N.V. Minh, J. Phys. Conf. Ser. **187**, 012011 (2009), https://doi.org/10.1088/1742-6596/187/1/012011

[50] A. Dubroka, J. Humlíček, M.V. Abrashev, Z.V. Popović, F. Sapiňa, and A. Cantarero, Phys. Rev. B **73**, 224401 (2006). https://doi.org/10.1103/PhysRevB.73.224401

[51] K. Daoudi, H. Alawadhi, S. El Helali, M. Boudard, Z. Othmen, M. Gaidi, M. Oueslati, and T. Tsuchiya, J. Phys. D: Appl. Phys. **50,** 395305 (2017), https://doi.org/10.1088/1361-6463/aa814f

[52] I. Krad, O. Bidault, N. Geoffroy, and M.E.L. Maaoui, Ceram. Int. **42,** 3751 (2016). http://dx.doi.org/10.1016/j.ceramint.2015.10.158

[53] A.E. Pantoja, H.J. Trodahl, A. Fainstein, R.G. Pregliasco, R.G. Buckely, G. Balakrishnan, M.R. Lees, and D. Mck. Paul, Phys. Rev. B. **63**, 132406 (2001). http://dx.doi.org/10.1103/PhysRevB.63.132406

ВПЛИВ РОЗМІРУ КРИСТАЛІТУ НА СТРУКТУРНІ, ОПТИЧНІ ТА МАГНІТНІ ХАРАКТЕРИСТИКИ НАНОКРИСТАЛІВ La$_{0.7}$Sr$_{0.15}$Ca$_{0.15}$MnO$_3$

Мохд Абдул Шукур[a,b], Катрапаллі Віджая Кумар[a], Гаде Нарсінга Рао[c]

[a]Кафедра фізики, Інженерний коледж університету JNTUH Раджанна Сірічілла, Аграхарам, район Раджанна Сірічілла, 505302, Телангана, Індія

[b]Кафедра фізики, Державний коледж мистецтв і науки SRR (автономний), Карімнагар, 505001, Телангана, Індія

[c]Кафедра фізики, Інститут технології та менеджменту Маррі Лаксман Редді, Дандігал, Хайдарабад, Телангана, Індія

Нанокристалічні манганіти La$_{0.7}$Sr$_{0.15}$Ca$_{0.15}$MnO$_3$ (LSCMO) були отримані в процесі спалювання та нагріті до різних температур відпалу (TA), щоб отримати кристаліти різного розміру. Картини рентгенівської дифракції (XRD) показали, що утворилася ромбоедрична структура з просторовою групою $R\bar{3}c$. Крім того, спостерігалося збільшення розміру кристалітів з 15,64 до 36,78 нм, коли температура (TA) зросла з 700°C до 1300°C. Мікрофотографії FESEM показали, що однорідні з пористістю. Спектри FTIR показали п'ять піків поглинання. Оптичний енергетичний проміжок нанокристалів LSCMO зменшується з 3,51 до 3,28 eВ із підвищенням температури відпалу, що показує, що наночастинки LSCMO є напівпровідниковими за своєю природою. Спектри комбінаційного розсіювання наночастинок LSCMO при кімнатній температурі демонструють значну залежність від температури відпалу. Коли раманівські моди аналізували відносно TA, було помічено, що коливальна фононна мода раманівського розсіювання нижче 200 см$^{-1}$ (A$_{1g}$) і чотири моди (Eg) в діапазоні 200-800 см$^{-1}$ показали значні зміщення та розширення, які були пов'язані з викривленням кисневої підгратки. Спостерігалися значні зміни як в інтенсивності, так і в напівмаксимумі повної ширини (FWHM) п'яти мод Рамана зі збільшенням температури відпалу. Магнітну поведінку за допомогою петлі M-H при кімнатній температурі виміряли магнітометром з вібраційним зразком і показали, що градація намагніченості насичення як функція температури відпалу. Таким чином, існує помітний вплив розміру кристалітів на оптичні та магнітні властивості нанокристалітів LSCMO.

Ключові слова: *розмір кристаліту; оптична заборонена зона; спектри FTIR; петля M-H; раманівські коливальні фонони*

MAGNETIC PROPERTIES OF SILICON WITH PARAMAGNETIC IMPURITY ATOMS[†]

Nurulla F. Zikrillayev[a], Giyosiddin Kh. Mavlonov[a], Levent Trabzon[b], Sergey V. Koveshnikov[a], Zoir T. Kenzhaev[a], Timur B. Ismailov[c]*, Yoldoshali A. Abduganiev[a]

*[a]Department of Digital Electronics and Microelectronics, Tashkent State Technical University
named after Islam Karimov, Tashkent, Uzbekistan*
[b]Department of Mechanical Engineering, Istanbul Technical University, Istanbul, Turkey
[c]Department of Semiconductor Physics, Karakalpak State University named after Berdakh, Nukus, Uzbekistan
*Correspondence Author e-mail: temurismoilov734@gmail.com
Received June 10, 2023; revised June 23, 2023; accepted June 24, 2023

One of the possible ways to obtain silicon with magnetic properties is the introduction of paramagnetic impurities into silicon: Cr, Mn, Fe, Ni, and Co. In our opinion, silicon materials containing magnetic nanosized clusters are most suitable for spintronic devices. The possibility of obtaining silicon with magnetic properties by diffusion doping was studied in this work. To obtain silicon doped with Cr, Mn, Fe and Ni impurity atoms, *p*-type single-crystal silicon with a specific resistance of ρ = 5 Ohm·cm and ρ = 0.5 Ohm·cm was used, and for doping with Co atoms, *n*-type silicon with resistivity ρ=10 Ohm·cm was used. The diffusion temperature and time were chosen such that, after diffusion annealing, the samples with impurity Cr, Fe, and Mn atoms remained highly compensated *p*-type, and when doped with impurity Co atoms, they remained high-resistance *n*-type. The results of the study showed that with decreasing temperature, the value of the negative magnetoresistance $\Delta\rho/\rho$ in the Si<Mn> samples increases and reaches its maximum value (about 800%) at T = 240 K, a further decrease in temperature leads to a decrease in the magnetoresistance, and at a temperature T = 170 K, the sign of the magnetoresistance is inverted. In Si <Cr> samples, with decreasing temperature, the positive magnetoresistance turns into a negative one, the value of which increases with decreasing temperature, and is achieved at T=100 K $\Delta\rho/\rho$ = 45–50%. In Si<Fe> samples, with decreasing temperature, the value of negative magnetoresistance increases monotonically and at T=100 K its value is $\Delta\rho/\rho$ = (100÷120) %. The study in Si<Co> samples showed that with decreasing temperature the value of positive magnetoresistance increases and at T=100 K it reaches $\Delta\rho/\rho$ = (17÷20) %. The study of magnetoresistance in samples - Si<Ni> showed that with decreasing temperature the value of positive magnetoresistance increases and at T=100 K it reaches $\Delta\rho/\rho$ = (10÷15) %. When studying the magnetic properties of p-Si <B, Mn> samples at low temperatures (below T=30 K), a ferromagnetic state was found, i.e. succeeded in obtaining a magnetic semiconductor material by the method of diffusion of a paramagnetic impurity. In the overcompensated Si <B, Mn> (*n*-type) samples, no magnetic hysteresis was found. This shows a significant effect on the magnetic properties of the manganese impurity in silicon of its charge and, accordingly, spin state. Based on the results obtained, it can be argued that diffusion doping of silicon with manganese can be used to obtain silicon with magnetic properties.
Keywords: *Silicon; Manganese; Nickel; Nanocluster; Magnetoresistance; Ferromagnetic; Hysteresis*
PACS: 61.82.Fk, 66.10.Cb, 75.50Pp, 87,50Mn, 85.70.-w

INTRODUCTION

Obtaining magnetic semiconductor materials for modern spintronics [1-3] and studying their magnetic properties is of great scientific and practical interest. One of the possible ways to obtain silicon with magnetic properties is the introduction of paramagnetic impurities into silicon: Cr, Mn, Fe, Ni, and Co. The electronic structure and parameters of these impurity atoms are presented in Table 1.

As can be seen from Table 1, these elements in the silicon lattice act as paramagnetic impurities with fairly high spin values. The main disadvantage is the low limiting solubility in the electroactive state. It was established [5] that chromium and manganese atoms are mainly located in interstitial positions in the silicon crystal lattice and act as donor impurities. Ni, Fe, and Co atoms can be located both in interstices and in the nodes of the silicon crystal lattice [5]. The concentration of electroactive atoms of these impurities, except for Ni and Co atoms [5], depends significantly on the diffusion conditions and the cooling rate. At the maximum cooling rate of silicon samples, it is possible to obtain a material in which all introduced impurity atoms (Cr, Mn, and Fe) are in an electroactive state [6].

In addition, the nonelectroactive part of the dissolved impurity in the silicon lattice in the form of interstitial atoms, dimers, nanoclusters, microclusters, precipitates, and magnetic silicides can also have magnetic properties.

The magnetic properties due to microclusters, precipitates and silicides are unsuitable for spintronic devices due to the strong inhomogeneity of the magnetic properties over the volume. An example of such an impurity is nickel, which easily forms microclusters, precipitates, and silicides, due to which the nonelectroactive nickel concentration near the surface reaches 10^{20}–10^{21} cm^{-3} [8, 9]. At the same time, the electroactive solubility of nickel does not exceed 10^{16} cm^{-3}; therefore, doping with nickel hardly changes the resistivity of the samples [10].

In our opinion, silicon materials containing magnetic nanosized clusters (including those containing atoms of other impurity elements – impurity complexes) are most suitable for spintronic devices. Such formations were found for

manganese impurities in the form of BMn_4 nanoclusters in the silicon lattice [11]. In addition, ferromagnetic properties have been found at room temperature in silicon containing boron and about 1% manganese atoms [2,12].

Table 1. Electronic structure and parameters of Cr, Mn, Fe, Ni, and Co impurity atoms in silicon [7].

Element	Electronic structure	Spin	Total limiting solubility, cm^{-3}	The electroactive part of the limiting solubility, cm^{-3}	Energy levels in silicon
Cr	$3d^5 4S^1$	$\frac{5}{2}$	10^{16}	10^{14}	Ec – 0.41
Mn	$3d^5 4S^2$	$\frac{5}{2}$	$2 \cdot 10^{16}$	10^{16}	Ec – 0.43 Ec – 0.53 Ev + 0.45
Fe	$3d^6 4S^2$	2	$4 \cdot 10^{16}$	$2 \cdot 10^{14}$	Ec – 0.14 Ec – 0.51 Ec – 0.40
Co	$3d^7 4S^2$	$\frac{3}{2}$	10^{16}	$6 \cdot 10^{15}$	Ev + 0.53 Ev + 0.35
Ni	$3d^8 4S^2$	1	$7 \cdot 10^{17}$	$7 \cdot 10^{14}$	Ev + 0.35 Ev + 0.23

The formation of magnetic structures in semiconductors can be carried out by various methods: chemical vapor deposition, molecular beam epitaxy, or ion implantation. Thus, the implantation of crystalline silicon with transition metal ions (Co, Ni, and Fe) is used to create magnetic nanoclusters, as well as metal silicides [13–16].

In this work, the possibility of obtaining silicon with magnetic properties due to diffusion doping with Cr, Mn, Fe, Ni, Co impurities was studied.

Project AL-202102215 is developing an integrated microfluidic system that captures circulating cancer cells with ferromagnetic clusters in silicon.

TECHNOLOGY AND RESEARCH METHODS

To obtain silicon doped with Cr, Mn and Fe impurity atoms, we used p-type single-crystal silicon with a resistivity ρ=5 Ohm·cm, and for doping with Co atoms, we used n-type silicon with a resistivity ρ=10 Ohm·cm. To obtain silicon doped with Ni impurity atoms, p-type silicon with a resistivity ρ=0.5 Ohm·cm was used. The diffusion temperature and time were chosen such that, after diffusion annealing, the samples with impurity Cr, Fe, and Mn atoms remained highly compensated p-type, and when doped with impurity Co atoms, they remained high-resistance n-type.

Before and after diffusion, the samples were subjected to mechanical and chemical treatment (cleaning in an ammonium peroxide solution and etching for 1 minute in a HF + HNO_3 1:3 mixture) to remove impurities and remove mechanical damage to the surface. The magnetoresistance of the obtained samples was measured on a setup that allows you to adjust the magnitude of the magnetic field from 0.1 to 2 Tl, as well as the electric field strength applied to the sample from 0.1 to 1000 V/cm, in the temperature range T=100÷300 K [7].

Measurements of the magnetization of the samples at low temperatures were carried out on a SQUID magnetometer.

THE RESULTS OBTAINED AND THEIR DISCUSSION

The electrical parameters of the obtained samples are shown in Table 2.

Table 2. Electrical parameters of silicon doped with Cr, Mn, Fe, Co, and Ni atoms

Samples	ρ, Ohm·cm	Conductivity type	Charge carrier concentration, cm^{-3}	The mobility of charge carriers, cm^2/V·c
Si <Cr>	$(5÷6) \cdot 10^3$	p	$3.8 \cdot 10^{12}$	250÷270
Si <Mn>	$(5÷8) \cdot 10^3$	p	$5.2 \cdot 10^{12}$	160÷200
Si <Fe>	$(5÷7) \cdot 10^3$	p	$4.2 \cdot 10^{12}$	200÷250
Si <Co>	$10^3÷10^4$	n	$6.2 \cdot 10^{11}÷6.9 \cdot 10^{12}$	900÷1000
Si <Ni>	0,5	p	$4 \cdot 10^{16}$	250÷350

Table 3 shows the values of the magnetoresistance ($\Delta\rho/\rho$) of the samples at T=300 K obtained with the same values of the electric (E=200 V/sm) and magnetic fields (near 2 Tl).

Table 3. Values of resistivity and magnetoresistance of samples at T=300 K

Samples	ρ (Ohm·cm)	Maximum value $\Delta\rho/\rho$, %	Type of magnetoresistance in the range of magnetic fields, (0÷2 Tl)
Si<Cr>	$5 \cdot 10^3$	from -7 to +8	Weak negative and positive
Si<Mn>	$5.3 \cdot 10^3$	-97	Big negative
Si<Fe>	$5.5 \cdot 10^3$	-7	Weak negative
Si<Co>	$5.1 \cdot 10^3$	5	Weak positive
Si<Ni>	0.5	6	Weak positive

It has been established that in samples doped with impurity Ni, Cr, and Co atoms, predominantly weak (less than 6%) positive magnetoresistance (PMS) takes place. At the same time, high (more than 100%) negative magnetoresistance (NMR) is observed in Si<Mn> samples. In Si<Fe> samples, NMR is also observed, but the value of NMR is much less than $\Delta\rho/\rho = 5$–7 %. It was found that the NMR value in the Si<Mn> samples increase significantly with an increase in the applied electric (E) and magnetic (B) fields.

Interesting results were obtained in the study of the temperature dependence of the magnetic resistance $\Delta\rho/\rho$ in the temperature range $T=100$÷380 K.

Previously, it was found that in silicon samples doped with impurity manganese atoms (Si<Mn>), with decreasing temperature, the value of the NMR increases and reaches its maximum value ($\Delta\rho/\rho = 300\%$) at a temperature of $T=235$÷240 K [17,18].

We have studied the magnetoresistance depending on temperature in the samples Si<Mn>, Si<Cr>, Si<Fe>, Si<Co>, Si<Ni> in the field E=200 V/cm and B=2 Tl (Fig. 1).
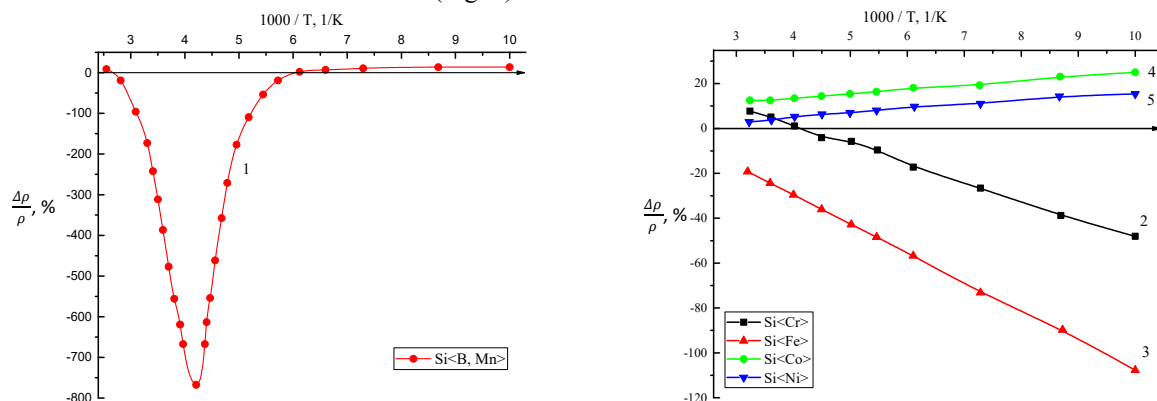
Figure 1. Temperature dependence of magnetoresistance for samples: 1- Si<Mn>, 2- Si<Cr>, 3- Si<Fe>, 4- Si<Co>, 5- Si<Ni> at E=200 V/cm, B =2 Tl.

The results of the study showed that with decreasing temperature, the NMR value in Si<Mn> samples increase and reaches its maximum value (about 800%) at $T=240$ K, further temperature decrease leads to a fairly rapid decrease in NMR and at temperatures $T=160$÷170 K there is an inversion of the sign of the magnetoresistance i.e. The NMR passes to the PMR, the value of the PMR in this temperature range weakly depends on temperature. At a temperature of $T > 380$ K, a slight PMR is also observed.

In Si<Cr> samples, with decreasing temperature, the PMR transforms into NMR, the value of which grows quite rapidly with decreasing temperature, and is reached at $T=100$ K $\Delta\rho/\rho = 45$–50%. In this case, the NMR value increases linearly with an increase in both the electric and magnetic field strengths.

In Si<Fe> samples, in contrast to Si<Mn> and Si<Cr>, with decreasing temperature, the value of the NMR increases monotonically and at $T=100$ K its value is $\Delta\rho/\rho = (100$÷$120)$ %. In these samples, the magnetoresistance sign inversion is not observed in the studied temperature range; always observed only NMR.

The study of the magnetoresistance in Si<Co> samples showed that with decreasing temperature, the value of the PMR increases and at $T=100$ K it reaches $\Delta\rho/\rho = (17$÷$20)$ %. This quantity depends very weakly on the applied electric and magnetic fields.

The study of the magnetoresistance in Si<Ni> samples showed that with decreasing temperature, the value of the PMR increases and at $T=100$ K it reaches $\Delta\rho/\rho = (10$÷$15)$ %.
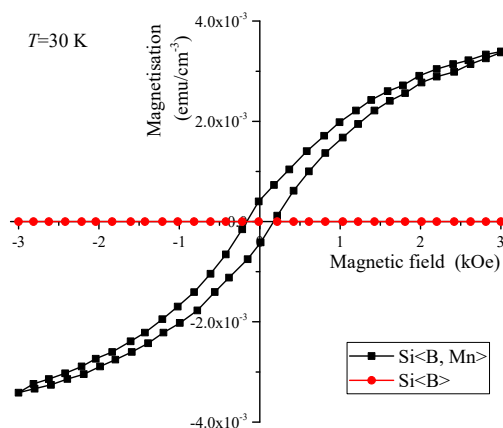
Figure 2. The dependence of the magnetization of the samples *p*-Si <B, Mn> and *p*-Si <B> on the magnetic field (hysteresis) at *T*=30 K

When studying the magnetic properties of p-Si <B, Mn> samples in the low temperature region, we found a ferromagnetic state at T=30 K (Fig. 2), i.e. succeeded in obtaining a new magnetic semiconductor material by impurity diffusion. In the overcompensated Si <B, Mn> (n-type) samples, no magnetic hysteresis was found. This shows a significant effect on the magnetic properties of the manganese impurity in silicon of its charge and, accordingly, spin state.

Previous studies using the EPR method showed that only in p-Si<B, Mn> samples, nanoclusters of the BMn_4 type with a high magnetic moment are formed [17-19]. Under optimal doping conditions, the concentration of such clusters reaches $N=10^{15}$ cm^{-3} [20, 21].

In the Si <Ni> samples, a ferromagnetic state was also found at T = 300 K, which is probably due to the presence of nickel precipitates [22-26] on the surface and in the bulk of the samples. This assumption is confirmed by the fact that when the samples are etched to a depth of 100 μm, the magnetization of the samples is greatly reduced.

On the basis of the obtained results, it can be argued that diffusion doping of silicon with manganese with the formation of BMn_4 nanoclusters can be used to obtain silicon with magnetic properties.

CONCLUSION

The high spatial homogeneity of the p-Si <B, Mn> samples with BMn_4 nanoclusters and the ferromagnetic state observed in them at T=30 K makes it possible to use this material in devices operating on the principle of spin polarization. A significant NMR value, reaching 50% at room temperature, makes it possible to create sensitive magnetoresistive sensors for magnetic measurements.

Conflict of Interest

The authors declare that they have no conflict of interest

ORCID

Nurulla F. Zikrillayev, https://orcid.org/0000-0002-6696-5265; **Giyosiddin K. Mavlonov,** https://orcid.org/0009-0008-8909-7908
Levent Trabzon, https://orcid.org/0000-0002-7323-3943; **Sergey V. Koveshnikov,** https://orcid.org/0000-0002-5158-8997
Zoir T. Kenzhaev, https://orcid.org/0000-0002-5335-0405; **Timur B. Ismailov,** https://orcid.org/0000-0001-9426-3095
Yoldoshali A. Abduganiev, https://orcid.org/0009-0008-1861-3805

REFERENCES

[1] A. Hirohata, K. Yamada, Y. Nakatani, I.L. Prejbeanu, B. Diény, P. Pirro, and B. Hillebrands, Journal of Magnetism and Magnetic Materials, **509**, 166711 (2020). https://doi.org/10.1016/j.jmmm.2020.166711

[2] M. Bolduc, C. Awo-Affouda, A. Stollenwerk, M.B. Huang, F.G. Ramos, G. Agnello, and V.P. LaBella, Physical Review B, **71**, 033302 (2005). https://doi.org/10.1103/PhysRevB.71.033302

[3] Hung-Ta Lin, Wei-Ji Huang, Shuo-Hong Wang, Hsiu-Hau Lin, and Tsung-Shune Chin, Journal of Physics: Condensed Matter, **20**(9), 095004 (2008). http://dx.doi.org/10.1088/0953-8984/20/9/095004

[4] D.J. Fisher, *Diffusion in Silicon: 10 Years of Research* (Scitec publications, 2010), pp. 339.

[5] B.I. Boltaks, *Diffusion and Point Defects in Semiconductors* (Nauka, Leningrad, 1972), pp. 384.

[6] C. Awo-Affouda, M. Bolduc, M.B. Huang, F. Ramos, K.A. Dunn, B. Thiel, G. Agnello, and V.P. LaBella, Journal of Vacuum Science and Technology A, **24**, 1644 (2006). https://doi.org/10.1116/1.2189265

[7] M.K. Bakhadyrkhanov, G.Kh. Mavlonov, and Kh.M. Iliev, Technical Physics, **59**(10), 1556 (2014). http://dx.doi.org/10.1134/S1063784214100089

[8] M.K. Bakhadyrkhanov, and Z.T. Kenzhaev, Technical Physics, **66**(7), 851 (2021). http://dx.doi.org/10.1134/S1063784221060049

[9] M.K. Bakhadyrkhanov, S.B. Isamov, Z.T. Kenzhaev, D. Melebaev, K.F. Zikrillayev, and G.A. Ikhtiyarova, Applied Solar Energy, **56**(1), 13 (2020). http://dx.doi.org/10.3103/S0003701X2001003X

[10] K.A. Ismailov, Z.T. Kenzhaev, S.V. Koveshnikov, E.Z. Kosbergenov, and B.K. Ismaylov, Physics of the Solid State, **64**(3), 154 (2022). https://doi.org/10.1134/S1063783422040011

[11] M. K. Bakhadirkhanov, G.H. Mavlonov, X.M. Iliev, K.S. Ayupov, O.E. Sattarov, and C.A. Tachilin, Semiconductors, **48**(8), 986 (2014). http://dx.doi.org/10.1134/S106378261408003X

[12] Y.H. Kwon, T.W. Kang, H.Y. Cho, and T.W. Kim, Solid State Communications **136,** 257 (2005). http://dx.doi.org/10.1016/j.ssc.2005.08.011

[13] A.F. Orlov, I.V. Kulemanov, Yu.N. Parkhomenko, N.S. Perov, and A.S. Semisalova, Russian Microelectronics, **41**(8), 443 (2012). https://doi.org/10.1134/S1063739712080136

[14] T. Kim, M. Shima, Journal of Applied Physics, **101**(9), 09M516 (2007). https://doi.org/10.1063/1.2712825

[15] H. Hejase, S.S. Hayek, S. Qadri, Y. Haik, Journal of Magnetism and Magnetic Materials, **324**, 3620 (2012). https://doi.org/10.1016/j.jmmm.2012.03.043

[16] A.B. Rinkevich, A.V. Korolev, M.I. Samoylovich, S.M. Kleshcheva, and D.V. Perov, Technical Physics, **61**(2), 194 (2016). https://doi.org/10.1134/S1063784216020183

[17] M.K. Bakhadyrkhanov, Kh.M. Iliev, G.Kh. Mavlonov, K.S. Ayupov, S.B. Isamov, and S.A. Tachilin, Technical Physics, M, **64**(3), 385 (2019). http://dx.doi.org/10.1134/S1063784219030046

[18] N.F. Zikrillaev, G.A. Kushiev, S.B. Isamov, B.A. Abdurakhmanov, and O.B. Tursunov, Journal of Nano- and Electronic physics, **15**(1), 01021,4pp (2023), https://doi.org/10.21272/jnep.15(1).01021

[19] J. Kreissl, and W. Gehlhoff, Physics Status Solid (b), **145**(2), 609–617, (1988), https://doi.org/10.1002/pssb.2221450227

[20] A.T. Lino, J.R. Leite, L.V.C. Assali, and V.M.S. Gomes, International Journal of Quantum Chemistry, **36**(S23), 701 (2009), https://doi.org/10.1002/qua.560360872

[21] Z.A. Yunusov, S.U. Yuldashev, K.T. Igamberdiev, Y.H. Kwon, T.W. Kang, M.K. Bakhadyrkhanov, S.B. Isamov, and N.F. Zikrillaev, Journal of the Korean Physical Society, **64**(10), 1461 (2014), https://doi.org/10.3938/jkps.64.1461

[22] G.P. Moharana, R. Kothari, S.K. Singh, P.D. Babu, H.K. Narayanan, Journal of Magnetism and Magnetic Materials, **555,** 169358, (2022), https://doi.org/10.1016/j.jmmm.2022.169358

[23] M. Zhang, X. Zeng, P.K. Chu, R. Scholz, and C. Lin, J. Vac. Sci. Technol. A, **18**(5), 2249 (2000).

[24] I. T. Yoon, C. J. Park, T.W. Kang, Journal of Magnetism and Magnetic Materials, **311**(2), 693–696. (2007). https://doi.org/10.1016/j.jmmm.2006.08.042

[25] G.P. Moharana, S.K. Singh, and H.K. Narayanan, Journal of Magnetism and Magnetic Materials, **527**, (2021), https://doi.org/10.1016/j.jmmm.2020.167707

[26] N. Filonenko, A. Babachenko, G. Kononenko, and E. Domina, East Eur. J. Phys. **4**, 90 (2020), http://dx.doi.org/10.26565/2312-4334-2021-4-14

МАГНІТНІ ВЛАСТИВОСТІ КРЕМНІЮ З ДОМІШКАМИ ПАРАМАГНІТНИХ АТОМІВ
Нурулла Ф. Зікріллаєв[a], Гійосіддін Х. Мавлонов[a], Левент Трабзон[b], Сергій В. Ковешніков[a],
Зоір Т. Кенжаєв[a], Тимур Б. Ісмайлов[c], Йолдошалі А. Абдуганієв[a]
[a]Кафедра цифрової електроніки та мікроелектроніки Ташкентського державного технічного університету імені Іслама Карімова, Ташкент, Узбекистан
[b]Факультет машинобудування, Стамбульський технічний університет, Стамбул, Туреччина
[c]Кафедра фізики напівпровідників Каракалпацького державного університету імені Бердаха, м. Нукус, Узбекистан

Одним із можливих шляхів отримання кремнію з магнітними властивостями є введення в кремній парамагнітних домішок: Cr, Mn, Fe, Ni та Co. На нашу думку, кремнієві матеріали, що містять магнітні нанорозмірні кластери, найбільш придатні для пристроїв спінтроніки. У роботі досліджено можливість отримання кремнію з магнітними властивостями шляхом дифузійного легування. Для отримання кремнію, легованого домішковими атомами Cr, Mn, Fe та Ni, використовували монокристалічний кремній p-типу з питомим опором ρ = 5 Ом·см і ρ = 0,5 Ом·см, а для легування атомами Co використовувався кремній n-типу з питомим опором ρ=10 Ом·см. Температуру та час дифузії вибирали так, щоб після дифузійного відпалу зразки з домішковими атомами Cr, Fe та Mn залишалися висококомпенсованими p-типу, а при легуванні домішковими атомами Co залишалися високоомними n-типу. Результати дослідження показали, що зі зниженням температури величина від'ємного магнітоопору $\Delta\rho/\rho$ у зразках Si<Mn> зростає і досягає максимального значення (близько 800%) при T = 240 K, подальше зниження температури призводить до до зменшення магнітоопору, а при температурі T = 170 K знак магнітоопору змінюється. У зразках Si <Cr> зі зниженням температури позитивний магнітоопір переходить у від'ємний, величина якого зростає зі зниженням температури, і досягається при T=100 K $\Delta\rho/\rho$ = 45–50%. У зразках Si<Fe> зі зниженням температури величина від'ємного магнітоопору монотонно зростає і при T=100 K його значення становить $\Delta\rho/\rho$ = (100÷120) %. Дослідження на зразках Si<Co> показало, що зі зниженням температури величина позитивного магнітоопору зростає і при T=100 K досягає $\Delta\rho/\rho$ = (17÷20) %. Дослідження магнітоопору в зразках - Si<Ni> показало, що зі зниженням температури величина позитивного магнітоопору зростає і при T=100 K досягає $\Delta\rho/\rho$ = (10÷15) %. При дослідженні магнітних властивостей зразків p-Si <B, Mn> при низьких температурах (нижче T=30 K) виявлено феромагнітний стан, тобто вдалося отримати магнітний напівпровідниковий матеріал методом дифузії парамагнітної домішки. У надкомпенсованих зразках Si <B, Mn> (тип n) магнітного гістерезису не виявлено. Це свідчить про істотний вплив на магнітні властивості домішки марганцю в кремнії його зарядового і, відповідно, спінового стану. На підставі отриманих результатів можна стверджувати, що дифузійне легування кремнію марганцем може бути використане для отримання кремнію з магнітними властивостями.
Ключові слова: *кремній; марганець; нікель; нанокластер; магнітоопір; феромагнетик; гістерезис*

EFFECT OF THE DIFFUSION OF COPPER ATOMS IN POLYCRYSTALLINE CdTe FILMS DOPED WITH Pb ATOMS[†]

Sharifa B. Utamuradova, Shakhrukh Kh. Daliev, Sultanpasha A. Muzafarova, Kakhramon M. Fayzullaev*

Institute of Semiconductor Physics and Microelectronics at the National University of Uzbekistan, Tashkent, Uzbekistan
Corresponding Author e-mail: qahramonfayzullayev8@gmail.com
Received July 8, 2023; revised July 28, 2023; accepted August 1, 2023

The process of diffusion of labeled copper ^{61}Cu atoms in p-CdTe<Pb> coarse-block films with a columnar grain structure has been studied. The CdTe<Pb> film is a p-type semiconductor, where an increase in the Pb concentration in the composition of the CdTe films increases the resistivity ρ of the structure. When the Pb concentration in CdTe changes from 10^{18} to $5 \cdot 10^{19}$ cm^{-3}, the hole concentration decreases by more than 3 orders of magnitude at a constant operating level depth of $E_V + (0.4 \pm 0.02)$ eV. This may indicate that the concentration of acceptor defects, which are formed in the films due to self-compensation upon doping with a Pb_{Cd} donor, exceeds the number of the latter. Electrical measurements by the Hall method were carried out at a direct current and a temperature of 300 K. As a result, an increase in the temperature of films on a Mo-p-CdTe<Pb> substrate during annealing affects the electrical parameter of charge carrier mobility μ, it decreases significantly. X-ray diffraction analysis showed that on the diffraction patterns of samples of p-CdTe<Pb> films, all available reflections correspond to the CdTe phase and up to x = 0.08 do not contain reflections of impurity phases and have a cubic modification. Based on the results of the calculation, it was established that the low values of the diffusion coefficient of Cu atoms are due to the formation of associates of the A type $Cu_i^+ Pb_{Cd}^-$, which are directly dependent on the concentration of Pb_{Cd} atoms. Diffusion length L_n and lifetime τ_n of minority current carriers in large-block p-type cadmium telluride films, which can also be controlled by introducing lead atoms into cadmium telluride.
Keywords: *Diffusion; Associate; Lifetime; Film; Acceptor center; Radioactive isotope; Distribution; Mobility, Resistivity; Diffusion coefficient; Enthalpy*
PACS: 71.20. – b, 71.28. + d

INTRODUCTION

In recent years, significant progress has been made in the technology of manufacturing thin-film solar cells based on A^2B^2 semiconductor compounds [1–4]. Unfortunately, $Cu_2S - CdS(ZnCdS)$ and $Cu_2S - CdTe$ thin-film solar cells tend to change their parameters during operation. The degradation of such solar cells is mainly associated with a change in the heterojunction interface and shunting of the base thin CdS(ZnCdS) and CdTe layers due to the high diffusion rate of copper atoms.

In [5], a hypothetical model was proposed - associations of doped Cu atoms with ionized acceptors of non-vacancy origin, leading to a sharp decrease in the diffusion rate in cadmium telluride films.

However, the microparameters of these local acceptor centers are not specified, their nature is not disclosed, it is only indicated that at the annealing temperature the Fermi level should be above the level of acceptor centers A′ of non-vacancy origin. This condition allows acceptor centers A to be in a charged state and form an associate (complex) with interstitial ions of copper atoms of the Cu_i^+ A′ type.

The development of a controlled reproducible technology for producing thin-film solar cells and their modules using layers of honey sulfide and telluride is mainly associated with the search for and determination of impurities that could localize copper atoms in the space of crystal lattices of cadmium sulfide and telluride by forming stable complexes.

It was shown in work [6] that impurities of Sn, Ge and Pb atoms in cadmium telluride dissolve in high concentration (up to $10^{19} \div 10^{20}$ cm^{-3}) and form levels, respectively, $E_C – (0,6 \div 0,9)$ eV; $E_V + 0,6$ eV; $E_V + 0,4$ eV.

Since Ge, Sn, and Pb impurities are located at the sites of the cadmium sublattice in cadmium telluride crystals, they can, in principle, play the role of ionized acceptor centers leading to the formation of associates with doped copper atoms. Among these impurities, Pb atoms have a certain advantage. Pb is highly soluble in CdTe, secondly, Pb can be doped at relatively low temperatures (773÷973 K), thirdly, Pb in CdTe gives a "shallower" level than impurities of Sn and Ge atoms.

The aim of the authors is to study the diffusion of labeled copper atoms in p-CdTe large-block films with different contents of Pb atoms in the temperature range 573÷723K.

MATERIALS AND METHODS

The distribution profiles of the concentration of labeled ^{64}Cu atoms in polycrystalline p-CdTe films in the temperature range 573÷723 K are shown in Fig. 1.
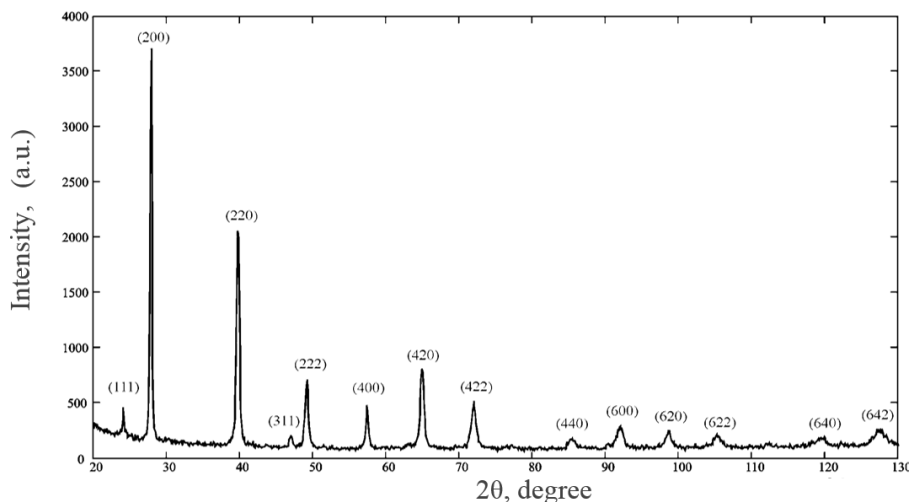
Figure 1. X-ray diffraction pattern of p-CdTe<Pb> films

The study showed that the concentration distributions of copper atoms over the thickness of the p-CdTe film in this temperature range are described by the function erfc (Fig. 2).

The initial p-CdTe films were synthesized by the gas transport method in a quasi-closed volume in a flow of purified hydrogen [7]. Pb atoms were introduced into a growing p-CdTe film during synthesis from a molybdenum substrate, which had a lead layer with a thickness of d = 2 mm deposited by magnetron ion sputtering on the surface of molybdenum [8]. Pb atoms were introduced into the growing p-CdTe film in the course of synthesis from a molybdenum substrate. The content of Pb impurities was controlled by the neutron activation method [9]. The thickness of the grown p-CdTe<Pb> films is $100 \div 120$ μm, the working area $S \geq 1$ cm^2. In such films, grains (crystallites) are oriented in the direction of growth, and their dimensions are not less than the film thickness. The diffusion volume was $\equiv 9$ cm^3. The radioactive isotope ^{64}Cu was used as a diffusant. The sample weight in the ampoule was 2 mg, which corresponded to a diffusant vapor pressure of $0,15 \div 0,2$ atm. Diffusion annealing was carried out in electric furnaces for 4 h, the temperature was maintained with an accuracy of ±3 K.

The composition of the p-CdTe<Pb> film samples obtained was monitored using a Jeol JSM-6380LV scanning electron microscope equipped with an IN-CAx-sight X-ray spectral microanalysis of the elemental composition. X-ray analysis of p-CdTe<Pb> films was carried out on a DR0N-4-07 diffractometer with a step of 0.01° and exposure at a point of 15 s (Fig. 1). The results of the indexing of the fingerprint comparison of the obtained results with a set of reference X-ray patterns (ASTM) made it possible to determine the composition of the p-CdTe<Pb> films. film composition, as predominantly homogeneous, cubic modification.

In samples, as a result of lead doping in all types of samples, the mobility μ decreases deeper into the thickness and the value of resistivity ρ increases. Table 1 shows the parameters of mobility μ and resistivity ρ of doped CdTe layers during layer-by-layer removal of film thickness d at room temperature.

Table 1. Electrophysical parameters of p-CdTe<Pb> films at a temperature of 300K

№	Film thickness, d, μm	Conductivity type	Hall mobility, μ, cm^2/(V·s)	Resistivity, ρ, Ohm·cm
1.	20	p	78	2.88- 10^4
2.	30	p	72	1.64- 10^4
3.	40	p	66	7.76- 10^4
5.	50	p	62	3.13 • 10^5
6.	60	p	56	3.66 • 10^5
7.	70	p	47	6.38- 10^5
8.	80	p	41	1.86- 10^6

The distribution profile of the concentration of labeled ^{64}Cu atoms in polycrystalline p-CdTe films with a columnar grain structure was recorded using the activation analysis method [9], the CdTe layers doped with ^{64}Cu isotopes were removed by chemical etching with Br:C$_2$H$_2$OH (1:5) bromomethyl. The activity of the removed layers was measured on a gamma spectrometer for 1 h.

RESULTS AND DISCUSSION

The distribution profiles of the concentration of labeled ^{64}Cu atoms in p-CdTe polycrystalline films in the temperature range $573 \div 723$ K are shown in Fig. 2.

The study showed that the concentration distributions of copper atoms over the depth of the p-CdTe film in this temperature range are described by the erfc function (Fig. 3).
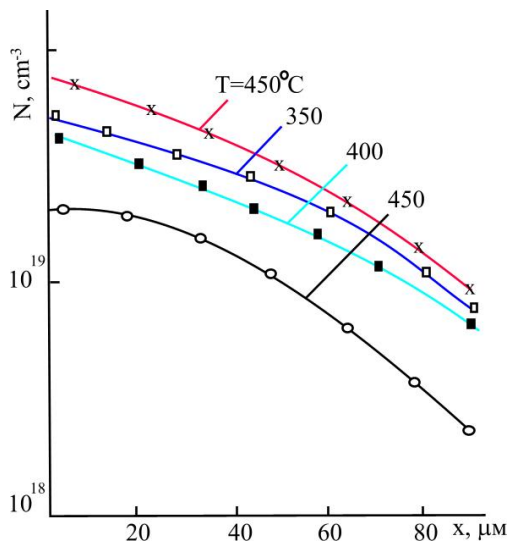
Figure 2. The distribution profiles of the concentration of labeled ^{64}Cu atoms in p-CdTe polycrystalline films
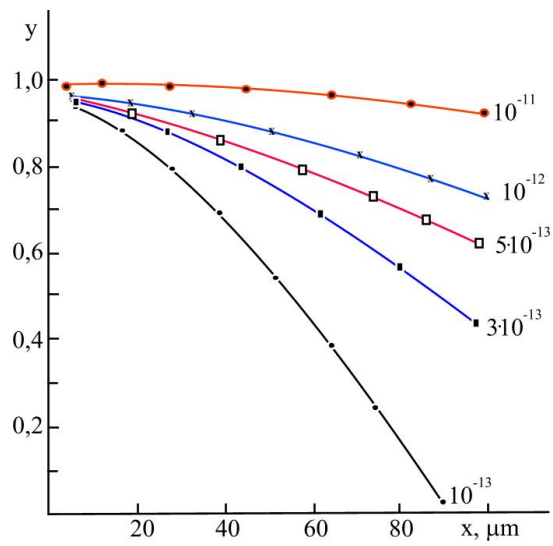

Figure 3. Calculated curves of the concentration distribution of impurity atoms over the thickness of the films at the constructed time t=4 h depending on the diffusion coefficient

In this case, the concentration and diffusion coefficient of copper atoms on temperature are described by an exponential dependence (Fig. 4) and the following analytical expressions

$$N_{Cu}(T) = 7{,}2 \cdot 10^{20} \exp\left(-\frac{0{,}32}{kT}\right) cm^{-3}, \tag{1}$$

$$D_{Cu}(T) = 6{,}7 \cdot 10^{-9} \exp\left(-\frac{0{,}49}{kT}\right) cm^2 \cdot cm^{-1}, \tag{2}$$

An analysis of the obtained results shows that the pre-exponential tallow factor D_0 and the diffusion activation energy Q correspond to the formula obtained in [10]:

$$Q_0 = A\exp\left(-\frac{Q}{kT_{melt.}}\right), \tag{3}$$

where $T_{melt.}$ is the melting point of the material;

$$A = Pa^2\nu \exp\left(-\frac{\Delta G}{kT}\right), \tag{4}$$

P - dimensionless coefficient depending on the geometry of the unit cell of the crystal and the diffusion mechanism; a is the period of the crystal lattice; ν - Debye frequency; ΔG - Gibbs free energy of activation at a temperature equal to $T_{melt.}$.
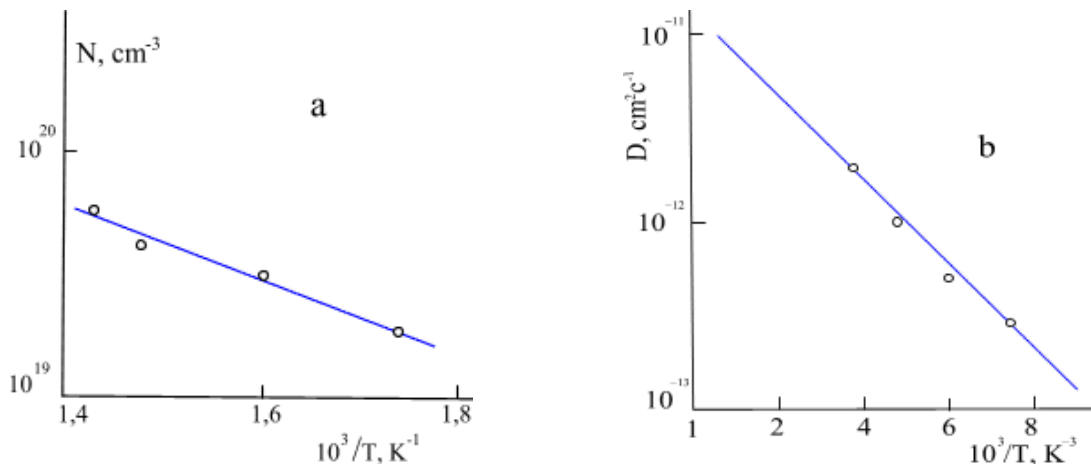

Figure 4. Temperature dependences of the concentration of doped impurity atoms (a), and the diffusion coefficient (b)

The numerical value of the coefficient A is determined by the impurity diffusion mechanism, A = 9.6·10^{-11} cm^2·s^{-1} during the diffusion of copper atoms in large-block p-CdTe films. Approximately for semiconductor materials, according to [11],

$$Q = 2.1 \cdot 10^{-4}[10 + \lg(D_0, cm^2/c)] \cdot T_{melt.} \tag{5}$$

Substituting the experimental value of the pre-exponential factor $D_0 = 6.7 \cdot 10^{-9}$ $cm^2 \cdot s^{-1}$ and $T_{melt}(CdTe) = 1315$ K into (5), we find $Q = 0.5$ eV. The value of Q calculated in this way satisfactorily agrees with the value determined directly from the experiment, which confirms the correctness of expression (3) in the calculation of the diffusion parameters of labeled copper atoms in large-block p-CdTe<Pb> films.

The low values of the effective diffusion coefficient of copper atoms $D(T) = 2,7 \cdot 10^{-13} \div 1.8 \cdot 10^{-12} cm^2 \cdot s^{-1}$ in the temperature range $573 \div 723$ K show that Cu diffuses in p-CdTe polycrystalline films by a complex mechanism. The most probable is diffusion with association [12]. This is also supported by the small value of $A = 9.6 \cdot 10^{-11} cm^2 \cdot s^{-1}$ in expression (3). It shows that the associate between the ions of Cu and Pb atoms is stable even at the melting temperature of cadmium telluride.

Assuming that the Pb acceptors are located in the cation sublattice, and the interstitial Cu atoms occupy tetrahedral interstices in equilibrium, we obtain the shortest distance between ions r = 2,8 Å. Assuming that only the Coulomb interaction contributes to the enthalpy of the associate, we estimate ΔH by the formula [13]: $\Delta H = e^2/4\pi\xi\xi0 = 0.50$ eV, where $\xi = 10.3$ is the low-frequency (static) permittivity of cadmium telluride.

The associate enthalpy value $Cu_i^+ Pb_{Cd}^-$ $\Delta H = 0.50$ eV coincides with the diffusion activation energy $Q = 0.49$ eV of Cu atoms in p-CdTe<Pb> coarse films. This result shows that all diffusing Cu atoms are completely bound in complexes with ionized Pb_{Cd}^- acceptor centers since $N(Pb_{Cd}^-) \geq Cu_i^+$. Therefore, the activation energy Q of diffusion of copper atoms is almost entirely determined by the binding energy of the $Cu_i^+ Pb_{Cd}^-$. associate. In this case, the rate of diffusion of interstitial copper ions depends on the probability of decay of the associate, and the diffusion process itself consists of the stages of decay and formation of $Cu_i^+ Pb_{Cd}^-$. The electronic structure of the ionized Pb_{Cd}^-. acceptor center probably plays an important role in the formation of such an associate. This, probably, explains the sharp difference between the diffusion coefficient of copper atoms $D(T=160°C) \cong 10^{-8}$ $cm^2 \cdot s^{-1}$ and the value of the pre-exponential factor $D_0 = 1.4$ $cm^2 \cdot s^{-1}$ obtained in [14,15], from our data.

The difference in the values of D(T) and D_0 is most likely due to the thermodynamic state of the system, the associate. Probably, in [16] an associate $Cu_i^+ Á$, is formed, in which the atomic energy of atoms is high, therefore, in the process of diffusion, when atoms pass into activated states, the change in entropy is large. Since D_0 is related to the entropy ΔS by the following relationship [17].

$$D_0 = avd^2 \exp\left(\frac{\Delta S}{R}\right), \tag{6}$$

then a noticeable change in ΔS leads to large values of D_0.

In the case of the formation of the $Cu_i^+ Pb_{Cd}^-$ associate, the system is apparently in a more stable position, closer to the equilibrium state. In such a material, diffusible Cu atoms rapidly dissolve; are mixed, and without much effort form associates of the $Cu_i^+ Pb_{Cd}^-$ type, which is facilitated by the Coulomb interaction between the Cu_i^+ and Pb_{Cd}^- ions. In this process, the change in the vibrational entropy can be neglected; therefore, the value of D_0 is small, which is observed in the experiment (see (6)).

Let us now consider the influence of the Pb content in p-CdTe on the diffusion parameters of Cu atoms. Pb concentration in films is within $N_{Pb}^0 = 10^{18} \div 10^{20}$ cm^{-3}. Studies have established the dependence of the diffusion coefficient of Cu atoms in p-CdTe on the concentration N_{Cd}^0, which is clearly manifested at $N_{Pb}^0 \leq 10^{19}$ cm^{-3}. For example, when the Pb concentration changes by two orders of magnitude, i.e., from 10^{20} to 10^{18} cm^{-3}, the diffusion coefficient increases from $2 \cdot 10^{-13}$ to $1,8 \cdot 10^{-9}$ $cm^2 \cdot s^{-1}$, almost by four orders of magnitude, at 573 K. Moreover, the increase in DT is mainly provided by increasing D_0, since the activation energy of diffusion of copper atoms in this case changes insignificantly, only by $0,07 \div 0,08$ eV, and becomes $Q = 0,55 \div 0,56$ eV.

The presented experimental results confirm the correctness of the proposed model of diffusion of Cu atoms, i.e., diffusion mechanism with the association $Cu_i^+ Pb_{Cd}^-$. Indeed, at concentrations $N_{Pb}^0 \leq 5 \cdot 10^{18}$ cm^{-3} in p-CdTe films, extra Cu atoms appear that are not bound in complexes, which begin to diffuse through other channels, among which dissociative diffusion is most likely, since free vacancies of cadmium atoms V_{Cd} are formed.

Recombination parameters were determined on p-CdTe<Pb> samples with different Pb content: diffusion length L_p, minority carrier lifetime τ_p, and surface recombination rate S.

To measure L_P in CdTe, a heterostructure with an upper optical window from a wide-gap semiconductor CdS was formed by vacuum deposition in a quasi-closed volume with an area of 1 cm^2 according to the technology described in [18]. The front contact, from the side of which illumination is provided, is made of indium deposited in a vacuum of $\sim 10^{-5}$ Torr in the form of a comb. In this case, the width of the contact strip was 0.8 mm, and the distance between the strips was ~ 2 mm. The back contact was a molybdenum substrate. The deposited indium contact on CdS was connected to the heterojunction in the blocking direction.

L_p was measured by the diffusion method described in [19], as well as by the method [20], including the measurement of the photocurrent depending on the absorption depth α^{-1} at a constant intensity F in the region of the intrinsic absorption spectrum. Both methods give almost identical results.

At high concentrations of Pb (N = $5 \cdot 10^{19} \div 10^{20}$ cm^{-3}) in p-CdTe<Pb>, the electron diffusion length reaches its maximum value, $\cong 60$ μm. With a decrease in N_{Pb}, the value of L_p also decreases at $N_{Pb} = 10^{18}$ cm^{-3}, $L_p \cong 14$ μm.

From the short-wavelength region of the photocurrent spectrum $I_{ph}(hv)$ ($hv \geq 2$ eV), the surface recombination rate S was determined for holes at the p-n junction boundary adjacent to the CdS wide-gap filter. The results show that S depends on the Pb content in CdTe, and it increases with an increase in the Pb content, and $S \cong 10^5$ cm·s^{-1} is maximum at $N_{Pb} = 5 \cdot 10^{19}$ cm^{-3}. Further, as N_{Pb} increases to 10^{20} cm^{-3}, the surface recombination rate remains constant. Note that S for holes has the lowest value of $\cong 7 \cdot 10^3$ cm·s^{-1} in the absence of impurities of Pb atoms in the samples under study.

The lifetime τ_p of minority current carriers was also determined on p-CdTe<Pb> samples by the phase difference method. At the same time, a certain correlation between τ_p and N_{Pb} was revealed. It has been established that τn reaches its maximum value $\cong 2 \cdot 10^{-6}$ s at $N_{Pb} \cong 10^{20}$ cm^{-3}, and at $N_{Pb} \cong 10^{18}$ cm^{-3} $\tau_p = 10^{-7}$ s.

The mobility of minority carriers μ_n was calculated using the experimental values of L_p and τ_p using the known formula $L_p = (kT/q\mu_n\tau_n)^{1/2}$. Found $\mu_p = 690$ cm^2/V·s at $L_p = 60$ μm, $\tau_p = 2 \cdot 10^{-6}$ s and $N_{Pb} = 5 \cdot 10^{19} \div 10^{20}$ cm^{-3}. μ_n remains practically constant in p-CdTe<Pb> samples with different contents of Pb impurities, so $\mu_n \cong 680$ cm^2/V s at $L_n = 14$ μm, $\tau_n = 10^{-7}$ s and $N_{Pb} \cong 5 \cdot 10^{18}$ cm^{-3}.

Thus, the presence of Pb atoms in large-block p-CdTe films leads to the formation of recombination centers with sharply different electron and hole capture cross sections, the ratio of which is directly dependent on the N_{Pb} concentration. These results do not contradict the data obtained in [21].

The diffusion and recombination parameters of control samples of large-block p-CdTe films with $\rho \cong 10^3 - 10^4$ Ω·cm, in which there are no Pb atoms, have also been studied. The control p-CdTe films and the p-CdTe<Pb> films were synthesized in identical technological modes, the only difference being that the control p-CdTe films were grown on mica substrates, while the p-CdTe<Pb> films were grown on substrates with an impurity of Pb atoms, of which, during the synthesis, Pb atoms were doped into growing films.

As for the recombination parameters, they are low in p-CdTe control samples and correspond to the literature data, for example, $L_p = 0,5 \div 0,6$ mkm and $\tau_p = 10^{-8} \div 5 \cdot 10^{-9}$ s coincides with the results [20].

CONCLUSIONS

Thus, by introducing impurities of Pb atoms, it is possible, firstly, to control the diffusion rate of copper Cu atoms in p-CdTe films, this opens up wide opportunities for using thin-film solar cells with Cu_2Te-CdTe and Cu_2S-CdS (ZnCdS) structures in terrestrial conditions. Secondly, the possibility of controlling the charge states of recombination centers in large-block p-CdTe films by introducing atomic impurities. Pb makes it possible to obtain semiconductor base materials with desired properties, i.e., given values of the microparameters Ln and τn, which is extremely important in materials science, for the microelectronic and semiconductor industries, especially for the creation of thin-film solar cells.

ORCID
Sharifa B. Utamuradova, https://orcid.org/0000-0002-1718-1122
Shakhrukh Kh. Daliev, https://orcid.org/0000-0001-7853-2777
Sultanpasha A. Muzafarova, https://orcid.org/0000-0001-5491-7699
Kakhramon M. Fayzullaev, https://orcid.org/0000-0001-7362-1439

REFERENCES
[1] S.A. Muzafarova, Sh.B. Utamuradova, A.M. Abdugafurov, K.M. Fayzullaev, E.M. Naurzalieva, and D.A. Rakhmanov, Applied Physics, **4**, 81 (2021). https://applphys.orion-ir.ru/appl-21/21-4/PF-21-4-81.pdf

[2] Sh.A. Mirsagatov, P.I. Knigin, M.A. Makhmudov, and S.A. Muzafarova. Applied Solar Energy (English translation of Geliotekhnika), **1**, 45 (1991). https://www.scopus.com/record/display.uri?eid=2-s2.0-0025927279&origin=resultslist&sort = plf-f

[3] D. Nematov, Kh. Kholmurodov, A. Stanchik, K. Fayzullaev, V. Gnatovskaya, and T. Kudzoev, Trends in Sciences, **20**(2), 4058 (2023). https://doi.org/10.33263/LIANBS123.067

[4] D. Nematov, Kh. Kholmurodov, A. Stanchik, K. Fayzullaev, V. Gnatovskaya, and T. Kudzoev. Letters in Applied NanoBioScience, **12**(3), 67 (2023). https://doi.org/10.48048/tis.2023.4058

[5] E.S. Nikonyuk, Z.I. Zakharuk, and M.I. Kuchma, Semiconductors, **42**, 1012(2008). https://doi.org/10.1134/S1063782608090029

[6] K. Biswas, and M.H. Du. New J. Phys. **14**, 063020 (2012). https://doi.org/10.1088/1367-2630/14/6/063020

[7] S.A. Muzafarova, Sh.A. Mirsagatov, and J. Janabergenov, Physics of the Solid State, **49**(6), 1168 (2007). https://doi.org/10.1134/S1063783407060248

[8] Sh.B. Utamuradova, S.A. Muzafarova, and A.A. Abdugafurov, in: *IX International Conference Photonics and Information Optics* (Moscow, 2022), p.217. [in Russian]

[9] A.A. Alieva, Sh.A. Mirsagatov, S.A. Muzafarova, and A.A. Abduvaitov, in: *II International Conference Fundamental and Applied Questions of Physics* (Tashkent, 2004), p.211.[in Russian]

[10] G.A. Korablev. Eur. Chem. Bull. **7**(1), 23 (2018). https://doi.org/10.17628/ecb.2018.7.23-29

[11] T.D. Dzhafarov, S.S. Yesilkaya, N.Y. Canli, and M. Çalişkan, Solar Energy Materials and Solar Cells, **85**(3), 371 (2005). https://doi.org/10.1016/j.solmat.2004.05.007

[12] T. Walker, M.E. Stuckelberger, T. Nietzold, and N. Mohan-Kumar, Nano Energy, **91**, 106595 (2022). https://doi.org/10.1016/j.nanoen.2021.106595

[13] B.G. Jang, M. Kim, S.H. Lee, W.Yang, S.H. Jhi, and Y.W. Son. Phys. Rev. Lett. **130**, 136401 (2023). https://doi.org/10.1103/PhysRevLett.130.136401

[14] S.A. Muzafarova, Sh.A. Mirsagatova, and J. Janabergenov, Physics of the Solid State, **49**(6), 1168 (2007). https://doi.org/10.1134/S1063783407060248
[15] S.A. Muzafarova, S.A. Mirsagatov, and F.N. Dzhamalov, Semiconductors, **43**(2), 175(2009). https://doi.org/10.1134/S1063782609020109
[16] A. Bosio, R. Ciprian, A. Lamperti, I. Rago, B. Ressel, G. Rosa, M. Stupar, and E. Weschke, Solar Energy, **176**, 186 (2018). https://doi.org/10.1016/j.solener.2018.10.035
[17] A. Chandran, A. Erez, S.S. Gubser, and S.L. Sondhi, Phys. Rev. B, **86**, 064304 (2012). https://doi.org/10.1103/PhysRevB.86.064304
[18] S.A. Muzafarova, *Physical processes in thin-film solar cells nCdS/pCdTe,* (LAP LAMBERT Academic Publishing RULAP LAMBERT, 2020), p.63.
[19] S. Lou, H. Zhu, S. Hu, C. Zhao, and P. Han. Scientific Reports, **5**, 14084 (2015). https://doi.org/10.1038/srep14084
[20] P. Wurfel, T. Trupke, and T. Puzzer. J. Appl. Phys. **101**, 123110 (2007). http://dx.doi.org/10.1063/1.2749201
[21] M. Bukała, P. Sankowski, R. Buczko, and P. Kacman, Nanoscale Research Letters, **6**, 126 (2011). http://www.nanoscalereslett.com/content/6/1/126

ВПЛИВ ДИФУЗІЇ АТОМІВ МІДІ В ПОЛІКРИСТАЛІЧНИХ ПЛІВКАХ CdTe, ЛЕГОВАНИХ АТОМАМИ Pb

Шаріфа Б. Утамурадова, Шахрух Х. Далієв, Султанпаша А. Музафарова, Кахрамон М. Файзуллаев
Інститут фізики напівпровідників та мікроелектроніки при Національному університеті Узбекистану,
Ташкент, Узбекистан

Досліджено процес дифузії мічених атомів міді ^{61}Cu в крупноблокових плівках p-CdTe<Pb> зі стовпчастою зернистою структурою. Плівка CdTe<Pb> є напівпровідником p-типу, де збільшення концентрації Pb у складі плівок CdTe збільшує питомий опір ρ структури. При зміні концентрації Pb в CdTe від 10^{18} до $5 \cdot 10^{19}$ см$^{-3}$ концентрація дірок зменшується більш ніж на 3 порядки при постійній глибині робочого рівня $E_V + (0,4 \pm 0,02)$ еВ. Це може свідчити про те, що концентрація акцепторних дефектів, які утворюються в плівках внаслідок самокомпенсації при легуванні донором Pb_{Cd}, перевищує кількість останнього. Електричні вимірювання методом Холла проводили при постійному струмі та температурі 300 К. У результаті підвищення температури плівок на підкладці Mo-p-CdTe<Pb> під час відпалу впливає на електричний параметр заряду. мобільність носія μ, вона значно зменшується. Рентгеноструктурний аналіз показав, що на дифрактограмах зразків плівок p-CdTe<Pb> усі наявні рефлекси відповідають фазі CdTe і до x = 0,08 не містять рефлексів домішкових фаз і мають кубічну модифікацію. За результатами розрахунку встановлено, що низькі значення коефіцієнта дифузії атомів Cu зумовлені утворенням асоціатів типу A $Cu_i^+ Pb_{Cd}^-$, які знаходяться в прямій залежності від концентрації Pb_{Cd}. Дифузійна довжина Ln і час життя τ_n неосновних носіїв струму у великоблочних плівках телуриду кадмію p-типу, якими також можна керувати шляхом введення атомів свинцю в телурид кадмію.

Ключові слова: *дифузія; асоційований; час життя; плівка; акцепторний центр; радіоактивний ізотоп; розподіл; рухливість, питомий опір; коефіцієнт дифузії; ентальпія*

INVESTIGATION OF STRUCTURAL, OPTICAL AND ELECTRICAL PROPERTIES OF MnO DOPED WITH Cu THIN FILMS PREPARED BY PLD TECHNIQUE FOR SOLAR CELL APPLICATIONS†

Doaa T. Mohammed*, Ghuson H. Mohammed

Department of Physics, College of Science, University of Baghdad, Baghdad, Iraq
*Corresponding Author e-mail: duaathamer111@gmail.com

In the current study, concentrated Nd:YAG laser pulses at 500 mJ with a second radiation at 1064 nm (pulse width 9 ns) and repetition frequency (6 Hz) for 300 laser pulses incident on the target surface were employed to coat glass substrates with MnO thin films. Using an X-ray diffractometer (XRD), an atomic force microscope (AFM), and a UV-Vis spectrophotometer, the structural, morphological, and optical characteristics of the films doped with different concentrations of Cu content (0.03, 0.05, 0.07, and 0.09) were examined. The results show that the films are polycrystalline, with the largest peak appearing at an angle of 35.31, or a reflection of (111). The crystalline size of the deposited thin films was calculated using Debye Scherer formula and found to increase from 11.8 nm for undoped MnO_2 to 29.6 nm for doped (MnO) with the increase of Cu content from x=0 to x=0.09 at preferred orientation of (111). All the samples have a cubic structure. Also, the results showed that Cu content of the films affects the surface morphology. From the results of AFM analysis, it was found that the roughness and average diameter change when adding Cu to the structure, with the highest value occurring at Cu ratio 0.09 equal to 65.40 and 71.21 nm, respectively. UV–Vis spectrophotometer was used to investigate the optical transmission. It was found that when Cu content of films increased, the transmittance of films decreased. Hall Effect measurements show that all prepared films at RT have two type of conductivity P-type and n-type. The electrical characteristics of the $(MnO)_{1-x}Cu_x/Si$ heterojunction Solar Cell have been studied and found that the efficiency (η) decreases with the increase of Cu content.

Keywords: *Cu Nanoparticles; MnO Thin Films; PLD Technique; Structural Properties; Optical Properties*
PACS: 73.61.-r, 61.05.C-, 61.05.cc, 61.05.cf, 61.05.cj, 75.70.Ak, 78.20.Ci

1. INTRODUCTION

The use of thin film semiconductors has generated significant interest in a growing range of applications in various electrical and optoelectronic devices due to their low production costs, and thin film technology has a major position in basic research. An examination of the literature reveals that numerous research teams have studied thin-film technology. As a result, a number of deposition processes have emerged, the majority of which depend on continuous, high-temperature power sources [1]. Nanoparticles are the fundamental structures in nanotechnology, which has many applications in different areas such as biosensor and electronic nanodevices [2]. An important class of nanostructured materials are the metal oxide thin films. It is possible to create the thin film's nanomaterials and grown using various methods. There are several widely used methods for depositing thin films onto a substrate, including pulsed laser deposition [3], chemical vapor deposition [4-5] reactive magnetron sputtering [6], spray pyrolysis [7], atomic layer deposition [8], chemical bath deposition [9] and so on. Manganese dioxide is one of the most attractive inorganic transition metal oxide materials from environmental and economic stand points. It is widely used in biosensors [10], catalysis [11], electrochromic multilayered nanocomposite thin films [12-13] and high-performance electrochemical electrodes and energy storage [14]. Typically, MnO is a transparent semiconductor that is conducting with an n-type carrier [15]. The pulsed laser deposition method involves ablating one or more targets that have been irradiated by a focused pulsed laser beam in order to produce thin films. This approach was originally used in 1965 by Smith and Turner [16]. Due to its outstanding chemical stability, transparency, low toxicity, low cost, functional biocompatibility, excellent adsorption capacity, catalytic capabilities, and global availability, nanostructured manganese dioxide (MnO) is a potential transition metal oxide [17]. The current study investigated the synthesis and characterization of optically transparent (MnO) films doped with different concentrations of Cu nanoparticles. The (MnO-Cu) thin films' structural, morphological, and optical characteristics were examined using UV-visible spectroscopy, atomic force microscopy, and X-ray diffraction (XRD).

2. EXPERIMENTAL
2.1 Preparation of Samples

Various concentrations of Cu nanoparticles (0.03, 0.05, 0.07, and 0.09 were used) were mixed with 99.99% pure MnO. In a gate mortar, the powder was mixed for five minutes. After that, it was compacted into pellets with a diameter of 1 cm and a thickness of 0.2 cm using a hydraulic press for 10 minutes at a pressure of 5 tons. After an hour of 400 °C sintering, the pellets were cooled to ambient temperature.

2.2 Deposition of Thin Films

The generated pellets were used to create thin films of (MnO)1-xCux on glass substrates with dimensions of 2.5×7.5 cm that had been cleaned employing an ultrasonic process and distilled water for 15 minutes. The pulsed laser deposition method was applied to produce thin films with the Nd:YAG laser. It produced 500 mJ of energy for 300 laser pulses that were incident on the target surface at a 45° angle and repeated at a frequency of 6 Hz. The deposition was done at (1-10-1) mbar of chamber pressure. The distance between the target and the substrate was 1.5 cm. The layer thickness of 200±5nm was estimated using the interference technique.

2.3 Measurements

By employing Cu-Ka (= 0.154 nm) throughout a 2-scan range of 10-80°, the structural properties of (MnO)$_{1-x}$ Cu$_x$ thin films were studied by an X-ray diffractometer (Philips PW1730). Atomic force spectroscopy (AFM) was used to investigate the surface morphological characteristics of the film. Using a UV-Vis-NIR spectrophotometer with a 190-1100 nm wavelength range (Metertech SP8001), the optical characteristics of thin films were investigated.

3.   RESULTS AND DISCUSSIONS
3.1 The X-rays Diffraction Results

Figure 1 displays the XRD patterns of different Cu concentrations in doped and undoped MnO thin films. The outcomes demonstrated the polycrystalline nature of the films. This outcome is consistent with Zahan et al. [18].
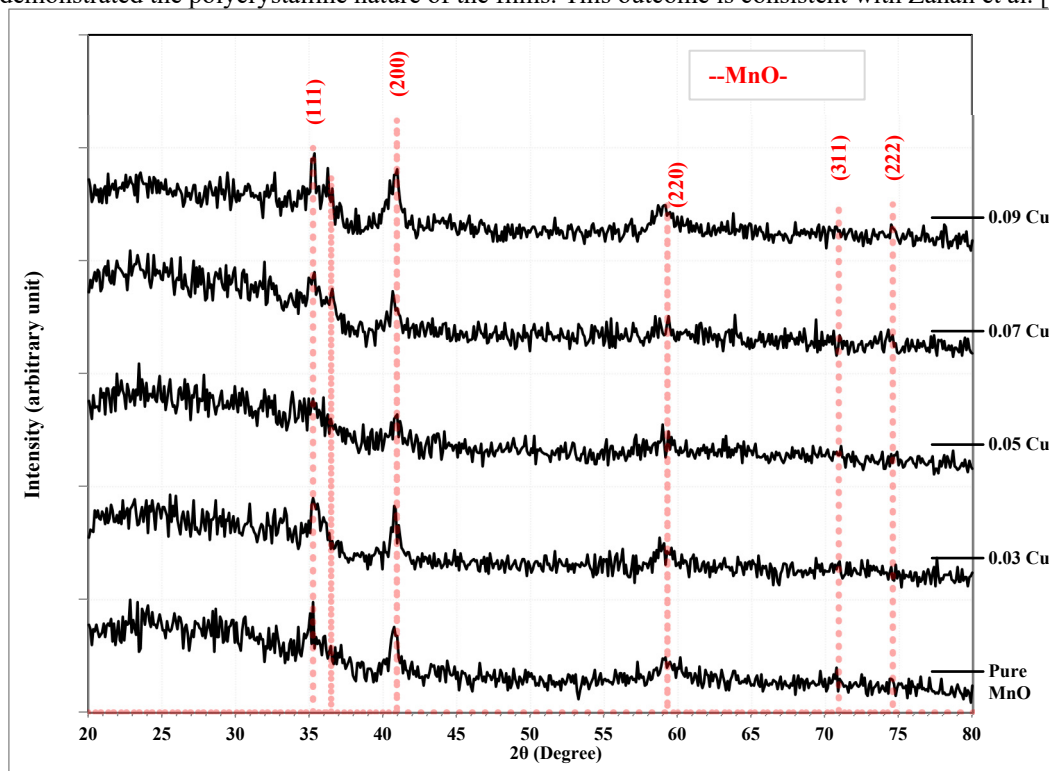

Figure 1. Shows the X-ray diffraction of Cu nanoparticles doped in different quantities in MnO

By comparing the results with ASTM card files (No. 96-900-6666), the diffraction peaks are identified. MnO-Cu thin films were discovered to have a cubic structure. There are two strong peaks and three other smaller ones in the X-ray diffraction spectra of MnO. It denotes the polycrystalline nature of the film. The strongest peak in the XRD pattern was at an angle of 35.31, which corresponds to a reflection of (111). It was observed that two additional strongest peaks developed at an angle of 40.85, which corresponded to a reflection of (200), when Cu with (0.05 and 0.07) content was added to the films. This demonstrates the impact of copper content. The Debye-Scherer equation was used to determine the crystal's size (Cs) [19-21].

$$C_s = \frac{0.9\lambda}{\beta\cos\theta}.$$

(1)

Where: θ the diffraction angle, **β** full width at half maximum (FWHM), and λ wavelength of the X-ray are all given.

In accordance with the Debye-Scherer equation as well. For (111) and (200), the findings are shown in Table 1. Average crystallite size, interplanar spacing, and the number of planes in the diffraction pattern of undoped and doped MnO thin films with various Cu contents Table 1 results showed that the average crystallite size had increased along with the increase in copper concentration. In contrast to earlier research, this study's findings revealed [18].

Table 1. Lists the crystal size, FWHM, and interplaner distance for (MnO) thin films doped with various concentrations of Cu nanoparticles.

Cu %	2θ (Deg.)	FWH M (Deg.)	dhkl Std.(Å)	C.S (nm)	hkl	Phase
MnO	35.10	0.7055	2.5548	11.8	(111)	Cubic MnO
MnO-Cu (0.03)	35.31	0.6349	2.5400	13.1	(111)	Cubic MnO
MnO-Cu (0.05)	40.85	0.7760	2.2072	10.9	(200)	Cubic MnO
MnO-Cu (0.07)	35.34	0.5643	2.5375	14.8	(111)	Cubic MnO
MnO-Cu (0.09)	35.31	0.2822	2.5400	29.6	(111)	Cubic MnO

3.2 Atomic force microscopic

Analysis of the surface morphology of films grown on glass substrates can be done by using 3D AFM images of MnO thin films doped with various concentrations of Cu nanoparticles to calculate the mean diameter, mean roughness, and mean square root (RMS). The fine morphology and roughness of the MnO films may be seen with various Cu activators. Roughness and RMS change increased with the addition of Cu, with a Cu ratio of 0.09 producing the maximum value. The 0.09 Cu ratio is the best among the other ratios, based on the findings of the XRD and AFM tests (it produced the highest roughness and largest crystalline size).
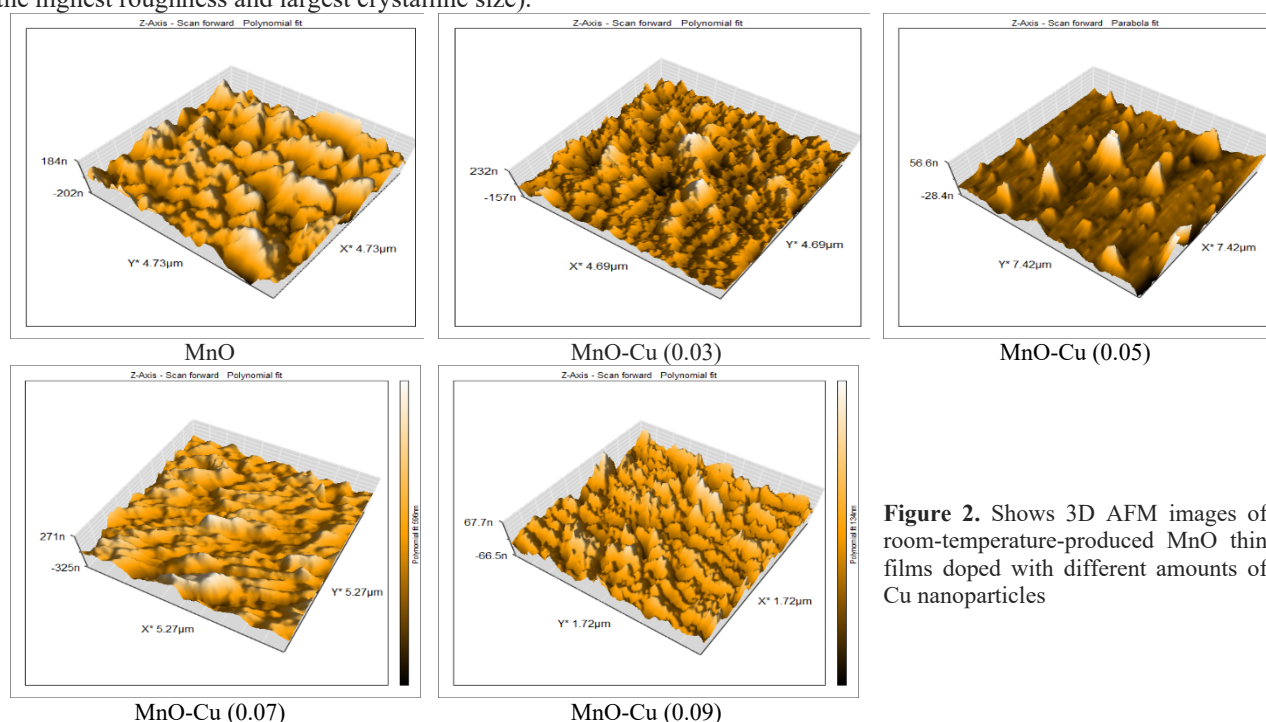
Figure 2. Shows 3D AFM images of room-temperature-produced MnO thin films doped with different amounts of Cu nanoparticles

Table 2. Granular content and total surface roughness of the produced films at room temperature

Sample	Avg.Diameter (nm)	Avg.Roughness (nm)	R.M.S (nm)	Peak-Peak (nm)
MnO	178.2	62.74	84.34	109.6
MnO-Cu (0.03)	44.17	37.40	45.41	96.13
MnO-Cu (0.05)	131.1	7.446	13.48	73.38
MnO-Cu (0.07)	58.97	59.76	76.15	228.4
MnO-Cu (0.09)	71.21	65.40	84.71	200.4

3.3 The optical properties

Undoped and doped (MnO) thin films with varying concentrations of Cu (0.03, 0.05, 0.07, and 0.09% wt.) were studied for transmission, absorption coefficient, extinction coefficient, refractive index, dielectric constant, and optical energy gap in the wavelength range of 500–1100 nm.For (MnO-Cu) produced at RT, Figure 3 depicts the transmission variation with wavelength. The image and Table 3 make it clear that the transmittance value is inversely proportional to the Cu concentration; as the Cu content in MnO films increased, so did the transmittance value.

The relation [22, 23] can be used to get the absorption coefficient:

$$\alpha = 2.303 \, A/t \, . \tag{2}$$

where t is the sample's thickness and A is the absorbance. The following relation [24] can be used to compute the optical energy gap's value:

$$\alpha h\nu = B(h\nu - E_g)r, \tag{3}$$

where B is a constant inversely proportional to the degree of amorphousness, hν is the energy of the input photon, r is the exponent denoting the kind of optical transitions in the material, and E_g is the optical bandgap.
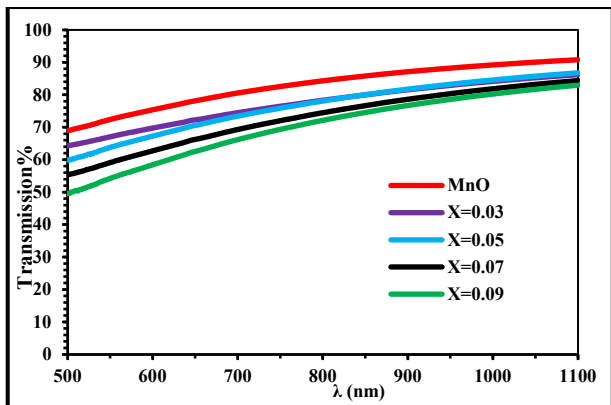

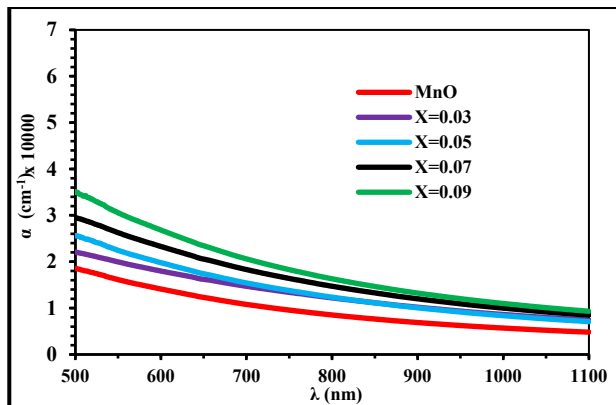**Figure 3.** Shows the transmittance spectra of Cu nanoparticle-doped MnO thin films at various concentrations

Figure 4. Shows the absorption coefficient of thin films of MnO doped with various concentrations of Cu nanoparticles

Band-to-band absorption causes a significant increase in an electron's absorption when it is moved up to the conduction band from the valence band, producing a new pair of charge carriers (an electron and a hole). The bandgap values for the various Cu contents are shown in Table 3. The absorbance increases as Cu concentration (x) increases and E_g decreases.

Table 3. Shows the transmittance, absorption coefficient, and optical constant of (MnO) thin films at room temperature that are both undoped and doped with (Cu) in the following ratios: 0.030.050.070.009.

Sample	T%	α (cm-1)	k	n	εr	εi	Eg (eV)
MnO	68.99	18561	0.074	2.257	5.088	0.333	2.69
MnO-Cu(0.03)	64.29	22085	0.088	2.370	5.609	0.417	2.6
MnO-Cu(0.05)	59.88	25640	0.102	2.463	6.057	0.503	2.4
MnO-Cu(0.07)	55.34	29585	0.118	2.543	6.454	0.599	2.23
MnO-Cu(0.09)	49.64	35018	0.139	2.614	6.815	0.729	2.19

Figure 5 shows that optical bandgap measurements fall from roughly 2.69 eV to 2.19 eV at room temperature when the Cu content increases from 0% to 9%.

Figure 6 shows the connection between the extinction coefficient (k) and wavelength in the 500-1100 nm range for samples made at room temperature, illustrating how the k values climb as the doping level increases. Table 3 provides an illustration of the results. The values of k were calculated based on the relationship shown in [25].
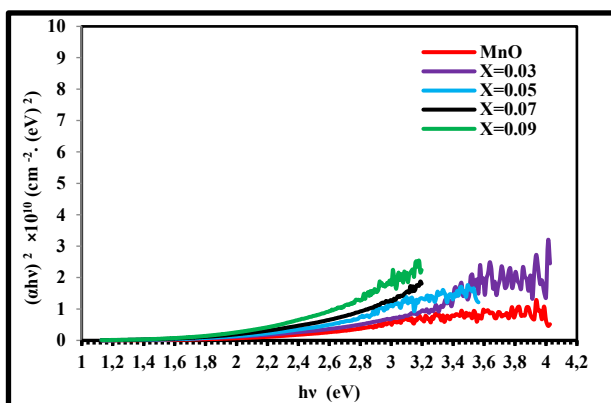

Figure 5. Shows the plot of (αhυ)² as a function of (hυ) for thin films of MnO doped with various concentrations of Cu nanoparticles
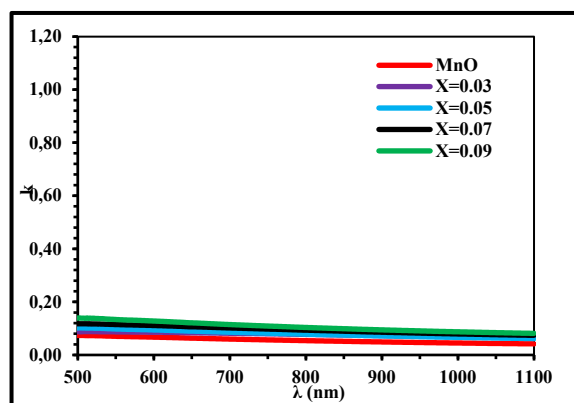

Figure 6. Shows the MnO thin films doped with various concentrations of Cu nanoparticles and their extinction coefficients (k)

extinction coefficients (k):

$$k = \frac{\alpha\lambda}{4\pi} \tag{4}$$

Figure 7 and Table 3 Show how the refractive index changes with wavelength for undoped and doped MnO with different amounts of Cu in the wavelength range of 500-1100 nm. It can be seen that the refractive index rises as the doping increases.
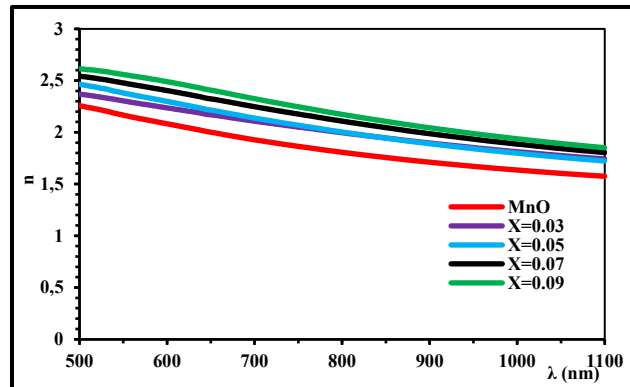

Figure 7. Shows the refractive index of thin films of MnO doped with various concentrations of Cu nanoparticles.

The complicated optical refractive index of thin films is described by equation (5) [26]:

$$n* = n - ik \qquad (5)$$

where (n) and (k) are the real portion and imaginary part of a complex refractive index, respectively, and (n*) is the complex refractive index. While the relationship [27] can be used to determine the simple refractive index:

$$n = \frac{1+R}{1-R} + \sqrt{\frac{4R}{(1-R)^2} - k^2} \ . \qquad (6)$$

Figures 8 and 9 show the real and imaginary portions of the dielectric constant of undoped and doped (MnO) thin films with different Cu concentrations (0.03, 0.05, 0.07, and 0.09), respectively, in the wavelength range (500–1100 nm) at room temperature. Since (k2) is much smaller than (n2), part (per Equation 7) simply depends on the value of (n2).
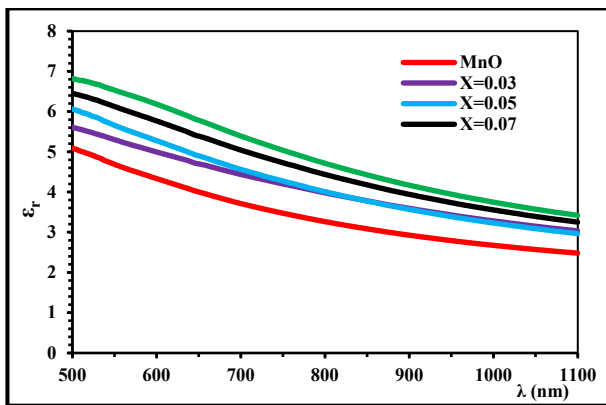

Figure 8. Shows the real component of the dielectric constant for thin films of MnO doped with various concentrations of Cu nanoparticles
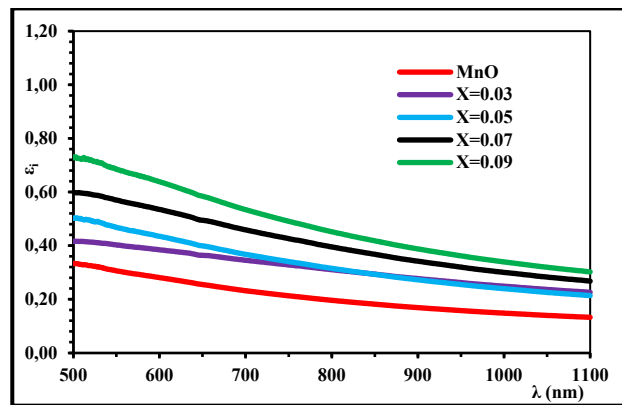

Figure 9. Shows the imaginary portion of the dielectric constant for thin films of MnO doped with various concentrations of Cu nanoparticles

The imaginary portion, however, is dependent on the value of (k) (see Equation 8). It was discovered that their values increased as the doping and wavelength were raised, as indicated in Table 3. Applying the equations [28], the real and imaginary components of the dielectric constant were computed.

$$\varepsilon_r = n^2 - k^2 \qquad (7)$$

$$\varepsilon_i = 2nk \qquad (8)$$

3.4 Hall Effect

Undoped and doped (MnO) thin films with varying Cu contents (0.03, 0.05, 0.07, and 0.09) wt were studied using Hall Effect measurements. Table (4) shows that all samples exhibit a positive negative Hall coefficient (i.e., n-type conductivity), with the exception of films doped at x = 0.05, 0.07, where the Hall coefficient sign has been transformed to p-type due to the high concentration of carriers. Additionally, the results demonstrate that a drop in the values of charge carriers (n) with a decrease in both the mobility (μ_H) and Hall coefficient (R_H) values causes an increase in the value of electrical conductivity (σ).

Table 4. Hall coefficient, Hall mobility, carrier concentration, and conductivity type for MnO films doped with various Cu at RT

Sample	σ (1/ Ω Cm)	ρ (Ω cm)	R_H(cm³/c)	n_H(1/cm³)	μ_H(cm²/v·sec)	type
MnO	3.12E+00	3.205E-01	-4.21E+01	-1.48E+17	1.32E+02	N
MnO-Cu(0.03)	1.22E+01	8.197E-02	-5.85E+01	-1.07E+17	7.14E+02	N
MnO-Cu(0.05)	2.83E+01	3.533E-02	2.90E+02	2.15E+16	8.21E+03	P
MnO-Cu(0.07)	2.47E+01	4.048E-02	4.20E+01	1.49E+17	1.04E+03	P
MnO-Cu(0.09)	3.44E+00	2.907E-01	-8.12E+01	-7.69E+16	2.79E+02	N

3.5 Current-Voltage Characteristics Measurements at Illumination

Show the J-V characteristics of the $(MnO)_{1-x}Cu_x/Si$ heterojunction made by pulsed laser deposition at different Cu concentrations (x = 0.03, 0.05, 0.07, and 0.09) under ambient lighting (100 mW/cm2) at room temperature. The values of J-V parameters (V_{oc}, I_{sc}, V_m, I_m, F.F and η) were tabulated in Table 5 . In general, it can be observed that the I_{sc} decreases as the cu content increases. It is noticed a decrease in the values of the fill factor and the efficiency value as the Cu content increases and further result in a poor electrocatalytic performance this outcome is consistent with Peng et al. [29].
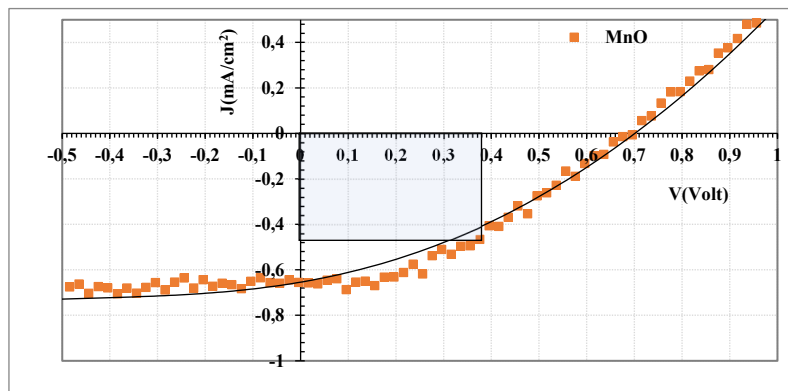

Figure 10. J-V characteristics under illumination by 100mW/cm² white light for MnO/p-Si at R.T.
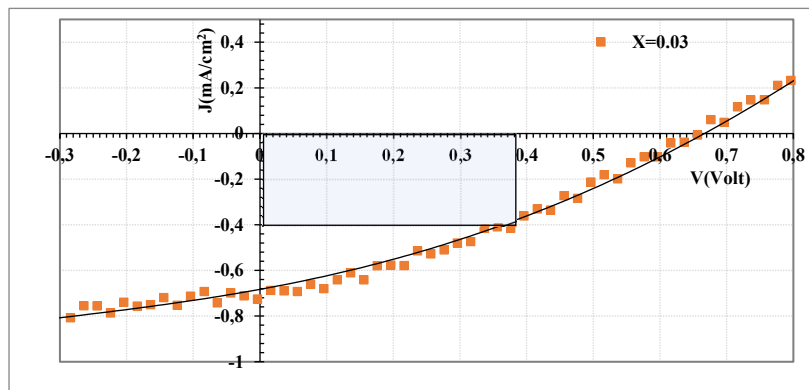

Figure 11. J-V characteristics under illumination by 100mW/cm² white light for $(MnO)_{1-x}$ Cu_x/p-Si with Cu content 3% at R.T.
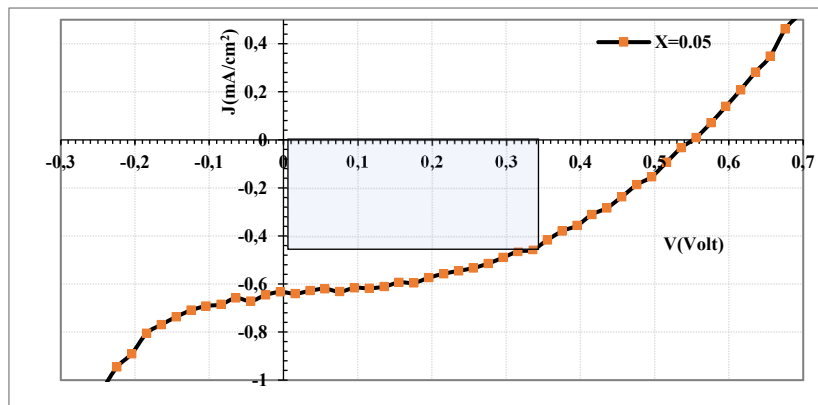

Figure 12. I-V characteristics under illumination by 100mW/cm² white light for $(MnO)_{1-x}$ Cu_x/n-Si with Cu content 5% at R.T.
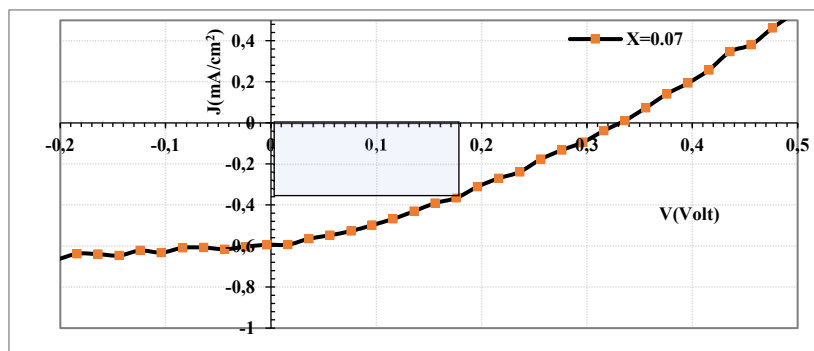
Figure 13. I-V characteristics under illumination by 100mW/cm2 white light for $(MnO)_{1-x}Cu_x$/n-Si with Cu content 7% at R.T.
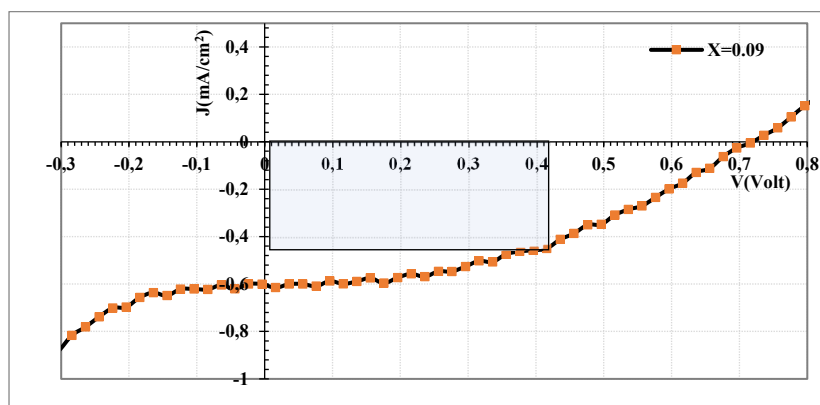

Figure 14. I-V characteristics under illumination by 100mW/cm^2 white light for $(MnO)_{1-x}Cu_x$/p-Si with Cu content 9% at R.T.

Table 5. Photovoltaic characterization (Voc, Isc, Vm, and Im) of $(MnO)_{1-x}Cux$/p and n-Si heterojunctions illuminated by 100mW/cm^2 white light with different Cu content prepared at RT

Sample	Isc (mA)	Im	Voc	Vm	FF	Pm (mW)	Efficincy (η)
MnO	0.66	0.47	0.70	0.38	0.39	0.1786	0.18
MnO-Cu(0.03)	0.70	0.38	0.65	0.54	0.45	0.2052	0.21
MnO-Cu(0.05)	0.64	0.46	0.55	0.34	0.44	0.1564	0.16
MnO-Cu(0.07)	0.60	0.36	0.33	0.18	0.33	0.0648	0.06
MnO-Cu(0.09)	0.62	0.45	0.72	0.42	0.42	0.189	0.19

4. CONCLUSION

The impact of doping (MnO) thin films with various Cu contents on their structural, morphological, and optical features was investigated in the current work. The films' polycrystalline nature was demonstrated by the XRD pattern, which had the highest peak present at an angle of 35.31, which corresponded to a reflection of (111). The ratio of 0.09 percent Cu is the best among the other ratios, according to the XRD and AFM analyses (it produced the highest crystalline size and the highest roughness). The absorbance coefficient rose for all samples as the doping ratio rose. It was discovered that as the doping ratio grew, the refractive index, extinction coefficient, and dielectric constant (real and imaginary parts) all increased. Hall Effect measurement showed that films have n-type to all samples except (0.03 and 0.05) in RT. J-V characteristic showed the maximum efficiency which was 0.21% at MnO-Cu (0.03) at RT and the value of the filling factor decreases with doped Cu at (RT).

ORCID

 Doaa T. Mohammed, https://orcid.org/0009-0001-7444-606X; **Ghuson H. Mohammed,** https://orcid.org/0000-0002-7401-3539

REFERENCES
[1] P.U. Asogwa, S.C. Ezugwu, F.I. Ezema, "Variation of optical and solid state properties with post deposition annealing in PVA-Capped MnO2 thin films," Superficies y Vacio, **23**(1) 18-22 (2010). https://www.fis.cinvestav.mx/~smcsyv/supyvac/23_1/SV2311810.pdf
[2] D.K. Naser, A.K. Abbas, and K.A. Aadim, "Zeta potential of Ag, Cu, ZnO, CdO and Sn nanoparticles prepared by pulse laser ablation in liquid environment," Iraqi Journal of Science, 2570-2581 (2020). https://doi.org/10.24996/ijs.2020.61.10.13
[3] J. Medina-Valtierra, J. Ramrez-Ortiz, V.M. Arroyo-Rojas, and F. Ruiz, "Cyclohexane oxidation over Cu2O–CuO and CuO thin films deposited by CVD process on fiberglass," Applied Catalysis A, **238**, 1-9 (2003). https://doi.org/10.1016/S0926-860X(02)00074-1

[4]   R. Naeem, R. Yahya, A. Pandikumar, N.M. Huang, M. Misran, Z. Arifin, and M. Mazhar, "Photoelectrochemical properties of morphology-controlled manganese, iron, nickel and copper oxides nanoball thin films deposited by electric field directed aerosol assisted chemical vapor deposition," Materials Today Communications, **4**, 141-148 (2015). https://doi.org/10.1016/j.mtcomm.2015.06.004

[5]   Z.S. Mahdi, and G.H. Mohammed, "Structural and Optical Properties of GO-doped (TiO_2: MoS_2) Films Prepared by Pulsed Laser Deposition," Journal of Survey in Fisheries Sciences, **10**(3S), 5658-5668 (2023). https://sifisheriessciences.com/journal/index.php/journal/article/view/1954/2010

[6]   F.K. Allah, S.Y. Abe, C.M. Nunez, A. Khelil, L. Cattin, M. Morsli, J.C. Bernede, *et al.*, "Characterisation of porous doped ZnO thin films deposited by spray pyrolysis technique," Applied Surface Science, **253**, 9241-9247 (2007). https://doi.org/10.1016/j.apsusc.2007.05.055

[7]   O. Nilsen, H. Fjellvag, A. Kjekshus, "Growth of manganese oxide thin films by atomic layer deposition," Thin Solid Films, **444**, 44-51 (2003). https://doi.org/10.1016/S0040-6090(03)01101-5

[8]   H. Unuma, T. Kanehama, K. Yamamoto, K. Watanabe, T. Ogata, M. Sugawara, "Preparation of thin films of MnO_2 and CeO_2 by a modified chemical bath (oxidative-soak-coating) method," Journal of Materials Science, **38**, 255-259 (2003). https://doi.org/10.1023/A:1021197029004

[9]   M.A. Abood, and B.A. Hasan, "A Comparison Study the Effect of Doping by Ga_2O_3 and CeO_2 On the Structural and Optical Properties of SnO_2 Thin Films," Iraqi Journal of Science, **64**(4), 1675-1690 (2023). https://doi.org/10.24996/ijs.2023.64.4.10

[10] S. Liang, F. Teng, G. Bulgan, R. Zong, and Y. Zhu, "Effect of Phase Structure of MnO_2 Nanorod Catalyst on the Activity for CO Oxidation," Journal of Physical Chemistry C, **112**, 5307-5315 (2008). https://doi.org/10.1021/jp0774995

[11] M. Nakayama, Y. Kashiwa, and K. Suzuki, "Electrochromic Properties of MnO_2-Based Layered Polymer Nanocomposite," Journal of the Electrochemical Society, **156**, D125-D130 (2009). http://dx.doi.org/10.1149/1.3072896

[12] N. Sakai, Y. Ebina, K. Takada, and T. Sasaki, "Electrochromic Films Composed of MnO2 Nanosheets with Controlled Optical Density and High Coloration Efficiency," Journal of the Electrochemical Society, **152**, E384-E389 (2005). https://doi.org/10.1149/1.2104227

[13] D. Yuping, M. He, L. Xiaogang, L. Shunhua, and J. Zhijiang, "The microwave electromagnetic characteristics of manganese dioxide with different crystallographic structures," Physica B, **405**, 1826-1831 (2010). https://doi.org/10.1016/j.physb.2010.01.055

[14] A.K.M. Farid ul Islam, R. Islam, and K.A. Khan, "Studies on the thermoelectric effect in semiconducting MnO_2 thin films," Journal of materials science: Materials in electronics, **16**, 203-207 (2005). https://doi.org/10.1007/s10854-005-0766-1

[15] H. Xia, W. Xiao, M.O. Lai, and I. Lu, "Facile Synthesis of Novel Nanostructured MnO_2 Thin Films and Their Application in Supercapacitors," Nanoscale Res. Lett. **4**, 1035–1040 (2009). https://doi.org/10.1007/s11671-009-9352-4

[16] R.K. Jamal, M.A. Hameed, and K.A. Adem, "Optical properties of nanostructured ZnO prepared by a pulsed laser deposition technique," Materials Letters, **132**, 31-33 (2014). https://doi.org/10.1016/j.matlet.2014.06.047

[17] K. Tian, M. Prestgard, and A. Tiwari, "A review of recent advances in nonenzymatic glucose sensors," Mater. Sci. Eng. C, **41**, 100-118 (2014). https://doi.org/10.1016/j.msec.2014.04.013

[18] Z. Muslima, and J. Podder, "Structural, optical and electrical properties of Cu: MnO_2 nanostructured thin films for glucose sensitivity measurements," SN Applied Sciences, **2**, 385-396 (2020). https://doi.org/10.1007/s42452-020-2191-8

[19] K.A. Aadim, R.A. Alansary, and S.A. Alhady, "Effect of Mn concentration on the structural and optical properties of SnO_2 thin films prepared by pulse laser deposition," Journal of Research and Method in Education (IOSR-JRME), **4**(4), 12-19 (2014). https://www.doi.org/10.9790/7388-04441219

[20] G.A. Al-Dahash, Q.M. Salman, and S.F. Haddawi, "Study the Effect of Copper (Cu) Doping on the Structure Properties of Zinc Oxide (ZnO) Prepared by Using Pulsed Laser Deposition (PLD)," J. Univ. Kerbala, **15**(2), 87-95 (2017). https://iasj.net/iasj/pdf/f612004da9aae7d2

[21] G.K. Williamson, and R.E. Smallman, "III. Dislocation Densities in Some Annealed and Coldworked Metals from Measurements on the X-Ray Debye-Scherrer Spectrum," Philos. Mag.: A journal of experimental and applied physics, **1**(1), 34-46 (1956). https://doi.org/10.1080/14786435608238074

[22] H. Kim, and C.M. Gilmore, "Transparent conducting aluminum-doped zinc oxide thin films for organic light-emitting devices," Appl. Phys. Lett. **76**(3), 259-261 (2000). https://doi.org/10.1063/1.125740

[23] S. Sami, S.S. Chiad, K. Haneen, T. Mubarak, N.F. Habubi, M.K. Mohammed, and A. Khadyair, "Fabrication and study the structure, optical and dispersion parameters of PMMA with $InCl_3$ additive," J. Glob. Pharma Technol. **11**(4), 369-374 (2019).

[24] M.G. Hutchins, O. Abu-Alkhair, M.M. El-Nahass, and K. Abd El-Hady, "Structural and optical characterisation of thermally evaporated tungsten trioxide (WO_3) thin films," Mater. Chem. Phys. **98**(2-3), 401-405 (2006). https://doi.org/10.1016/j.matchemphys.2005.09.052

[25] M. Thakurdesai, N. Kulkarni, B. Chalke, and A. Mahadkar, "Synthesis of CdSe Films by Annealing of Cd/Se Bilayer," Chalcogenide Lett. **8**(3), 223-229 (2011). http://chalcogen.ro/223_Thakurdesai.pdf

[26] S. Sönmezoğlu, A. Arslan, T. Serin, and N. Serin, "The effects of film thickness on the optical properties of TiO_2–SnO_2 compound thin films," Phys. Scr. **84**(6), 65602, 2011. https://doi.org/10.1088/0031-8949/84/06/065602

[27] A. Gultekin, "Effect of Au Nanoparticles Doping on The Properties of TiO_2 Thin Films," Materials Science (Medžiagotyra), **20**(1), 1392-1320 (2014). https://doi.org/10.5755/j01.ms.20.1.3709

[28] D. Na, L. Satyanarayana, G.-P. Choi, Y.-J. Shin, and J.S. Park, "Surface morphology and sensing property of NiO-WO_3 thin films prepared by thermal evaporation," Sensors, **5**(12), 519-528 (2005). https://doi.org/10.3390/s5120519

[29] A. Peng, Y. Gao, Q. Yang, X. Zuo, H. Tang, and G. Li, "MoC/MnO composite materials as high efficient and stable counter electrode catalysts for dye-sensitized solar cells," Journal of Materials Science: Materials in Electronics, **31**, 1976-1985 (2020). https://doi.org/10.1007/s10854-019-02717-8

ДОСЛІДЖЕННЯ СТРУКТУРНИХ, ОПТИЧНИХ ТА ЕЛЕКТРИЧНИХ ВЛАСТИВОСТЕЙ ЛЕГОВАНОГО MnO З МІДНИМИ ТОНКІМИ ПЛІВКАМИ, ПІДГОТОВЛЕНИМИ ЗА ТЕХНІКОЮ PLD ДЛЯ ЗАСТОСУВАННЯ У СОНЯЧНИХ ЕЛЕМЕНТАХ

Доаа Т. Мохаммед, Гусон Х. Мохаммед

Факультет фізики, Науковий коледж, Багдадський університет, Багдад, Ірак

У поточному дослідженні концентровані лазерні імпульси Nd:YAG при 500 мДж з другим випромінюванням при 1064 нм (ширина імпульсу 9 нс) і частотою повторення (6 Гц) для 300 лазерних імпульсів, що падають на поверхню мішені, використовувалися для покриття скляних підкладок тонкими плівками MnO. За допомогою рентгенівського дифрактометра (XRD), атомно-силового мікроскопа (АСМ) та спектрофотометра UV-Vis визначено структурні, морфологічні та оптичні характеристики плівок, легованих різними концентраціями Cu (0,03; 0,05; 0,07; і 0,09). Результати показують, що плівки є полікристалічними, з найбільшим піком, що з'являється під кутом 35,31, або дзеркальним (111). Кристалічний розмір осаджених тонких плівок був розрахований за допомогою формули Дебая-Шерера, і було виявлено, що він збільшується від 11,8 нм для нелегованого MnO_2 до 29,6 нм для легованого (MnO) зі збільшенням вмісту Cu від x=0 до x=0,09 за переважної орієнтації (111). Усі зразки мають кубічну структуру. Крім того, результати показали, що вміст Cu в плівках впливає на морфологію поверхні. За результатами АСМ-аналізу було виявлено, що шорсткість і середній діаметр змінюються при додаванні Cu до структури, причому найбільше значення спостерігається при співвідношенні Cu 0,09, що дорівнює 65,40 і 71,21 нм відповідно. Для дослідження оптичного пропускання використовували спектрофотометр UV–Vis. Було виявлено, що при збільшенні вмісту Cu в плівках пропускна здатність плівок зменшується. Вимірювання ефекту Холла показують, що всі підготовлені плівки при кімнатній температурі мають два типи провідності: p-тип і n-тип. Було вивчено електричні характеристики $(MnO)_{1-x}Cu_x/PSi$ сонячної батареї з гетеропереходом і виявлено, що ефективність (η) зменшується зі збільшенням вмісту Cu.

Ключові слова: *наночастинки Cu; тонкі плівки MnO; техніка PLD; структурні властивості; оптичні властивості*